SLAG METAL ENTRAINMENT IN GAS STIRRED LADLES

Model Studies of Slag Metal Entrainment in Gas Stirred Ladles

by

ANAND SENGUTTUVAN, M.Tech.

A Thesis Submitted to the School of Graduate Studies

in Partial Fulfillment of the Requirements for the Degree

Doctor of Philosophy

McMaster University

DOCTOR OF PHILOSOPHY (2016)

Department of Materials Science and Engineering

McMaster University

Hamilton, Ontario, Canada

TITLE	Model Studies of Slag Metal Entrainment in Gas Stirred Ladles
AUTHOR	Anand Senguttuvan, B.E. (GCE Salem, India), M.Tech. (IIT Kanpur, India)
SUPERVISOR	Dr. Gordon A. Irons
NUMBER OF PAGES	xxix; 275

Lay Abstract

The entrainment of liquid slag into liquid steel in gas stirred-steelmaking ladles is known to increase the rate of refining drastically. However, there is lack of correlation between degree of entrainment and ladle operating conditions, which this thesis addresses through mathematical modeling.

Abstract

In gas stirred steelmaking ladles, entrainment of slag into metal and *vice versa* takes place. The slag entrainment has been shown to abruptly increase the mass transfer rates of refining reactions through high temperature and water modeling studies of the past. However such an effect has not been correlated with the degree of entrainment, since the latter has not been quantified in terms of operating parameters like gas injection rate and fluid properties. Much of the past works are limited to finding the critical conditions for onset of entrainment. The difficulty lies in measuring the degree of entrainment in industrial ladles or even in a water model. Mathematical modeling is also challenging due to the complexity of the multiphase phenomena. So in this thesis, a modular mathematical modeling approach is presented wherein the phenomena of slag entrainment into metal is resolved into four aspects, models developed for each and finally integrated to study its role.

The individual models are (1) multiphase large eddy simulations to simulate slag entrainment in a narrow domain that receives its boundary conditions from (2) single phase RANS simulation of a full ladle, (3) a Lagrangian particle tracking method to compute the residence times of slag droplets in metal phase and (4) a kinetic model that integrates the above three models to compute mass transfer rate as a function of degree of entrainment.

Mass transfer rate predictions comparable to a literature correlation were obtained. This supports the modeling approach and also the assessment of role of various system parameters on entrainment characteristics. In essence, the present work shows a systematic approach to model and study the complex multiphase phenomena.

Acknowledgements

I am blessed to have Dr. Irons as my supervisor. I have heard my friends say ‘not every professor could be Dr. Irons’! Do I have to say anything more? At this point I should thank my M.Tech supervisor Dr. Dipak Mazumdar at IIT Kanpur for his strong recommendation that landed me here.

My sincere thanks to my supervisory committee members Dr. Ken Coley and Dr. Stephen Tullis for their critical suggestions at various stages of this project.

My special thanks to Dr. Stéphane Popinet, for creating the valuable and elegant *Gerris Flow Solver*, the lifeline of this thesis, and making it free for the scientific community. Huge thanks to the open source software community for their multitude of applications that made the transition to Ubuntu possible.

I appreciate the help of Mr. Owen Kelly during my experiments in the water modeling lab. I thank Mr. Ed McCaffery for his help in setting up and fixing my computers. I would like to thank the staff members of Materials Science and Engineering Department, particularly Ms. Diana Maltese, Ms. Nanci Cole and Ms. Danielle Marcellin for their sweet disposition and Ms. Carolina Castellanos for her friendship. I would like to extend the thanks to McMaster University as a whole for all its services to the graduate students.

The generous financial support from Natural Sciences and Engineering Research Council of Canada and McMaster is gratefully acknowledged.

I want to thank the city of Hamilton, its courteous people, for providing a safe and a comfortable living throughout my grad studies. Special thanks to Hamilton Street Railway (HSR) for their best service for commuting anywhere in Hamilton.

I thank my friends, Kumar Krishnapisharody, Ganesh Niranjan, Kashif, Hamed Asgari, Tai Xi, Alan Galindo, Kavita & Jeyakumar, Sagar, Rahul, Madhumanti, Sayantee, Mukesh and Ameya for their friendship and support in various ways.

Finally I thank the support from my family, especially my parents for their unconditional love that gave me the freedom to be whatever I am.

Table of Contents

List of Figures

List of Tables

List of Symbols

Abbreviation

DBD	Drop by Drop Kinetic model
LES	Large Eddy Simulation
LP	Lower phase
LPT	Lagrangian Particle Tracking
QSP-RANS	Quasi Single Phase RANS
RANS	Reynolds Averaged Navier Stokes
SEM	Synthetic Eddy Method
TKE	Turbulence Kinetic Energy
UL	Interface between Lower and Upper phases
UP	Upper phase
VOF	Volume of Fluid
WDR	LES performed With Droplet Removal
WODR	LES performed Without Droplet Removal

Roman

$\boldsymbol{a}$	acceleration vector
a_{ij}	Cholesky decomposition of Reynold stress tensor
A	Area
A_{ULeye}^{nom}	Nominal area of UL at eye
C_{AM}	Added mass coefficient
C_D	Drag coefficient
d	droplet diameter
$\overline{d}$	Arithmetic mean diameter
d_{32}	Sauter mean diameter
d_P	equivalent particle diameter defined based on the particle volume

D	Generic or mass diffusion coefficient.
D_{ves}	Vessel or ladle diameter
DFS	Distance to Free Surface
Eo	Eotvos number
f	Frequency of a probability distribution function
F	Volume fraction function
$\boldsymbol{F}$	Force vector
g	gravitational constant, 9.8 m/s^2
h	thickness or depth of a phase, channel half thickness
i, j, k	counter index
k	Turbulence kinetic energy (TKE)
k	Mass transfer coefficient
l	length
L	GfsBox length, length of a cell in cellular flow case in LPT
L_S	Partition coefficient of species S
$LSfac$	Length scale factor
`Level`	Refinement level of a cell in Gerris flow solver
m	mass, counter index
n	counter index, coordinate of normal direction
n	exponent, number of moles
N	Number of eddies, any number
$\dot{N}$	Number entrainment rate
p	Probability, pressure in Navier Stokes equation
Q	Gas flow rate
Q_{sp}	Specific gas injection rate
r, z	Cylindrical coordinates: r - radial; z - axial
R^2	Correlation coefficient
R_P	Plume radius
R_{ij}	Reynolds stress tensor

R_{eye}	Radius of slag eye
R_{ves}	Radius of Vessel or ladle
Re_P	Radius of particle
Re	Reynolds number
Re_τ	Reynolds number based on friction velocity
S	species
Sc	Schmidt number
t	Time
t_c	Contact time in Penetration theory
t_{res}	Residence time
$\bar{t}_{res}$	Mean residence time
TI	Turbulence intensity
TTS	Thickness of thin slice
$\boldsymbol{u}$	Instantaneous Velocity vector
$\boldsymbol{u}^{'}$, $u_i^{'}$	Fluctuating velocity vector
$\boldsymbol{U}$, U_i	Mean velocity vector
$\boldsymbol{U}_F$	Instantaneous fluid velocity vector known to a particle
$\boldsymbol{U}_P$	Instantaneous particle velocity vector
U_0	Maximum velocity in cellular flow case in LPT
u_τ	Friction velocity
U_b	Bulk velocity
U_{term}	Terminal velocity of particle
U_{ch}	Characteristic velocity
U_P	Plume velocity
U^+	Velocity scaled by friction velocity
u, v, w	Instantaneous velocity components in Cartesian coordinates
U, V, W	Mean velocity components in Cartesian coordinates
U_r, U_z	Mean velocities of QSP-RANS (cylindrical coordinates)

ULdrop	UL interface at a *drop*
ULeye	UL interface at *eye*
ULflat	UL interface at *flat*
$\overline{v}_L$	Average velocity near *ULeye* extracted from LES
$\overline{v}_{RANS}$	Average velocity near *ULeye* extracted from RANS
$\dot{V}$	Volumetric entrainment rate
V_B	Volume of eddy box
V_P	Volume of particle
VPU	Scaled and normalized volumetric entrainment rate
$\mathbf{x}$	Grid point, $\mathbf{x}=(x, y, z)$, in the inlet plane (for SEM)
$\mathbf{x}^k$	Random variable for location of eddies (for SEM)
$\boldsymbol{x_P}$	Particle location in LPT, $\boldsymbol{x_P} = (r_P, z_P)$
x_{32}	Sauter mean droplet diameter
$\bar{x}$	Arithmetic mean droplet diameter
x, y, z	Cartesian Coordinates

Subscript

0	Initial
150	Ladle with metal capacity of 150 ton
44	Ladle with metal capacity of 44 ton
A	Area averaged
AM	Added mass
G	Buoyancy
cl	Centre-line
crit	Critical
D	Drag
E	Eddy
eff	Effective
eq	Equilibrium

F	Fluid
L	Lower phase
max	Maximum
min	Minimum
P, $part$	Particle
PG	Pressure Gradient
res	Residence
tr	Transitional
U	Upper phase
y	y plane, channel LES

Superscript

nom	Nominal

Greek

α	Void fraction
β	Mass transfer rate constant
δ_s	Kronecker delta
Δ	Cell size, change in a quantity,
∇	delta operator
ε	Specific stirring rate, dissipation of TKE
ϵ_j	Random variable for eddy spin direction in SEM
η	normal coordinate to *ULeye*
θ	angle (of interface)
κ	Curvature of interface (in force due to surface tension)
λ	decay constant, linear scaling factor
μ	also mean, also μ_U.
ν	kinematic viscosity
ϕ	Generic variable
π	3.1416...

ψ	Blending function in free surface correction
ψ_i	Random variables in Eddy interaction model
ρ	density
σ	Interfacial tension, also standard deviation
τ_R	Particle relaxation time
ω	Specific rate of dissipation of TKE

Brackets

$(\ )$	Concentration of a species in bulk of Upper phase
$[\ ]$	Concentration of a species in bulk of Lower phase
$[\ ]_i$	Concentration of a species at the interface from LP side
$\langle\ \rangle$	Reynolds or Ensemble Averaged

1. Introduction

1.1 Secondary Steelmaking

Secondary steelmaking, also referred to as Ladle Metallurgy, is where the liquid steel received from a primary steelmaking furnace is fine tuned to produce steel of desired composition and thereafter sent to casting. Whereas the primary steelmaking is aimed at rapid refining to arrive at broad steel specifications, the growing requirements of steel quality has demanded a separate steel processing facility, namely the secondary steelmaking, to enable finer control over furnace atmosphere, to lower sulphur contents, to remove and/or modify inclusions and to control temperature (MSTS, 1998, Gosh & Chatterjee, 2008). Mainly carried out in ladles, various secondary steelmaking operations are argon purging to float out inclusions, degassing to remove dissolved Hydrogen and Nitrogen, decarburization, deoxidizer and alloying additions, lime injection for desulphurization and addition of Ca-Si alloy for inclusion modification. Moreover, the temperature lost since the liquid steel tapping from furnace until teeming into casting mould is usually compensated by arc heating provided by electrodes introduced through the slag.

1.2 Ladle Furnace and Multiphase Flow

The ladle is a refractory lined vessel used to contain liquid steel tapped from primary steelmaking furnace and take the steel to casting. Since the 1970s it has been used to carry out various secondary steelmaking operations and hence referred to as ladle furnace (LF). A schematic of LF facility is shown in Fig. 1.1. The height of LF can vary between 2.5 to 4 m for liquid steel of capacity 45 and 240 ton, respectively. At the bottom of the vessel are the porous plug for inert gas (Argon) injection and a slide gate to discharge the liquid steel. As labeled in a schematic in Fig. 1.2, a typical LF consists of various fluid zones namely the bulk liquid slag, the bulk liquid steel (metal), the gas-liquid plume, slag eye and spout. Although industrial ladles have eccentric gas injection, as in Fig. 1.1, the schematic in Fig. 1.2 is depicted with a

central gas injection, since that has been the case with numerous fundamental studies of the past on fluid flow in the ladle and also the case with the present work. The central gas injection presents a simplified flow field (axisymmetric) for the investigation of certain fundamental aspects of ladle flow that are not strongly dependent on the eccentricity of gas injection.

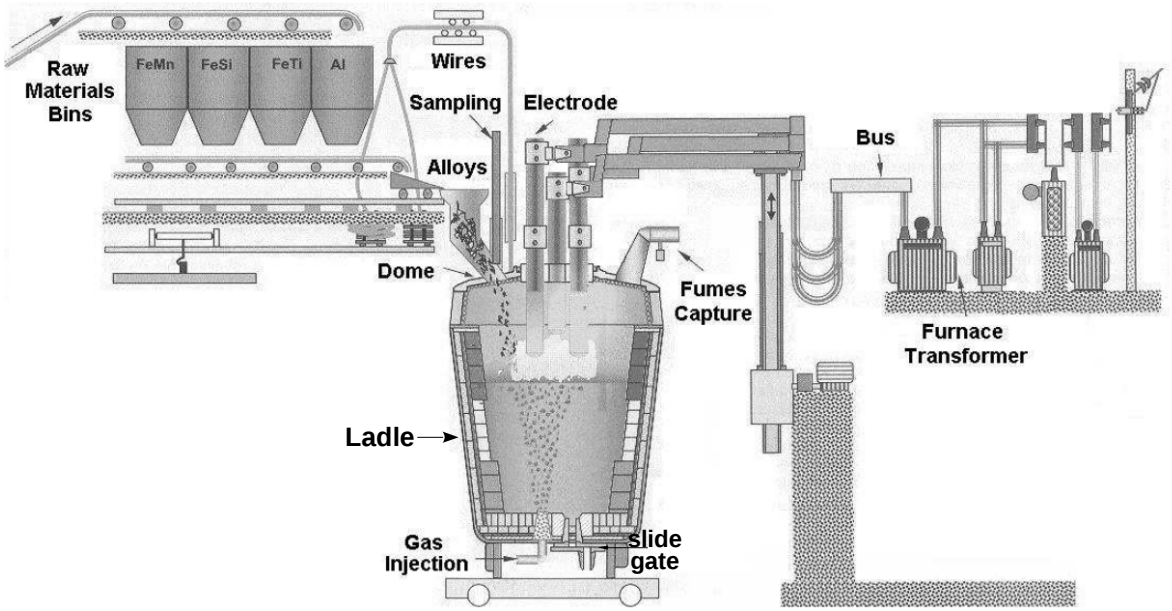

Figure 1.1. Ladle furnace station showing gas stirred ladle supplied with electric arc heating and power supply systems (right) and alloying addition systems (left) (Sampaio *et al*, 2007)

In a LF, a synthetic basic and non-oxidising slag (CaO-Al_2O_3-MgO-SiO_2) is added on the top of the metal to absorb non-metallic products of refining treatment, to protect the metal from picking up atmospheric gases and minimize heat loss through radiation (Gosh & Chatterjee, 2008). Usually the slag layer is thin with a thickness of around $1/20^{th}$ of the metal height.

The liquid steel is stirred by gas injection to maintain thermal and chemical homogeneity, float out inclusions and control the rate of slag-metal refining reactions when needed. The gas injection rates are low for homogenization and somewhat high for refining reactions (Mazumdar & Guthrie, 1995), but not high enough to form a jet. The injected gas,

while rapidly expanding due to heating, soon breaks into bubbles and rises in the metal due to buoyancy. Due to the drag exerted by bubbles the surrounding liquid rises along with the bubbles. This two phase region in motion is called the plume and is the momentum source to cause stirring in the ladle. Due to further bubble breaking and lateral lift the plume expands with height (Sheng & Irons, 1995) described by a parabolic profile for plume radius with height (Krishnapisharody & Irons, 2007b).

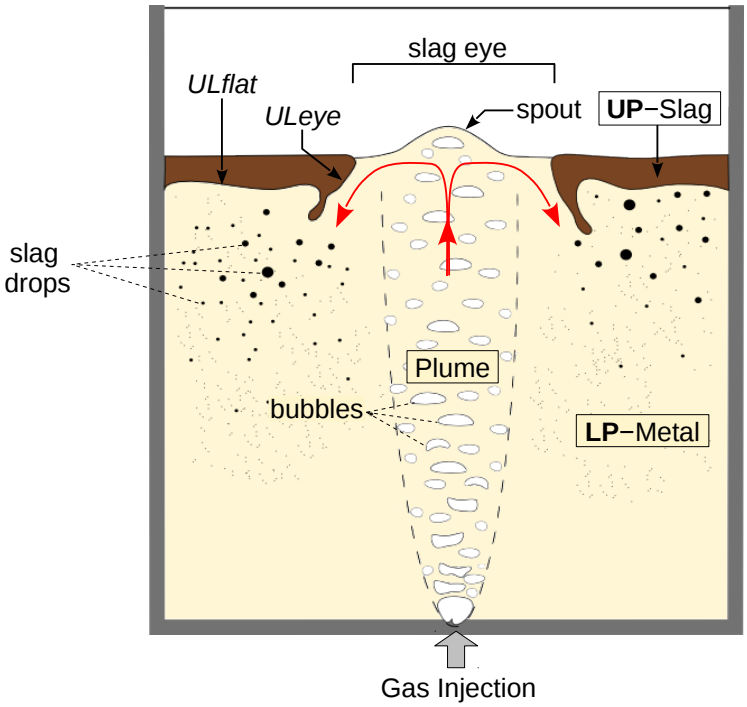

Figure 1.2. Schematic of gas stirred ladle showing various fluid zones. Arrows in the slag eye region depict the liquid flow direction. LP−lower phase; UP−upper phase; *ULflat* and *ULeye* are the interfaces between LP and UP at more or less horizontal and slag eye regions, respectively.

When the rising plume reaches the top slag, the slag layer is pushed laterally exposing a portion of surface area of metal to the atmosphere known as ‘slag eye’. The upward momentum of the plume causes a raised surface at the slag eye known as ‘spout’. While all the bubbles escape at the spout, the metal is confined to flow horizontally which further pushes the slag laterally and widens the slag eye. While the slag eye enables addition of alloying elements directly into metal, it also exposes the metal to atmosphere, which is undesirable.

In the eye region, the laterally flowing metal then flows downwards near the slag metal interface and the relative motion between the two phases cause entrainment of slag into metal. By another mechanism, entrainment of metal into slag also takes place.

Many past studies have shown that slag metal entrainment greatly increases the slag metal interfacial area and hence the interfacial mass transfer rates for refining reactions such as desulphurization. Figure 1.3 shows results of mass transfer experiments in a 2.5 ton pilot scale ladle (Ishida *et al*, 1981) wherein there is a sudden increase in mass transfer rate above certain gas injection rate; water modeling studies in the later years confirmed that this phenomenon is due to slag entrainment. However the entrained phases may become entrapped without rejoining their parent phases: entrapped slag in metal may lead to cleanliness issue and entrapped metal into slag may lead to a yield loss issue. Although such effects have been observed in the past works both in industrial ladles and their water models, they were not related to the operating parameters like gas injection rate and fluid properties in a quantitative manner. Therefore the overall objective of this thesis is to provide a quantitative model for entrainment in ladle and assess the aforementioned effects.

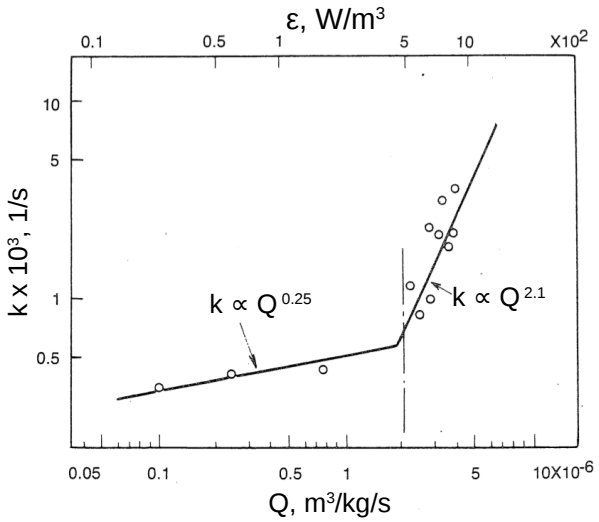

Figure 1.3. Plot of mass transfer rate constant (k) versus gas flow rate (Q) obtained from a 2.5 ton converter (Ishida *et al*, 1981)

1.3 Motivation

1.3.1 Degree of Entrainment

To assess the effects of entrainment, the 'degree of entrainment' must be quantified, which can be defined through the following parameters:

1. Rate of entrainment
2. Size distribution of entraining drops and
3. Residence time distribution of entrained drops.

1.3.2 Scope for Experimental Measurements

Experiments to measure the degree of entrainment in industrial ladles are very challenging and any such measurements made to this date are of very limited scope. So entrainment has been studied mostly in aqueous models. Even in these aqueous models measurements of the degree of entrainment are very limited due to lack of appropriate entrainment detection methods. In aqueous models, water and various oils have been used as the phases simulating steel and slag, respectively. An electrical resistivity method generally used to detect gas bubbles in water, when the bubbles intercept the probe element, cannot be applied to detect oil droplets due to the problem of wetting (Tanaka, 1986). A non-contact inductive-conductance based method, similar to that used to detect slag entrainment in teeming (Theissen, 2004), is also not applicable both in aqueous and industrial ladle†. Fluid sampling methods have been used in limited studies (reviewed in Sec. 2.3). However from preliminary trials by the author, wetting of oil in walls of sampling tube (despite using a Teflon® tube) deformed the droplets and therefore only time averaged volume fraction of entrainment drops at the sampling location could be detected and information regarding degree of entrainment cannot be obtained.

With all these limitations for experimental measurements, it was decided to study entrainment through mathematical models supplemented by experimental measurements wherever available.

† This is because, the small change in electrical resistance in a detecting probe due to the passage of droplet of upper phase (oil/slag) is superseded by larger resistance offered by the surrounding lower phase (water/metal). Lower phase having more conductance than upper phase, has more induced eddy currents that eventually increases the electrical resistance in the probe.

1.3.3 Need for Mathematical Modeling

Entrainment being a multiphase fluid flow phenomenon requires a multiphase model in conjunction with solution of Navier-Stokes equation. Of the many multiphase models (briefly reviewed in Sec. 2.6.2), interface tracking methods are the only class where the actual interface location of every particle and therefore their shapes are computed. However, this requires increased mesh and time resolutions which in turn increases the computational cost.

Secondly, entrainment being a dynamic phenomenon, requires at least the resolution of the large eddies in the flow, to trigger instability in the slag metal interface that eventually lead to entrainment. So Large Eddy Simulations (LES) are required to simulate the fluid flow, which is again computationally intensive. These issues make the complexity and cost of mathematical modeling prohibitively high. This is the reason, as will be reviewed in Chapter 2, why the past mathematical modeling studies are very limited in scope.

Since a brute force approach cannot be taken, in the present study, the entrainment problem is divided into several steps that are not mutually coupled. Generic and specific mathematical models for each of these steps are constructed through careful consideration of various system parameters and are finally integrated to assess the role of entrainment on the aforementioned effects.

1.4 Objectives of the Research

The complexity and economics of mathematical modeling of entrainment necessitated the breakdown of the problem into following steps. These are one way coupled in the order they are listed and also as depicted in Fig. 1.4.

I. **To estimate the rate and size distribution of slag entrainment**: This involves multiphase LES of the onset of slag entrainment for various conditions namely gas injection rate and fluid properties and is the most time consuming step. The aim of these simulations is to obtain the rate and size distribution of entrained droplets only at the time of their onset; shortly after a droplet entrains into the metal it is removed from the simulation. Since this is concerned with the events around a smaller region of onset

of entrainment, the LES domain is confined. The inflow conditions for this confined LES domain are obtained from inexpensive RANS simulations of metal flow for the whole ladle. These aspects are detailed in Ch. 4. This multiphase LES approach is first tested on an aqueous model in Ch. 5 and then applied to the steel-slag system in Ch. 6.

II. **To calculate residence time distribution**: Using the RANS flow field that provided inflow conditions for Step I, the residence times of various size groups of slag droplets generated in Step I are computed. This is achieved by the Lagrangian particle tracking method described in Ch. 7. The cleanliness issue is addressed through this Step in Ch. 8.

III. **To simulate mass transfer due to entrainment**: The entrainment rate and size distribution obtained from Step I and the residence time distribution obtained from Step II are fed into a kinetic model, known as drop-by-drop model, developed in Ch. 3, to calculate the overall mass transfer rate in Ch. 8.

Thus, the kinetics of mass transfer and metal cleanliness are assessed as function of gas injection rate and fluid properties. However, the third effect of entrainment, namely the problem of metal entrainment in slag is not addressed in this thesis and is a topic for future research.

1.5 Other Details

Nomenclature: The following is a list of certain symbols and terms widely used in this thesis:

- **LP** - **L**ower **P**hase - appear as **L** in subscripts to mathematical quantities
- **UP** - **U**pper **P**hase - appear as **U** in subscripts to mathematical quantities
- **UL** - Interface between the bulk **U**pper and **L**ower phases as in ***ULflat*** and ***ULeye*** (labeled in Fig. 1.2).
- `Gfs` - Prefix of objects of Gerris Flow Solver, the CFD software used in this Thesis.
- Specific gas injection rate, Q_{sp} - gas injection rate per ton of lower phase
    - Gas injection rate - volume of inert gas injected per unit time at standard temperature and pressure (STP)

- Gas flow rate, Q - volumetric flow rate of inert gas calculated for *in situ* temperature and pressure conditions inside a ladle at half bath height

Other Details:

- All smooth curves of plots in the charts of this thesis are interpolated using cubic-splines
- Best fits for various model results were performed using the curve fitting tools of Libreoffice Calc and data analysis software, Qtiplot.
- All CFD simulations were run on a AMD FX™–8350 Eight-Core Processor–8 GB RAM–machine

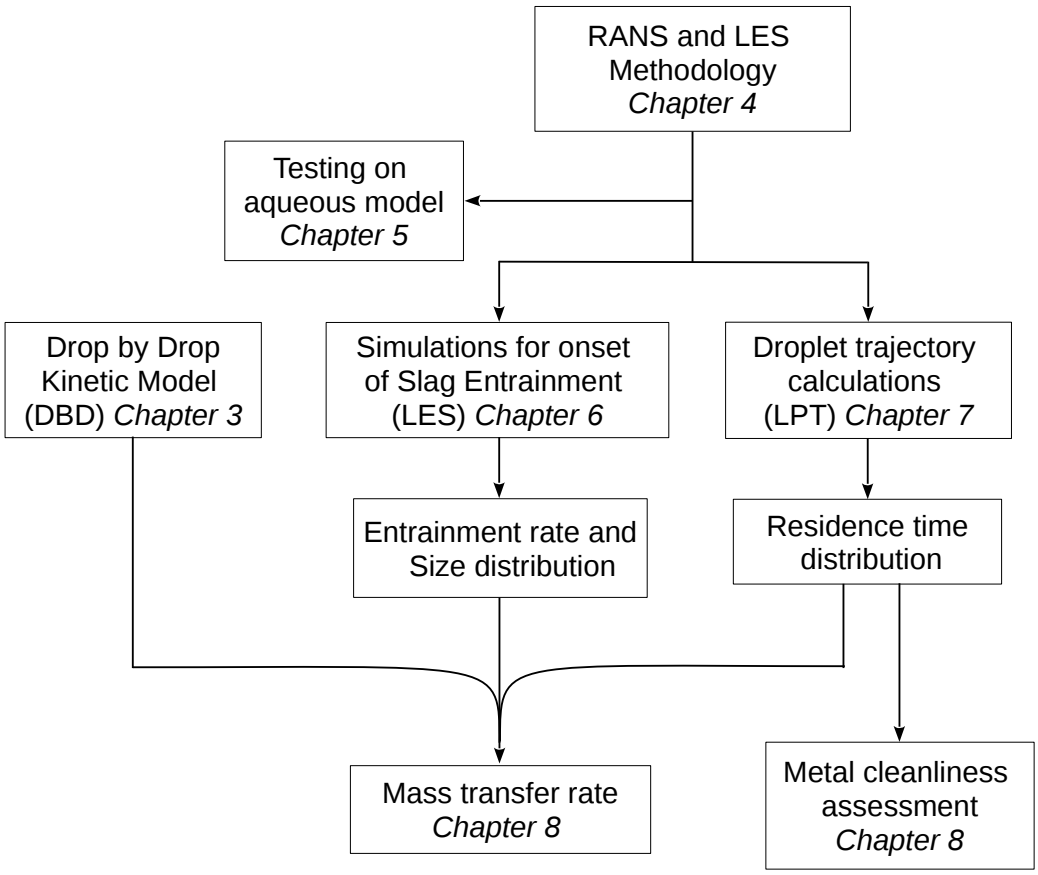

Figure 1.4. Flowchart of major steps in mathematical modeling of the entrainment phenomena in this thesis

2. Literature Review

Over the past three decades a considerable amount of research on entrainment and its effects on gas stirred ladles have been reported in the open literature. Though few studies on industrial ladles have been made to obtain more realistic picture, due to difficulties in observation and measurements they pose, entrainment phenomenon has been conveniently and mostly studied in laboratory scale water models. Most of them have been devoted to find the critical conditions for entrainment and role of entrainment on liquid-liquid mass transfer in gas stirred systems. Various types of mechanisms and models of entrainment have been proposed. The type and mechanism of entrainment varied between studies depending on the system dimensions and the method used to create flow in the system. This chapter will review the possible entrainment mechanisms and their effect in gas stirred ladles. Additionally the past works on CFD simulations of slag metal entrainment and RANS modeling aspects of gas liquid flow in gas stirred ladle are reviewed.

2.1 Entrainment of Upper Phase into Lower Phase

When the downward flow of lower phase (LP) close to the two phase interface at 'eye' (*ULeye*), as shown schematically in Fig. 1.2, exceed a critical velocity, the layer of upper phase (UP) is pulled down into as ligaments, which might tear down into droplets. The droplets being carried away by the stream of downward flow is called entrainment of UP.

2.1.1 Critical Conditions for Onset of Entrainment

Asai *et al* (1988) assumed that a droplet of UP detaches when the LP kinetic energy pulling the droplet exceeds the energy due to new surface creation and the buoyancy work done; for a spherical droplet this is expressed as,

$$\underset{\text{(Kinetic energy)}}{1/2(\rho_U \pi d^3/6)U^2} \geq \underset{\text{(Surface energy)}}{\pi d^2 \sigma} + \underset{\text{(Buoyancy work done)}}{(\rho_L - \rho_U) g \pi d^3/6 \cdot d/2}, \tag{2.1}$$

where, d is the droplet diameter, U is droplet velocity ρ_U and ρ_L are the densities of UP and LP, respectively and σ is the interfacial tension. The balance of energies in Eq. (2.1) gives the critical velocity for entrainment,

$$U_{crit} = \left[\frac{1}{\rho_U}\left(\frac{12\,\sigma}{d} + \Delta\rho g\, d\right)\right]^{1/2}, \tag{2.2}$$

The minimum critical velocity existing at the minimum droplet size (obtained by setting $\partial / \partial d(U_{i,crit}) = 0$),

$$d_{crit} = \left[\frac{12\,\sigma}{\Delta\rho g}\right]^{1/2} \tag{2.3}$$

is

$$U_{crit} = \left[48\,\frac{\Delta\rho g\ \sigma}{\rho_U^2}\right]^{1/4} \tag{2.4}$$

Moreover Asai *et al* measured critical velocities for various combinations of liquid-liquid properties from video recordings of flow in a two dimensional model†. For those fluid properties, the critical velocities were calculated using Eq. (2.4). The comparison of calculated and measured velocities in Fig. 2.1 shows that the former are in fairly good agreement with the latter.

Similarly, Mietz *et al* (1991b), using force balance and considering the inclined interface at eye obtained,

$$d_{crit} = \left[\frac{6\,\sigma}{\Delta\rho g\,\cos\,\theta}\right]^{1/2} \tag{2.5}$$

and

$$U_{crit} = \left[\frac{128}{3}\cos\,\theta\,\frac{\Delta\rho g\ \sigma}{\rho_U^2}\right]^{1/4} \tag{2.6}$$

† Although the details about the 2D model are not given in the reference, it is most likely similar to the setup of Krishnapisharody (2007) or that of Savolainen *et al* (2009) whose details are provided in Figs. 5.1 and 2.12, respectively.

where θ is the angle of inclination of interface with respect to the vertical axis. These expressions are similar to, but not verified as that of Asai *et al*. For $\theta = 30°$, the U_{crit} predicted by Eq. (2.6), for the cases in Fig. 2.1, is <10% smaller than those predicted by Eq. (2.4), but are closer to the measured velocities.

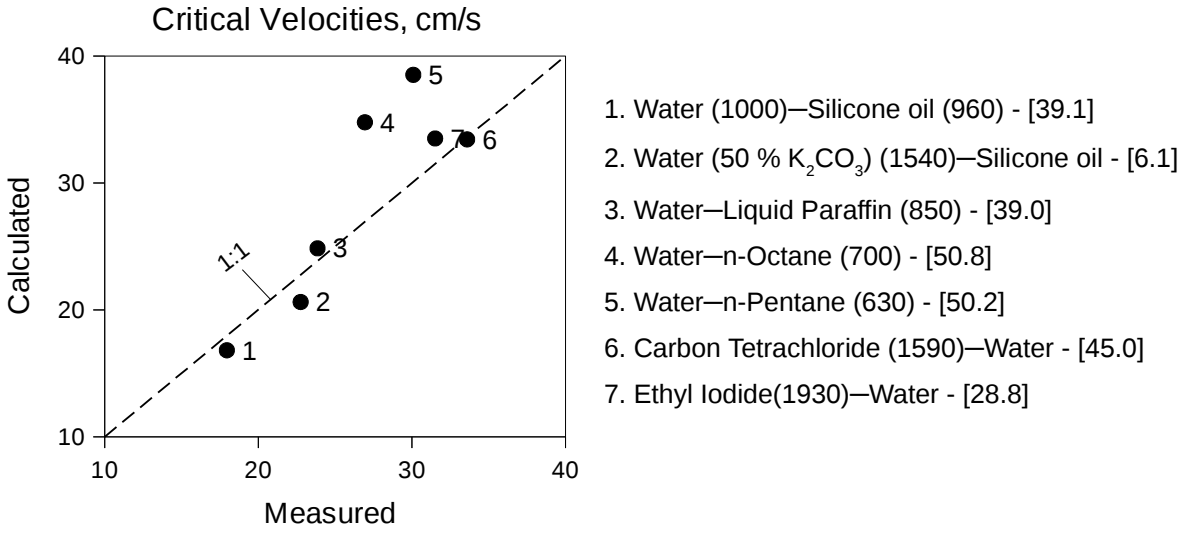

Figure 2.1. Comparison between measured and calculated (using Eq. (2.4)) critical velocities for onset of entrainment, from Asai *et al* (1988). The system labels also contain phase densities in kg/m^3 in parenthesis and interfacial tension in mN/m in square brackets.

From visual observations, Kim *et al*. (1987a) noted the critical gas flow rates for onset of entrainment in gas stirred vessel for several combinations of aqueous phases and various thicknesses of upper phase. In their study a detached droplet was considered as entrainment only if it was pulled as deep as 3 cm from the location of two phase interface before gas injection. They found that the critical gas flow rate (Q_{cr}) was a function of interfacial tension, density difference between the two phases and the LP bath height (h_L) and obtained a correlation through dimensional analysis as,

$$Q_{cr} = 1.71 \times 10^{-3} h_L^{1.81} \left[\frac{\Delta \rho g \sigma}{\rho_U^2} \right]^{0.35} \qquad (2.7)$$

Equation (2.7) is functionally similar to the previous previous correlations in Eqs. (2.4) and

(2.6) except for the factor of h_L. In all the trials they found that Q_{cr} was not a function of UP viscosity, although the number of droplets created was dependent on it. They also observed that increasing the UP thickness made the droplet break up possible at lower flow rates; however higher flow rates were still required to entrain those droplets overcoming their buoyancy. Hence UP thickness did not influence the critical conditions for entrainment significantly provided the volumetric ratio of LP to UP is less than 0.1.

Krishnapisharody (2006) studied the onset of entrainment process in a gas stirred cylindrical vessel as well as in a thin slice model, a 2-D replica of the cylindrical vessel. In the thin slice model, the author observed detachment of oil ligaments from the interface occurred when the amplitude of the interface wave was roughly equal to the thickness of the ligament. Considering the inviscid Kelvin-Helmholtz instability (KHI) criterion for horizontal incompressible inviscid fluids,

$$\Delta U_{crit} = \left[\frac{2(\rho_U+\rho_L)}{\rho_U\rho_L}\right]^{1/2} \left(\Delta\rho\, g\ \sigma\right)^{1/4} \tag{2.8}$$

and applying to his model experiments a value of 0.19 m/s was found for ΔU_{crit}. By assuming an order of magnitude difference in velocities of UP and LP, the free stream velocity of LP was calculated to be 0.21 m/s which is close to the value of 0.26 m/s obtained from PIV measurements in the thin slice model. Based on these, it was concluded that droplet formation process in gas stirred vessels is because of surface instability and KHI to be the most probable mechanism. The model combined with various other models for plume velocity and slag eye radius (Krishnapisharody & Irons, 2007a, 2007b, 2008) was subsequently applied to predict the critical gas flow rate for the onset of entrainment in aqueous models of gas stirred ladle. Reasonable agreement was found between experimental measurements and predictions as seen in Fig. 2.2.

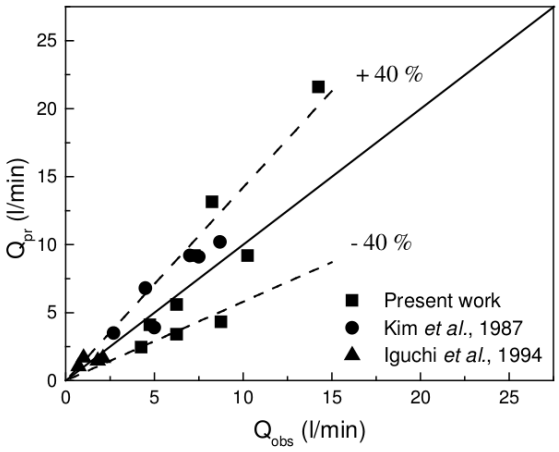

Figure 2.2. Comparison of predicted (Q_{pr}) and observed (Q_{obs}) critical gas flow rates for onset of entrainment in 3D water models of gas stirred ladle (Krishnapisharody, 2007)

2.1.2 Model for Rate of Entrainment

Using boundary layer theory Mietz *et al* (1991a) calculated the total kinetic energy available per unit time to layer of UP through the momentum transfer from LP, as,

$$\dot{E}_{kin} = 0.415\, d\left(l\,\rho_U \mu_U U_{eye}^5\right)^{1/2} \tag{2.9}$$

where l is the contact length of interface at *ULeye,* U_{eye} is the velocity at *ULeye* and d is the droplet diameter and from the work done to detach a droplet of UP,

$$W = \pi d^2 \sigma + \frac{1}{6}\pi d^4 g(\rho_L - \rho_U)\cos\alpha \tag{2.10}$$

they derived the total number of droplets generated per unit time as,

$$\dot{N} = \frac{0.4153\, D_{eye}\left(l\,\rho_U \mu_U U_{eye}^5\right)^{1/2}}{d^2\sigma + \frac{1}{6} d^4 g(\rho_L - \rho_U)\cos\alpha} \tag{2.11}$$

In addition to various other models to express the velocity at *ULeye*, Wei & Oeters (1992) applied Eq. (2.11) to predict entrainment rate of cyclohexane droplets in their experiments wherein water jet was injected from the top of the cyclohexane layer at an angle. A good

agreement was reported between the model predictions and their measurements. However, while Eq. (2.9) was derived for a flat interface, the experiments had a narrow curved interface surrounding the tube from which water jet was issuing. Therefore the good agreement with experiments may not be possible when the model [Eq. (2.11)] is applied at an actual eye as in a gas stirred vessel or in a similar scenario (2D models).

2.2 Entrainment of the Lower Phase into Upper Phase

While most of the entrainment studies observed and focused on entrainment of UP into LP, few workers have observed the reverse. Reiter and Schwerdtfeger (1992) and Lin & Guthrie (1994) observed this in their water models, but using very small gas flow rates and small vessel size, respectively, that are not representative of a gas stirred ladle.

Industrial trials were carried out by a Swedish research group (Beskow *et al*, 2006 and Dayal *et al*, 2006) using their newly developed cylindrical sampler to take slag-metal samples including the slag-metal interface. Separate samples were taken (Beskow *et al*, 2006) for various conditions of induction stirring and gas stirring from a 65 ton ladle. One such sample is shown in Fig. 2.3. By analyzing the slag portion, they found iron droplets in slag in all the samples from both induction and gas stirring and measured the iron content at various heights to be < 1%. They also found almost no compositional gradient existing in the slag in all the samples indicating that stirring of metal and hence the slag are identical between the two stirring processes. They concluded that LP entrainment is not due to bubbles passing through slag alone, but also because of the relative flow at the 'flat' interface (similar to *ULflat* in Fig. 1.2) which could be the only mechanism in induction stirred system.

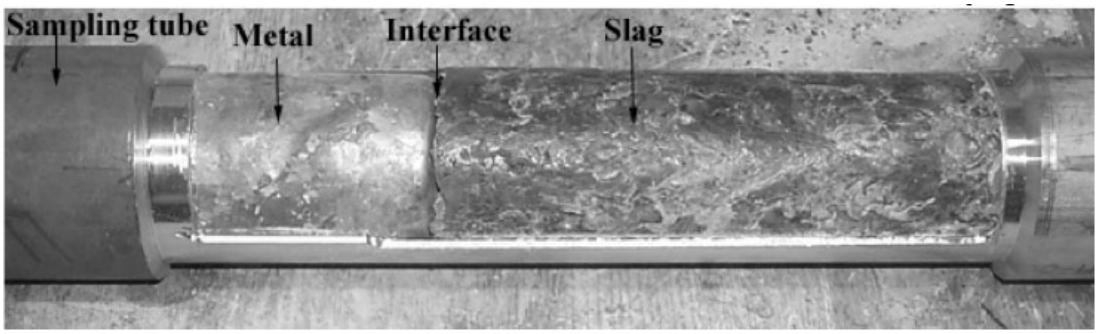

Figure 2.3. Cut opened sampler showing solidified metal, slag and their interface sampled from a 65 ton ladle in operation (Beskow *et al*, 2006)

As a follow up, Dayal *et al* (2006) did extensive slag sampling and microscopically analyzed the presence of Fe droplets in slag. For a better understanding they conducted water modeling studies in two different setups. In one of these, a water jet was introduced at one end of a rectangular tank parallel to a 'flat' interface and was removed at the other end, so as to create a flow similar to that in an induction stirred ladle. The other setup consisted of the regular cylindrical vessel stirred by gas injection. The following events were observed in the *gas stirred cylinder*:

1. At very low gas flow rates entrainment of LP occurred due to bubble rising through UP
2. With increase in gas flow rate formation of open eye prevented the gas-UP interaction
3. With further increase in gas flow rate entrainment of UP started and upon rejoining they carried with them a film of LP thereby leading to entrainment of LP.

In the water jet stirred setup, the relative motion between two phases, caused entrainment of UP into LP which upon rejoining caused entrainment of LP into UP, similar to Step 3 above.

In their micrographs of slag samples, they found 'closed loops' of fine Fe droplets, as in Fig. 2.4, which they described as collapsed film of metal that had been carried by rejoining slag drops.

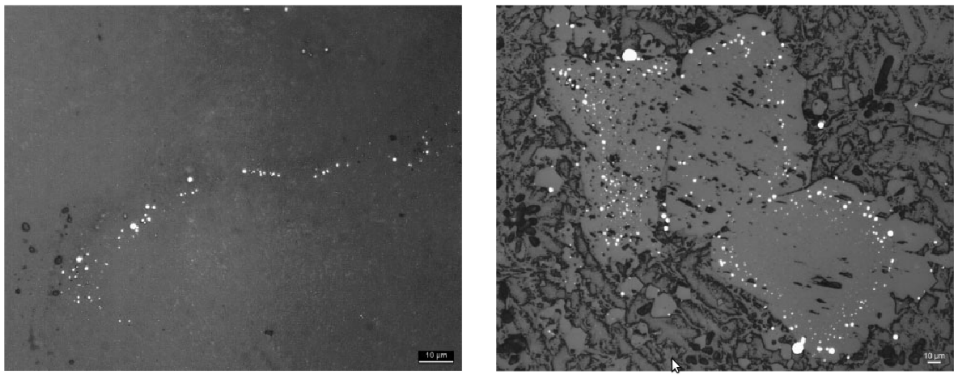

Figure 2.4. Optical micrographs of slag sample showing array of a Fe droplets (white areas) in the left image and a closed loop of droplets in the right image which were once a film over slag droplet that carried them here (bulk slag phase), upon rejoining back (Dayal *et al*, 2006)

2.3 Sampling of Fluids

The volume of entrained UP was measured in the cold model works of Verhelst (1991), Mietz *et al* (1991a) and Thunman *et al* (2007) by pumping out LP from various locations in the vicinity of the two phase interface. In Verhelst's experiments, pumped-out fluid was passed through a transparent tube that was monitored by a sensor made of a LED-photodiode couple. The differences in refractive indices and light absorption between the two phases enabled detection of phases and therefore measurement of the number of entrained drops per litre of sample; whereas, in Mietz *et al* and Thunman *et al*, fluid was pumped out only to measure the volume of UP entrained per litre of sample. Mietz *et al* used aqueous models of varying vessel diameter and bath height, whereas, Thunman *et al* used Ga-In-Sn alloy as LP and aqueous UP for varying UP thicknesses.

In both Verhelst and Mietz *et al*, in addition to the first critical gas flow rate for the onset of entrainment, there is another critical gas flow rate above which entrainment rate increases drastically. This second critical gas flow rate, however, depended on both the UP thickness and bath height. In contrast to these two works, Thunman *et al*, did not find any entrained UP in their sample. They also carried out industrial trials by taking metal samples close to the steel-slag interface using the same sampling technique developed by Beskow *et al*

(2006). Again they found no entrained slag except for an inclusion of size 20 micron in only one sample.

From their sampling study, Valentin *et al* (2009a) have found in their 170 ton ladle trials that an increase in slag eye size (due to increase in gas flow rate) decreased the metal cleanliness and increased the inclusion size. In fact they found that the inclusion size increase occurs only after the slag eye has formed, which is indicative of slag entrainment.

In another paper by the same group (Valentin *et al*, 2009b), inclusion size and compositional measurements of large number of metal samples were carried out, in the presence of variety of top slags. Of the large number of inclusions counted, around 70% were less than 5 micron and 2% were in the range of 25 and 60 micron. Figure 2.5 shows the similarity of their measured top slag and inclusion compositions. Despite the absence of Calcium treatment, CaO is present in many of the inclusions. The authors concluded that since top slag is the only source for CaO, it could have found its way to SiO_2-Al_2O_3 inclusions only through slag entrainment.

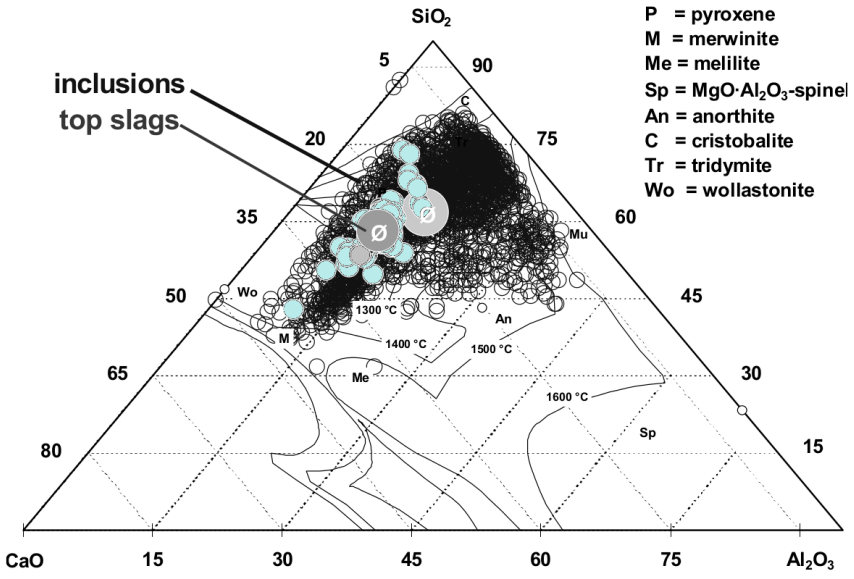

Figure 2.5. Position of top slags and inclusions in the system, CaO-Al_2O_3-SiO_2-5%MgO (Valentin *et al*, 2009b). Closed circles - top slag composition; open circles - inclusion composition

Lachmund *et al* (2003) conducted a large sampling experiment to study slag

entrainment in an industrial ladle of 185 ton capacity and 3.1 m high. They made a large rectangular box (dimensions of inner space: 1.5m x 1m x 30 mm) by welding a steel sheet on a heavy steel slab of 2.1 ton leaving a gap of 30mm (shown in Fig. 2.6a). With five holes in the middle of the box, they immersed this sampler in the ladle in operation to take samples. The acquired samples were analyzed using quantitative microscopy. The size distribution of 885 droplets counted is shown in Fig. 2.6b. From the counted droplets the specific mass of slag entrained was calculated to be ≈ 3.1 kg/m^3 and extrapolation to whole ladle volume gave $\approx 5 \times 10^7$ number of droplets. Using the model of Mietz and Oeters, Eq. (2.11), and calculating the rate of entrainment to be $1.1 \times 10^7 s^{-1}$, they calculated the average residence time to be ≈ 5 s. Moreover, they calculated the total interfacial area due to drops, based on the steady state number and a 1 mm mean diameter, to be $\approx 173 m^2$, which according to them translates to ≈ 25 times the nominal area of slag metal interface before any gas injection, with respect to interfacial mass transfer.

In estimating the total number of droplets and hence the total slag metal interfacial area Lachmund *et al* have assumed that the measured size distribution is the same everywhere in the ladle. The depth of sampling from the slag metal interface is not given in that reference. Given that their gas injection rate is somewhat in the higher end, ≈ 5 lpm per ton of steel, their assumption of uniform concentration may be reasonable and hence their estimate of number of droplets. However the estimated mean residence time of 5 s is too low because, this would require the mean rising velocity of droplets (averaged over the bath height of 3.1 m) be as large as 0.3 m/s, which is not possible even for a quiescent bath! This also questions the validity of the entrainment rate model of Mietz and Oeters [Eq. (2.11)] that was used to estimate the mean residence time.

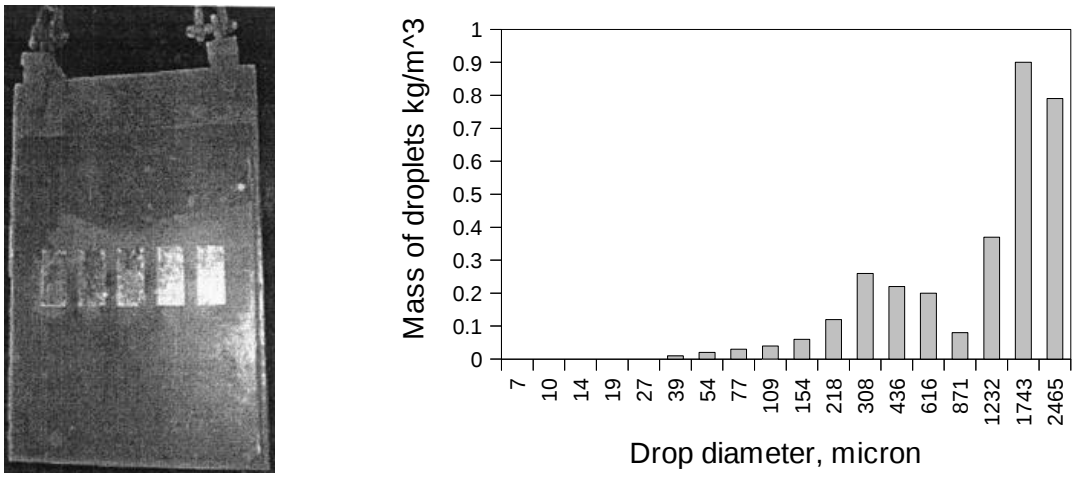

(a) **(b)**

Figure 2.6. From experiments of Lachmund *et al* (2003): (a) Sampler used to sample liquid steel from ladle (b) Entrained slag droplet distribution for a specific slag mass of 3.11 kg per m^3 of metal.

Ekengard *et al* (2008) took measurements of entrained Fe droplets into slag (LP into UP) from ladles of two different steel plants. Slag sampling was done by a simple sampling scoop for 10 heats in the two steel plants combined and the analysis of samples for metal droplets was carried out using optical microscopy. The size of entrained Fe droplets ranged between ~ 5 and 40 microns. They found that such Fe droplets formed a negligible fraction in the volume of slag, although they estimated the total interfacial area due to drops to be 3 to 14 times larger than the area of undisturbed interface.

In 9 out of the 10 heats that they have sampled, they found the amount of Fe droplets in the slag after 'vacuum degassing' to be much less than the amount after 'stirring' that always preceded degassing. This indicates that under mild stirring conditions, as that would prevail during deoxidation, alloying and or/heating operations, the Fe entrainment accumulates gradually and when stirring is vigorous as in vacuum degassing operations, not that the entrainment rate becomes low, but the rate of sinking back to LP should be high. The authors estimated slag viscosities at various stages and found a substantial drop in viscosity after degassing attributing which to the reason for high rejoining rate.

The above literature sources show us various characteristics of slag and metal

entrainment within the reach of sampling methods. Despite strong evidence for entrainment both in aqueous and industrial systems, it is unclear why Thunman *et al*, (2007) could not sample any significant trace of entrainment.

2.4 Role of entrainment on Interfacial Mass Transfer

The beneficial effect of entrainment, studied many times in the past, is the drastic increase of interfacial mass transfer rate in gas stirred ladles. In modeling liquid-liquid mass transfer in ladles, mass transfer has been assumed to be controlled by the metal phase (LP) in the literature. So let us consider the rate equation for transfer of a species S from lower to upper phases, with LP side control:

$$\frac{-d[S]}{dt} = \frac{k_L A}{V_L}\left([S] - [S]_i\right), \tag{2.12}$$

where, $[S]$ and $[S]_i$ are the bulk and interface concentration of S in LP, respectively, k_L is the LP side mass transfer coefficient, A is the interfacial area in the system and V_L is the volume of LP. Equation (2.12) after integration was often used to fit the experimental data on $[S]$ *vs* time profile to find the quantity, $k_L A$. Since in gas stirred systems estimates for interfacial area, A, cannot be made without estimates for amount and residence time of entrained droplets, the lack of these estimates has left the true values of A and k_L remain unknown. Therefore the quantity, $k_L A$ has remained the rate characterizing parameter. In many of the aqueous and high temperature ladle models studied, $k_L A$ has been found to vary with gas flow rate, Q, according to $k_L A \propto Q^n$.

Based on the value of exponent to gas flow rate, n, from their water modeling study, Kim & Freuhan (1987) characterized three flow rate regimes (with reference to Fig. 2.7):

- Regime I, where there is no entrainment and *ULflat* is mostly undisturbed except for weak waves.
- Regime II marked by increase in the exponent to Q, coinciding with the onset of entrainment of UP.
- Regime III marked by fall in the exponent value, is where almost the entire bulk UP is broken into droplets.

These regimes have been observed several times through change in exponent values to Q, for example, as summarized by Asai *et al* (1988) in Fig. 2.8 for both aqueous models and high temperature systems.

Kim & Freuhan (1987) have further done an extensive experimental investigation on the influence of various parameters on mass transfer rates; although the role of interfacial tension was not studied. Influence of some selected parameters are summarized in Table 2.1 and explained using various $k_L A - Q$ plots (not discussed here).

In Table 2.1 we see that the eccentric positioning of gas injection tuyere lowers $k_L A$ of Regime II drastically such that transition from Regime I to II is faint. However this is mostly due to their smaller vessel capacity (75 litre). Considering the experimental results of Mietz *et al* (1991a), the mass transfer rate plots for a smaller vessel (180 litre) in Fig. 2.10a is similar to the corresponding plot of Kim and Freuhan in Table 2.1, *i.e.*, significantly lowered rate for eccentric tuyere position. However in the case of a larger vessel (700 litre), in Fig. 2.10b, the three characteristic flow rate regimes are clearly present in the eccentric case as well. This shows that the vessel size has significant influence on the $k_L A - Q$ characteristics.

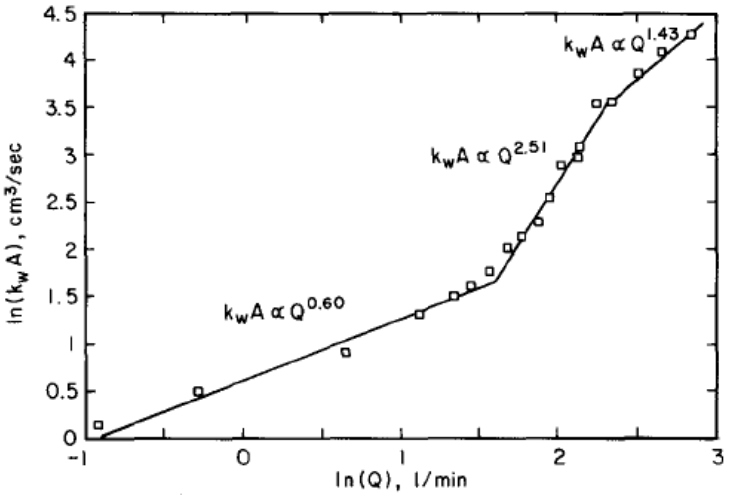

Figure 2.7. Plot showing three regimes of gas flow rate (Q) wherein rate constant (k_wA) takes different exponent values on Q (Kim & Freuhan, 1987)

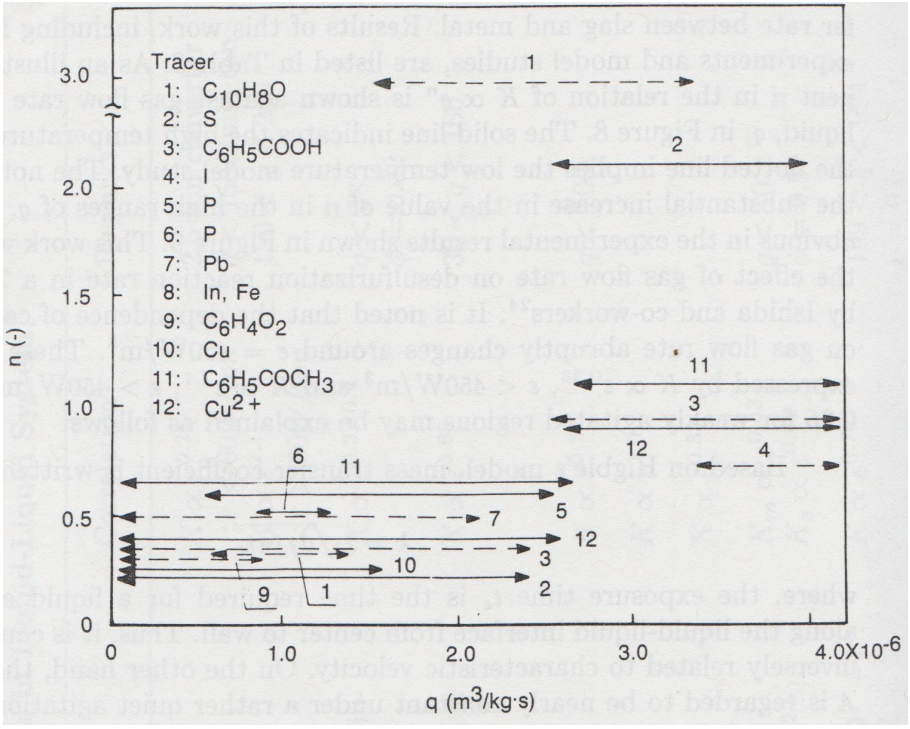

Figure 2.8. Exponents (n) to flow rate (q) in the $k_L A - Q$ relation for both aqueous systems (dashed lines) and high temperature systems (continuous lines), Asai *et al* (1988).

Table 2.1. Role of various parameters on liquid-liquid mass transfer rate $(k_L A)$, from the study of Kim & Fruehan (1987). In charts, flow rate, Q, lpm and $k_L A$, cm^3/s are in the x and y axes, respectively and labels correspond to their respective parameter values.

Parameters	$\ln(k_L A)$ *vs* $\ln(Q)$	Effect
UP viscosity (Poise)	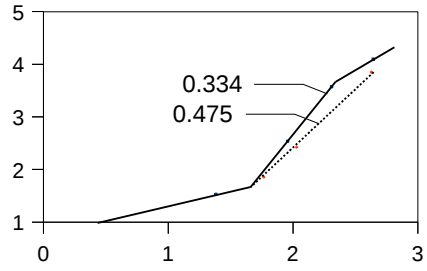	Increasing UP viscosity - lowers $k_L A$ slightly
UP volume fraction (ratio of UP to LP volumes)	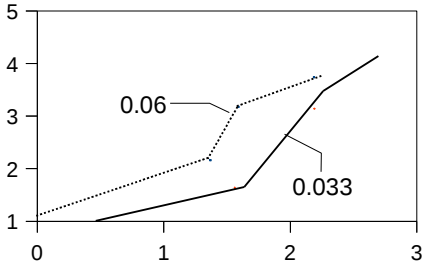	Increasing UP volume fraction, - increases $k_L A$ - earlier transition from Regime I to II - shortens Regime II
Number of tuyeres (see Fig. 2.9 for tuyere arrangement)	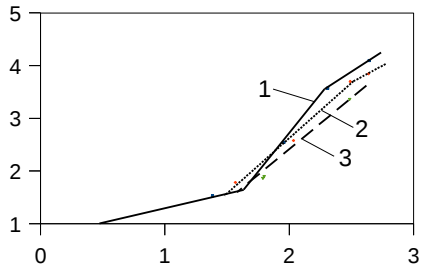	Increasing number of tuyeres - decreases $k_L A$ - lowers exponent to Q
Tuyere position (see Fig. 2.9 for tuyere arrangement)	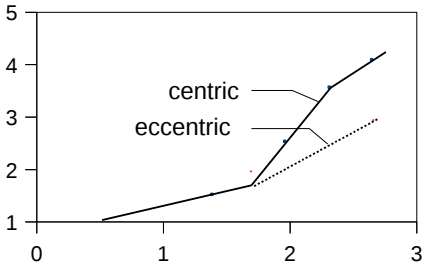	Eccentric gas injection - decreases $k_L A$ - lowers exponent to Q

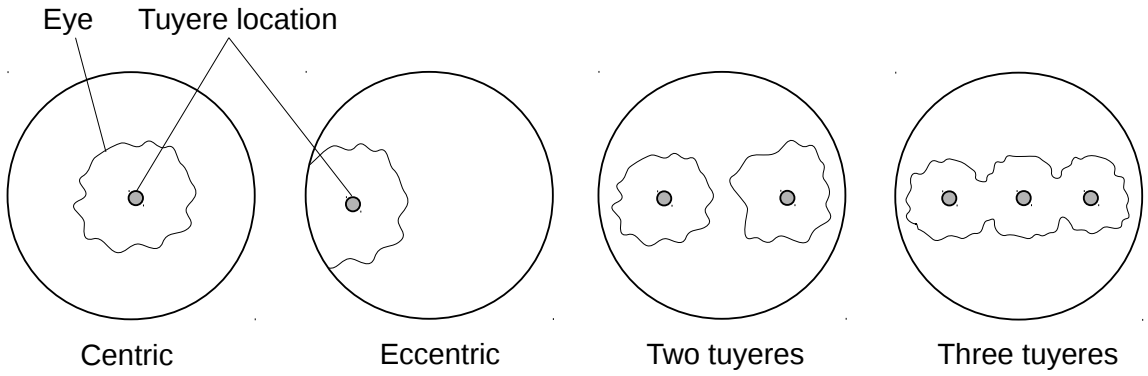

Figure 2.9. Schematic of top view of a gas stirred vessel showing various arrangements of gas injection tuyeres in the study of Kim & Fruehan (1987).

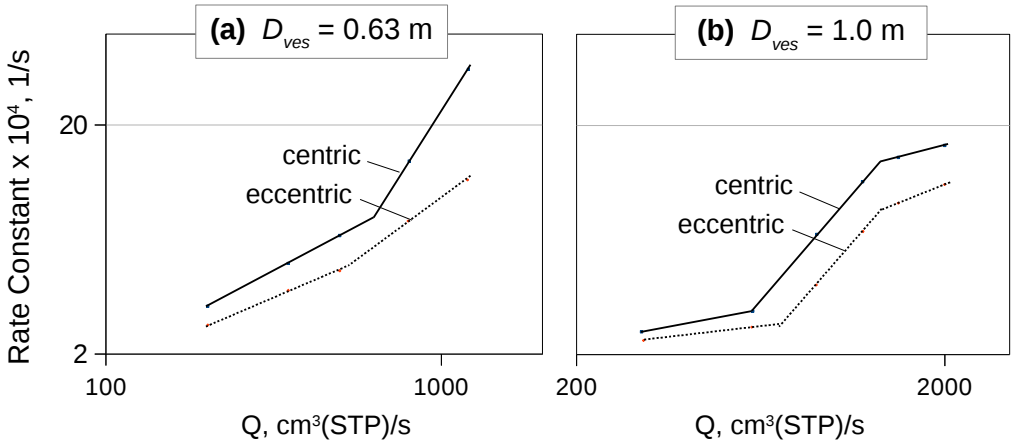

Figure 2.10. Mass transfer rate (Rate constant $\propto k_L A$) versus gas flow rate (Q) for two vessel diameters (D_{ves}) and two tuyere positions in the study of Mietz *et al* (1991a). Common y-axis.

2.5 Entrainment studies using CFD

There are very few studies that have simulated fluid flow in ladle with an upper phase. Much of these (Jonsson & Jonsson, 1996; Han *et al*, 2001, Ridenour *et al*, 2006; Li *et al*, 2007) have simulated fluid flow around slag metal interface to the extent of eye formation and wave formation but not the entrainment of slag. The difficulty lies in the resolution of the two phase interface to the order of a millimeter, given the large size of the domain, an industrial ladle or even a laboratory scale water model.

To study the mechanism of entrainment of oil into water Krishnapisharody (2007) constructed a thin Plexiglas model† that approximates a 2D circulatory flow of a lab scale gas stirred ladle. Moreover to reduce the violent oscillations of interface as in a gas stirred ladle, stirring was done by a water jet issuing from the base of the model. The author developed a 2D CFD code with Volume of Fluid method to the track oil-water interface with Young's PLIC (Piecewise Linear Interface Construction) method (Youngs, 1982) and simulated the multiphase flow for various inlet velocities. In his simulations, at a velocity of 0.24 m/s in water near the interface, interface waves appeared followed by growth of ligaments that eventually broke up as oil droplet as shown in Fig. 2.11. These events were confirmed from video frames and the velocities measured using Particle Image Velocimetry.

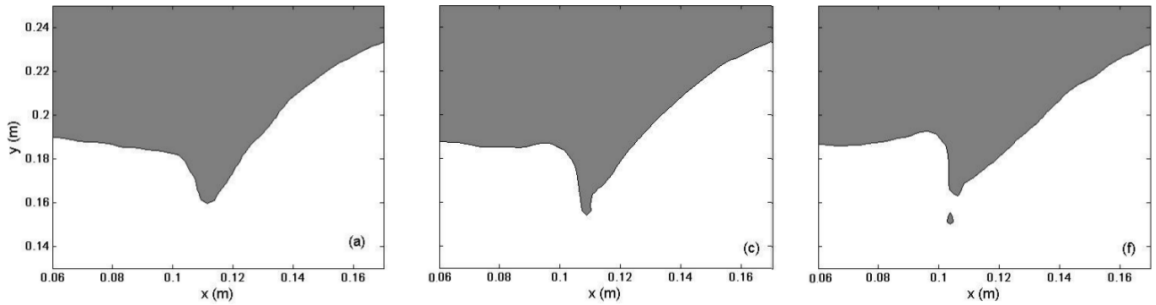

Figure 2.11. Series of snapshots of simulation interface leading up to detachment of droplet (Krishnapisharody, 2006)

† being the subject of modeling studies in Ch. 5, its physical details can be found there.

Sulasalmi *et al* (2009) did large eddy simulations (LES) of entrainment in the experimental setup of Savolainen *et al* (2009). The setup shown in Fig. 2.12 is a Plexiglass container of 10 cm width and 50 cm length. The setup has two compartments separated by weir arrangement such that when water from the right side enters the left, there is a relative motion between oil and water that cause oil entrainment. Savolainen *et al* (2009) have measured critical liquid velocities and critical droplet sizes from video recordings of flow for various combinations of fluid properties; of these Sulasalmi *et al* performed four LESs, using FLUENT, with more than half a million grid points, in a reduced domain as seen in the snapshot of LES in Fig. 2.13a. More number of droplets seen in the snapshot tells that the velocity is well above the critical velocity for the LES model. The comparison of LES results with data for mean droplet size at critical velocity for entrainment in Fig. 2.13b shows that drop sizes are under predicted, probably due to their higher inlet velocity. Or, this can be due to weak interface representation. From Fig. 2.13a it can be seen that their interface representation is not sharp but smeared over some thickness, which generally leads to weak estimates of interface curvature, interfacial tension and hence the size of droplets.

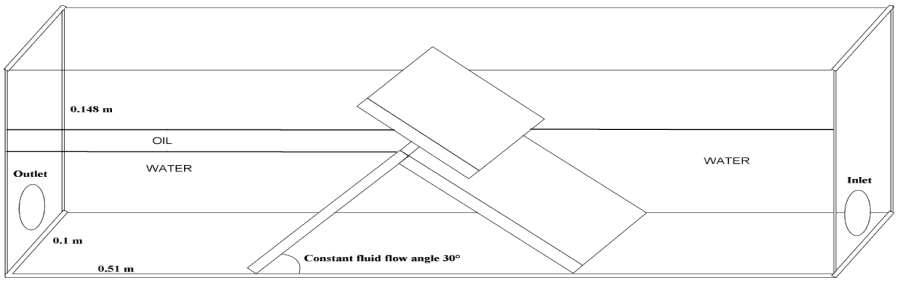

Figure 2.12. Experimental setup of Savolainen *et al* (2009). In the figure, Inlet and outlet for water are located in the right and left end of the setup, respectively.

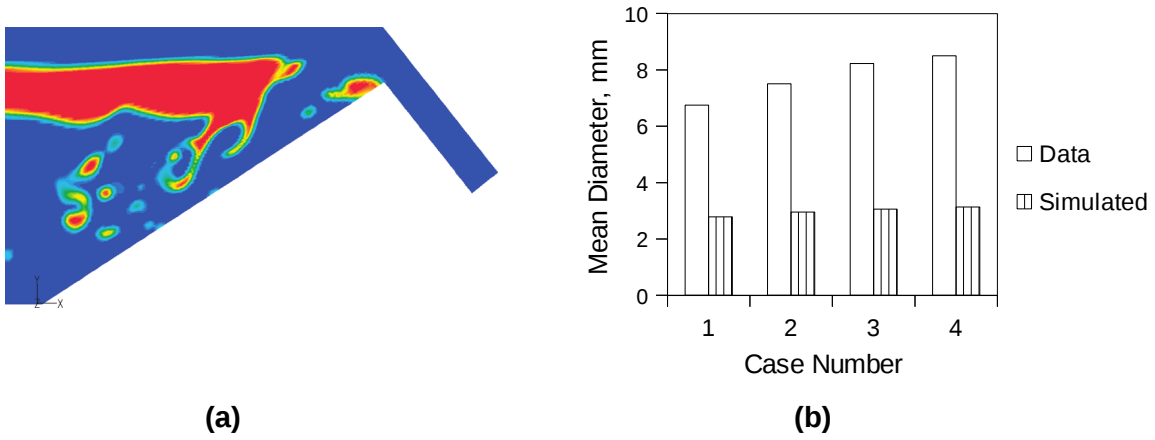

Figure 2.13. LES results of Sulasalmi *et al*, (2009): (a) Snapshot of oil-water interface (b) Comparison of mean drop diameter of simulation with data.

2.6 RANS Modeling of Metal Flow in Gas Stirred Ladle

The steady state flow field of gas stirred ladle is required as input to Large Eddy Simulations performed in this thesis. So in this section a concise review of relevant literature is presented. Numerical modeling of turbulent fluid flow usually consists of solving Reynolds Averaged Navier-Stokes (RANS) equation with a suitable turbulence model and boundary conditions. However for gas stirred ladle, since the fluid flow is bubble driven, appropriate modeling of the gas-liquid plume is also required.

2.6.1 RANS Overview

The following concepts in this section are taken from Wilcox (1994). The Navier-Stokes equations are the partial differential equations of conservation of mass and momentum, given by,

$$\frac{\partial \rho}{\partial t} + \nabla \cdot (\rho \boldsymbol{u}) = 0, \tag{2.13}$$

and

$$\rho\left[\frac{\partial \boldsymbol{u}}{\partial t} + \boldsymbol{u}\cdot\nabla\boldsymbol{u}\right] = -\nabla p + \mu\nabla^2\boldsymbol{u}, \tag{2.14}$$

respectively, where $\boldsymbol{u}$ is the velocity field, p is the pressure, ρ and μ are the fluid density and viscosity, respectively. The highly non-linear nature of these equations require extensive numerical techniques to discretize (spatially and temporally) and solve with appropriate boundary conditions, the branch of science known as Computational Fluid Dynamics (CFD). When the fluid flow is turbulent, instabilities in flow occur at a wide range of time and length scales and resolution of all these scales increases the computational expense prohibitively. Moreover, from engineering standpoint, resolution of all scales of flow is often not required. So a modified form of the Navier-Stokes equations are used that are obtained by applying a procedure known as Reynolds Averaging. This consists of decomposing the variables of the Navier-Stokes equations (ϕ) into mean ($\overline{\phi}$) and fluctuating components (ϕ') as,

$$\phi = \overline{\phi} + \phi' \tag{2.15}$$

where,

$$\overline{\phi} = \lim_{N\to\infty}\frac{1}{N}\sum_{i=1}^{N}\phi_i \tag{2.16}$$

is the ensemble average and N is the total number of independent realizations of the variable, ϕ. Often the mean component, $\overline{\phi}$, is also represented as time average.

Ensemble averaging Eqs. (2.13) and (2.14) after decomposing all variables as in Eq. (2.15) and using the property $\overline{\phi'} = 0$, we get the RANS equations,

$$\nabla\cdot(\rho\boldsymbol{U}) = 0, \tag{2.17}$$

and

$$\rho\,\boldsymbol{U}\cdot\nabla\boldsymbol{U} = -\nabla P + \mu\nabla^2\boldsymbol{U} + \nabla(\rho\overline{\boldsymbol{u}'\boldsymbol{u}'}) \tag{2.18}$$

where the variables now in upper case that were in lower case in Eqs. (2.13) and (2.14) are the mean flow variables and $\boldsymbol{u}'$ is the fluctuating velocity vector.

The term, $\rho\overline{\boldsymbol{u}'\boldsymbol{u}'}$ in Eq. (2.18) known as Reynolds stress tensor has six independent components. In three dimensions, Eqs. (2.17) and (2.18) together yield four equations for four

unknowns: three mean velocities and one mean pressure. The lack of additional equations for the six Reynolds stress components therefore poses a closure problem that is at the heart of turbulence modeling. The Reynolds stress tensor is often expressed using mean velocity gradients, for incompressible fluids, as,

$$\rho\overline{\boldsymbol{u}'\boldsymbol{u}'} = \mu_T(\nabla \boldsymbol{U} + \nabla^T \boldsymbol{U}) - \frac{2}{3}\rho k \tag{2.19}$$

where μ_T is a new coefficient known as eddy viscosity that needs to be modeled and k is the turbulent kinetic energy. Equation (2.19) is known as the Boussinesq eddy viscosity approach.

The problem now shifts to modeling of the eddy viscosity that consists of appropriate specification of turbulent length and velocity scales. This is achieved through models as simple as algebraic equations to complex partial differential equations of conservation of some turbulence quantities related to turbulence length and velocity scales, eg., the popular $k-\varepsilon$, $k-\omega$ models. However, the Boussinesq eddy viscosity approach has the drawback in its assumption of turbulence isotropy which is not always true particularly in the boundary layers. Yet, the eddy viscosity approach has lead to numerous turbulence models for variety of problems.

2.6.2 RANS Modeling of Plume

As described in Sec. 1.2, the plume in a gas stirred ladle is a two phase mixture of rising bubbles and liquid. The goal of RANS modeling is to compute both the mean velocity and the phase fraction distributions. Excluding the interface tracking methods, the two phase flows are most commonly modeled via three approaches, namely quasi single phase or the single phase-variable density method, Eulerian-Eulerian (E-E) and Eulerian-Lagrangian (E-L) approaches. In the quasi single phase method a phase fraction distribution known *a priori* is applied to the RANS equations to compute only the velocity distribution. In the E-E approach, the two phases are assumed as inter-penetrating continua and separate conservation equations are solved for each phases. In the E-L approach, statistically large number of particles are tracked (based on Newton's II law of motion) for phase fraction distribution, coupled with simultaneous solution of RANS equations, until stead state. In E-E and E-L the influence of

discrete phase on the continuous phase and vice versa are accounted through various forces such as the drag, buoyancy, added mass, pressure force, lift etc.

The choice of modeling approaches are generally based on various factors (Ferry & Balachandar, 2001) namely the number density and size distribution of the discrete phase particles and the effect of discrete phase on the flow of continuous phase. If the particles are very small that their effect on flow of continuous phase is insignificant, the quasi single phase formulation would suffice. For a given volume fraction of discrete phase, with the increase in particle size (and hence decrease in number density) the two phase interaction becomes significant that either E-E or E-L approach has to be employed. An E-E approach is more appropriate when the number density of particles is sufficiently high for the continuum treatment of discrete phase to be valid and when particle sizes are uniform enough to be represented by a unique velocity field in a mesh volume. With increased distribution in particle sizes, the number of conservation equations to be solved for each size class increases, making the E-E approach expensive. Under such conditions the E-L approach can be employed, although large increase in the number of trajectories to be tracked would make this approach expensive as well.

In the context of modeling of gas liquid plume in ladle, all the three approaches have been successfully applied despite the structure of gas liquid plume defying some of the considerations discussed above. Standard $k-\varepsilon$ turbulence model has been widely used with both standard and modified coefficients. In all the approaches turbulence has been considered as a property of liquid alone. This is due to the difficulty in Reynolds averaging the multiphase conservation equations for turbulence quantities (Jakobsen *et al*, 1999). Although the accuracy of turbulence kinetic energy predictions differ among the approaches, the bulk fluid flow are reasonably well predicted invariably.

Since in this thesis, the correlations for gas fraction distribution were readily available, quasi single phase approach was used and hence only that is reviewed below. The other approaches can be found in the following references for modeling of gas stirred ladles: E-L: Johansen & Boysan (1988), Mazumdar & Guthrie (1994), Sheng & Irons, (1995) and Guo & Irons (2000); E-E: Ilegbusi & Szekely (1990) and Turkogulu & Farouk (1990).

In the **quasi single phase** approach, the plume region is assumed to consist of single phase liquid but with a density of mixture of gas and liquid given by a simple rule of mixtures. The fluid density is therefore defined as,

$$\rho = \begin{cases} \alpha\rho_G + (1-\alpha)\rho_L & 0 < r < R_P \\ \rho_L & \text{elsewhere} \end{cases} \tag{2.20}$$

where, α is gas volume fraction ρ_G is gas density and R_P is plume radius. This density is then used in the RANS equations with buoyancy term included and the local density differences cause flow. The model is simple because all it requires is the specification of spatial distribution of gas fraction and radius of the plume; but the *a priori* requirement is also the drawback in cases where such inputs are neither available nor when reasonable assumptions about the profiles can be made.

In cases where estimates for plume radius and plume rise velocity were available, gas fraction distribution has been derived based on volume continuity as,

$$\alpha(z) = \frac{Q - \pi R_P^2 \alpha(1-\alpha) U_s}{\pi R_P^2 \overline{U}_z} \tag{2.21}$$

where $\overline{U}_z$ is the axial distribution of plume-cross section area-averaged velocity and U_s is the bubble slip velocity calculated for single bubble rising. Some times $\overline{U}_z$ has been derived theoretically (Grevet *et al*, 1982) or the volume averaged plume rise velocity has been applied (Sahai & Guthrie, 1982, Mazumdar & Guthrie, 1985). Bubble slippage has been both considered and disregarded $(U_s = 0)$. Alternatively a Gaussian type of distribution has been applied for spatially varying gas fraction distribution of the form,

$$\alpha(r, z) = \alpha_{cl}(z)\exp(-b\, r^c) \tag{2.22}$$

with α_{cl}, the plume-centre-line gas fraction and b and c, the empirical coefficients. Theoretically derived α_{cl} has been applied by Balaji & Mazumdar (1991) whereas Castillejos *et al* (1989) have applied their experimentally deduced correlation. Sheng & Irons (1993) have directly used their own measured gas fraction distributions.

2.7 Summary

From literature it is understood that significant effort has been dedicated, but limited mostly, to finding critical conditions for onset of entrainment of UP, namely velocity near interface and gas injection rate. Much work needs to be done to characterize entrainment in terms of their birth rate, size and residence time distributions. Sampling methods have shown possible size ranges of entrained phases and mechanisms of entrainment. With respect to mass transfer studies the role of entrainment on mass transfer is well understood in water models; however the rate parameters have not been related to entrainment parameters, fluid properties and scale of the system. Developments in numerical simulations of the two phase flow phenomena is still in its infancy due to the lack of modeling techniques, robust representation of interface topology, stable and efficient solvers and finally necessary computational resource to study entrainment in full scale industrial systems.

3. Drop by Drop Kinetic Model

The slag metal interfacial mass transfer in a ladle takes place at various rates at various distinct interfaces namely, the bulk upper phase and the entrained droplets. The problem of calculating the overall mass transfer rate is complicated by the fact that there are droplets of various sizes and residence times so that the effective interfacial area to mass transfer cannot be simply the total interfacial area. Therefore a model is necessary to calculate the overall rate based on droplet number, size and residence time statistics, apart from the information on bulk phases. This chapter first discusses a theoretical model that derives the effective interfacial area and scope of the model. Later, a numerical model is presented to directly calculate the mass transfer rate without the need to define any 'effective' parameter. Various parametric studies were conducted using the model. The last of the parametric studies develops the initial theoretical model further and in comparison with the numerical model, its scope is assessed.

3.1 Effective Interfacial Area

Let us call the entrainment of slag droplet into metal as 'birth' and rejoining of slag droplet back into bulk slag as 'death'. The entrainment problem consists of birth of slag droplets of various sizes at various rates, their residence in the metal phase for different time periods, at the end of which is their death and interfacial mass transfer taking place in between.

The birth and death process is illustrated as shown in Fig. 3.1 wherein droplets of various sizes enter a control volume with an overall birth rate of $\dot{N}$, reside for various time periods (residence times) and exit the control volume; here birth rate is defined as the number of droplets entering the control volume per unit time. For simplicity, let us assume that the residence time for all droplets within each size group is constant and no agglomeration between any of the droplets.

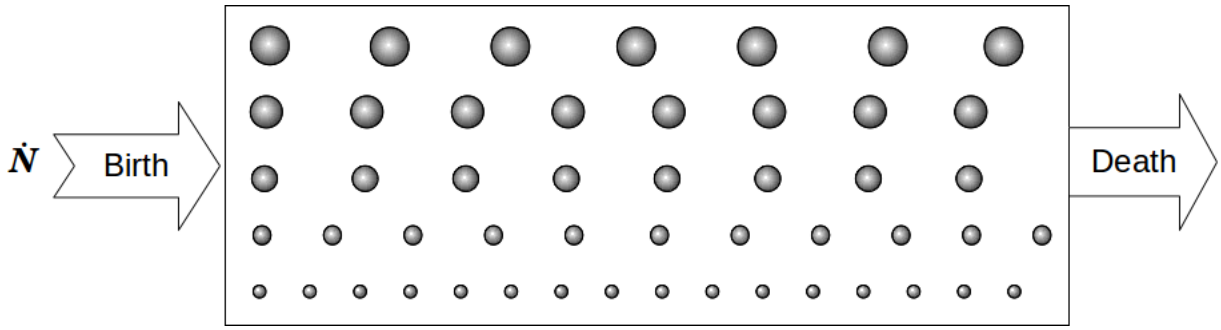

Figure 3.1. Schematic of droplets of various sizes entering the control volume (bounding box) at overall rate of $\dot{N}$ drops per unit time (birth) and leaving (death). For clarity droplets of various sizes are shown as stratified. The number of droplets in the control volume for each size depends on their probability of birth and their residence time.

In certain group of size x, the number of droplets in the control volume at steady state is expressed as,

$$N(x) = \dot{N}\, t_{res}(x)\, p(x), \tag{3.1}$$

where $t_{res}(x)$ is the residence time and

$$p(x) = \frac{f(x)}{\Sigma f(x)} \tag{3.2}$$

is the probability of birth of droplets of size x and $f(x)$ is the discrete frequency distribution of droplet sizes at the time of birth. The total number of drops in the entire size range is,

$$N = \dot{N}\frac{\Sigma\, t_{res}(x) f(x)}{\Sigma f(x)}, \tag{3.3}$$

or for a continuous frequency distribution,

$$N = \dot{N}\frac{\int t_{res}(x) f(x)\, dx}{\int f(x) dx}, \tag{3.4}$$

At steady state, the transitional or the net interfacial area due to all droplets is therefore,

$$A_{drop,\, net} = \dot{N}\frac{\int A(x) t_{res}(x) f(x)\, dx}{\int f(x)\, dx}. \tag{3.5}$$

From Eq. (3.5) it is apparent that given the size distribution function for droplets at the time of birth, their residence time distribution and entrainment rate, the transitional interfacial area can be estimated. Since smaller droplets saturate rapdily, the residence time in Eq. (3.5) has to be replaced by 'active time' defined as the minimum of time for saturation, t_{sat} and residence time,

$$t_{active} = \mathrm{MIN}(t_{sat}, t_{res}). \tag{3.6}$$

The saturation time can be defined as the time taken for concentration of species to reach some fraction (say 95%) of its equilibrium value in the droplet. However with the progress of mass transfer on the global scale, due to decrease in driving force that is due to concentration gradient, t_{sat} itself varies and cannot be known *a priori.* Secondly integration of Eq. (3.5) using t_{active} may not be possible since the latter is not well defined (due to the 'MIN' function). Therefore the effective or the transitional area for mass transfer cannot be estimated using a simple model like Eq. (3.5).

3.2 Numerical Model for Mass Transfer

The difficulty in evaluating the effective interfacial area for mass transfer through analytical models necessitates numerical modeling of the process. A new model called 'drop by drop kinetic model' (DBD) was developed and is described in this section. The model consists of modeling the birth and death of droplets and mass transfer at all distinct two phase interfaces. The model was constructed using C programming language (code in Appendix A.1) and the steps involved are outlined in Fig. 3.2 and detailed in subsequent sub-sections.

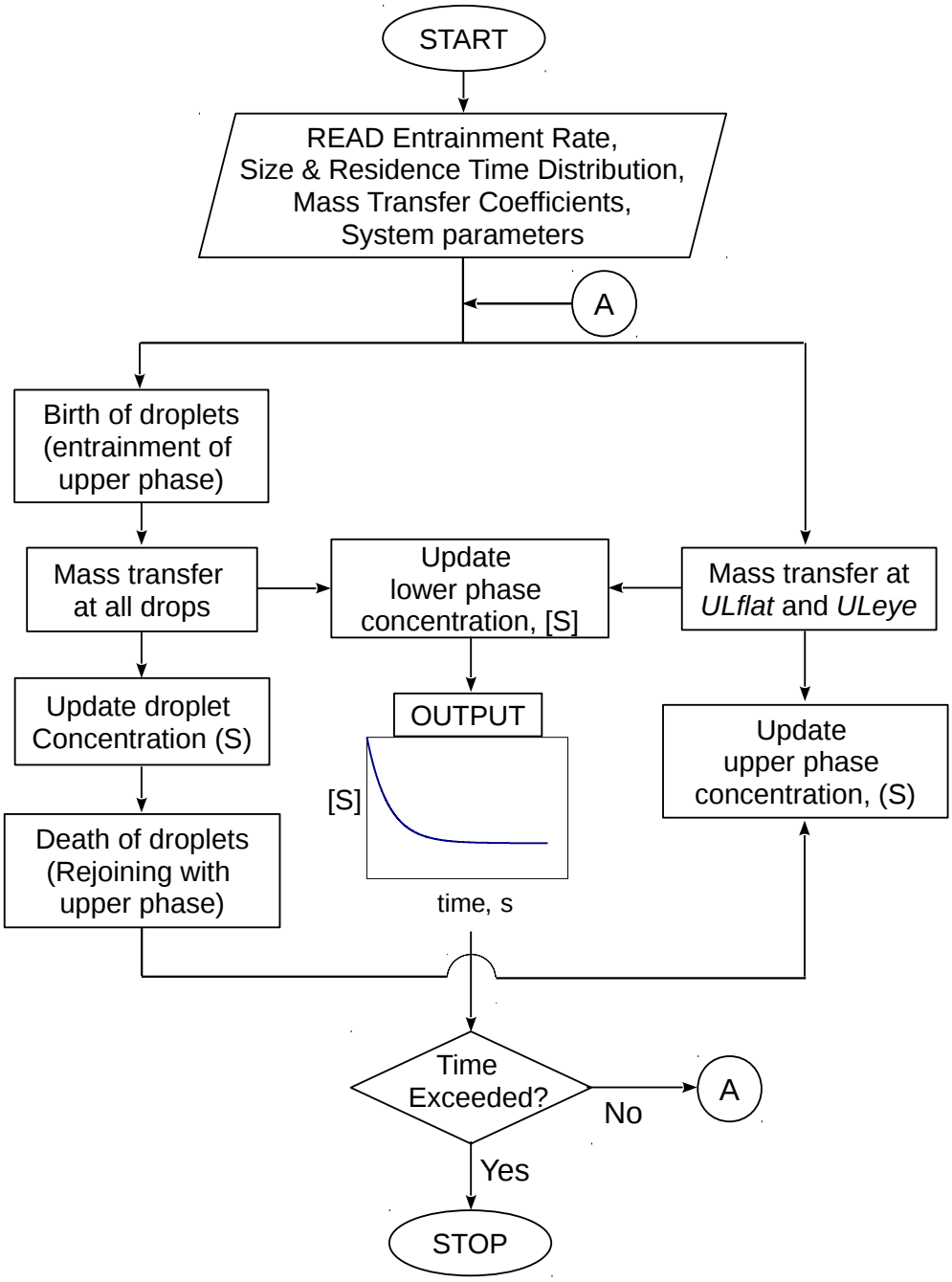

Figure 3.2. Flowchart outlining the steps involved in the *drop by drop* kinetic model

3.2.1 Major Assumptions

1. Both Lower and Upper phases are always homogeneous with respect to concentration of the species transferred.
2. Mass transfer takes place at three zones as shown in Fig. 1.2 classified based on the geometry and flow features near the two phase interface.
3. Mass transfer rate is controlled by the lower phase as in a ladle desulphurization process.
4. Entrainment of LP into UP has no role in mass transfer and hence disregarded.
5. All the entrained droplets are considered to be spherical.
6. Finally, no breakup or coalescence is assumed to take place to the entrained drops, so that the sizes and number are preserved throughout their residence in LP.

3.2.2 Input Parameters

It can be inferred from Sec. 3.1 that the model requires entrainment rate, size distribution and residence time distribution as input parameters. So the model parameters are:

1. Entrainment rate in percentage volume of upper phase entrained per unit time, VPU: When studying the effect of droplet sizes on mass transfer it was necessary to have volumetric entrainment rate rather than number entrainment rate, $\dot{N}$.
2. Parameters of droplets size distribution at the time of birth.
3. For residence time, either the parameters of a function relating average residence time with particle size are inputted or a set of values (discrete function) of these variables are inputted.
4. Mass transfer coefficients, k_{flat}, k_{eye} and k_{drop} – one for each mass transfer zone, namely *ULflat*, *ULeye* and *ULdrop*, respectively, from LP side.
5. Partition coefficient, for distribution of a species between two phases.
6. Geometrical parameters, namely heights of LP, h_L and UP, h_U, vessel radius, R_{ves} and slag eye radius R_{eye}.

3.2.3 Birth and Death Process

Birth of a droplet means sampling its size and residence time from their respective input distributions, and deciding its initial concentration. The sampling process involves generating random numbers from given distributions for size and residence time. If not required, the random sampling for residence time can be turned off and only the average residence time for a given size be applied. At a given time step, the following steps are involved in the birth process:

1. The function to sample droplet sizes is called to sample droplets of the total volume for a given time step, determined by the volumetric entrainment rate.
2. The average residence time for a given droplet size is interpolated from the input values. If required, a random residence time can be sampled based on this average residence time and a prescribed distribution (an example is noted later in Sec. 3.3.1). The sum of birth and residence times is equal to the time of death of a droplet.
3. The initial concentration of a droplet is set as the current bulk concentration.
4. The loss of volume and species mass in the bulk phase due to entraining droplets is accounted.

When current time equals or exceeds the time of death of a droplet the volume of rejoining droplets and species mass gained by the droplets is added to the bulk phase. The steps related to birth and death are executed for every time step.

3.2.4 Mass Transfer

This step involves applying the mass transfer rate equation to calculate the amount of species transferred across the interface of bulk phases and every alive droplet, distinctly. The concentration of bulk phases are then updated every time step based on the net transfer of species mass.

3.2.4.1 Rate Equation and its Discretization

The rate equation for flux of species, S, transfered from LP to UP at a given interface is,

$$\frac{-1}{A}\frac{dn_{[S]}}{dt} = k_L\left([S]-[S]_i\right). \tag{3.7}$$

where A is the interfacial area, $n_{[S]}$ is the number of moles of species leaving LP, k_L is LP side mass transfer coefficient, $[S]$ and $[S]_i$ are the species concentration (moles/m^3) in the bulk of LP and interface, respectively.

If thermodynamic equilibrium is assumed to exist at the two phase interface, then it can be written (Deo & Boom, 1993) that

$$\frac{(S)_i}{[S]_i} = \frac{(S)_{eq}}{[S]_{eq}} = L_S \tag{3.8}$$

where, the S represented inside the parenthesis denotes the UP side concentration with subscripts eq and i for equilibrium and interface, respectively and L_S is the partition coefficient of S. For LP mass transfer controlled, it is reasonable to assume that $(S) = (S)_i$. Therefore Eq. (3.8) gives,

$$[S]_i = \frac{(S)}{L_S} \tag{3.9}$$

Using Eq. (3.9) into Eq. (3.7) and that since the number of moles of species lost by LP is the same as that of the gain by UP we obtain the rate equation,

$$-\frac{dn_{[S]}}{dt} = \frac{dn_{(S)}}{dt} = k_L A\left([S] - \frac{(S)}{L_S}\right). \tag{3.10}$$

Concentration defined as the number of moles per unit volume,

$$(S) = \frac{n_{(S)}}{V_U} \tag{3.11}$$

is used to cast Eq (3.10) into an integrable form as,

$$\frac{d(S)}{dt} = \frac{k_L A}{V_U}\left([S] - \frac{(S)}{L_S}\right) \tag{3.12}$$

By separating the variables, Eq. (3.12) can be integrated over a small time step, from t to $t+\Delta t$, within which $[S]$ can be assumed to constant. The resulting discretized rate equation can be rearranged to yield the species concentration,

$$(S) = L_S[S] + \left((S)_0 - L_S[S]\right)\exp\left[-\frac{k_L A}{L_S V_U}\Delta t\right], \tag{3.13}$$

in which (S) and $(S)_0$ are the UP species concentration at current and previous time steps, respectively. Equation (3.13) is applied for every time step at every distinct interface (*ULflat*, *ULeye* and *ULdrop*) to update the concentration of UP at various zones.

3.2.4.2 Mass Balance

Following are the steps involved in mass balance:

1. The number of moles gained at a given interface is calculated from,

$$\Delta n_{(S)} = V_U\left[(S) - (S)_0\right] \tag{3.14}$$

2. The net gain at bulk UP is calculated as sum of number of moles gained, $\Delta n_{(S)}$, at *ULflat* and *ULeye* and due to rejoining droplets less the number of moles lost due to entraining droplets:

$$\sum\Delta n_{(S)}^{gain} = \Delta n_{(S)}^{ULflat} + \Delta n_{(S)}^{ULeye} + \sum\Delta n_{(S)}^{death} - \sum\Delta n_{(S)}^{birth} \tag{3.15}$$

3. The concentration of bulk UP is once again updated [apart from the one by Eq. (3.13)] as,

$$(S) = \frac{n_{(S)} + \sum\Delta n_{(S)}^{gain}}{V_U} \tag{3.16}$$

4. Unlike at UP, where species mass is gained due to droplets only when they rejoin, the loss at LP due to species transfer across all interfaces is made instantaneous by updating the species concentration every time step as,

$$[S] = \frac{n_{[S]} - \sum\Delta n_{(S)}^{loss}}{V_L} \tag{3.17}$$

where $\sum\Delta n_{(S)}^{loss} \neq \sum\Delta n_{(S)}^{gain}$ at a given step.

3.2.5 Model Output

The primary output of the model is the transient profile of $[S]$. The profiles are taken to Qtiplot and curve-fitted. The profiles were well represented by first order exponential decay,

$$[S] = a + b\,\exp(-\lambda t) \tag{3.18}$$

where a and b are the model parameters and λ is the decay constant to which the overall rate constant $\beta = k_L A/V_L$ is related as,

$$\lambda = \beta\left(1 + \frac{1}{L_S}\frac{V_L}{V_U}\right) \tag{3.19}$$

where the quantity inside the parenthesis is system constant.

3.3 Parametric Studies Using the Model

3.3.1 Mass Transfer Rate vs Gas flow Rate

To test the model, it was attempted to simulate the change of $k_L A$ or β as a function gas flow rate Q as in Fig. 2.7, for example, using the model. The idea is to choose model parameters in some fashion, to compute concentration, $[S]$, versus time profiles and obtain β for each. The parameters namely, the mass transfer coefficients and entrainment rate were varied as how they would likely vary with with gas flow rate. Each combination is called a *Trial* and the resulting rate constants are plotted against *Trial numbers*.

Apart from the above parameters, the size and residence time distributions are likely to vary with gas flow rate; however to limit the number of parametric combinations, they were fixed. For the droplet size distribution at the instant of birth, a log-normal distribution of the form,

$$f(x) = \frac{C}{x}\exp\left[-\left(\frac{\ln x - A}{B}\right)^2\right], \tag{3.20}$$

was chosen for droplet size, x in mm, with parameters

$$A = 2.0,\ B = 0.707,\ C = 0.8 \tag{3.21}$$

that would give a size distribution as shown in Fig. 3.3. Droplet sizes were randomly sampled from this distribution and the sampling procedure is given in Appendix A.2.

For each size class there could be a distribution of residence times. However it was verified† that the results are practically unchanged if only the mean residence time is applied for a given size. The mean residence times were taken from,

$$\bar{t}_{res} = A_t \exp(-x/B_t) \tag{3.22}$$

so as to have an inverse relation with droplet size. Two set of parameters were considered namely,

$$A_t = 30.0 \quad B_t = 5.0 \tag{3.23}$$

and

$$A_t = 60.0 \quad B_t = 5.0 \tag{3.24}$$

such that smallest droplet has a residence time approximately equal to A_t. The mean residence times are plotted in Fig. 3.3.

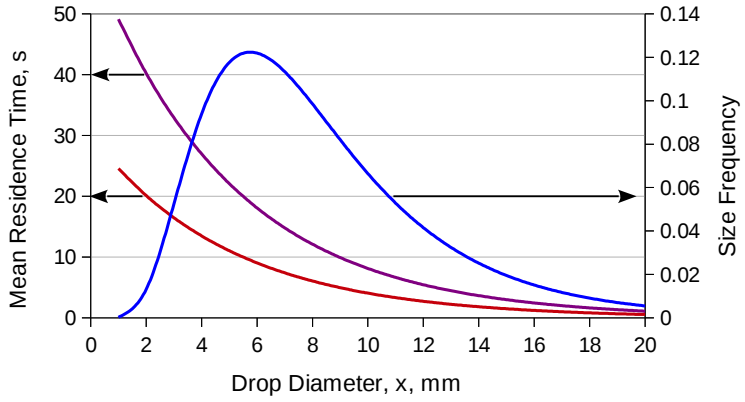

Figure 3.3. Distributions of mean residence times and droplet sizes for the parametric study. The lower and upper curves of mean residence times are given by Eq. (3.23) and (3.24), respectively.

† The verification details are not provided, however the C program has the implementation to sample residence times from a lognormal distribution of the type given by Eq. (3.20), with parameters, $A = \ln\left(\mu/\sqrt{1 + \sigma^2/\mu^2}\right)$, $B = \sqrt{2\ln\left(1 + \sigma^2/\mu^2\right)}$ and $C = 1/(B\sqrt{\pi})$ with μ as mean given by Eq. (3.22) and σ as standard deviation taken to be unity.

The maximum droplet diameter was limited to 20 mm in this parametric study.

The system dimensions for this investigation correspond to a lab scale (≈ 1/5th industrial scale) aqueous model. The following system parameters were fixed for all trials.

1. Vessel diameter = 50 cm
2. Height of LP = 50 cm
3. Thickness of UP = 3 cm
4. Partition coefficient, L_S = 50
5. Initial concentration of S in LP, $[S]_0$ = 1.0 mole/m^3.

The values of partition coefficient and initial species concentration are arbitrary since they are not functions of gas flow rate.

The ratio of radii of eye to vessel was increased from 0 to 0.2 linearly with *Trial number* from 1 to 5 and was set constant thereafter. This was set to simulate the varying eye area with increasing gas flow rate. With the progress of entrainment the volume of UP reduces and therefore the eye radius is increased accordingly. The description of varying UP thickness and eye radius are given in Appendix A.3.

The following are the description and the results of the Sets of trials considered.

Set-I: The first Set was formulated by assuming linear variations in all the parameters as seen in Fig. 3.4. The value for *VPU* (its axis on the right side of the chart) was set to zero until *Trial* 5; it was then increased slowly from *Trial* 6 and linearly from *Trial* 8. The mean residence times were taken from Eq. (3.23). The rate constant values obtained from each trial are plotted in Fig. 3.5. Interestingly there is a change in slope at *Trial* 8 and it is also where the entrainment rate actually picks up!

Set-II: To verify the trend of rate constants in Set-I another set of trials without entrainment were performed with the same parameters as in Set-I. The results in Fig. 3.5 show absence of any change in slope and therefore confirm that the slope change in mass transfer rate is solely due to entrainment.

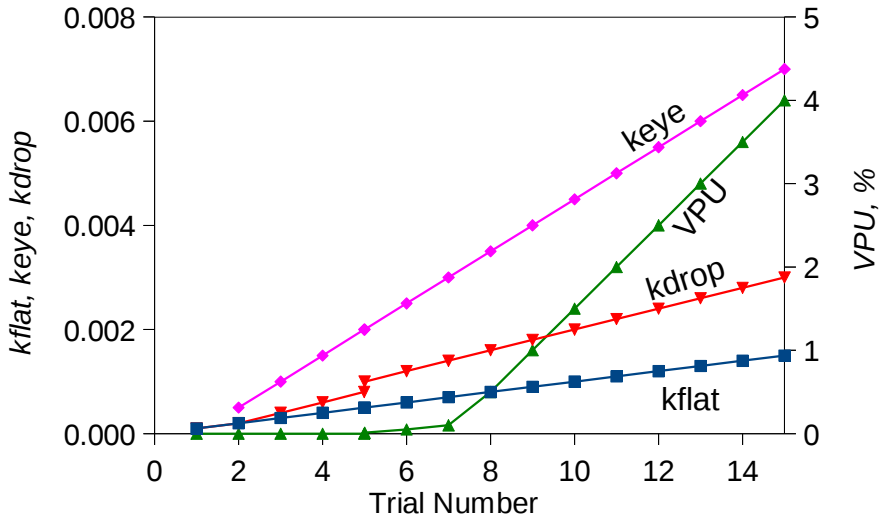

Figure 3.4. Various trends of values (mostly linear) for parameters inputted for Sets I and II.

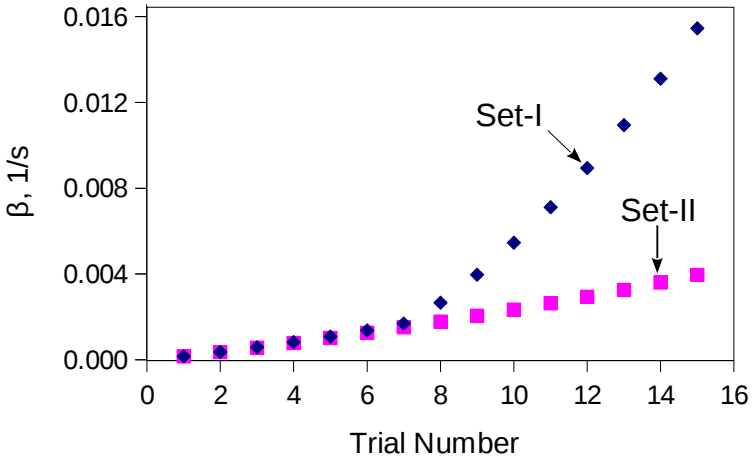

Figure 3.5. Computed rate constant for two Set of Trials. Set-I showing the change of slope when entrainment rate picks up. Set-II without entrainment confirms the role of entrainment in Set-I

Set-III: Non linear trends were considered for the input parameters as shown in Fig. 3.6. The rate of increase of mass transfer coefficients were decreased with *Trial numbers*. However, after an initial passivity, VPU was increased linearly so as to quickly reach the point of completely entraining the UP at higher *Trial numbers*. This is to aim for the second change in slope of the rate curve. Despite setting higher VPU, complete entraining of UP did not take place. So, the mean residence time distribution was changed to Eq. (3.24), which is the double that of Eq. (3.23), so as to delay the droplet rejoining process. Results of 20 trials for this set are shown in Fig. 3.7 that also has illustrative lines drawn over the points to delineate the three regimes. During computations it was observed that starting from *Trial* 13 the upper phase got completely drained which is also seen from the change of slope in that figure.

The model results hitherto, can be summarized as follows:

1. Onset of entrainment causes the first change in slope which is in line with numerous water modeling studies of the past.
2. The second change in slope occurs right at the point where UP is drained out completely, same as observed in the literature (Kim *et al*, 1987a, Mietz *et al*, 1991b). The model results show that the increase in mass transfer rate, that was due to increasing entrainment rate, ceases with no more possibility of increasing the entrainment rate; any increase in mass transfer rate has to be caused only by increase in values k_{drop} with the *Trial numbers* or with gas flow rate as in a real system.

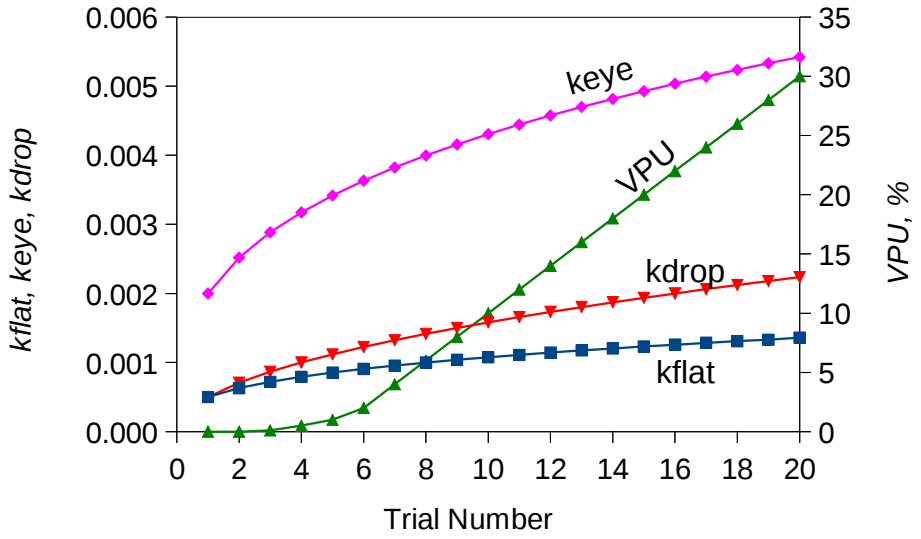

Figure 3.6. Various trends of values (non-linear) for parameters inputted for Set-III

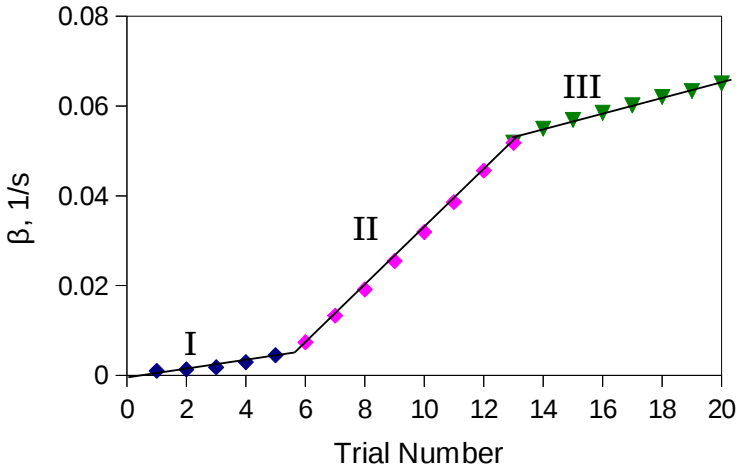

Figure 3.7. Results of the model for Set-III showing the three regimes of mass transfer

3.3.2 Effect of Size Distribution

To test the effect of size distribution, Lognormal distributions with two extreme cases namely, distributions of finer droplets (*finer*) and coarser droplets (*coarser*) were considered in addition to the base case *(base*) considered throughout Sec. 3.3.1. The parameters of all the three distributions are summarized in Table 3.1 along with their arithmetic and Sauter mean droplet diameter, $\bar{x}$ and x_{32}, respectively. The Sauter mean diameter is defined as,

$$x_{32} = \frac{\sum\left(x^3 f(x)\right)}{\sum\left(x^2 f(x)\right)}. \tag{3.25}$$

Table 3.1. Parameters of three size distributions

Size Distribution Label	*A*	*B*	*C*	$\bar{x}$, mm	x_{32}, mm
finer	0.5	1.414	0.4	3	9
base	2.0	0.707	0.8	8	11
coarser	4.0	0.707	0.8	17	18

Trials 6 to 13 of Set-III described in Sec. 3.3.1 were performed for these distributions and the results are plotted in Fig 3.8a. It is obvious that for any trial, $\beta_{finer} > \beta_{base} > \beta_{coarser}$, *i.e.*, for a given volumetric entrainment rate, finer the droplets, larger is the mass transfer rate. A linear relation is revealed between β and x_{32} in Fig. 3.8b, when values of β normalized by β of *Trial* 13 are plotted against x_{32}. This sort of correspondence is absent if we consider the arithmetic mean, $\bar{x}$ (not shown). This proves that x_{32} is more appropriate than $\bar{x}$ in characterizing the mass transfer rate.

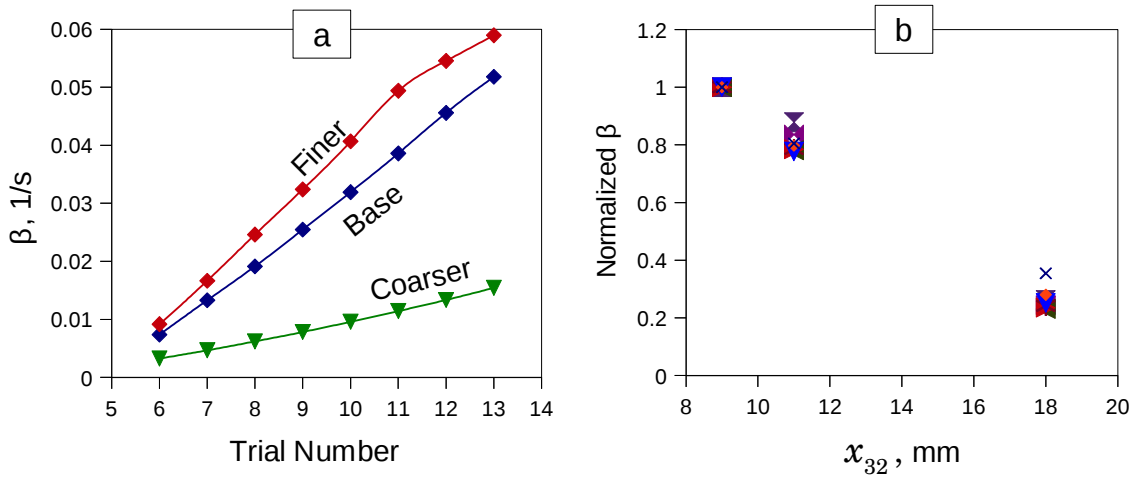

Figure 3.8. (a) Comparison of rate constants (β) obtained for three size distributions and input parameters of Set-III described in Sec. 3.3.1. (b) Values in (a) are normalized and plotted against Sauter mean (x_{32}).

3.3.3 Direct Estimation of Rate Constant from Input Parameters

It is attempted to directly estimate β, by using the input parameters of Sec. 3.3.1 into the models described in Sec. 3.1, without performing the mass transfer calculations. One of the outputs of the DBD model is the time average of net droplet area, $A_{drop,\,net}$ (transitional droplet area). This quantity can also be evaluated numerically using Eq. (3.5) given the entrainment rate, droplet size distribution and mean residence times. The number entrainment rate, $\dot{N}$, in Eq. (3.5) can be evaluated from the volumetric entrainment rate, VPU through,

$$\dot{N} = \frac{V_U VPU}{100} \frac{1}{\frac{\int V(x) f(x)\, dx}{\int f(x) dx}} \tag{3.26}$$

where $V(x)$ is the volume of droplet of size x. Here the minimum and the maximum droplet sizes for the limits of the integrals must be the same as that in the DBD computations to be able to compare. Figure 3.9 compares $A_{drop,\,net}$ obtained by numerical evaluation of Eq. (3.5) (trapezoidal rule for integrals) and from the DBD output, for various trials of Set III described in Sec. 3.3.1. Until *Trial* 13, the good agreement between them mutually verifies Eq. (3.5) and

the droplet birth and death processes implemented in the DBD. The split after Trial 13 is because the upper phase is completely entrained into the lower phase.

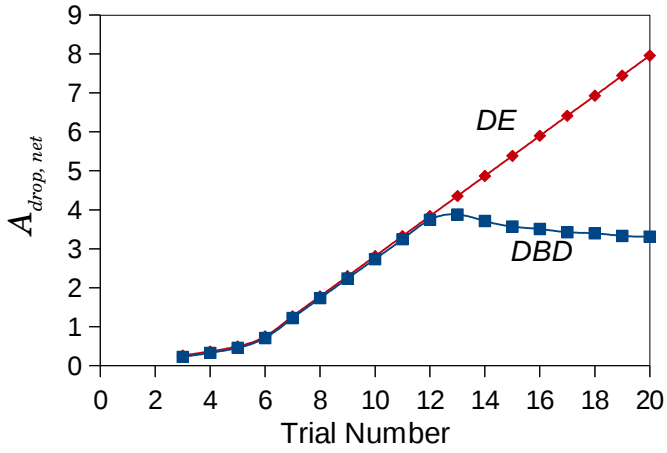

Figure 3.9. Comparison of $A_{drop,\,net}$ between the output of drop by drop model (DBD) and numerical evaluation of Eq. (3.5) (DE) for various Trials of Set III.

Extending Eq. (3.5), the net value for kA due to the entrained droplets at steady state can be estimated from,

$$kA\big|_{drop,\,net} = \dot{N}\frac{\int k(x)A(x)t_{res}(x)f(x)dx}{\int f(x)dx}. \tag{3.27}$$

where $k(x)$ is mass transfer coefficient of the droplet of size x. Let us define an effective coefficient,

$$kA\big|_{eff} = kA\big|_{flat} + kA\big|_{eye} + kA\big|_{drop,\,net} \tag{3.28}$$

where the values for $kA\big|_{flat}$ and $kA\big|_{eye}$ were computed directly from input parameters and that of $kA\big|_{drop,\,net}$ was obtained by numerically evaluating Eq. (3.27). Let the rate constant for this direct estimation be defined as,

$$\beta_{DE} = \frac{kA\big|_{eff}}{V_L} \tag{3.29}$$

and that from the DBD be called as β_{DBD}.

The values of β_{DE} were estimated using the input parameters of all trials of Set-III in Sec. 3.3.1, for the three distributions in Sec. 3.3.2 and are compared with β_{DBD} in Fig. 3.10. Here β_{DBD} is considered to be the precise estimate. Figure 3.10 also has plots of relative difference between β_{DBD} and β_{DE} with respect to β_{DBD}. The over estimation of the rate by β_{DE} is severe for *finer* and negligible for *coarser* size distributions. The over estimation is because of using t_{res} in Eq. (3.27) instead of t_{active} $[= \mathrm{MIN}(t_{sat}, t_{res})]$, which would be smaller due to early saturation of finer droplets. For the cases of *coarser*, β_{DBD} and β_{DE} match well because the droplets are too big to saturate quickly; this matching also mutually verifies Eq. (3.27) and the mass transfer calculations in DBD.

Since, in the most general case, the degree of coarseness of droplet size is not well defined, the approximation to rate constant by β_{DE} is not reliable. The model described by Eqs. (3.27) and (3.28), therefore, stops short of estimating rate constant precisely because of the inability to model t_{active}, for the reasons discussed in Sec. 3.1.

In Sec 2.3 it was mentioned that Lachmund *et al* (2003) and Ekengard *et al* (2008) estimated the transitional area of slag droplets in bulk metal and metal droplets in bulk slag to be 25 and 3 to 14 times the slag metal interfacial area before gas injection, respectively. They used these area estimates directly into $k\,A\big|_{eff}$ to find the mass transfer rates in their works. However, given the shortcomings of a rather complicated model described by Eqs. (3.27) and (3.28), such a simple approach is highly questionable!

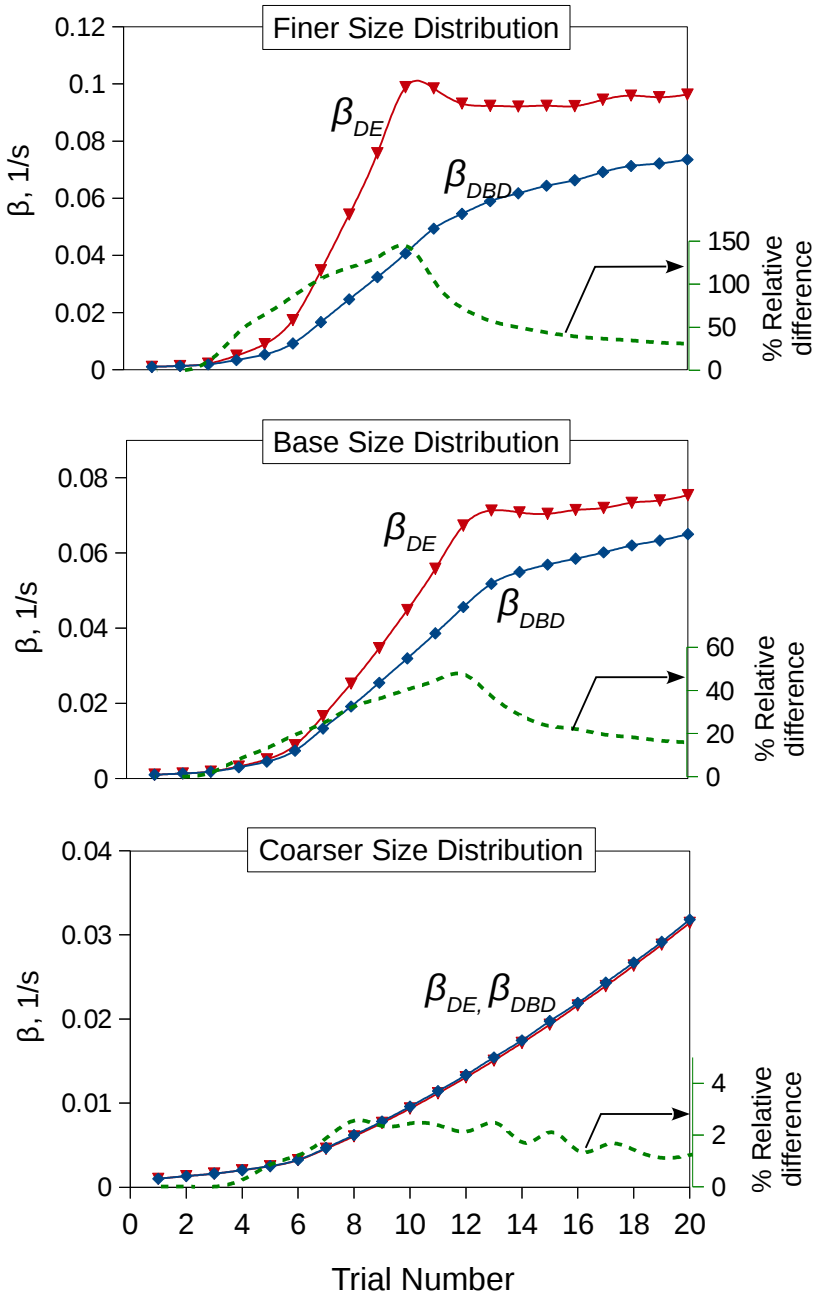

Figure 3.10. Comparison of rate constants of drop by drop model (β_{DBD}) and direct estimation (β_{DE}) for various Trials of Set III and size distributions. The % relative difference between β_{DBD} and β_{DE} with respect to β_{DBD} is shown by dotted lines. Common x-axis.

The results hitherto prove that DBD model is a potential tool to analyze the influence of various parameters on mass transfer rate. Some more analyses are possible as follows:

- The current DBD model assumes metal side (LP side) mass transfer controlled (Assumption 3 in Sec. 3.2.1); this can be straightforwardly extended to mixed mass transfer control in metal and slag (see Deo & Boom (1993) for rate expression).
- The mixing in the bulk phases have been assumed to be instantaneous so that these phase always remain homogeneous (Assumption 1 in Sec. 3.2.1). However in real systems there is finite mixing time and hence the inhomogeneity in species concentration. The effect of this inhomogeneity can be tested by 1) varying the initial concentration of entraining droplets at the time of birth and 2) subjecting the entrained droplets to concentration fields in LP different from the average bulk concentration at a given time instant.

3.4 Summary

The drop by drop kinetic model was developed to calculate mass transfer rate incorporating the entrainment parameters, namely entrainment rate, droplet size and residence time distributions. Various parametric studies were conducted and the following conclusions are drawn:

1. The sudden increase in liquid-liquid mass transfer rate is associated with the onset of slag entrainment which causes increased two phase interfacial area. The ability to simulate the classic three flow rate–regimes of mass transfer demonstrates the capability of the model.
2. Droplet size distribution has significant influence on mass transfer rate with the latter varying linearly with the inverse of Sauter mean droplet diameter.
3. Attempt to estimate rate constant from a theoretical model showed that the ‘active time’ parameter is an impediment and therefore necessitates a numerical model like the DBD. However the theoretical model served to verify the DBD.
4. DBD is a potential tool for studying the role of various parameters on mass transfer rate.

4. Multiphase LES Methodology

4.1 LES in Reduced Domain

Due to large grid requirements, the entire ladle cannot be simulated using LES and recognizing the axial symmetry of the fluid flow problem, only a thin slice of the fluid domain is considered as shown in Fig 4.1a. In Fig 4.1b various boundaries of the domain namely the inlet, outflow, walls and free surface boundaries are marked. Since a three phase contact is not possible in the flow solver, to be introduced in Sec. 4.2, the air phase above the liquid slag and metal phases is replaced by a free surface boundary condition, to avoid the slag-metal-air three phase edge. For the two lateral faces periodic boundary condition would be the appropriate condition; however, from trial simulations it was found that it resulted in very unstable two phase interface leading to unphysical entrainment, hence wall boundary conditions were given. This may not be a serious limitation since,

- the grid resolution is not high enough to capture the boundary layer and therefore introduce wall effects and
- in the circular eye region (of the cylindrical ladle) waves of the two phase interface (*ULeye*) are confined to a small arc and therefore are not strongly periodic.

The problem is therefore narrowed to providing appropriate inlet conditions to the thin slice LES domain. The inlet condition for the LES is the velocity profile at location of the *inlet surface* in the ladle. In the absence of data, these conditions can be extracted from a RANS simulation performed for the entire ladle. Since only mean velocities are obtained from RANS simulation, these conditions have to be supplemented by methods to generate fluctuating velocities that are required for appropriate LES inlet conditions. In this chapter, first the fluid flow solver used for the multiphase LES and RANS is introduced, followed by the method to generate turbulence at inlet with various verification cases. Finally the gas-liquid two phase RANS models to simulate steel flow in ladle are discussed with verification cases.

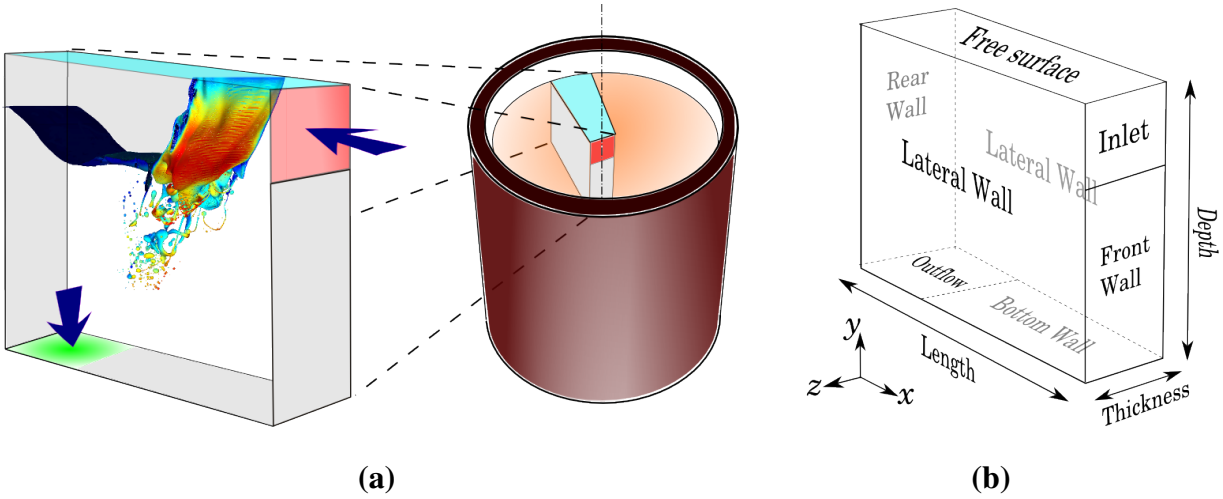

Figure 4.1. (a) Schematic of thin slice of fluid domain in the ladle, considered for the Large Eddy Simulations. (b) Nomenclature of various boundaries of the LES domain

4.2 Gerris Flow Solver

The Gerris Flow Solver (hereafter Gerris) is chosen for multiphase simulations for it superior capabilities to simulate complex interface topologies (Fuster *et al*, 2009) that is due to better representation of interface tension and adaptive mesh refinement capability.

Mathematical Modeling of multiphase phenomena have been dealt with considerable success through the volume of fluid method popularly known as the VOF method, first developed by Hirt and Nichols (1981). The superior volume conservation properties of VOF method has made it popular among all the multiphase modeling techniques, despite its weak ability to represent the interface curvature (Fuster *et al*, 2009).

Within the VOF framework most of the past works have reduced the stress boundary condition at the interface into merely a balance between pressure jump and the interface tension force. The surface force is then converted into volume force and added to the momentum equations, as formulated by Brackbill *et al* (1992) in their continuum surface force (CSF) method. In the case of a stationary droplet in a continuous phase of the same density, the pressure gradient in the momentum equation should exactly balance the volumetric surface tension force; however, when this balance is not achieved there is a spurious velocity field

surrounding the drop and this has been a problem since the inception of VOF method.

Popinet (2009) developed a new method called 'balanced-force CSF' whereby choosing proper discretization operators between the pressure gradient and the tension force, the spurious velocities are brought down to machine precision. Moreover by using the height-function method, second-order accurate estimates for interface curvature are obtained (Fuster *et al*, 2009). Within the height function method, curvatures for under-resolved interface are estimated by 'parabola-fitted curvature' method. Collectively, these procedures to precisely add the effect of surface tension to Navier Stokes equation are known as the 'accurate interfacial tension model', implemented in Gerris, developed by Popinet (2009).

4.2.1 Gerris Objects, Grid Generation and Refinement

Gerris is a free and open-source software that can solve the 2D and 3D-incompressible-variable density-Navier-Stokes equation (Popinet, 2003 & 2009) and is coded in *C* programming language. A simulation is set up by the user by writing various Gerris objects in a text file known as simulation or parameter file and run from a terminal (in a Linux operating system). Through Gerris objects, the domain geometry, boundary conditions, physical properties of fluids and grid refinement are specified as user defined functions. A user defined function handled by the object, `GfsFunction`, is any valid *C* code that can use velocities and various other domain variables.

The grid generation process is totally automatic in that only the domain boundary and mesh specification must be inputted. The domain boundary is formed by invoking a unit computational volume (or area in 2D) known as GfsBox of dimensions $L\times L\times L$ with $L=1$ by default and adding any solid boundaries if required; any number of GfsBoxes can be added and joined in a desired fashion. Within those boxes, solid boundaries can be added through `GfsFunction`, using boolean operations between basic geometric objects (line, plane, circle, sphere etc) or importing from a CAD package. Based on the user-defined initial and evolving meshing schemes, the grid is generated based on quad/octree discretization for 2D and 3D respectively. A scheme of quadtree discretization is shown in Fig. 4.2 along with the levels of refinement hierarchically. The size of cell (Δ) at a certain level can be estimated from,

$$\Delta = \frac{L}{2^{\texttt{Level}}} \tag{4.1}$$

where L is the length of the GfsBox and `Level` is the level of refinement.

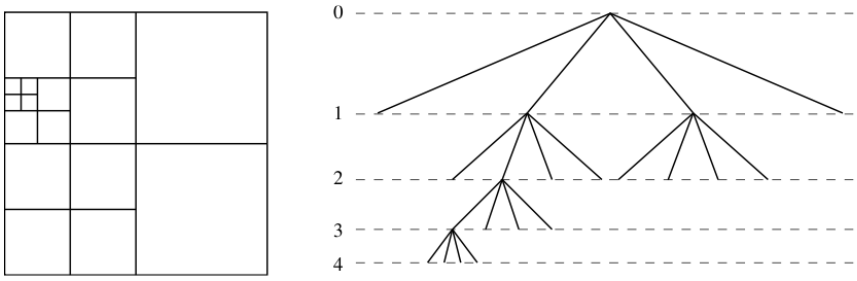

Figure 4.2. Example of quadtree discretization and the corresponding tree representation of the levels refinement (Popinet, 2003). Level zero correspond to unit GfsBox and level four is of the four leaf cells of the largest tree.

An important feature of Gerris is the Adaptive Mesh Refinement (AMR) capability. Through `GfsFunction`, one can specify maximum and minimum levels of refinement, limit the total number of affordable cells, turn off adaptive refinement in certain areas, in any regions of interest. AMR offers enormous computational savings while being well able to resolve dynamic flow features. Due to its efficient algorithm AMR takes less than 5% of the total effort even if performed for every time step (Fuster *et al*, 2009).

4.2.2 Gerris Equations

Apart from the multiphase simulations, Gerris being a generic Navier-Stokes equation solver can be used for RANS simulations as well. It does not have any in-built turbulence model, but allows any number of scalars to be transported. So turbulence models can be added through various GfsObjects and using `GfsFunction`. All calculations in Gerris are time unsteady; however, for steady state problems the temporal variations in solutions decrease with simulation time (as with number of iterations in a steady state simulation) and eventually reaches steady state. So Gerris was used for all CFD simulations performed in this project. There are two versions of Gerris available, of interest: `GfsSimulation` and `GfsAxi` for Cartesian and Axisymmetric coordinate systems, respectively. The governing equations for

fluid flow including surface tension are as follows:

Variable density, incompressible Navier-Stokes equation:

$$\rho\left[\frac{\partial \boldsymbol{u}}{\partial t} + \boldsymbol{u}.\nabla \boldsymbol{u}\right] = -\nabla p + \nabla\cdot(2\mu \boldsymbol{S}_{ij}) + \sigma\kappa\delta_s \boldsymbol{n} \tag{4.2}$$

Incompressiblitiy condition:

$$\nabla\cdot\boldsymbol{u} = 0 \tag{4.3}$$

Advection of volume fraction, $\boldsymbol{F}$:

$$\frac{\partial \boldsymbol{F}}{\partial t} + \nabla\cdot(\boldsymbol{F}\boldsymbol{u}) = 0 \tag{4.4}$$

Advection–Diffusion of Scalar:

$$\frac{\partial \phi}{\partial t} + \nabla\cdot(\boldsymbol{u}\phi) = \nabla\cdot(D_\phi \nabla\phi) + S_\phi \tag{4.5}$$

In Eqs. (4.2) to (4.5), $\boldsymbol{u}$ is the velocity vector, p is the pressure, $\boldsymbol{S}_{ij} = 1/2(\nabla\boldsymbol{u} + \nabla^T\boldsymbol{u})$ is the deformation tensor, μ and σ are the dynamic viscosity and interfacial tension coefficients, D_ϕ and S_ϕ are the diffusion coefficient and various sources added for the transport of the scalar ϕ.

Conventionally standard $k-\varepsilon$ turbulence model has been used to simulate the fluid flow in the ladle and its water models. However in the present work, SST $k-\omega$ model of Menter, (2003) has been implemented. This was required for the RANS simulations of the thinslice water model discussed in Ch. 5 to yield grid independent solution and hence is the only model discussed in this Thesis. Since the standard $k-\varepsilon$ model and the likes cannot be integrated up to the wall, wall functions are used to compute the wall shear stress that provides the necessary boundary condition. However, this requires a large minimum grid size at the wall thereby affecting the flow resolution, more so for the flow through thin sections. Complex wall functions can be added to the $k-\varepsilon$ models to achieve sufficient resolution, however, this often lead to numerical instability which can therefore be overcome by using a $k-\omega$ type model (Ansys CFX 2009). Although the $k-\omega$ type of model can be integrated up to the wall without

the need for wall functions, to minimize the cost when high resolutions are not needed, wall functions have been formulated to permit desired mesh resolution at the wall. The SST $k-\omega$ model is generally regarded as a robust two equation turbulence model that combines the best of performances of standard $k-\omega$ model in the near wall region and of standard $k-\varepsilon$ in the far field region (Fluent, 2009). The model equations and wall functions implemented in Gerris for the present work are provided in Appendices B.1 to B.2 along with the verification against various benchmark cases. The verification cases show that the implementation is satisfactory.

For LES, the same equations, Eqs. (4.2) to (4.4), are solved, but in conjunction with a sub-grid scale model (SGS) that replaces the viscosity coefficient, μ with $(\mu + \mu_{SGS})$ in Eq. (4.2), where μ_{SGS} models the turbulence of small scales. For the present work a simple algebraic model of Smagorinsky-Lilly was used. The model assumes that at the small scales of turbulence all the energy received from larger scales are dissipated instantaneously (Smagorinsky, 1963) and is given by,

$$\mu_{SGS} = \rho(C_S \Delta)^2 \sqrt{2\bar{\boldsymbol{S}}_{ij}\bar{\boldsymbol{S}}_{ij}} \tag{4.6}$$

where $C_S = 0.1$, Δ is the grid size and $\bar{\boldsymbol{S}}_{ij} = \boldsymbol{S}_{ij}$ in Gerris, when the SGS model is applied.

4.3 Synthetic Eddy Method

Synthetic Eddy Method (SEM) of Jarrin (2008) is a method to generate fluctuating velocity components. It generates large scale coherent structures and is therefore compatible with the idea of LES. The method is simple because it requires turbulence statistics such as Reynolds stresses and eddy length distributions that can be, for the most part, extracted from RANS simulations. Moreover, it has a very little computational overhead (<1%) on the LES computations.

4.3.1 SEM Principles

In this section, some of the SEM principles are reviewed based on Jarrin's thesis (Jarrin, 2008). The method views a turbulent flow field as composed of many coherent eddies. So, it consists of distributing *N* number of eddy locations randomly in a virtual box enclosing the

inlet plane and marching them in the mean flow direction at mean velocity as shown in Fig. 4.3; based on the prescribed turbulence statistics, the strength and size of eddy interaction zone are determined; the summation of intensities of various eddies that pass by a point in the inlet plane, therefore gives the fluctuating component at that point; by adding the generated fluctuating velocity, $u_i^{'}$ to the mean velocity, U_i (from RANS in our case), the instantaneous velocity is thus obtained as,

$$u_i = U_i + u_i^{'} \tag{4.7}$$

where is the index of coordinate directions.

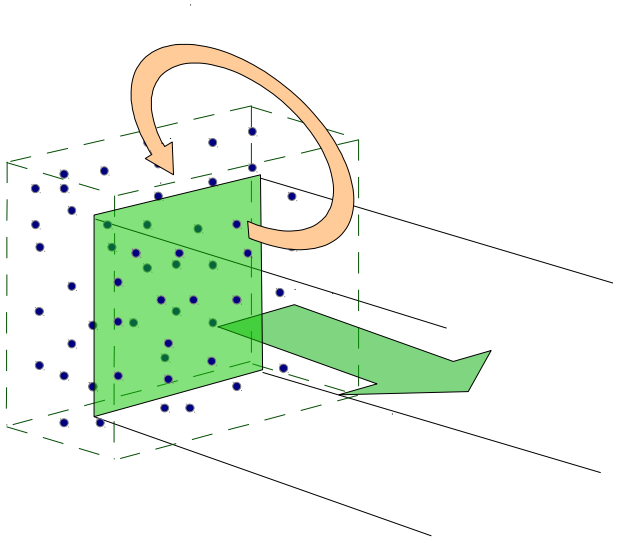

Figure 4.3. Schematic of the Synthetic eddy method showing the inlet plane of a duct surrounded by a virtual eddy box (dashed line) and the points representing various eddy locations at an instant of time; the straight arrow shows the mean flow direction and the circular arrow indicates the re-circulation of eddies

The fluctuating velocity is given by,

$$u_i^{'} = \frac{1}{\sqrt{N}} \sum_{k=1}^{N} a_{ij} \epsilon_j^k f_{LS(\mathbf{x})}\left(\mathbf{x}-\mathbf{x}^k\right) \tag{4.8}$$

where the product $a_{ij}\,\epsilon_j^k$ is the intensity of an eddy and velocity distribution within an eddy, prescribed through the shape function, $f\left(LS(\mathbf{x}),\ \mathbf{x}-\mathbf{x}^k\right)$; $LS(\mathbf{x})$ is the spatial distribution of length scale of eddies, $\mathbf{x}=(x, y, z)$ is the grid point on the inlet plane and $\mathbf{x}^k=(x^k, y^k, z^k)$ is

the centre of k^{th} eddy, a random variable. The coefficient a_{ij} is the Cholesky decomposition of the Reynolds stress tensor R_{ij}, given by,

$$a_{ij} = \begin{pmatrix} \sqrt{R_{11}} & 0 & 0 \\ R_{21}/a_{11} & \sqrt{R_{22}-a_{21}^2} & 0 \\ R_{31}/a_{11} & (R_{32}-a_{21}a_{31})/a_{22} & \sqrt{R_{33}-a_{31}^2-a_{32}^2} \end{pmatrix} \tag{4.9}$$

The value of ϵ_j for j^{th} velocity component is based on the eddy spin direction that takes value from the sample space, $\{1,-1\}$ with equal probability. The eddy box is bound by the limits,

$$x_{i,min} = \text{MIN}(x_i - LS(\mathbf{x})) \text{ and } x_{i,max} = \text{MAX}(x_i + LS(\mathbf{x})), \tag{4.10}$$

where x_i are the three dimensions of the box. Consequently, the eddy box volume is given by,

$$V_B = \prod_i \left[\text{MAX}\left(x_i + LS(\mathbf{x})\right) - \text{MIN}\left(x_i - LS(\mathbf{x})\right)\right] \tag{4.11}$$

The location of eddies are updated according to,

$$\mathbf{x}^k(t+dt) = \mathbf{x}^k(t) + U_m dt \tag{4.12}$$

where U_m is the mean velocity at the inlet. The eddies that leave the eddy box are recirculated, although at different location in the inlet plane of the eddy box.

4.3.1.1 Shape Function

The shape function f can be any function of length scale, LS and the distance between a gird point and k^{th} eddy, $(\mathbf{x}-\mathbf{x}^k)$. However Jarrin imposes a criterion on the shape function as,

$$\frac{1}{V_B}\int_{-LS}^{+LS} f_\sigma^2\left(\mathbf{x}-\mathbf{x}^k\right) d\,\mathbf{x}^k = 1 \tag{4.13}$$

The following discussion will show how SEM reproduces input statistics if condition, Eq. (4.13) is met.

Using Eq. (4.8), the second moments $\left\langle u_i' u_j' \right\rangle$, of the synthesized signal can be derived as,

$$\left\langle u_i' u_j' \right\rangle = \frac{1}{N}\sum_{k=1}^{N}\sum_{l=1}^{N}\left\langle a_{im} a_{jn}\, \epsilon_m^k\, \epsilon_n^l\, f_{LS}\left(\mathbf{x}-\mathbf{x}^k\right) f_{LS}\left(\mathbf{x}-\mathbf{x}^l\right)\right\rangle \tag{4.14}$$

Since both ϵ_j and $\mathbf{x}^k$ and hence f are independent random variables, we can write,

$$\left\langle u_i' u_j' \right\rangle = \frac{1}{N} \sum_{k=1}^{N} \sum_{l=1}^{N} a_{im} a_{jn} \left\langle \epsilon_m^k \epsilon_n^l \right\rangle \left\langle f_{LS}\left(\mathbf{x}-\mathbf{x}^k\right) f_{LS}\left(\mathbf{x}-\mathbf{x}^l\right) \right\rangle \tag{4.15}$$

Again, ϵ_j being a random variable with equal probability distribution, we have,

$$\left\langle \epsilon_m^k \epsilon_n^l \right\rangle = \left\langle \epsilon_m^k \right\rangle \left\langle \epsilon_n^l \right\rangle = \begin{cases} 0, & k \neq l \\ 1, & k = l \end{cases} \tag{4.16}$$

Using Eq. (4.16), Eq. (4.15) simplifies to,

$$\left\langle u_i' u_j' \right\rangle = \frac{1}{N} \sum_{k=1}^{N} a_{im} a_{jn} \left\langle f_{LS}^2\left(\mathbf{x}-\mathbf{x}^k\right) \right\rangle \tag{4.17}$$

In Eq. (4.17),

$$\left\langle f_{LS}^2\left(\mathbf{x}-\mathbf{x}^k\right) \right\rangle = \int_{-\infty}^{+\infty} p(\mathbf{x}^k) f_{LS}^2\left(\mathbf{x}-\mathbf{x}^k\right) d\mathbf{x}^k \tag{4.18}$$

where $p(\mathbf{x}^k)$ is the probability density function (PDF) for the random variable, the eddy location. For a uniform distribution of eddy location, the PDF is,

$$p(\mathbf{x}^k) = \begin{cases} \dfrac{1}{V_B}, & \text{eddy box} \\ 0, & \text{elsewhere} \end{cases} \tag{4.19}$$

Using Eq. (4.19) in Eq. (4.18) we obtain,

$$\left\langle f_{LS}^2\left(\mathbf{x}-\mathbf{x}^k\right) \right\rangle = \frac{1}{V_B} \int_{-LS}^{+LS} f_{LS}^2\left(\mathbf{x}-\mathbf{x}^k\right) d\mathbf{x}^k \tag{4.20}$$

Since RHS of Eq. (4.20) is unity according to Eq. (4.13), from Eq. (4.17), we obtain,

$$\left\langle u_i' u_j' \right\rangle = a_{im} a_{jn} \tag{4.21}$$

which is also true by the definition of Cholesky decomposition of Reynold stress tensor [Eq. (4.9)]. Thus theoretically, SEM can reproduce the exact second moments at the inlet.

The shape function essentially decides the eddy interaction volume with respect to the grid point in the inlet. By specifying various shape functions and length scales for each

directions it allows to control the anisotropy of turbulence. To simplify, Jarrin defined an isotropic shape function,

$$f_{LS(\mathbf{x})}\left(\mathbf{x}-\mathbf{x}^k\right)= \sqrt{\frac{V_B}{LS^3}}\ f_{LS}\left(x-x^k\right)f_{LS}\left(y-y^k\right)f_{LS}\left(z-z^k\right), \tag{4.22}$$

with components for each direction defined by a tent function as,

$$f_{LS}(x_i-x_i^k) = \begin{cases} \sqrt{\frac{3}{2}}(1-|X|), & |X|<1 \\ 0 & \text{otherwise} \end{cases}, \quad X = \frac{x_i-x_i^k}{LS}. \tag{4.23}$$

4.3.1.2 Number of eddies

From Sec. 4.3.1.1 we see that the second moments are independent of the number of eddies. In the derivations of Jarrin, the fourth moments, also known as the 'flatness' of a distribution, has a dependence on the number of eddies. This was demonstrated in the effect of number of eddies on the fluctuating velocity signal of isotropic turbulence. As the number of eddies tend to infinity, the PDF of fluctuating velocities tend to a Gaussian distribution and as the number of eddies tend to zero, the PDF had a sharp peak around zero; in the latter case, the eddy box is barely filled and is not representative of actual turbulence and in the former, the cost of generating, transporting the eddies and performing calculations on those eddies increase. So an optimal value is required.

Although based on the expression for 'flatness', Jarrin recommends a value for expression for number of eddies through,

$$N = C\,\mathrm{MAX}\left(\frac{V_B}{LS^3}\right) \tag{4.24}$$

there is a *ad hoc* parameter C to match performance of SEM with available data. Later in Sec. 4.3.2, the effect of number of eddies on SEM statistics will be assessed.

4.3.1.3 Eddy Size Distribution

Based on the turbulence statistics obtained from his own periodic LES simulations for fully developed plane channel flow at $Re_\tau = 395$, Jarrin was able to specify anisotropic length scale distributions and by varying them between a factor to 0.25 to 2.0 he studied the downstream development of the coefficient of friction on the channel wall. It was observed that over specification of length scales did not affect the flow development whereas underspecification delayed the development which highlight the role of eddy length scale.

The eddy sizes can be taken from the turbulent length scale that a RANS simulation can provide. For an SST $k-\omega$ model, the length scale is as defined as,

$$LS = \frac{\sqrt{k}}{\beta^* \omega} \tag{4.25}$$

Since, closer to the wall LS can become zero, Jarrin recommends to limit LS by the local grid size, Δ, as

$$LS = \mathrm{MAX}\left(\frac{\sqrt{k}}{\beta^* \omega},\ \Delta\right) \tag{4.26}$$

4.3.2 SEM Implementation and Verification in Gerris

The implementation of SEM in Gerris consists of reading the inlet statistics, generating fluctuating velocities and applying them as boundary conditions; these steps are explained in Fig. 4.4. A typical implementation of SEM within Gerris parameter file is provided in Appendix B.3. The implementation is compatible with Gerris parallelization, although a probable issue is addressed in Appendix B.4.

The verification step consists of performing 3D simulations with defined set of input turbulence statistics and comparing the resulting statistics with the same inputs. Here, turbulence statistics of the plane channel flow (*i.e.*, two dimensional flow between two infinite parallel planes) at $Re_\tau = 395$ were taken from DNS data of Kim *et al* (1987b) of which, W, $\langle v'w' \rangle$ and $\langle w'u' \rangle$ were set to zero and the length scale was calculated according to Eq.

(4.26). The input statistics are shown in Fig 4.5. Since output statistics were aimed only at the inlet plane, a uniform mesh refinement of `Level` 6 in a unit `GfsBox` was given. This resulted in a 64×64 grid at the inlet and elsewhere a coarser grid was specified, since downstream flow has little relevance here. Two simulations were performed for two different total number of eddies; the first case was with 1430 eddies obtained using Eq. (4.24) setting the constant to unity and second case was with 10,000 eddies.

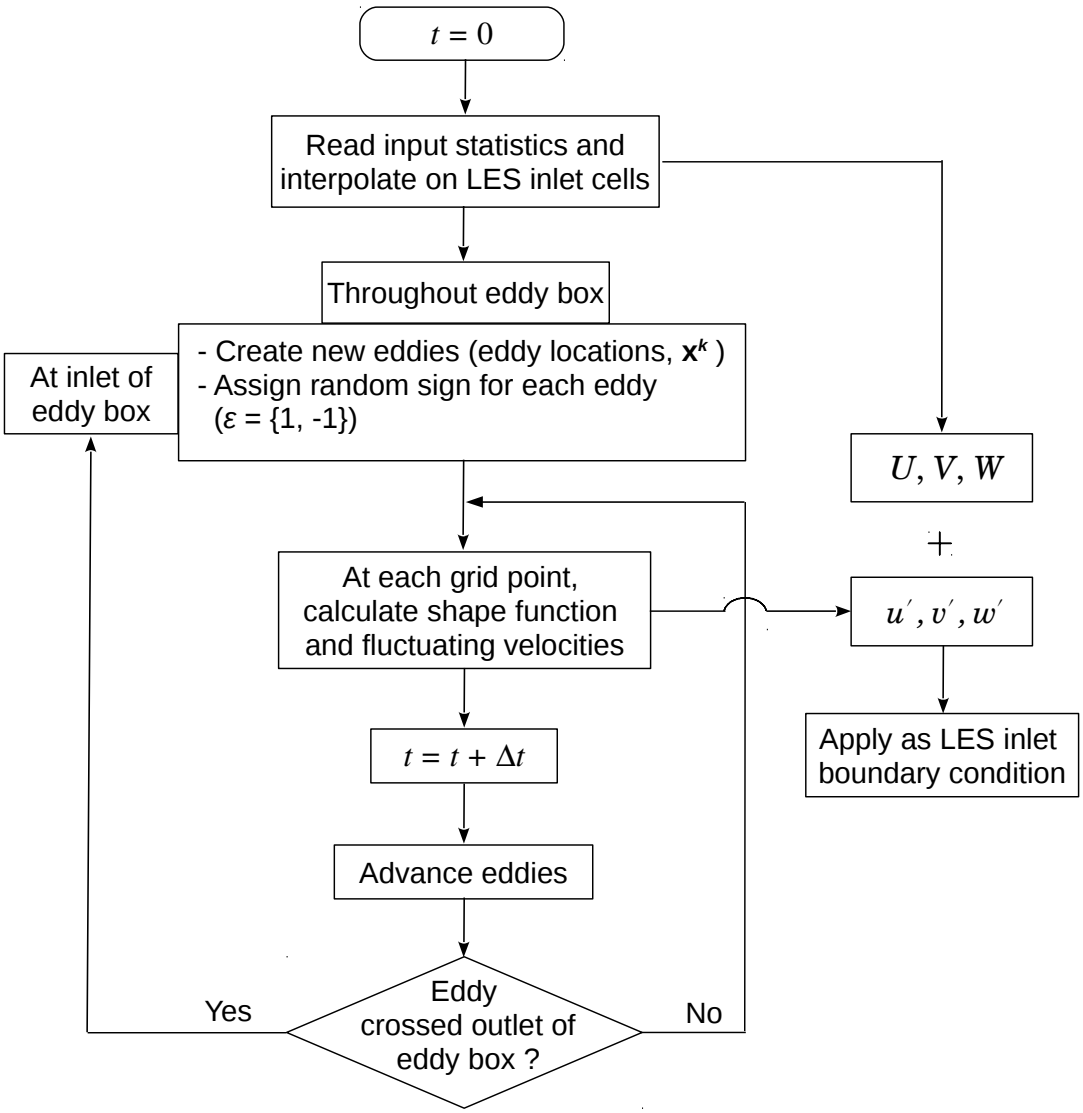

Figure 4.4. Flowchart of steps involved in Synthetic Eddy Method implemented in Gerris

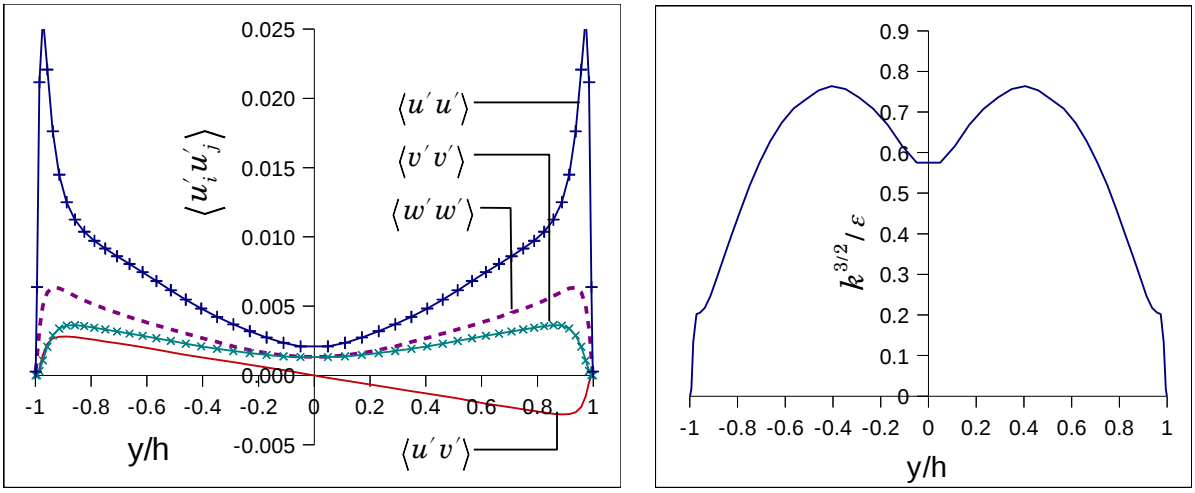

Figure 4.5. Various DNS statistics as input for SEM: (a) Reynolds stresses (b) length scale calculated from DNS data using $LS = k^{3/2}/\varepsilon$. h is the half channel width and y is the coordinate in that direction.

Figure 4.6 shows snapshots of contours of fluctuating velocity components at the inlet plane. The contours demonstrate the coherency of the velocity field produced by SEM; they also show the size distribution of eddies across the channel width – smaller eddies near the walls and larger eddies at the centre – in accordance with the input distribution shown in Fig. 4.5b. Since for the mean velocities, U_i, the agreement between input and SEM results is very good, they are not discussed here.

Figures 4.7 (a) and (b) compare input turbulence kinetic energy, $k = 1/2\left\langle u_i' u_i' \right\rangle$, and the Reynolds shear stress, $\left\langle u'v' \right\rangle$, with the SEM generated statistics for two values of number of eddies. Generally the good agreement between the input and output statistics verify the implementation in Gerris. Secondly there are only marginal differences between the cases with 1430 eddies and 10,000 eddies. This shows that the coefficient in Eq. (4.24) is not a critical parameter as along as the number of eddies is large enough to fill the eddy box.

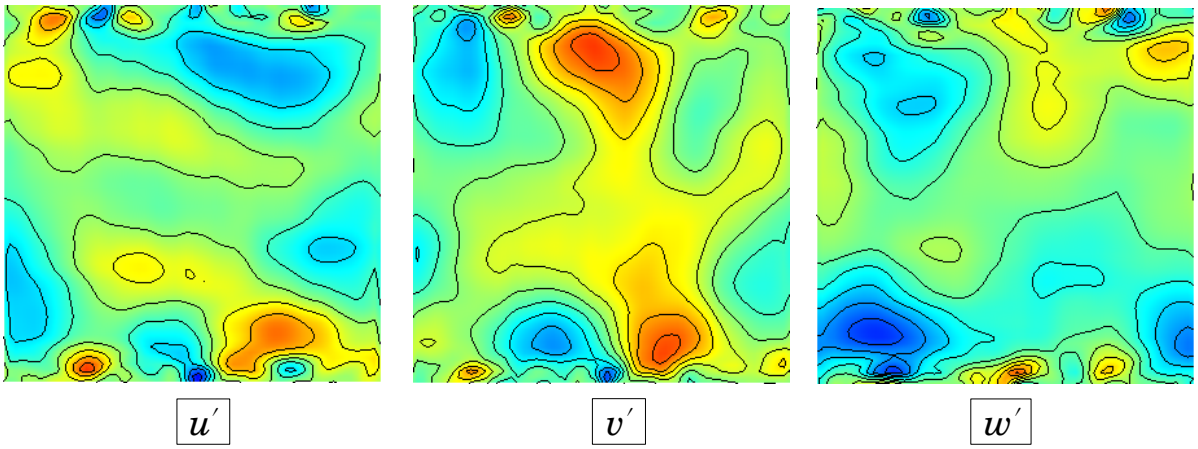

Figure 4.6. Snapshots of contours of fluctuating velocities at the inlet plane. The two parallel planes of the channel are located at the top and bottom of these images

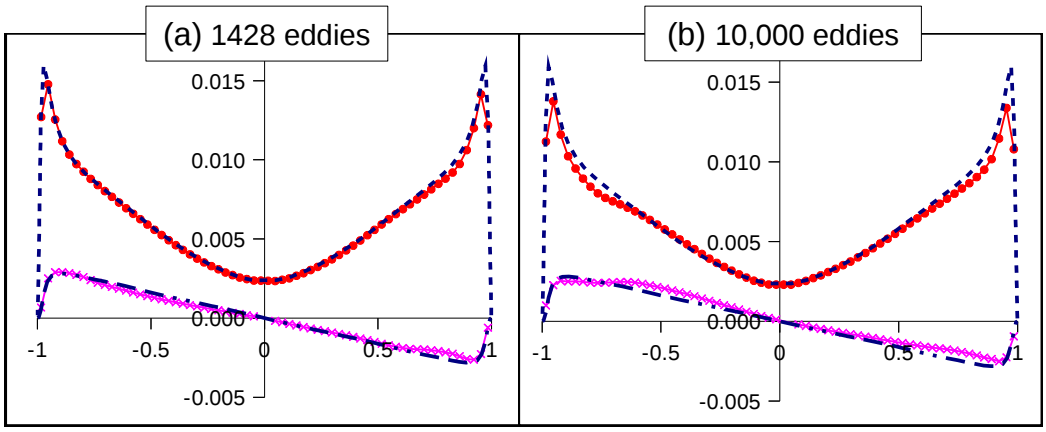

Figure 4.7. Charts comparing SEM generated statistics at channel inlet for two different number of eddies. Legend: DNS data for ····· k and ·· – – · $\langle u' v' \rangle$; SEM results for —●— k and —×— $\langle u' v' \rangle$

4.3.3 Periodic LES of Turbulent Plane Channel Flow - Reference Case

In the previous section only the implementation at the inlet was verified. However checking the performance of SEM generated flow downstream will tell how well the turbulence is developed. Before doing this LES of turbulent plane channel flow at $Re_\tau = 395$ was performed in Gerris in a periodic domain as a reference case.

4.3.3.1 Geometry and Mesh Details

The simulation setup and the parameters for this reference simulation were taken from PhD thesis of Villiers (2006). The simulation domain consists of a finite region of flow between two infinite parallel plates as shown in Fig. 4.8. The cuboid domain has dimensions of $2h \times 4h \times 2h$ with h being the half channel thickness and periodic boundary conditions are applied in the streamwise and spanwise directions.

Since in 3D Gerris the only affordable type of mesh is cubic, the mesh aspect ratio cannot be controlled to allow lower spatial resolution in streamwise and spanwise directions while maintaining a higher resolution close to the walls, in the wall normal direction. However, the cell size can be increased gradually, although through steps, by changing the level of refinement. This resulted in a total of 844,000 cells with cell dimensions (scaled in wall units) of $\Delta^+ \in [8,\ 32]$ as against 180,000 cells for the mesh of Villiers with cell dimensions of $\Delta y^+ \in [2,\ 20]$ in the wall normal direction and 35 and 20 in streamwise and spanwise directions. The mesh details are given Fig. 4.9.

4.3.3.2 Momentum Source

Since periodic boundary conditions were applied, the pressure gradient had to be specified to drive the flow that is defined by,

$$\frac{dP}{dx} = \frac{\rho u_\tau^2}{(h - y_P)}; \tag{4.27}$$

where u_τ is the friction velocity and y_P is the distance of near wall node to wall. The pressure gradient was added as the momentum source term for streamwise velocity in Gerris. The friction velocity in Eq. (4.27) was computed using Dean's correlation (Dean, 1978),

$$Re_\tau \approx 0.175\, Re_b^{0.875} \tag{4.28}$$

where $Re_\tau = u_\tau h/\nu$ and $Re_b = U_b h/\nu$ are the Reynolds numbers based on friction velocity and bulk velocity, U_b, respectively and using the auxiliary relation,

$$Re_\tau / Re_b = u_\tau / U_b \ . \tag{4.29}$$

Equation (4.28) also gives the value of bulk Reynolds number for full channel width, $Re_{b,2h} = 13620$ for $Re_\tau = 395$.

4.3.3.3 Turbulence Initialization

In actual flow, at sufficiently high Reynolds number, turbulence initiates due to growth of small perturbations and that takes some downstream distance for transition; whereas, in this periodic LES, it has to be artificially introduced. Villiers had a dedicated approach to generate 'streamwise streaks of fluid' close to wall, which also in real turbulence, interact with mean shear and therefore induces vortex formation and further instabilities. In our case fluctuating components were generated using SEM and added to the mean velocities, for one flow-through-cycle. This was sufficient to initiate turbulence and turbulence was fully developed within 7 or 8 flow-through-cycles. The turbulence statistics to be inputted to the SEM were the same as discussed in Sec. 4.3.2.

4.3.3.4 Results of Periodic LES

The simulation was carried out for more than 80 flow-through-cycles after the fully developed turbulence was achieved. Output statistics of first and second moments were obtained by arithmetic averaging the values at every plane in the *y* direction and time averaging them for 80 flow-through-cycles, *i.e.*,

$$\langle \phi \rangle = \frac{1}{N_t N_y} \sum_{i}^{N_t} \sum_{j}^{N_y} \phi_{ij} \ , \tag{4.30}$$

where N_t is the number of time steps and N_y is the number of cells in every *y* plane. Due to the periodicity of the channel, the events at every cell in *x* direction and at every time step can be considered as independent realizations and hence Eq. (4.30) considered as ensemble averaging.

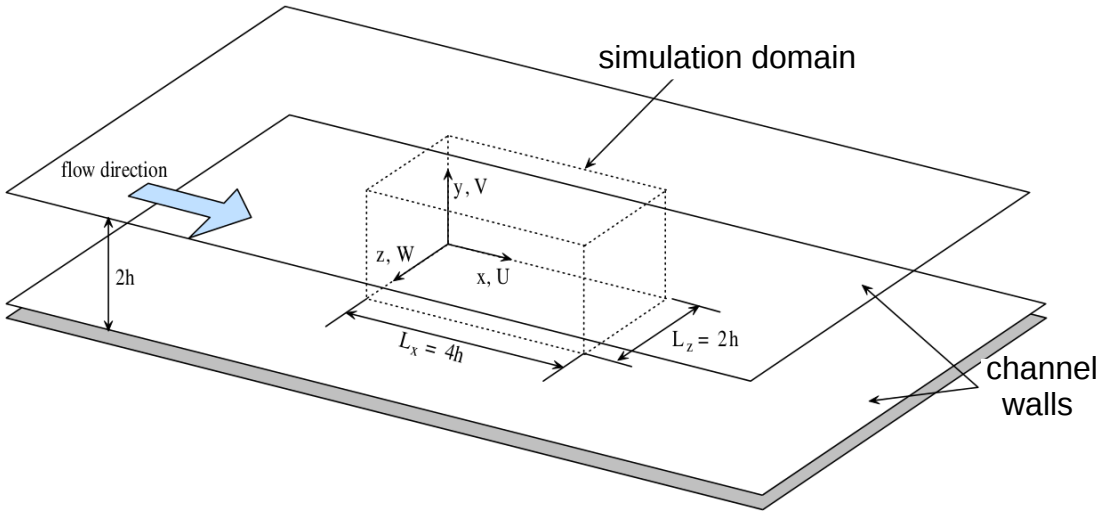

Figure 4.8. Schematic of simulation domain in flow between parallel plates taken from Villiers (2006).

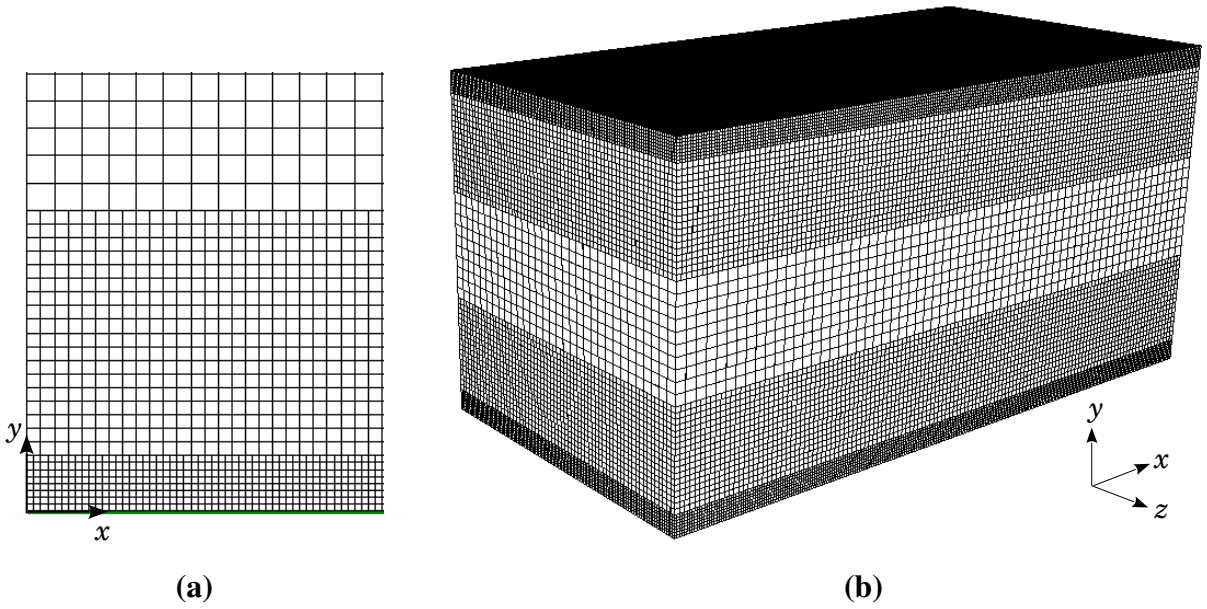

Figure 4.9. (a) Mesh used for periodic LES of plane channel flow shows three levels of refinement from wall to centre of the channel (b) 3D view of mesh employed

The results are plotted in Figures 4.10 (a) to (c) and compared against input statistics. Since a relatively coarse grid was used at the walls (Sec. 4.3.3.1) the u_τ used for scaling the results were obtained from Eq. (4.28) and not from the simulation result. The agreement is generally good and are comparable to that of Villiers (not shown here).

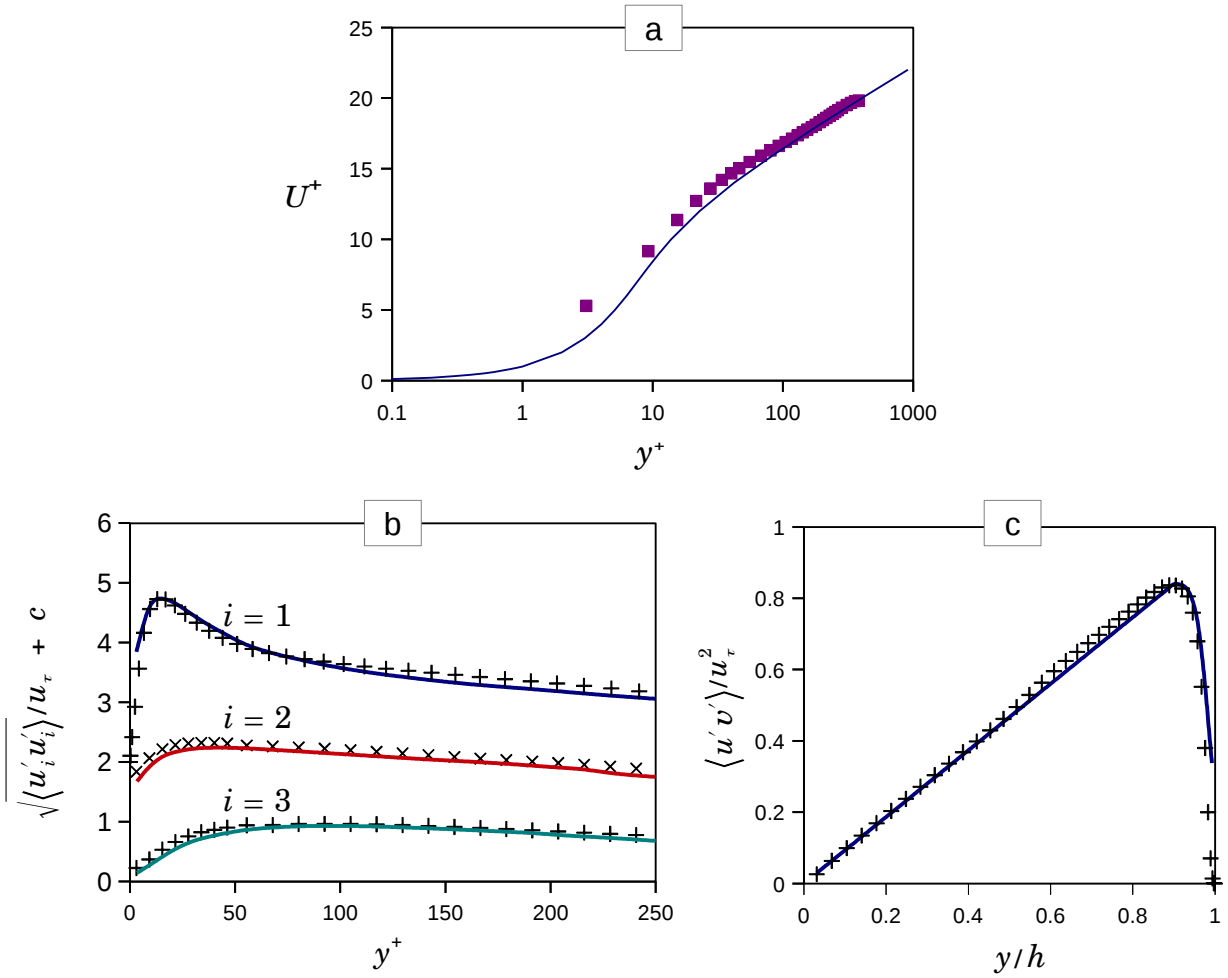

Figure 4.10. Ensemble averaged statistics of LES compared against DNS data for plane channel flow. In figures (b) and (c) symbols are of DNS data and lines are of LES and in (a) it is otherwise. All profiles are across the channel width. Channel wall is at $y = h$ or $y^+ = 0$ where, $y^+ = (h - y)u_\tau / \nu$.

4.3.4 LES using SEM Generated Inflow

Here the plane channel flow case was simulated with SEM generated inlet conditions only until the entire channel length was swept once. This is to verify how well the turbulence is developed by a SEM generated inflow. The mesh distribution is same as in Sec. 4.3.3.1 and the inlet conditions and the two simulations cases are same as in Sec. 4.3.2.

Output statistics of second moments were obtained using Eq. (4.30), except that results are only for one flow through time (mean velocities are not discussed due to very good agreement); the results are plotted in Figures 4.11 (a) to (c). Compared to the Periodic LES, the agreement between the input and output statistics is rather weak, which means the SEM generated turbulence is not fully developed. This is not surprising because, however precise the specification of inlet conditions to SEM was, the flow development always took some entrance length in the cases studied by Jarrin.

Generally in using turbulence generation methods like SEM to generate inflow conditions, the inlet is located well ahead of the LES domain to let the flow develop, wherever possible. However in our ladle simulations this is not possible as flow is continuously changing its direction in the slag eye region where the inlet of LES domain is located. However, it can also be said that the SEM generated statistics are not altogether bad and since the fluctuating velocity is only a fraction of the time averaged velocity, the inlet conditions for ladle LES are not going to be unphysical. In fact, it will be shown Chapter 6 that varying the turbulence length scale [Eq. (4.26)] by a factor of four did not significantly affect the entrainment characteristics.

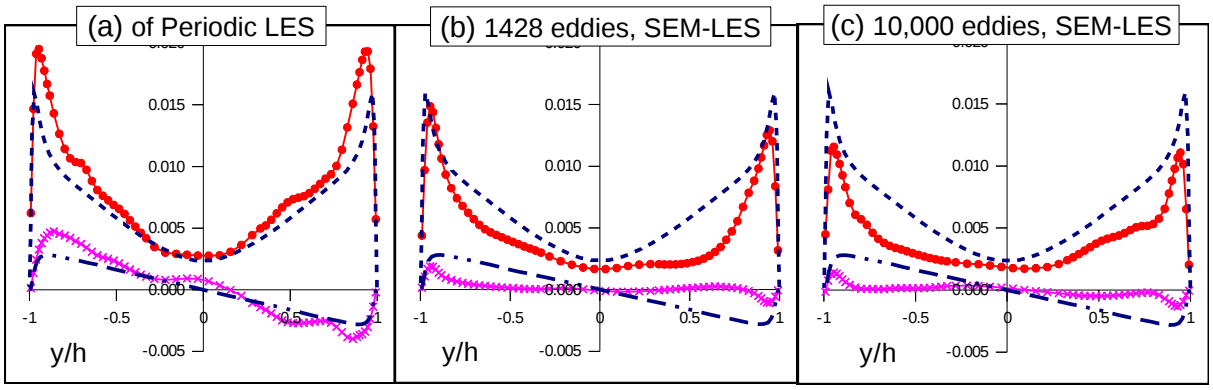

Figure 4.11. Comparison of ensemble averaged statistics of turbulent flow equivalent to one flow through time in a plane channel, against DNS data. Legend: DNS data for ····· k and - - - $\langle u' v' \rangle$; LES results for —●— k and —×— $\langle u' v' \rangle$

4.4 RANS simulations in Ladle

The defining sketch of various zones, dimensions and profiles of the axisymmetric gas stirred vessel referred to in this and future sections are labeled in Figure 4.12.

The inlet condition to the LES domain is derived from the flow field at the location of the inlet plane from a RANS simulation, shown as a line (*Extract profiles*) in Fig. 4.12 and also discussed in Sec. 4.1. Considering the liquid steel flow due to central gas injection, due to its axial symmetry, it is sufficient to carry out RANS simulations in axisymmetric coordinates (2D cylindrical coordinates). The gas-liquid plume is the momentum source for flow in the ladle and therefore appropriate modeling of the plume is required. If the gas fraction distribution in the plume is known *a priori* the buoyancy term for momentum equation can be deduced using the 'quasi single phase' that was discussed in Sec. 2.6.2 and that being the case, these simulations are hereafter referred to as 'QSP-RANS'.

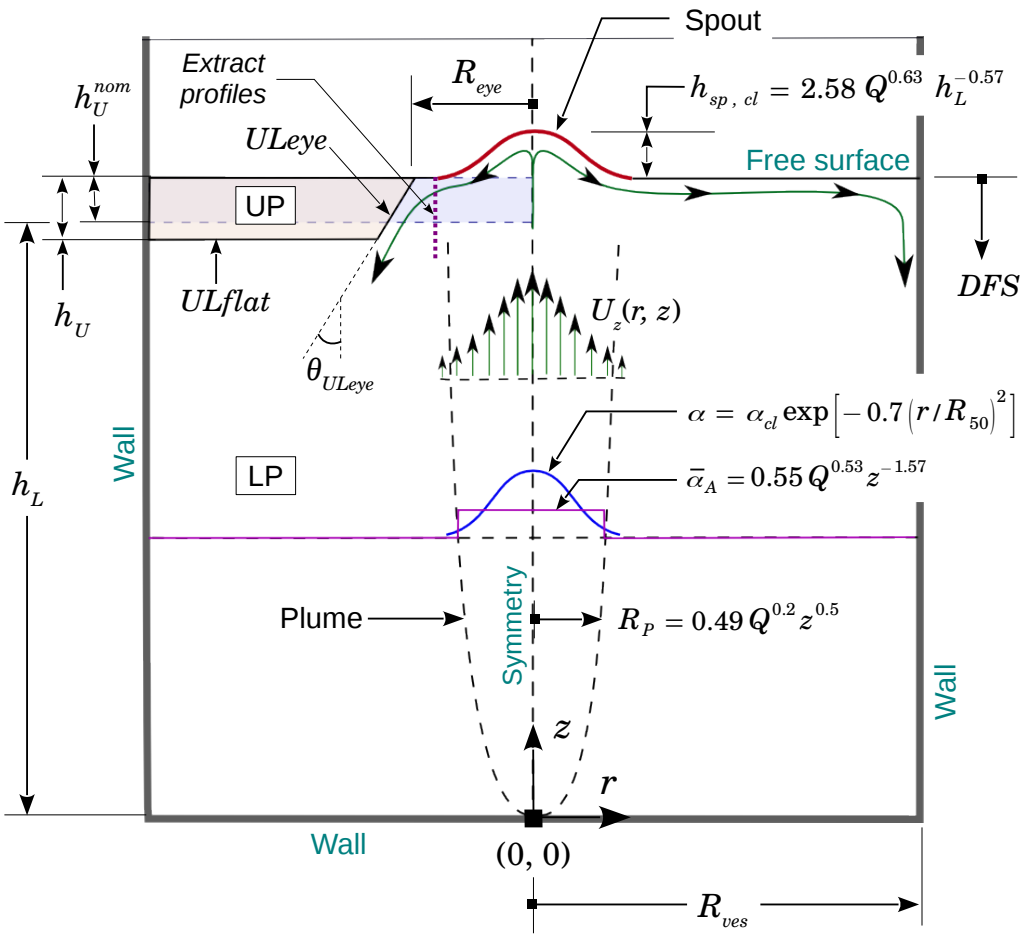

Figure 4.12. Schematic of cylindrical gas stirred vessel showing various zones, dimensions and profiles used for RANS modeling of fluid flow, explained in the sections ahead. The right side of the ladle axis represents various water modeling studies performed without upper phase and the left side represents otherwise, including the industrial ladle.

4.4.1 Simulation Parameters

Many parameters discussed in the following are based on various models of Krishnapisharody and Irons (K&I, hereafter), which themselves are based on the results of extensive water modeling works of the past and also their own experimental measurements, to characterize the dynamics of plume, spout and slag eye.

4.4.1.1 Gas Fraction Distribution in the Plume

The unified plume models of K&I (2010) give axial distributions of plume cross section area averaged gas fraction,

$$\bar{\alpha}_A = 0.55 Q^{0.53} z^{-1.57} \tag{4.31}$$

and plume radius

$$R_P = 0.49 Q^{0.2} z^{0.5} \tag{4.32}$$

where, Q is the gas flow rate at half bath height in m^3/s, and z is the axial location in the ladle in meter. In a plume whose cross section is essentially circular (axisymmetric) at all heights, the gas fraction distribution has been shown to be Gaussian by many past works. However the form of Gaussian distribution considered in this work is that of K&I (2007a), who used it to integrate the area averaged gas fraction values from various data on gas fraction distributions:

$$\alpha = \alpha_{cl} \exp\left[-0.7\left(\frac{r}{R_{50}}\right)^2\right] \tag{4.33}$$

where α is the gas fraction distribution, α_{cl}, the centre line value, R_{50}, the radius of plume at which $\alpha = 0.5\alpha_{cl}$. Moreover the authors considered the distance from plume centre where $\alpha = 0.1\alpha_{cl}$ to be the total radius of the plume, R_P. Using these and Eq. (4.33), it can be shown that,

$$R_P = 1.816\ R_{50} \tag{4.34}$$

and

$$\alpha_{cl} = 0.39\ \bar{\alpha}_A \tag{4.35}$$

Equations (4.31) through (4.35) enable the description of the Gaussian gas fraction distribution that is used in the quasi single phase model [Eq. (2.20)] to compute the variable density used in the RANS equations. The 'top-hat' [Eq. (4.31)] and Gaussian [Eq. (4.33)] gas fraction profiles at an axial location in the ladle are depicted in Fig. 4.12.

4.4.1.2 Other Parameters

Refer Fig. 4.12 for various physical dimensions.

Eye Radius, R_{eye}: Although the RANS simulations were essentially single phase, the presence of slag and spout were incorporated into the 2D domain, as fixed boundaries but with Neumann boundary condition (free surface BC). The slag eye radius was calculated from the eye-area-correlations of K&I (2008):

$$A^*_{eye} = -0.76(Q^*)^{0.4} + 7.15(1-\rho^*)^{-0.5}(Q^*)^{0.73}(h^*)^{-0.5}$$
$$A^*_{eye} = \frac{A_{eye}}{h_L^2} \; ; \; Q^* = \frac{Q}{g^{0.5}h_L^{2.5}} \; ; \; \rho^* = \frac{\rho_U}{\rho_L} \; ; \; h^* = \frac{h_U^{nom}}{h_L} \qquad (4.36)$$
$$R_{eye} = \sqrt{A_{eye}/\pi}$$

where ρ is the density, h_L is height of LP and h_U^{nom} is thickness of UP before any gas injection, all in SI units.

Spout Shape: This is given by the radial distribution of spout height, h_{sp}. Due to the direct correspondence between plume spread and spout width, the Gaussian distribution same as in Eq. (4.33) was used to compute the spout shape (α replaced by h_{sp}). The centre-line heights of the spout were calculated from K&I (2007b),

$$h_{sp,\,cl} = 2.58\, Q^{0.63}\, h_L^{-0.57} \qquad (4.37)$$

Inclination of Slag Metal Interface at Eye, θ_{ULeye}: The fixed boundary representing the slag-metal interface at the slag eye was tapered at an angle of 40º with respect to the axis of the ladle; this value is taken from the range of 30 to 50º based on observations from water model experiments (Krishnapisharody, 2006).

Actual Slag thickness, h_U: The slag thickness after the eye is formed was found from the

volume conservation equation,

$$\pi R_{ves}^2 h_U - \frac{\pi}{3}(R_1^2 + R_1 R_2 + R_2^2) h_U = \pi R_{ves}^2 h_U^{nom}$$
$$R_1 = R_{eye}, \; R_2 = R_{eye} + h_U \tan\theta_{ULeye} \tag{4.38}$$

Since this is a non linear equation, the Newton Raphson method was used to iteratively find h_U at the start of a simulation.

4.4.1.3 Free Surface Correction for Eddy Viscosity

Handler *et al* (1993), from their DNS simulations of open channel flows, observed redistribution of turbulent kinetic energy between the three components near the free surface, in which the majority of the energy lost by the surface-normal component went to increase the spanwise energy component. The redistribution causes a decrease in length scale equivalent to increased dissipation rates near the surface (Naot & Rodi, 1981) which means a lowered free surface eddy viscosity. Following this, Johansen & Boysan (1988) used the Naot and Rodi model for specifying the only non-zero Reynolds stress component that is due to the streamwise and surface normal fluctuating velocities. The model has three fitting coefficients of which one of them is an exponential decay function of distance to free surface scaled by turbulence length scale. However the difficulty lies in the implementation, since a two equation model like the SST k-ω cannot take a Reynolds shear stress as input and this was not discussed in their paper.

Since it is known that eddy viscosity is dampened near the free surface region, in their RANS modeling study of open channel flows, Nakayama & Yokojima (2003) defined their eddy viscosity simply as

$$\nu_T = f_S \frac{k}{\omega}, \tag{4.39}$$

where f_S is a free surface damping function that becomes less that unity near the free surface. The coefficient f_S is defined by two other coefficients of which one of them is an exponential decay function of distance to free surface scaled by turbulence length scale similar to Johansen & Boysan.

In their theoretical study of turbulence diffusion near the free surface, Shen *et al* (1999) performed Direct Numerical Simulation (DNS) of flow near a free surface. From the profiles of mean shear (gradient of surface parallel velocity in surface normal direction) at various instances, they found that as the surface is approached, the mean shear exhibit a local minimum and maximum before dropping abruptly to zero at the surface. The depth to the minimum and maximum were respectively identified as the 'outer' and 'inner' layers. Correspondingly, the value of eddy viscosity dropped gradually in the outer layer and then abruptly in the inner layer to values comparable to the molecular viscosity.

Based on similarity theory, they developed a model for mean velocity profile that well fitted their DNS computations. In that they assumed a Gaussian distribution for variation of eddy viscosity with depth as,

$$\nu_T = \nu_{T,a} - (\nu_{T,a} - \nu_{T,0}) \exp\left(-\frac{z^2}{c^2}\right) \tag{4.40}$$

where, the subscripts a and 0 denote the location in depth at outer layer thickness and at free surface, respectively; z is the depth from surface and c is a constant proportional to outer layer thickness.

In Eq. (4.40), using the observation of Shen *et al* that $\nu_{T,0} \approx \nu$, taking the eddy viscosity at outer layer to be the one calculated without any free surface corrections, $\nu_T \leftarrow \nu_{T,a}$, changing the symbols: ν_T by ν_{eff} and the exponential term by ψ and finally rearranging the equation as,

$$\nu_{eff} = \nu\psi + \nu_T(1 - \psi), \tag{4.41}$$

we see that the model is essentially a blend between the eddy and molecular viscosities for the effective viscosity, ν_{eff}, with ψ as a blending function. Generalizing, the blending function can be any function of distance scaled with some length scale proportional to the outer layer thickness.

From the discussions above it is motivating to choose the blending function as some

form of exponential decay function of distance to free surface scaled with turbulence length scale. From many trials the blending function that fitted with much of the available data reasonably well was,

$$\psi = \exp\left[-2.5\left(\frac{DFS}{LS}\right)^2\right], \tag{4.42}$$

where, DFS is the distance to free surface (labeled in Fig. 4.12) and LS, the turbulence length scale that can be obtained from a RANS simulation, namely Eq. (4.25). Thus Eqs (4.41) and (4.42) were used compute the effective viscosity in the turbulence model in Gerris.

4.4.1.4 RANS Equations for Gerris

Apparently, the hurdle in using Gerris for this ladle RANS simulations is that it does not impose the continuity,

$$\nabla\cdot(\rho_m \boldsymbol{U}) = 0 \tag{4.43}$$

for conservation of the mixture mass, but only imposes the incompressibility condition,

$$\nabla\cdot\boldsymbol{U} = 0 \tag{4.44}$$

[essentially, Eq. (4.3)]. To overcome this, the approach of Kuzmin *et al* (2005) is used. Starting from the two fluid model, they derived the momentum equations for bouyancy-driven bubbly flows, analogous to the Boussinesq approximation for natural convection; *ie.*, the reduced density is present only in the gravity term and elsewhere is the liquid density. The authors suggest that this approximation holds for gas fraction $<10\%$ which is the case in typical ladle operation, except near the nozzle. The RANS equations then become,

$$\nabla\cdot(\boldsymbol{U}\,\boldsymbol{U}) = -\nabla P^* + \nabla\left[(\nu + \nu_T)\nabla\boldsymbol{U}\right] - \alpha\boldsymbol{g} \tag{4.45}$$

where $P^*$is the reduced pressure. Therefore, implementation in Axisymmetric version of Gerris requires just the addition of the gravity term $(-\alpha\boldsymbol{g})$ as momentum source for the axial velocity component.

4.4.1.5 Boundary Conditions

It was found from various verification cases that the use of wall function (Appendix B.1.1) resulted in loss of grid independency, whereas, computations without that gave both grid independency as well as reasonably good agreement with the data. Although the reason is unclear, all QSP-RANS in the present and future Chapters were performed without the wall functions. However it should be noted that at wall nodes, the eddy viscosity (ν_T) was set equal to molecular viscosity (ν). Neumann boundary conditions namely,

$$U_n = \frac{\partial \phi}{\partial n} = 0, \ \phi = U_r, U_z \text{ and } k \tag{4.46}$$

were applied at free surface, symmetry, eye, spout, *ULeye* and *ULflat* surfaces (see Fig. 4.12), wherein, U_n and n are the velocity and direction normal to a surface.

4.4.2 QSP-RANS Model Verification

The verification cases correspond to the reduced scale water model studies of plume dynamics of Sheng (1992), and Johansen *et al* (1988). The vessel dimensions tabulated in Table 4.1 show that system of Johansen *et al* is quite larger than that of Sheng and also has a small wall-taper of 8°. In both the works, Laser Doppler Anemometry was used to measure the mean and fluctuating velocities of liquid (U_i and u_i', respectively); radial distributions of vertical and horizontal components of these velocities were reported at various axial locations. For the present verification exercise, the turbulence kinetic energy (TKE) was extracted from data using $k = 1/2\left\langle u_i' u_i' \right\rangle$ and assuming that the two horizontal components of u_i' are equal. From these radial profiles, the plume area averaged axial velocities and TKE were numerically integrated (trapezoidal rule) according to,

$$\bar{\phi}_A = \frac{2}{R_P^2} \int_0^{R_P} \phi \, r \, dr, \ \phi = U_z, k \tag{4.47}$$

with a fitted Gaussian profile for ϕ † and the plume radius, R_P given by Eq. (4.32); for $\phi = U_z$, $\bar{\phi}_A$ is known as the plume velocity, U_P.

Table 4.1. System parameters of literature cases used for QSP-RANS model verification.

Lit. Cases	Vessel Diameter, m		Bath Height, m	Scaling factor*	Gas flow Rates studied, lpm
Sheng (1992)	0.50		0.420	1/6	3, 6, 9, 12
Johansen *et al* (1988)	Base	0.93	1.237	1/3	7.8, 16.2, 28.2, 36.6
	Top	1.10			

*Scaling factor is with respect to a 200 ton industrial ladle

Two meshing schemes were tested for the verification simulations namely, 1) *base*: cell size, $\Delta = 2$ mm along the walls and elsewhere, $\Delta = 8$ mm and 2) *finer*: same scheme but half the cell size as that as the *base*.

QSP-RANS simulations were performed using the *base* mesh from which U_P and $\bar{k}_A$ were computed using Eq. (4.47) and their axial profiles are plotted in Fig. 4.13 for the highest flow rate cases of Sheng and Johansen *et al*. In Sheng's case, U_P is over predicted unlike that of Johansen *et al*; $\bar{k}_A$ is largely under predicted in both the cases, the reason being the neglect of turbulence production due to the bubbles in the plume. However, radial velocity profiles near the free surface are well predicted in both the cases. The results from the *finer* mesh are also compared for the plume and radial velocities in Figs. 4.13 (a) & (c). It shows that grid independency is sufficiently achieved at the *base* refinement and is hence used for all the verification cases. The comparison of velocity profiles for the other flow rates are shown in Figs. 4.14 and 4.15; here also, the radial velocities are reasonably well predicted than the plume velocities.

The bubble induced turbulence due to bubble drag, wake shedding and wobbling is not

† Often, due to the large velocity gradient in the plume region combined with the lack of resolution in the data, applying Eq. (4.47) directly under-estimated $\bar{\phi}_A$. To circumvent, a Gaussian profile of the type of Eq. (4.33) was assumed (for both U_z and k), with the coefficient to the (r/R_{50}) term inside the exponential, deduced by fitting the Gaussian to all data for a given ϕ.

accounted in the QSP-RANS model. Regarding the accounting of such bubble induced turbulence, Rzehak & Krepper (2013) rationalizes various approaches in the literature that, in a two equation turbulence model, for the TKE equation, a simple drag force based source term is added and for the dissipation equation, the TKE source term divided by a time scale and a constant coefficient is added; the time scale is some function of local void fraction, bubble size and velocity scale. The difficulty in using such models is the requirement of bubble size data that is not readily available. It can be demonstrated that, by manipulating the bubble size and the constant coefficients, best matching between the data and simulation can be obtained for both U_P and $\bar{k}_A$ profiles, but with loss of generality. Although the addition of source terms had a different basis, Sheng & Irons (1995) too reflect a similar opinion in the use of *ad hoc* coefficients.

However, for our case of LES, the velocity profiles were required only near the free surface, where generally good agreement has been obtained, more so in the case of Johansen *et al* which is a larger vessel. Moreover the TKE predictions near the free surface almost converge with the data near the free surface (Fig. 4.13b). Therefore, the inability for better predictions of plume velocity is only secondary.

4.5 Summary

The methodology to perform multiphase LES of slag entrainment in steel ladle presented in this Chapter is summarized as follows: It starts with performing QSP-RANS simulations in the ladle to extract profiles of mean velocities and Reynolds stresses near the slag eye; this involves combination of various literature models namely, the gas fraction distribution in the plume, the spout shape and the slag eye size. The extracted RANS profiles are fed into the Synthetic Eddy Method to generate turbulent inflow at the inlet of multiphase LES domain. The multiphase simulations are carried out using Gerris that employs VOF method and accurate surface tension model for precise interface tracking. The SST $k-\omega$ turbulence model, SEM and the QSP-RANS models were implemented in Gerris that it lacks and the verification against benchmark cases or data from the literature proved to be satisfactory.

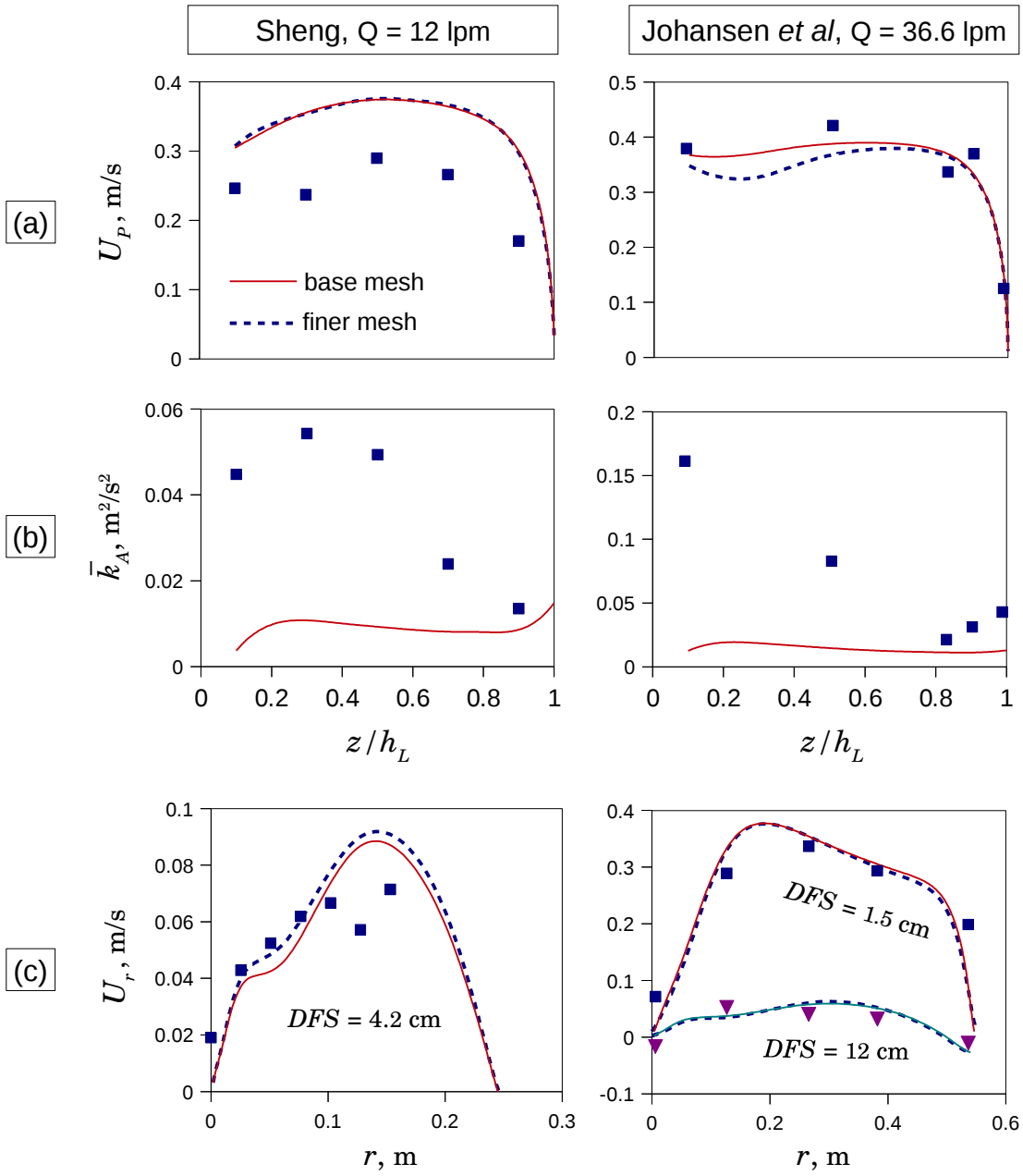

Figure 4.13. Comparison of RANS simulation results (lines) against data of Sheng and Johansen et al (points) at highest flow rates: axial distributions of (a) plume velocity (U_P) and (b) area averaged TKE $(\bar{k}_A)$, (c) radial distribution of radial velocity (U_r) at various distances to free surface (DFS). Other symbols explained in Fig. 4.12. The results of *finer* mesh refinement are also plotted for (a) and (c). Common x-axis for (a) and (b) and common legend.

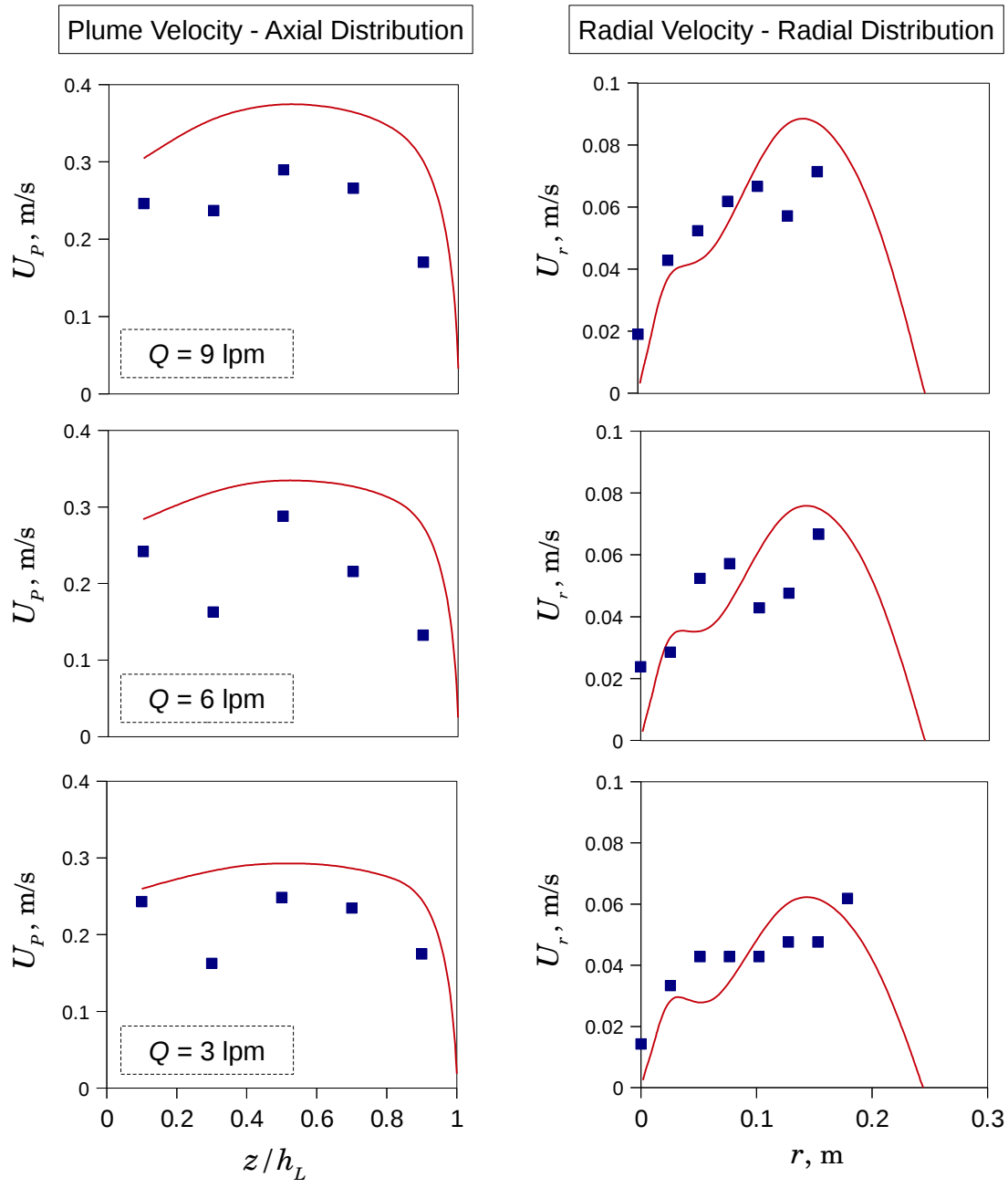

Figure 4.14. Comparisons, similar to Fig. 4.13, but for three other gas flow rates (noted in inset) of Sheng's cases. Common x-axis.

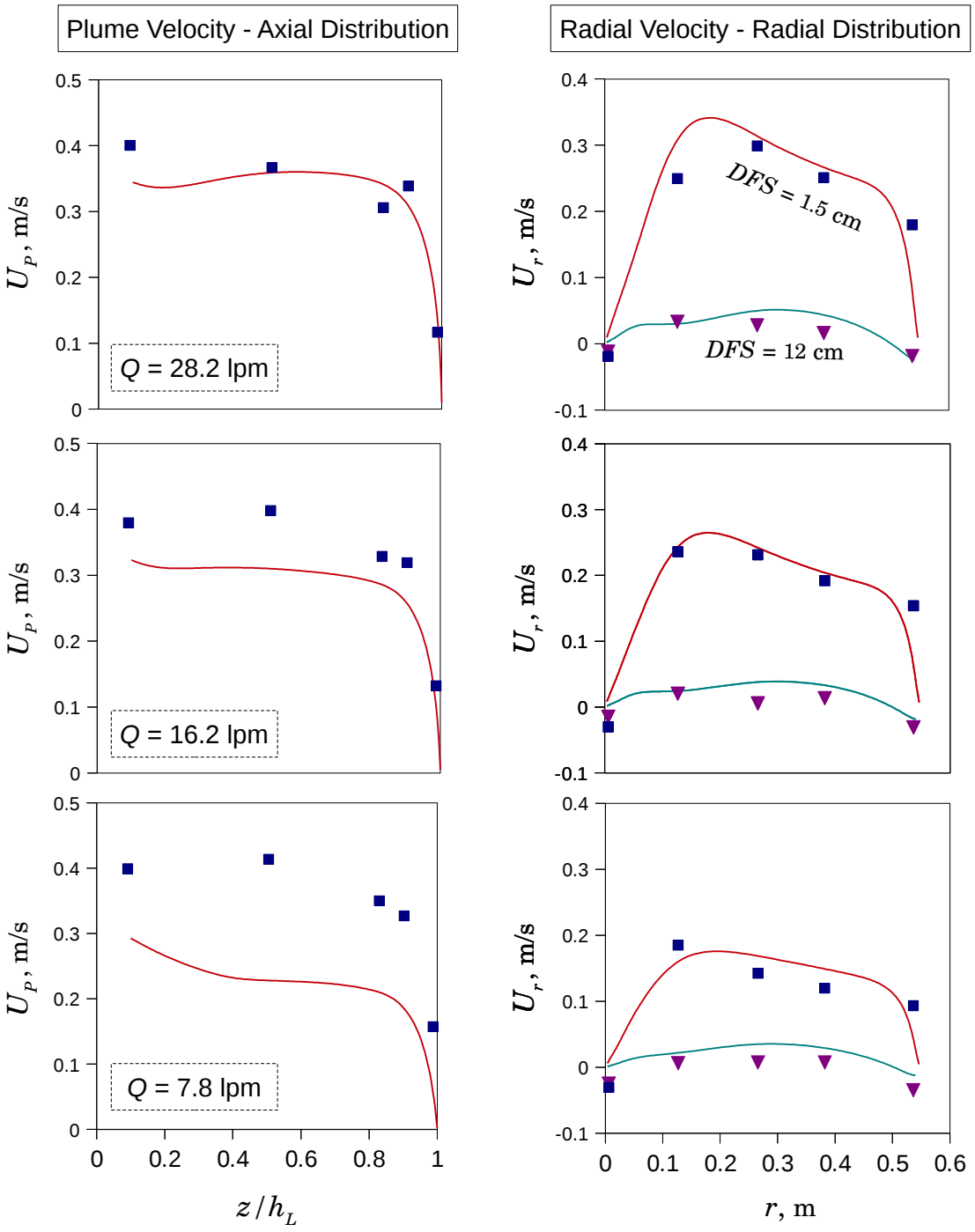

Figure 4.15. Comparisons, similar to Fig. 4.13, but for three other gas flow rates (noted in inset) of Johansen *et al* cases. Common x-axis.

5. Multiphase LES in Aqueous Model

This chapter presents physical and mathematical modeling of entrainment of the upper phase into the lower phase in an aqueous model. Experiments to measure entrainment rate and droplet size distributions were performed using the model. The scope of these experiments are limited in that the results cannot be scaled up to an industrial ladle since the model creates an idealized flow situation to conveniently observe entrainment. However they serve as cases for testing numerical models of entrainment. Accordingly, the approach of multiphase LES presented in Ch. 4 is applied to simulate entrainment in the physical model and the results are compared with the data. This Chapter also introduces various other aspects of LES setup that will be used in Ch. 6 for the LES of slag-metal system.

5.1 Physical Model

5.1.1 Construction

The Plexiglass model of Krishnapisharody (2006), constructed for studying entrainment was used to perform experiments and numerical modeling of the same, whose schematic shown in Fig. 5.1. The model is called as 'thin slice model' (TSM) because it represents a thin slice of volume of longitudinal section of a cylindrical gas stirred vessel. The aim of the model is to provide a cut through view of slag eye region where entrainment takes place, a view that is not possible in a cylindrical vessel. Moreover to avoid violent oscillations of interface between the upper and lower phases, due to random passage of bubbles in a gas stirred system, fluid flow in the eye region was achieved by a water jet issuing from a slot in the false base of the model. The false base divides the model into a top working chamber and the bottom buffer zone that enables recirculation to maintain the liquid level in the working chamber.

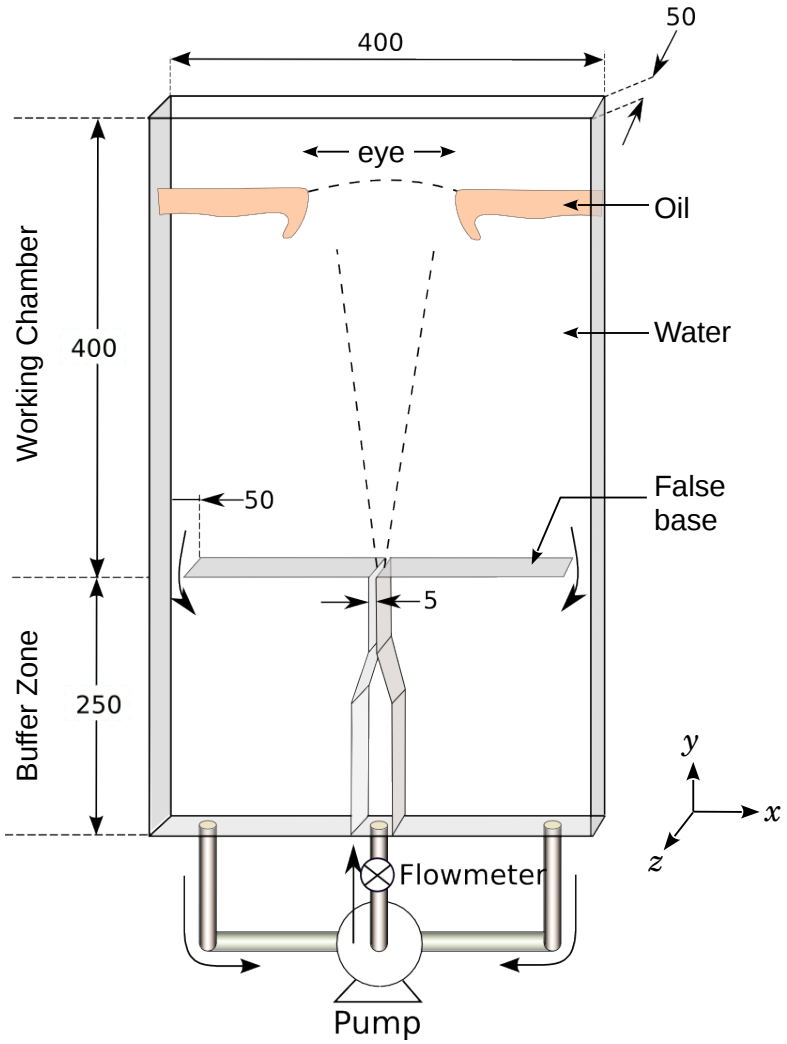

Figure 5.1. Schematic of the Thin slice model; arrows show water flow direction. All dimensions in mm.

5.1.2 Video Recordings and Measurements

Entrainment process in the TSM was video recorded using a 30 fps camera for a system of oil as upper phase and water as lower phase, whose properties are tabulated in Table 5.1. The height of oil and water were 18 mm and 250 mm, respectively. Three flow rates were chosen, namely 12, 14 and 16 lpm, as read from the flow meter, such that at the lowest flow rate significant entrainment of oil droplets took place and at the highest flow rate the oil layer was not pushed too much toward the walls. Using 'ImageJ', an open source Image analysis software, every frame of the video for each flow rate was swept to check for the time at which

an oil droplet entrains (birth) and its size was measured using a ruler of the software. All counted droplets were more or less spherical with diameters starting from 2 mm, below which it was difficult to measure, and up to 14 mm were observed. Due to symmetry of flow across the jet axis of the TSM, all observations were made for only one half of the TSM and so are the data and LES results presented in this chapter.

Table 5.1. Properties of fluids used for experiments (Krishnapisharody, 2006)

Fluid	**Density Kg/m^3**	**Viscosity Pa.s**	**Interfacial Tension, N/m**
Water	1000	0.001	0.055
Paraffin oil	870	0.065	

To determine if the droplet counting had reached steady state, number entrainment rate $(\dot{N})$ and cumulative mean of droplet size $(\overline{d})$ for various time spans were calculated from

$$\dot{N}(t) = \frac{N(t)}{t} \tag{5.1}$$

and

$$\overline{d}(t) = \frac{1}{N(t)} \sum_{i=1}^{N(t)} d_i, \tag{5.2}$$

respectively, where, $N(t)$ is the number of droplets until time, t. The results plotted against normalized time in Figs. 5.2 (a) & (b) show that the droplet counting has sufficiently reached steady state.

Number and volumetric entrainment rates and mean droplet size statistics for the total time span of measurements are tabulated in Table 5.2. Except for the dip in $\dot{N}$ for 14 lpm case, all values generally increase with flow rate. The values of volumetric entrainment rate show a disproportionate increase at 16 lpm. This ‘second critical’ phenomenon was observed also in the water modeling studies of Verhelst and Mietz *et al*, noted in Sec. 2.3, although its mechanism is unknown.

The size distribution for the three cases are plotted in Figs. 5.3. All the three have different characteristics - the first one has one peak and positively skewed whereas the second is almost a flat distribution and the third one is bimodal.

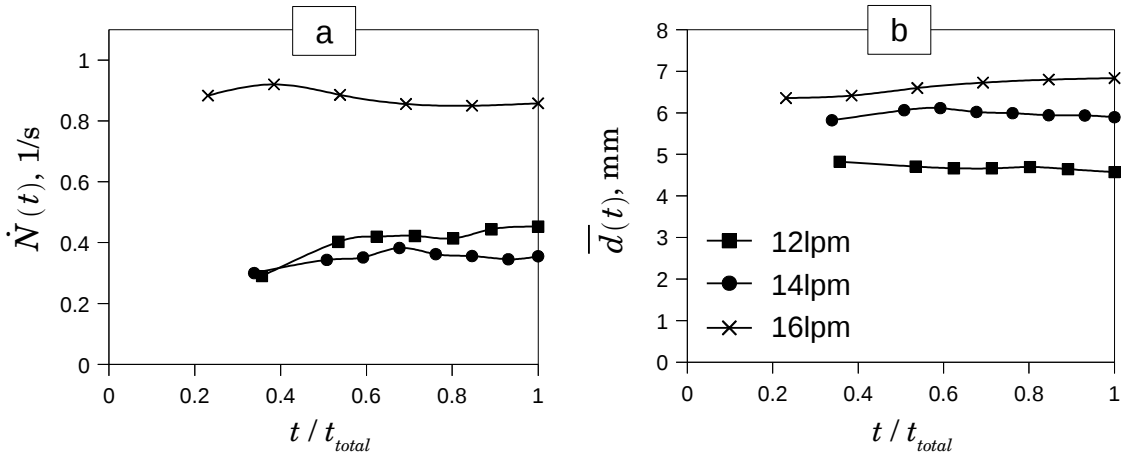

Figure 5.2. Evolution of (a) entrainment rate $(\dot{N})$ and (b) cumulative mean of droplet size $(\overline{d})$ with time (normalized by total time), all for droplets ≥ 2 mm. Common legend.

Table 5.2. Number and volumetric entrainment rates, $\dot{N}$ and $\dot{V}$, respectively and arithmetic mean diameters, $\overline{d}$ of entrained droplets measured from the TSM experiments.

Q, lpm	Time span of measure-ments, s	Droplets counted ≥ 2 mm	Entrainment Rate			Arithmetic Mean diameter, $\overline{d}$, mm	
			$\dot{V}$, mm³/s ≥ 2 mm	$\dot{N}$, 1/s			
				≥ 2 mm	≥ 3mm	≥ 2 mm	≥ 3mm
12	570	255	37.1	0.447	0.374	4.8	5.3
14	600	211	62.4	0.352	0.292	6.0	6.8
16	270	224	234.5	0.830	0.715	6.8	7.2

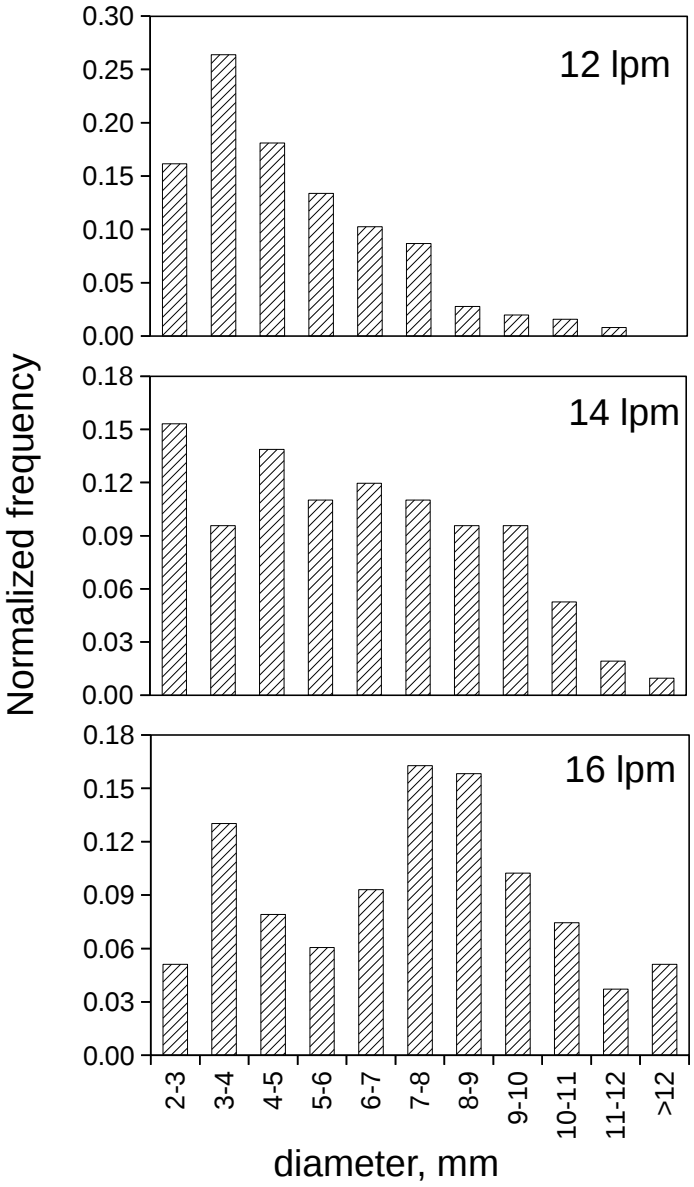

Figure 5.3. Charts showing the size distribution of droplets at the time of *birth* for three flow rates. Common x-axis.

5.2 Numerical Model

The numerical model is based on the same principles outlined in Ch. 4, *i.e.*, it consists of RANS simulation of single phase fluid flow in the TSM to supply inlet conditions for the following multiphase LES simulations. All snapshots of VOF surfaces of LES presented in this section are taken from GfsView, the visualization application of Gerris.

5.2.1 Single Phase RANS Simulations

Single phase RANS simulations were performed in Gerris using the SST $k-\omega$ turbulence model. Due to symmetry of flow across the jet axis and across the thickness of the TSM, only a quarter of the volume is simulated. The simulation domain constructed using `GfsFunction` with various boundary conditions is shown in Fig. 5.4. It again consists of a working volume and buffer zone, although the latter was included only to maintain continuity and flow features are not resolved there. No free surface correction of viscosity was done for these simulations, as done for ladle (Sec. 4.4.1.3), due to uncertainty in coefficients, since velocity measurements were not carried out in the TSM. However it was found that the velocity profiles near *ULeye* obtained from RANS simulations performed using the free surface correction given by Eq. (4.42) was not much different from those obtained *without* using the free surface correction†.

5.2.1.1 Representation of Multiphase Interfaces

Similar to the method discussed in Sec. 4.4.1.2, the multiphase interfaces (formed by contact of oil, water and air) were represented by solid boundaries with Neumann boundary conditions. For each flow rate, from around 20 video frames (at various instances), dimensions of oil-water interface were measured using ImageJ and their averages, shown in Table 5.3 with reference to Fig. 5.5, were used to construct the corresponding solid boundary. However the air-water interface at 'eye', raised due to jet momentum, was constructed using the height calculated using Bernoulli's energy equation $(h = U^2/(2g))$ and *free jet* models of Rajaratnam (1976) for jet spread and velocity profile.

† This is unlike the ladle cases which showed significant differences between with and without free surface correction.

5.2.1.2 Boundary Conditions

The following boundary conditions were applied, with reference to Fig. 5.4:

- Wall functions at all solid boundaries above the inlet.
- Neumann boundary condition for the multiphase interface representing solids and the symmetry faces.
- Inlet conditions that consist of specifying only the vertical velocity and no turbulence parameters. In all the cells of inlet volume (slot, labeled in Fig. 5.4), velocity magnitude, equal to the inflow rate divided by inlet cross section area, was imposed for vertical velocity component for every time step. This decouples the influence of flow field in the buffer zone on the inlet.

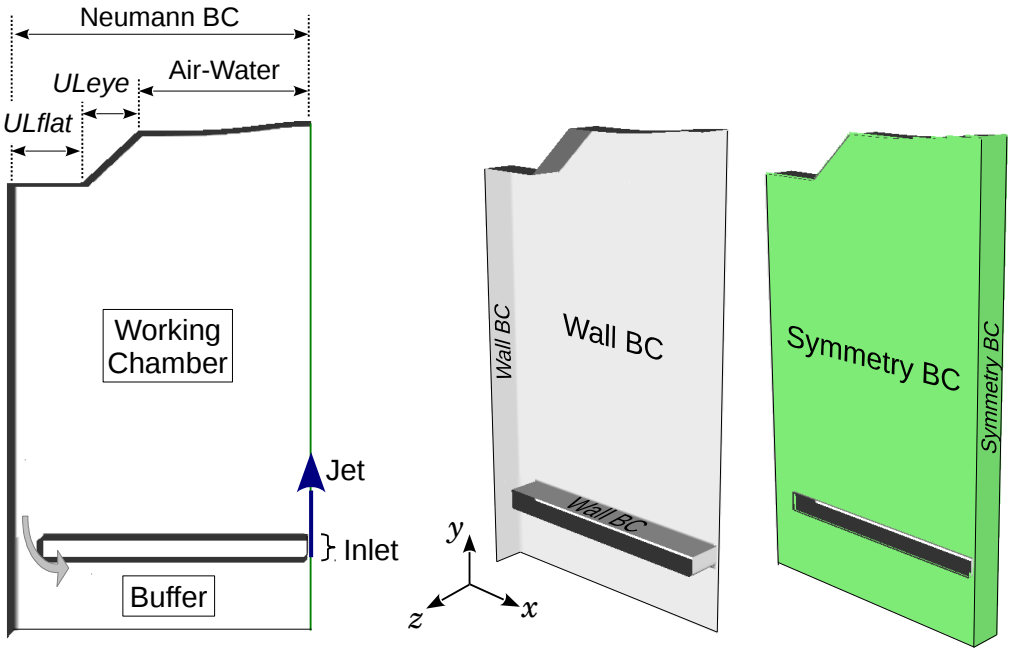

Figure 5.4. Various views and boundary conditions (BC) of the simulation domain (snapshots from GfsView), which is only a quarter of the TSM volume.

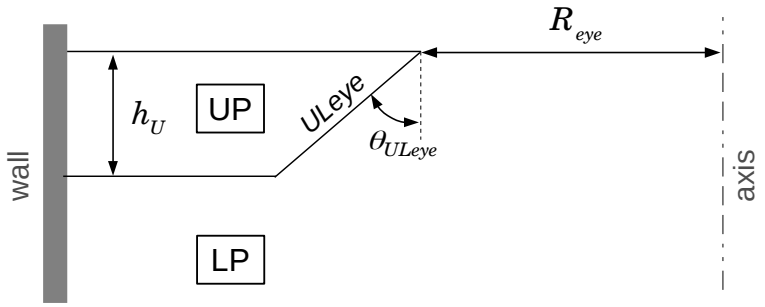

Figure 5.5. Nomenclature of physical parameters for RANS simulations; UP - oil; LP - water

Table 5.3. Dimensions of upper phase (with reference to Fig. 5.5), obtained from average of 20 snapshots of fully developed flow in TSM experiments, for the RANS simulations.

Flow rate, Q, lpm	**Actual Oil thickness, h_U, mm**	**Eye width, R_{eye}, mm**	**Interface angle, θ_{ULeye}, degree**
12	25	83	38
14	28	108	44
16	34	114	47

5.2.1.3 Grid and Grid Independency

The meshing scheme is shown in Figs. 5.6 (a) & (b). At walls (Fig 5.6a), fine mesh (cell size, Δ = 1.6 mm) was applied above inlet and finest mesh (Δ = 0.8 mm) was applied along the jet width including the inlet and the eye region where larger velocities are encountered. As a result the highest y^+ in the entire domain is less than 27.0 which is well below that obtained for wall jet verification case (Appendix B.2.5). The rest of the working volume (Fig. 5.6b) was given a coarse mesh (Δ = 3.2 mm) whereas the buffer zone was given a coarser mesh.

To verify grid independency, the volume of jet width and eye regions were refined to the same level as that of the wall of these regions (as if the *finest* mesh in Fig 5.6a is extruded in the thickness direction). The profiles of mean velocities and three normal Reynolds stresses taken at a plane near the inclined oil-water interface for the case of *16 lpm* are compared in Fig. 5.7. The smaller differences show that grid independency is achieved and the base mesh is

sufficiently refined. The base meshing scheme was used for RANS simulations of *12 lpm* and *14 lpm* cases.

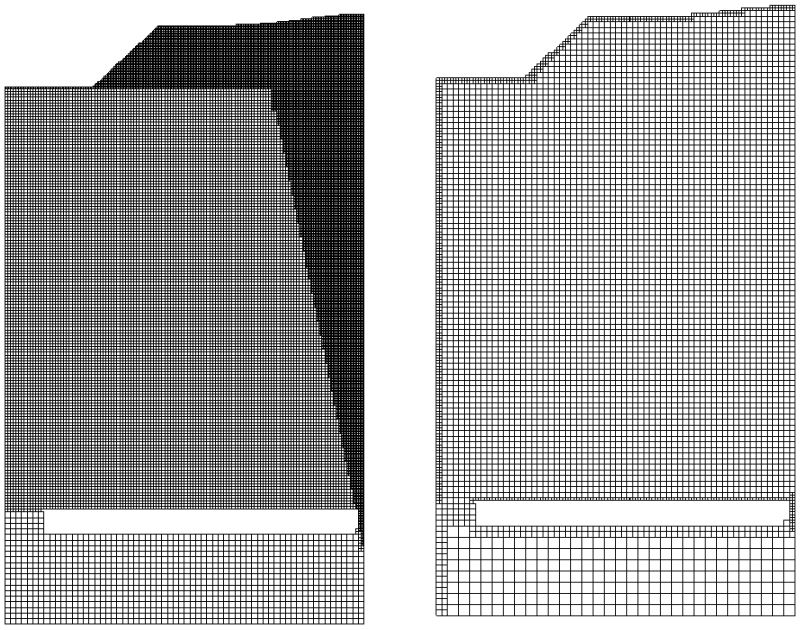

(a) At wall **(b)** Rest of the volume

Figure 5.6. Typical meshing scheme, shown for 16 lpm

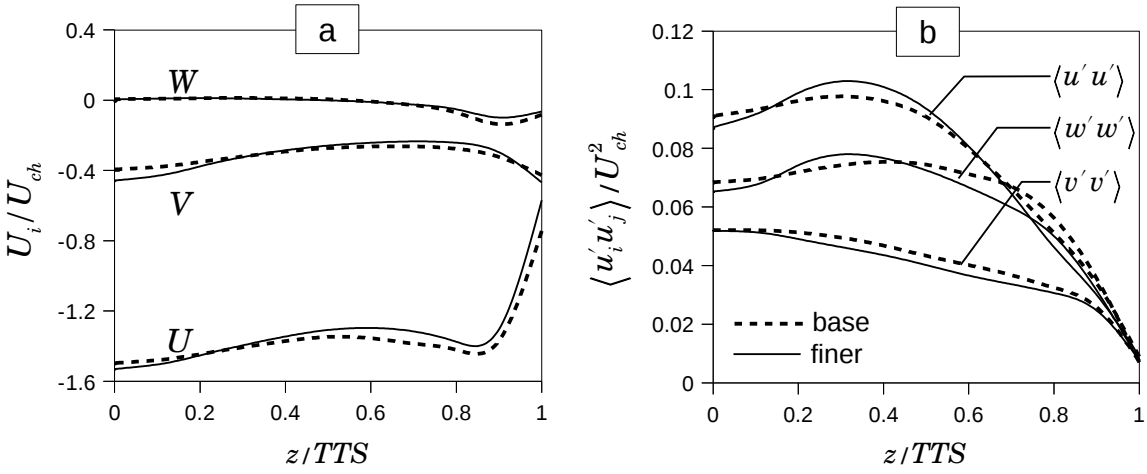

Figure 5.7. Charts comparing RANS outputs (a) mean velocities and (b) Reynolds stresses of base refinement (base) and more refinement (finer) of *16 lpm* taken across the width of thin slice (z direction), near *ULeye* at a distance from the free surface. TTS is thickness of thinslice. U_{ch} is the inlet-area average of velocity norm. Common legend.

5.2.2 Multiphase Large Eddy Simulations

5.2.2.1 Simulation Setup

Boundary and Initial Conditions: The LES domain is a cuboid as shown in Fig. 5.8a with boundary conditions essentially the same as in Fig. 4.1b. The initial shape of the oil-water interface was fixed according to the scheme in Fig. 5.5.

Inlet Conditions: The RANS outputs, namely the mean velocities and Reynolds stresses were extracted (using `GfsLocation`) on a Cartesian grid, in the *y*–*z* plane, located at a distance of R_{eye} from TSM axis (see Fig. 5.5), of height equal to 50 mm (larger than the largest h_U in Table 5.3) and width equal to $TTS/2$. Since the RANS domain was only a half of the TSM in the z direction, the mirror image of those RANS outputs were created for the other half. The RANS profiles for full TTS were then interpolated on the inlet grid of the LES domain and fed into the Synthetic eddy method (SEM). The direction of motion of eddies is set from right to left, parallel to the *x* direction.

The **number of Eddies** for SEM was set to 10,000 for all cases, well above that predicted by Eq. (4.24), setting $C = 1$ and using the extremes for eddy length scales from Table 5.4 to calculate the eddy box volume. The procedure to obtain the eddy length scales in Table 5.4 and therefore the eddy box dimensions are given in Appendix C.1.

Table 5.4. Maximum turbulent length scales in three directions – *x* (LSx), *y* (LStop, LSbottom) and *z* (LSz) – at locations in TSM where RANS profiles were extracted. While applying at SEM, all LSz values were limited to 2.0 mm.

Q, lpm	Turbulent Length Scales, mm			
	LSx	LStop	LSbottom	LSz
12	29	16	25	1.2
14	31	25	26	1.1
16	32	27	28	1.2

Meshing Schemes: Various meshing schemes were used to resolve the VOF surface and turbulent flow while minimizing the computational cost. An instance of such is seen from the snapshots in Figs. 5.8 (b) and (c). The VOF surface was adaptively refined based on the local radius of curvature (using `GfsAdaptFunction`) where regions of higher curvature received the highest refinement ($\Delta \approx 0.8$ mm). For the bulk lower phase, the next highest refinement was set ($\Delta \approx 1.6$ mm) from the inlet, until some distance downstream and was adaptively refined based on the local vorticity magnitude (using `GfsAdaptVorticity`). The rest of the bulk regions were left with coarse grid. The total number of cells was around 110,000 and the time step size was around 10^{-3} s.

Droplet Counting: The droplets were counted using `GfsOutputDropletSums`, the Gerris object that outputs the volume of every discrete phase present in a user defined region, at a given time instant. In a spreadsheet, the volumes, V, were converted to diameters using $(6V/\pi)^{1/3}$ and sorted to eliminate those below specified size limits.

Droplet Removal: In Gerris, immediately after droplet counting, droplets were replaced with the continuous phase (LP) using another Gerris object, `GfsRemoveDroplets` that would prevent re-counting the droplets in the future steps.

Compensation of UP Volume: Since the entraining droplets were removed regularly, the loss in UP volume has to be compensated to maintain the initial thickness of UP. This was achieved by a velocity boundary condition that pumps in UP fluid as a pulse (within one time step) whenever the volume loss exceeds 1% of volume of UP at $t = 0$ (details in Appendix C.2).

Non-Dimensionalization: As a general guideline for running stable Gerris simulations, all LES simulations were non-dimensionalized such that the largest velocities are around unity. The characteristic velocity scale (U_{ch}) was chosen as the mean of norm of velocities averaged over the RANS output grid and the characteristic length scale was set equal to TTS.

A typical simulation setup in Gerris parameter file is provided in Appendix D.3, although for a steel-slag case.

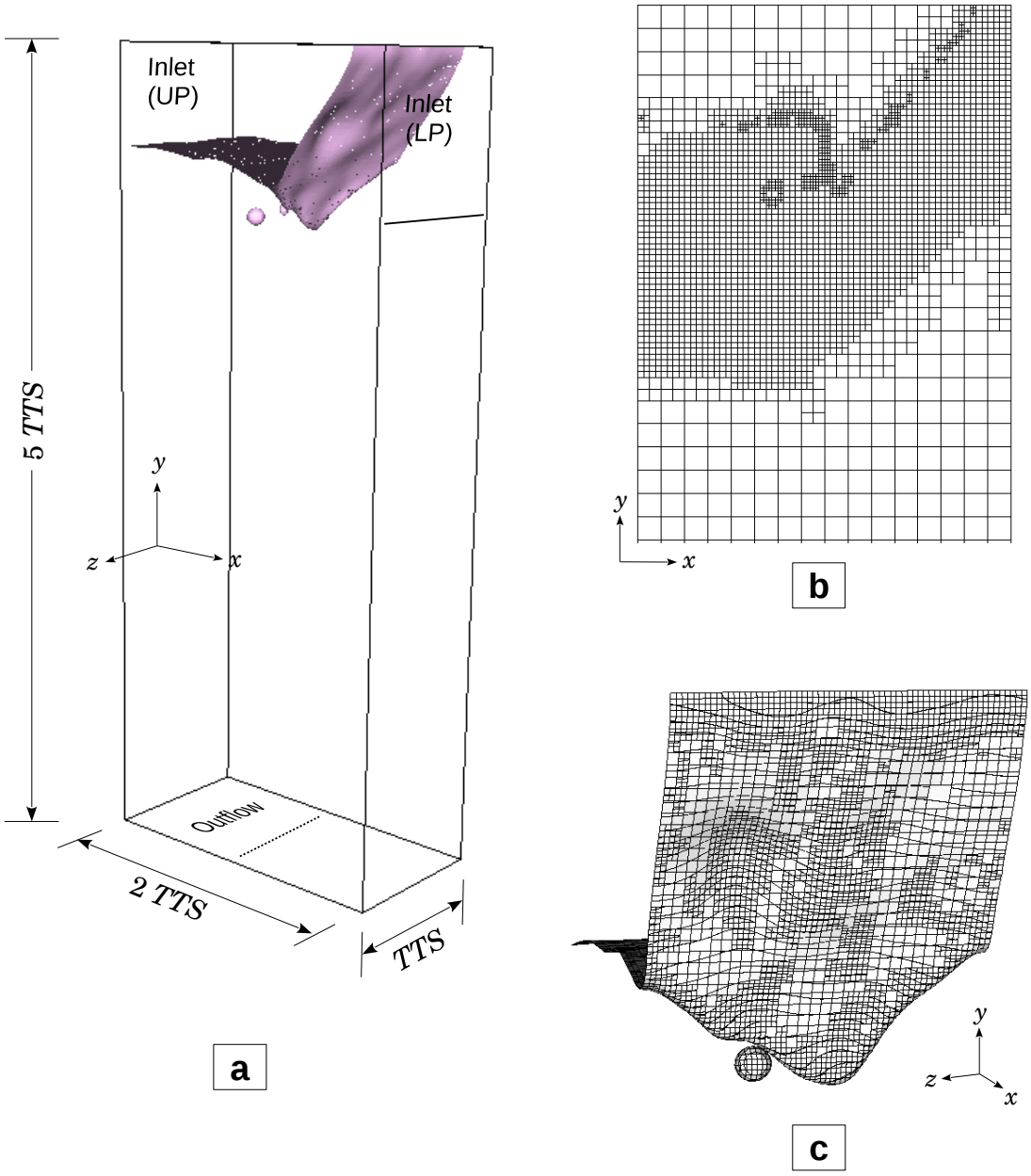

Figure 5.8. (a) LES domain; inlet for UP is for compensating its lost volume in due course. (b) Snapshot of mesh in the $z = TTS / 2$ plane showing various levels of refinement and highest refinement along the VOF surface (c) Snapshot of mesh mapped on the VOF surface showing varying levels of refinement based on the local curvature

All simulations were run until the cumulative averages of entrainment rate and mean droplet size given by Eqs. (5.1) and (5.2), respectively, became steady with time. The time for simulating varied from one to two weeks, much longer than the slag metal simulations in Ch. 6, because of the too small entrainment rates to reach statistical steady state.

5.2.2.2 Droplet Formation

Various stages of droplet formation are shown in Fig. 5.9 by two typical series of snapshots from video recordings of the 14 lpm case, although in the second series, droplet never detached. The stages in the first series are better explained using the corresponding LES results in Fig. 5.10. Initially three dimensional waves and ripples are seen in the VOF surface. The waves, due to relative motion between the two phases, grow into a lip in (i) and (ii), from which a ligament grows from (iii) onwards. As the lower phase momentum drags the ligament downwards, it eventually breaks into one large and few satellite droplets due to capillary instability. The LES results are qualitatively similar to the series (i) to (v) in Fig. 5.9. Similar observations were reported by Krishnapisharody (2006) from his experiments in the same TSM, although for a very thick upper phase.

Figure 5.11 shows another series of snapshots of VOF surface and iso-surfaces of velocity magnitude of 0.34 m/s. Each of these closed iso-surfaces can be seen as individual eddies of high velocity. The timing for these snapshots correspond with that in the series shown in Fig. 5.10; for example, the event in Fig. 5.11 (iv) is the same as that in Fig. 5.10 (i). If closely observed at $t' = -3$ a lip has formed, but it did not grow further; only after $t' = 0$ the lip formed grows as described above. Observing the eddies, we see that although their number and size are relatively large at $t' = -3$, they have quickly diminished until another larger batch of eddies surge at $t' = 0$ that has persisted for a while. This is the reason why the lip formation resulted in droplet formation only after $t' = 0$. This indicates that the strength of eddies characterized by their velocity magnitude and size influence the droplet formation.

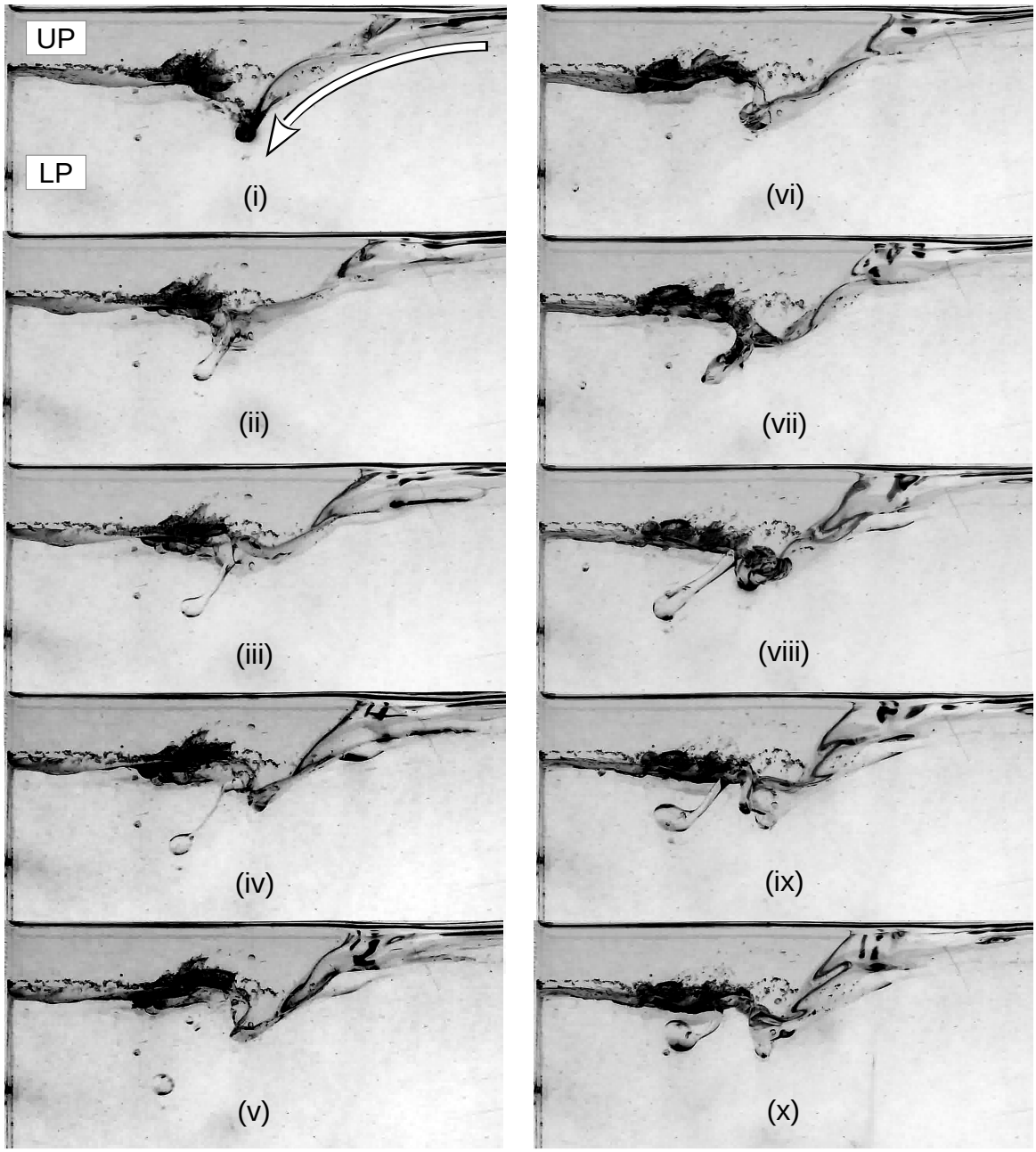

Figure 5.9. Two typical series of snapshots from video recordings of flow in TSM at 14lpm, (i) to (v) and (vi) to (x), showing formation of lip, ligament and droplet detachment, although in the second series the ligament 'rejoined' UP before droplet detachment. The view is same as the schematic in Fig. 5.1 but confined to the upper left region. The arrow in (i) shows the LP flow direction.

In almost all figures, the two phase interface at *ULeye* can be identified from two distinct lines, the lower and upper, which correspond to the interface close to wall and in the interior of TSM, respectively.

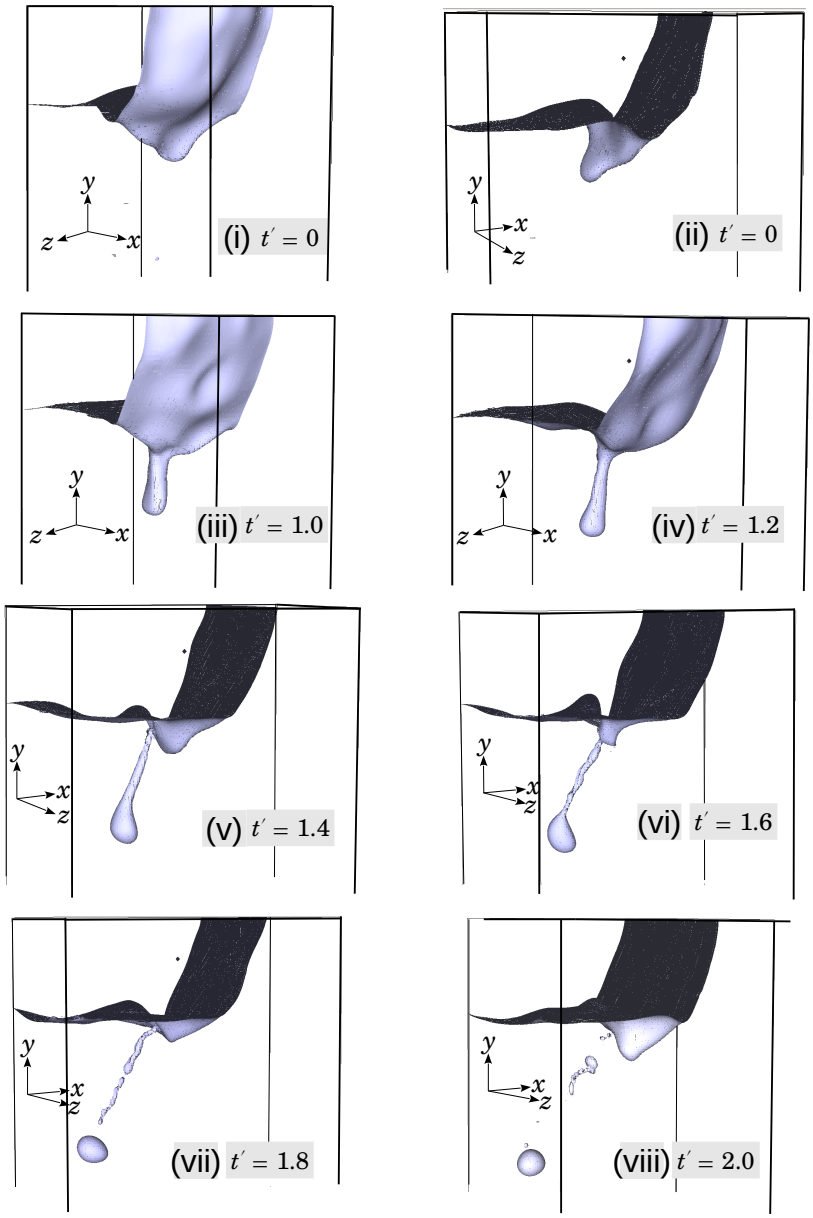

Figure 5.10. Series of snapshots showing formation of lip in (i) & (ii), ligament and its elongation in (iii) to (v) and break up into one large drop (11 mm) and few satellite drops in (vi) to (viii). Real time, $t = 0.26\ t'$.

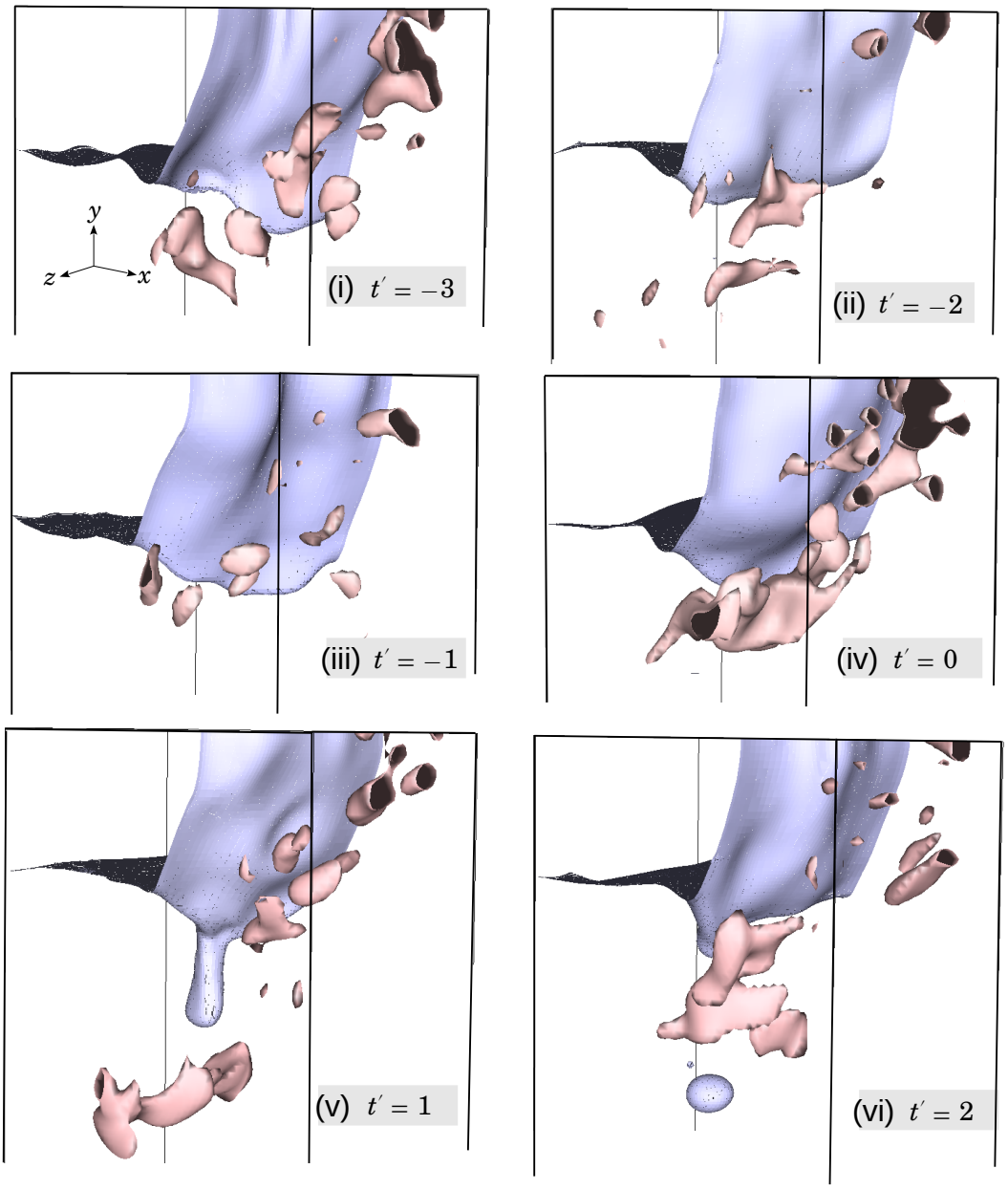

Figure 5.11. Series of snapshots showing iso-surfaces of velocity of magnitude 0.34 m/s and their interaction with the VOF surface. Scaled time t' corresponds with events in Fig. 5.10

Comparing the interface at *ULeye* between experiment (Fig. 5.9) and LES (Fig. 5.10), we see that the average inclination (θ_{ULeye}, defined in Fig. 5.5) is smaller in the LES. Moreover a sharp discontinuity between the two phases at free surface in the LES is visible. These differences arise due to the inability to model the water-oil-air-three phase contact in Gerris, as noted already (Sec. 4.1). Currently the impact of this approximation on entrainment characteristics is unknown.

5.2.2.3 Entrainment Rate and Size Distribution

From various simulation trials it was found that the entrainment characteristics are significantly influenced by eddy length scales (LS); these values were obtained from RANS simulation using Eq. (4.26). However in the free shear region RANS predictions of LS are considered to be inaccurate (Jarrin *et al*, 2009). The plane where RANS outputs were extracted is near the free shear region. So, many trials were performed by varying a factor multiplied to LS, called as $LSfac$. The entrainment rate $(\dot{N})$ and the mean droplet diameter $(\overline{d})$ for various trials are summarized in Table 5.5 and their values of data and model are compared in Figs. 5.12 (a) & (b); the size distributions are presented in Figs. 5.13 (a) to (f). (Note that the order of results presented are jumbled as 16, 12 and 14 lpm.) Since the smallest mesh used to resolve the VOF surface is 0.8 mm, only droplets ≥ 3 mm are considered for model assessments.

Considering the **16 lpm cases**, with larger length scales (larger $LSfac$), $\dot{N}$ is largely over-predicted (Fig. 5.12a) until when the $LSfac$ is decreased to 1/10. Although $\overline{d}$ is fairly well predicted for all $LSfac$ it is better at $LSfac$ = 1/10. Moreover, at this value, the droplet size distribution becomes bimodal (Fig. 5.13c) similar to the data (Fig. 5.3).

For the **12 lpm cases**, prediction of $\dot{N}$ improves at smaller $LSfac$, similar to the 16 lpm case. However values of $\overline{d}$ are generally over-predicted and the size distributions are more or less flat, unlike the data (Fig. 5.3).

For the **14 lpm case**, $LSfac$ of 1/6 was chosen, intermediate of the 16 and 12 lpm cases. Both $\dot{N}$ and $\overline{d}$ are fairly well predicted although the size distribution shows multiple peaks uncharacteristic of the data (Fig. 5.3).

Table 5.5. Entrainment rates and mean diameters of droplets ≥ 3mm for various cases

Flow rate, Q, lpm	**Length scale factor, $LSfac$**	**Number of droplets counted**	**Entrainment rate, $\dot{N}$, 1/s**	**Mean diameter, $\overline{d}$, mm**
16	1/4	381	6.63	13.5
	1/8	200	1.68	9.0
	1/10	243	0.56	8.0
12	1/2	389	1.90	12.2
	1/3	262	0.82	10.8
14	1/6	178	0.39	10.7

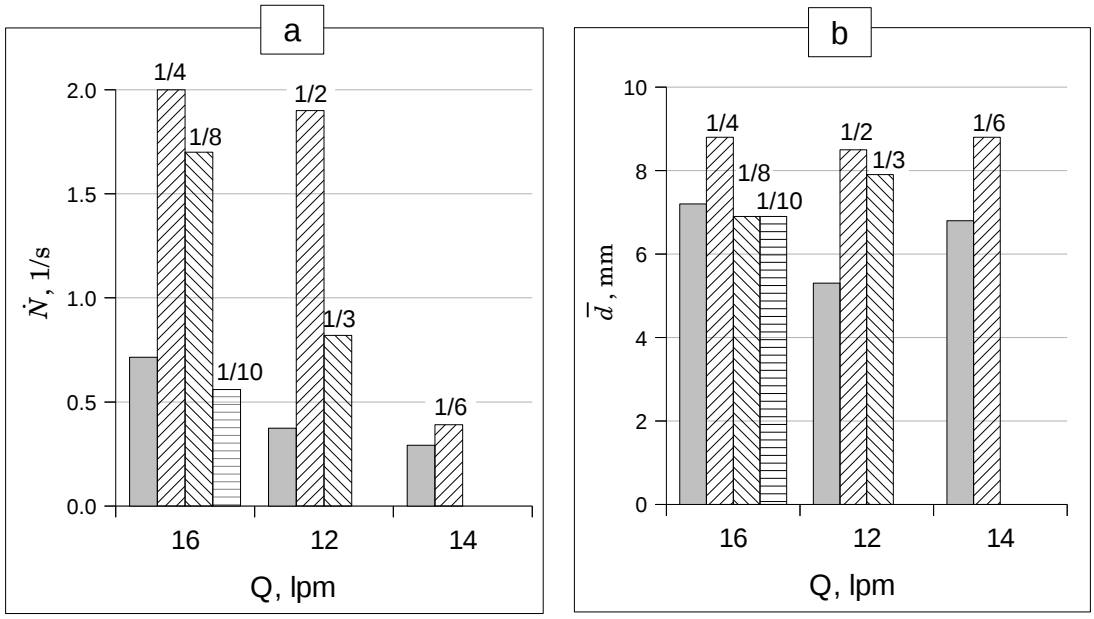

Figure 5.12. Comparison of Data (un-labeled bars) with LES results of various trials for (a) entrainment rate $(\dot{N})$ and (b) mean diameter of droplets $(\overline{d})$, tabulated in Table 5.5. The labels against each bar are their respective length scale factors ($LSfac$). In (a) the value for 16 lpm, $LSfac$ = 1/4 is clamped for clarity.

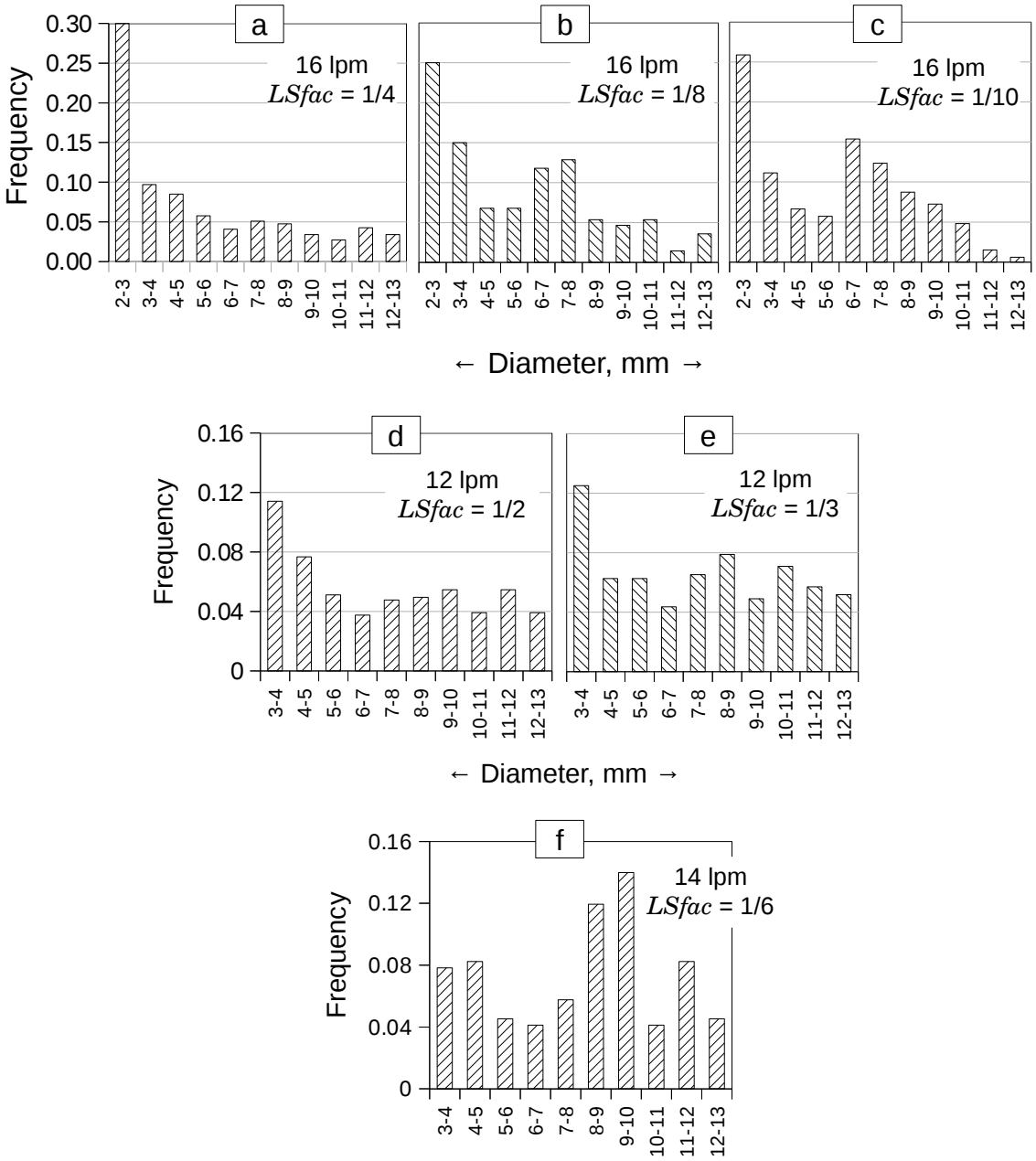

Figure 5.13. Droplet size distribution of three flow rate cases for various length scale factors $(LSfac)$. Common y-axis between (a) to (c) and between (d) and (e).

From these simulations it is inferred that the entrainment characteristics are sensitive to the eddy length scale, LS. This is in-line with the role of eddy strength on droplet formation discussed in Sec. 5.2.2.2. In the absence of appropriate length scales, manipulation of $LSfac$ was required to obtain better agreement with the data; generally the optimal $LSfac$ decreased with increasing flow rate. Therefore there is no common value for $LSfac$ that is appropriate for all flow rates. The effect of further mesh refinement of VOF surface was not investigated. However, for the entrainment characteristics being much sensitive to the eddy length scale variations, further mesh refinement is less likely to mitigate this sensitivity. The sensitivity to eddy length scale is chiefly because of the small flow rates in the TSM experiments as will be clarified later in Ch. 6.

5.3 Summary

Experiments were performed in a thin slice model to measure entrainment rate and droplet size distribution for entrainment of oil into water for three flow rates. The approach to simulate entrainment, presented in Ch. 4, was applied to these three flow rate cases that consisted of performing single phase RANS simulation to supply inlet conditions for the following multiphase LES. Although the simulated droplet formation is qualitatively similar to experiments, the agreement of simulation with data for entrainment rate and droplet size distribution showed large dependence on the choice of turbulence length scale, which is determined by the length scale factor, $LSfac$. Upon manipulating $LSfac$, better agreement between the data and the LES results for entrainment rate and mean droplet size were obtained, although not for the droplet size distribution. However since the optimal value for $LSfac$ varied with flow rate it leaves room for uncertainty in simulating the entrainment phenomena, at least in the small scale systems like the thin slice model.

6. Multiphase LES in Steelmaking Ladle

The methodology to perform entrainment simulations, detailed in Chapter 4 and applied to the thin slice model in Chapter 5, is applied to a ladle of industrial scale, albeit, of small capacity. A survey of various parameters is presented at first, from whose combinations various simulation cases are designed to study the role of each of these parameters. In the following sections the results are discussed. Finally an analysis of LES velocity profiles and the resulting correlation with entrainment rate, along with physical properties, are presented.

6.1 LES Cases and Setup

Each LES case constitute a combination of various parameters. The parameters that were kept constant are the ladle dimensions chosen to be 2 m diameter and 2 m bath depth yielding a capacity of 44 ton of liquid steel, the temperature set to 1600 °C, the steel density taken as 7000 kg/m^3 and the thickness of thin slice (TTS) set to 0.1 m.

6.1.1 Parameters

The parameters that likely affect the entrainment characteristics are the gas flow rate, slag viscosity, slag metal interfacial tension, slag thickness and slag metal density ratio. To study the independent effect of the first three parameters, three values were chosen in each, such that the first and third values are half and double the second value, respectively. The choice of values for these parameters are described further. Some special cases were performed by varying slag thickness, density ratio and gravity although practically, density ratio varies narrowly and gravity is constant.

6.1.2 Gas flow rate

A survey of literature for gas injection rates in common industrial practice, presented in Table 6.1, shows a more common range of 1 to 4 lpm(STP)/ton of steel for specific gas injection rate, (Q_{sp}) although 4 lpm/ton is in the upper limit for single plug, for gentle stirring as indicated by

Case 5. So three values for Q_{sp}, namely, 1, 2 and 4 lpm/ton were chosen. The gas flow rates for *in-situ* temperature and pressure conditions were calculated using the relation,

$$Q = Q_{sp} \frac{(T/273)\times 10^5}{\left(P_{atm} + \rho_L g z\right)} \times \rho_L \times \pi R_{ves}^2 h_L, \tag{6.1}$$

and were 178, 355 and 710 lpm†, respectively, at half bath depth $(z = h_L/2)$.

Table 6.1. Ranges of specific gas injection rates (Q_{sp}) in ladles in common industrial practice

	Gas injection Rates in industrial ladles	Q_{sp}, lpm(STP) per ton of steel		Comments	Reference
		MIN	MAX		
1.	0.001–0.015 m^3(STP) /ton of steel /min	1.0	15	General range quoted in reference	Mietz *et al*, 1991a
2.	50–400 (N)lpm for 200 -250 ton ladles	0.25	2.0	Aimed at slag eye; Q_{sp} values calculated for a 200 ton ladle	MSTS, 1998
3.	2.6 m^3 (STP)/min for 185 ton ladle, 3 plugs	-	14	Tank degasser	Lachmund *et al*, 2003
4.	≈10 to 40 N m^3/hr for 165 ton ladle, 2 plugs	1.0	4.0	Aimed at slag eye	Graham, 2008
5.	≈10 to 35 STP m^3/hr, for 170 ton ladle	1.0	3.4	Aimed at slag eye; splashing was observed at *MAX* Q_{sp}	Valentin *et al*, 2009b,

† However, this is not the correct way to calculate Q from Q_{sp} for the present ladle, if it has to correspond with the ranges provided in Table 6.1. First a ladle of dimensions more representative of the cases in that Table, say 3 m bath depth and 3 m diameter has to be chosen (that has a capacity of 150 ton of steel). Equation (6.1) has to be applied to this ladle for the three Q_{sp} values chosen at half bath depth. These values have to be then scaled down to the present ladle using the scaling law, $Q_1/Q_2 = \left(h_{L,1}/h_{L,2}\right)^{2.5}$ which would give 180, 360 and 720 lpm. Although this procedure was overlooked during the calculations, incidentally, these values are close to our present values.

6.1.3 Slag Viscosity

Three slag viscosities were considered by halving and doubling the base value of 0.11 Pa.s. This value was calculated using the National Physical Laboratory model† for slag of 35–50–7–8 mass% of Al_2O_3–CaO–SiO_2–MgO, a typical composition of ladle desulphurization slags and is also close to the value reported by Ekengard *et al* (2008). The slag with viscosity of 0.22 Pa.s corresponds to a lime saturated slag with high desulphurization potential.

6.1.4 Slag Metal Interfacial Tension

Numerous experimental measurements in the past (Riboud & Lucas, 1981, Gaye *et al,* 1984, Jimbo *et al*, 1996) show that the slag metal interfacial tension coefficient, σ, for various combinations of Fe alloys and slags range between 1.0 to 1.8 N/m depending upon the activity of surface active elements. Gaye et al (1984) showed that σ, measured after achieving chemical equilibrium (w.r.t. [O] or [S]), decreased with increased activity of both oxygen and sulphur. The effect is such that an increase in activity of either [S] or [O] by a order of magnitude can decrease σ by half and to as low as 0.5 N/m. This was attributed to the increased concentration (or activity) of surface active element at the interface. When mass transfer of a surface active element takes place in slag metal reactions, it was shown that, σ can even 'disappear' where there is large flux of the element across the interface, which can lead to 'spontaneous emulsification'. Based on these, three values for σ were chosen for simulations namely, 0.5, 1.0 and 2.0 N/m to study its role on entrainment.

6.1.5 Other Parameters

The **slag density** was taken as 2800 kg/m^3 computed using the Mills and Keene model (1987)† for the slag with 35–50–7–8% of Al_2O_3–CaO–SiO_2–MgO.

The **nominal slag thickness** was taken to be 0.1 m for all cases, except when they were varied. This gives a slag to metal volume ratio of 1/20, which is in the range of industrial practice.

The **length scale factor** (*LSfac*) of 1/10 gave better results for the highest flow rate

† implemented in a spreadsheet by Graham for his thesis (2008)

case of TSM, discussed in Sec. 5.2.2.3, and therefore that was used for the present LESs. Cases with varying *LSfac* are discussed in the Results Section.

The list of simulation cases is presented in Table 6.2. The choice of combination of parameters for each case is explained in Results section. It is apparent that gas injection rate is a commonly varied parameter among most of the cases.

6.1.6 SEM Inlet Profiles

For the SEM of LES inlet, QSP-RANS simulations were performed for a 2 m bath depth and 2 m diameter vessel in `GfsAxi` based on the formulation detailed in Sec. 4.4. Since flow rate is the only variable here, three QSP-RANS were performed. Preliminary simulations performed at $Q_{sp} = 4$ for three meshes with the smallest cell size, $\Delta \approx$ 2.4, 1.2 and 0.6 mm, showed that velocity and Reynolds stress profiles, at the locations mentioned above, were grid independent for $\Delta \approx 1.2$ mm and below and hence the meshing scheme corresponding to $\Delta \approx 1.2$ was used for computing the flow field for all cases.

The plume velocities [defined by, Eq. (4.47)] for various Q_{sp} were computed and plotted in Fig. 6.1 against the axial distance, in comparison with the correlation of K&I (2010),

$$U_P(z) \;=\; 2.52\, Q^{0.32}\, z^{-0.28} \tag{6.2}$$

where Q is as defined by Eq. (6.1). It should be noted that Eq. (6.2) is good only until the axially rising liquid in the plume turns radially, above which U_P actually drops to zero. In Fig. 6.1, although the RANS results deviate more from Eq. (6.2) at the higher Q_{sp}, they converge around the point where the plume liquid turns radially, which is where the profiles for LES inputs were extracted.

Table 6.2. List of various simulation cases performed. Base cases (italicized) are only shown for clarity

Specific gas injection rate, Q_{sp}, lpm/ton →		1			2			4		
Varying slag viscosity, μ_U and slag metal interfacial tension, σ	σ, N/m →	0.5	1.0	2.0	0.5	1.0	2.0	0.5	1.0	2.0
	μ_U, Pa.s ↓									
	0.055				1	2	3			
	0.11	10	11	12	4	5	6	13	14	15
	0.22				7	8	9			
Varying Length scale factors, *LSfac*, for μ_U= 0.11 Pa.s and and σ = 1.0 N/m.	*LSfac* ↓									
	1/5		16			17			18	
	1/10 (base)		*11*			*5*			*14*	
	1/20		19			20			21	
Varying maximum level of mesh refinement at VOF (maxlevVOF) Δ is smallest cell size	maxlevVOF ↓									
	6 (base) $\Delta \approx$ 1.6 mm				*4*		*6*			*15*
	7 $\Delta \approx$ 0.8 mm				22		23			24
Varying actual slag thickness, h_U	h_U, m ↓									
	half the base					25				
	base, 0.117					*5*				
	1.2 times the base					26				
Varying slag density, ρ_U	ρ_U, kg/m^3 ↓									
	half the base					27				
	base, 2800					*5*				
	twice the base					28				
Varying gravity, g	g, m/s^2 ↓									
	half the base					29				
	base, 9.81					*5*				
	twice the base					30				

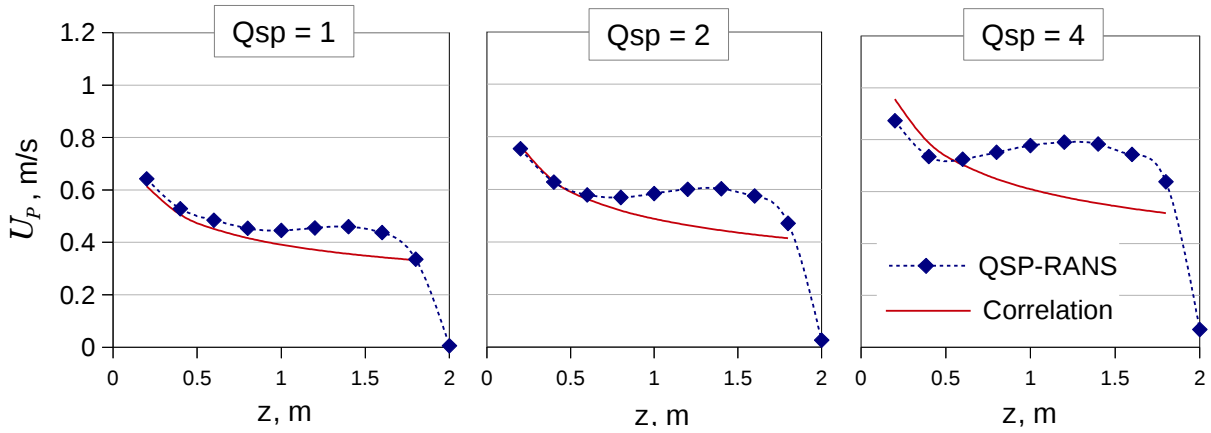

Figure 6.1. Comparison of profiles of plume-cross sectional area averaged velocity (U_P, m/s) obtained from RANS simulation and the correlation, $U_P = 2.52\ Q^{0.32}\ z^{-0.28}$, of K&I (2010), for three gas injection rates (Qsp, lpm/ton); 'z' is the axial coordinate of ladle. Common legend and y-axis.

For SEM of LES inlet, the mean velocity and Reynolds stresses profiles were extracted at a radii of 5, 5 and 2 cm off the eye location (i.e., at r, m $= R_{eye} - 0.05$ or 0.02) for $Q_{sp} = 4$, 2 and 1 lpm/ton, respectively, for a length equal to thickness of upper phase, from the location of free surface at that radial coordinate; these profiles are presented in Fig. 7.15 (continuous lines) and are excluded here to avoid repetition, although the velocity vectors and turbulent length scale distribution are shown in Figs. 6.2 and 6.3, respectively. Coordinate transformation is required for the profiles extracted at QSP-RANS that are in axisymmetric coordinates before applying at the SEM in Cartesian coordinates. This is discussed in Appendix D.1. The derivation of Reynolds stresses, based on Boussinesq eddy viscosity approximation, is given in Appendix D.2.

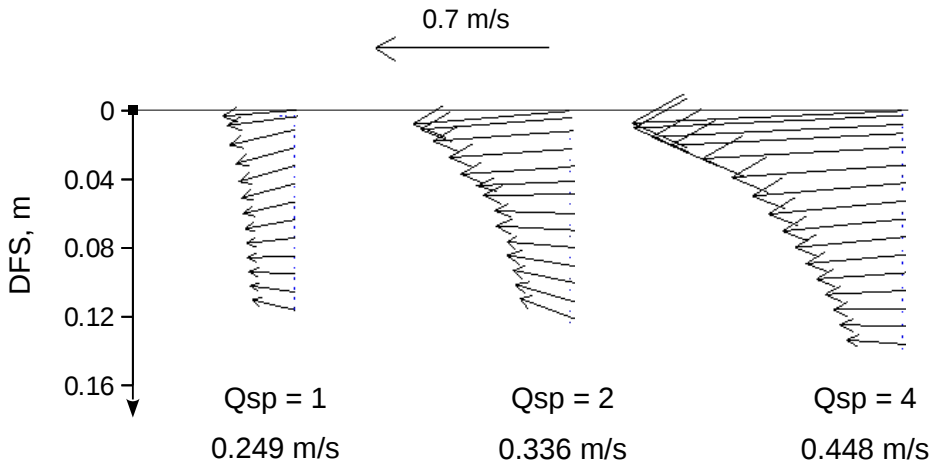

Figure 6.2. Vectors of velocity profile extracted from QSP-RANS and applied at the LES inlet plane, for three gas injection rates (Qsp, lpm/ton). DFS - Distance from Free Surface (labeled in Fig. 4.12). The line averaged velocities [m/s, defined by Eq. (6.3)] are also given for each Qsp.

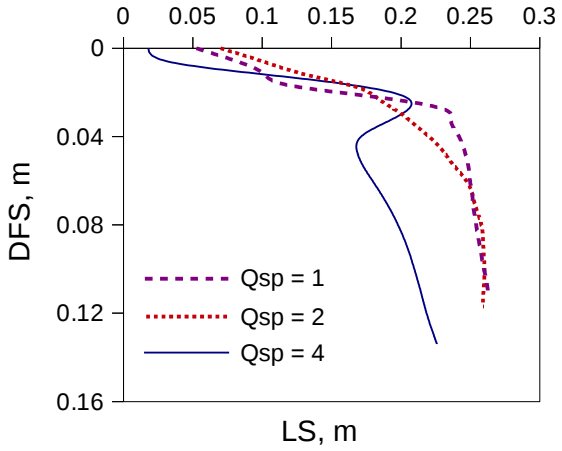

Figure 6.3. Distribution of turbulence length scales (LS) across distance from free surface (DFS) for three gas injection rates (Qsp, lpm/ton) extracted from QSP-RANS at locations corresponding to the LES inlet.

6.1.7 Other Details of LES Setup

The **meshing scheme** (including the adaptive mesh refinement) is similar to that outlined in Sec. 5.2.2.1, except that the highest refinement was not limited to the VOF surface but was applied throughout the lower phase region from the inlet until some distance downstream. At highest refinement $\Delta \approx 1.6$ mm. The total number of cells varied between 0.5 to 1.5 million (in proportion to entrainment rate) and the time step size was generally less than 10^{-3} s. For this *base* meshing scheme (maxlevVOF = 6 in Table 6.2) it took 3 to 5 days for each simulation to obtain steady state results; for an increase in mesh refinement by one level (maxlevVOF = 7 in Table 6.2) it took more than 3 weeks.

Non-Dimensionalization: Similar to Ch. 5 the LES calculations were run in non-dimensional units. The lengths were non-dimensionalised by the thickness of thin slice $(\boldsymbol{TTS})$. The velocities and Reynolds stresses were non-dimensionalized by a characteristic velocity defined by the line average,

$$\bar{v}_{RANS} = \frac{1}{h_U}\int_0^{h_U} \left|\boldsymbol{U}\right| dz, \qquad \left|\boldsymbol{U}\right| = \sqrt{U_r^2 + U_z^2}, \quad z = \boldsymbol{DFS} \tag{6.3}$$

where, h_U is the actual UP thickness and U_r and U_z are the mean velocities of QSP-RANS. The values of $\bar{v}_{RANS}$ are labeled in Fig. 6.2.

The following were the same as described in Sec. 5.2.2.1:

- droplet counting and removal, compensation of upper phase
- initial shape of VOF (also in Fig. 5.5) – with θ_{ULeye} of 40 degree for all cases.
- eddy box dimensions – but using the turbulence length scale $(\boldsymbol{LS})$ distributions in Fig. 6.3 and assuming same maximum $\boldsymbol{LS}$ for the *x* and *z* directions.

Correction near inlet: In some LES cases† the fluctuating interface (VOF surface) at *ULeye* was too close to the inlet that occasionally it touches the inlet, due to floating up of large drops

† due to small flow rate or large gravity or large density difference

of UP or even the fluctuating *ULeye*. Since the inlet, described only by the velocity boundary conditions, cannot distinguish between phases, the inflowing phase will change from LP to UP, thereby blowing up the simulation. To avoid this, any UP encountered was removed in the volume of a small thickness from the inlet plane. However this happens only after droplet removal, so that the droplets floating up in this region do not go unaccounted.

A typical simulation setup in Gerris parameter file is provided in Appendix D.3.

6.2 Results

The results constitute the 1) entrainment rate, 2) Sauter mean droplet diameter [d_{32}, defined by Eq. (3.25)] and 3) droplet size distribution.

Entrainment Rate: Unlike in Ch. 5 but same as in Ch. 3, volumetric entrainment rate is considered. Since the simulations are only for a thin slice, entrainment rate has to be scaled up for a cylindrical ladle. The scaling is based on the ratio of two nominal areas of *ULeye* – 1) the curved surface area of a truncated cone formed by *ULeye* about the ladle axis, given by

$$A_{ULeye}^{nom} = \pi\left(2R_{eye} + h_U \tan\theta_{ULeye}\right) h_U / \cos\theta_{ULeye} \tag{6.4}$$

and 2) the *ULeye* area at $t = 0$ in the LES, given by,

$$A_{ULeye,LES}^{nom} = TTS\ h_U / \cos\theta_{ULeye}, \tag{6.5}$$

both with reference to Fig. 5.5, although Eq. (6.4) is for cylindrical ladle and Eq. (6.5) is for the thin slice. After scaling, the entrainment rate is normalized with the volume of upper phase to yield the percentage volume of upper phase entrained per unit time, altogether defined as,

$$VPU\,(\%/\mathrm{s}) = \underbrace{\left(\frac{1}{t_{tot}}\sum_t V_d\right)}_{\dot{V},\ m^3/s} \underbrace{\left(\frac{A_{ULeye}^{nom}}{A_{ULeye,LES}^{nom}}\right)}_{\substack{Scaling\ up \\ factor}} \underbrace{\left(\frac{100}{\pi R_{ves}^2 h_{U,nom}}\right)}_{\substack{normalizing \\ factor}} \tag{6.6}$$

where t_{tot} is total simulation time, V_d, volume of droplets, R_{eye}, slag eye radius, R_{ves}, ladle radius, TTS, thickness of thinslice and $h_{U,nom}$ and h_U are the slag thicknesses before any gas

injection and after reaching steady state (*nominal* and *actual*, respectively). In all the RANS simulations, θ_{ULeye} was 40 degrees; however the LESs resulted with different the angles of inclination. By ensemble averaging several instances of interface positions (consisting of various time instances and various cases within each Q_{sp}), θ_{ULeye} were estimated to be approximately, 15, 25 and 30 degrees for $Q_{sp} = 1$, 2 and 4 lpm/ton, respectively. Only these values were used in Eq. (6.6) to normalize the entrainment rates.

All simulations were run until the cumulative time averages of $\dot{V}$ and d_{32} reached steady state [using formulas similar to Eq. (5.1) and (5.2)]. It was always found that droplet size distribution became time invariant earlier than the cumulative time average of entrainment rate. Typical times for reaching steady state varied between 4 to 15 s, directly proportional to resistance to entrainment.

Since the smallest mesh size is 1.6 mm, only droplets above 4 mm were counted for the results of *VPU* and d_{32} presented in this Section. However the size distribution plots are shown with droplets starting from 1 mm, just to show the drop in frequency of occurrence of finer droplets. For some cases *VPU* and d_{32} were calculated for only droplets up to 15 mm, to show the effect of droplet size range on these statistics.

6.2.1 Roles of Slag Metal Interfacial Tension and Slag Viscosity

To see the roles of slag metal interfacial tension and slag viscosity independently and also their combined effect on entrainment, 9 cases were considered at Q_{sp} = 2, namely Cases 1 to 9 listed in Table 6.2. *VPU* for two droplet diameter ranges, namely, less than 15 mm (d < 15 mm) and all droplets, are plotted in Fig. 6.4 (a) & (b), respectively. The charts show that the trends of entrainment rate *vs* interfacial tension among various values of μ_U are not entirely consistent. To determine if this were due to insufficient sampling of droplets, the simulations for some cases were run for longer times; however none of the results changed significantly. As of now it is unclear about this lack of clear trends. Despite this, the following overall effects are clear:

- Entrainment rate is lowered by increasing interfacial tension, but only for smaller

droplets; as the larger droplets are included, it is more or less unaffected.

- Slag viscosity has only a minor effect on entrainment rate.

The Sauter mean diameter plots for the Cases 1 to 9 in Fig. 6.6a show that d_{32} increases with interfacial tension while being barely affected by slag viscosity. The droplet size distribution plots in Fig. 6.7 reveal that the increase in d_{32} with σ was due to more larger droplets produced; again slag viscosity has no effect on size distribution. Summarizing, the decreasing entrainment rate with σ for $d < 15$ mm (Fig. 6.4a) and the increasing droplet size with σ (Fig. 6.6a and 6.7a) has resulted in more or less σ-independent overall entrainment rate (Fig. 6.4b). In other words, for a given flow rate, same volume of droplets are pinched off at *ULeye* while interfacial tension determines their size distribution.

Snapshots of VOF surface (slag metal interface) at *ULeye*, viewed at an angle, as the schematic in Fig. 4.1, are shown in Fig. 6.10 for varying σ at $\mu_U = 0.11$. To give a better idea of these surface deformations/waves, Fig. 6.9 has the side view of *ULeye*. Generally three dimensional waves, seen as surface corrugations, propagate downwards and breakdown into droplets past the slag thickness. With decreasing σ the surface corrugations are seen to increase, resulting in production of finer droplets. At lower σ, the network of ligaments of UP seen are yet to detach into separate droplets and hence not removed in Gerris at the time of these snapshots, which is why larger entrainment depths are seen compared to the higher σ case.

6.2.2 Effect of Gas Injection Rate

Six more cases at $\mu_U = 0.11$ were performed for the two other Q_{sp} and the three σ values, namely Cases 10 to 15 in Table 6.2, to study the effect of gas injection rate; the results of entrainment rate are shown in Fig. 6.5 (a) and (b). Generally entrainment rate has a strong linear relationship with gas injection rate. Similar to the results discussed in Sec. 6.2.1, the effect of σ is pronounced in the smaller droplets range ($d < 15$ mm) that, as σ increases more larger droplets are produced at the expense of smaller droplets. In addition, lowering of *VPU* due to increasing σ is pronounced at the highest Q_{sp}.

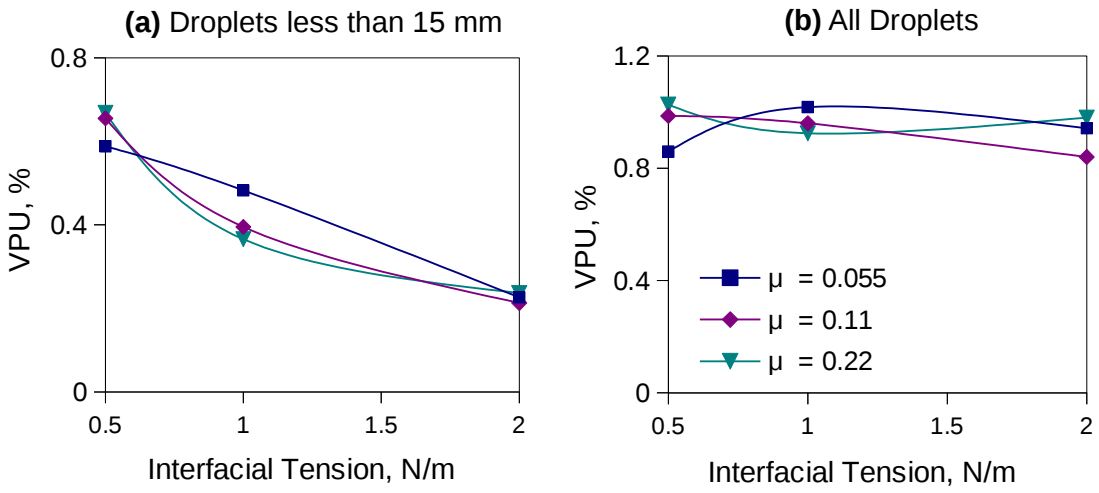

Figure 6.4. Entrainment Rate (VPU, % / s) *vs* Interfacial tension for various slag viscosities (μ, Pa.s), at Q_{sp} = 2 lpm/ton. Common legend.

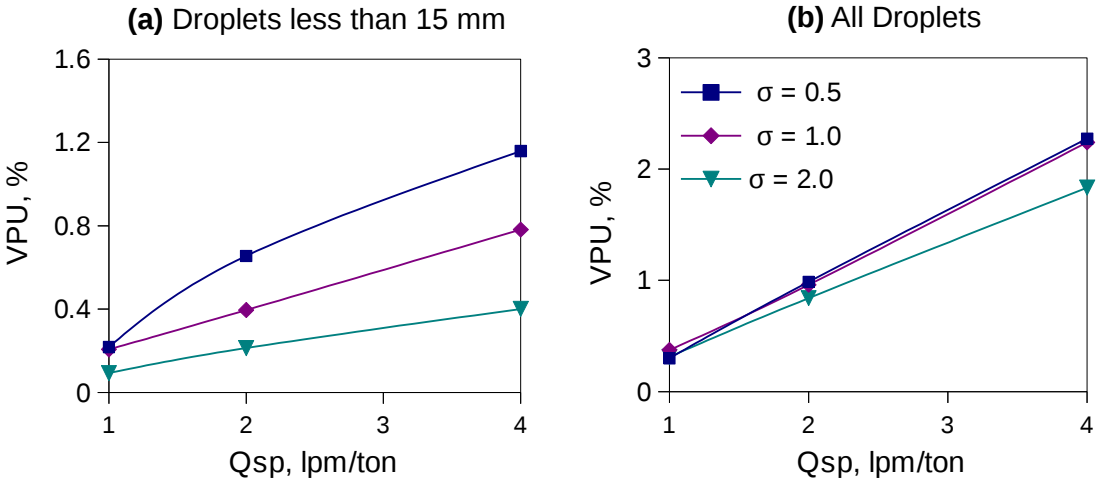

Figure 6.5. Entrainment Rate (VPU, %) *vs* specific gas injection rate (Qsp) for various interfacial tension at μ_U = 0.11 Pa.s. Common legend.

The Sauter mean diameter plot in Fig. 6.6b show a trend similar to Fig. 6.6a that the mean droplet size increase with σ; a mild but steady increase in mean droplet size with Q_{sp} is also visible. The droplet size distributions plotted in Fig. 6.8 also show only mild differences between various Q_{sp} for a given σ.

The snapshots of VOF surfaces (similar to Fig. 6.10) in Fig. 6.11 clearly show the increasing interface deformation and hence droplet production with Q_{sp}.

From these observations it can be stated that, entrainment rate is predominantly affected by gas injection rate with smaller role of interfacial tension and a minor role of slag viscosity whereas the droplet size statistics is affected mostly, only by the interfacial tension.

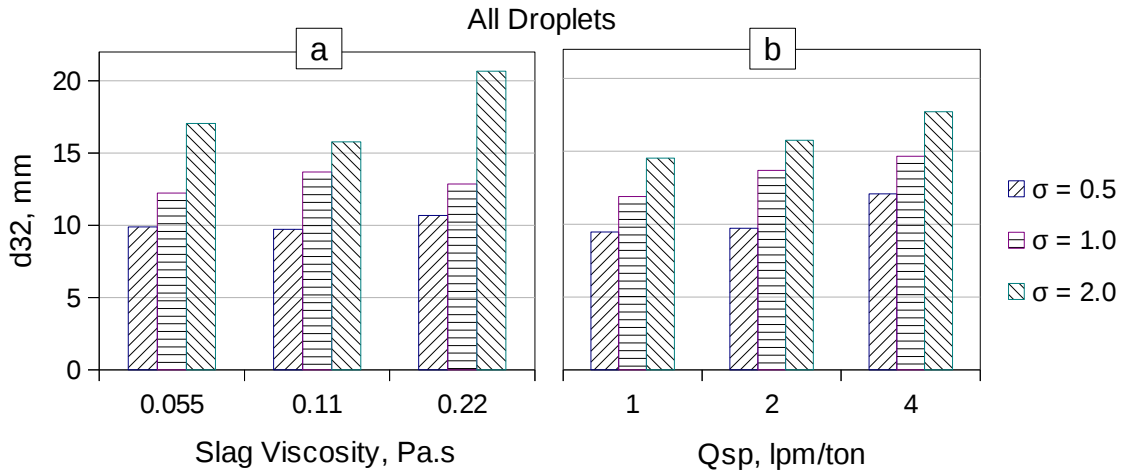

Figure 6.6. Sauter mean (d32, mm) *versus* (a) slag viscosity at Q_{sp} = 2 and (b) gas injection rate (Qsp) at μ_U = 0.11, both for various interfacial tension (σ, N/m). Common y-axis and legend.

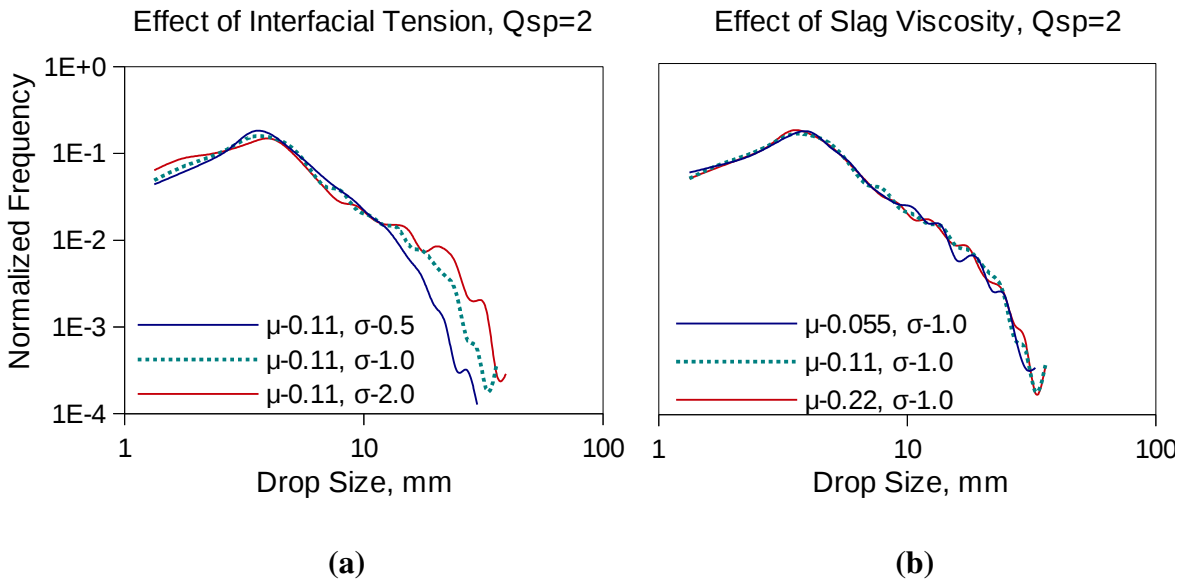

Figure 6.7. Effect of (a) interfacial tension (σ, N/m) and (b) slag viscosity (μ, Pa.s) on droplet size distribution for one gas injection rate, Qsp = 2 lpm/ton

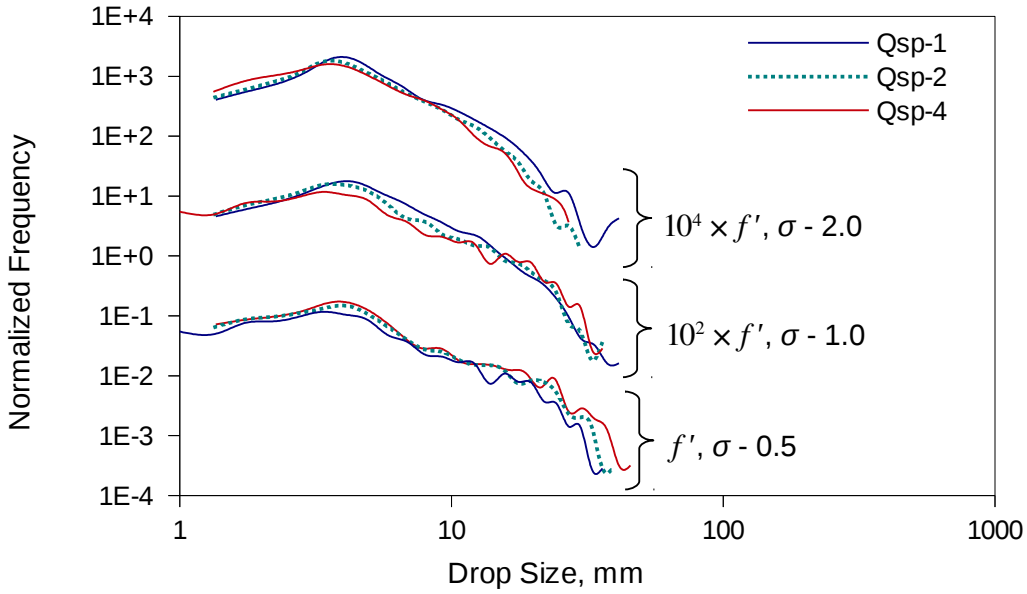

Figure 6.8. Effect of gas injection rate (Qsp, lpm/ton) on droplet size distribution for various interfacial tension (σ, N/m) at μ_U = 0.11 Pa.s. f' is normalized frequency.

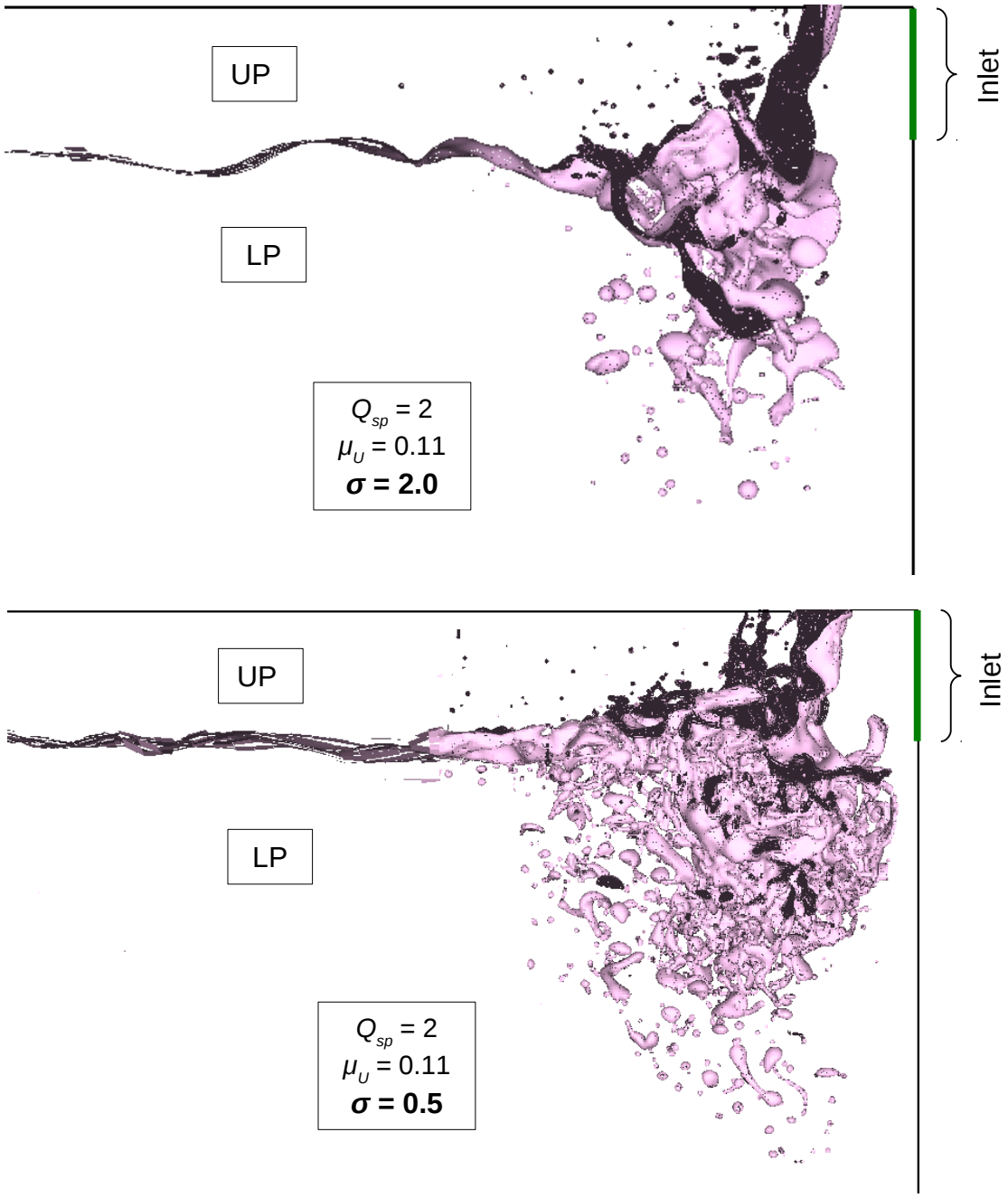

Figure 6.9. Side view of VOF surface at *ULeye* for two cases corresponding with snapshots in Figs. 6.10 and 6.11.

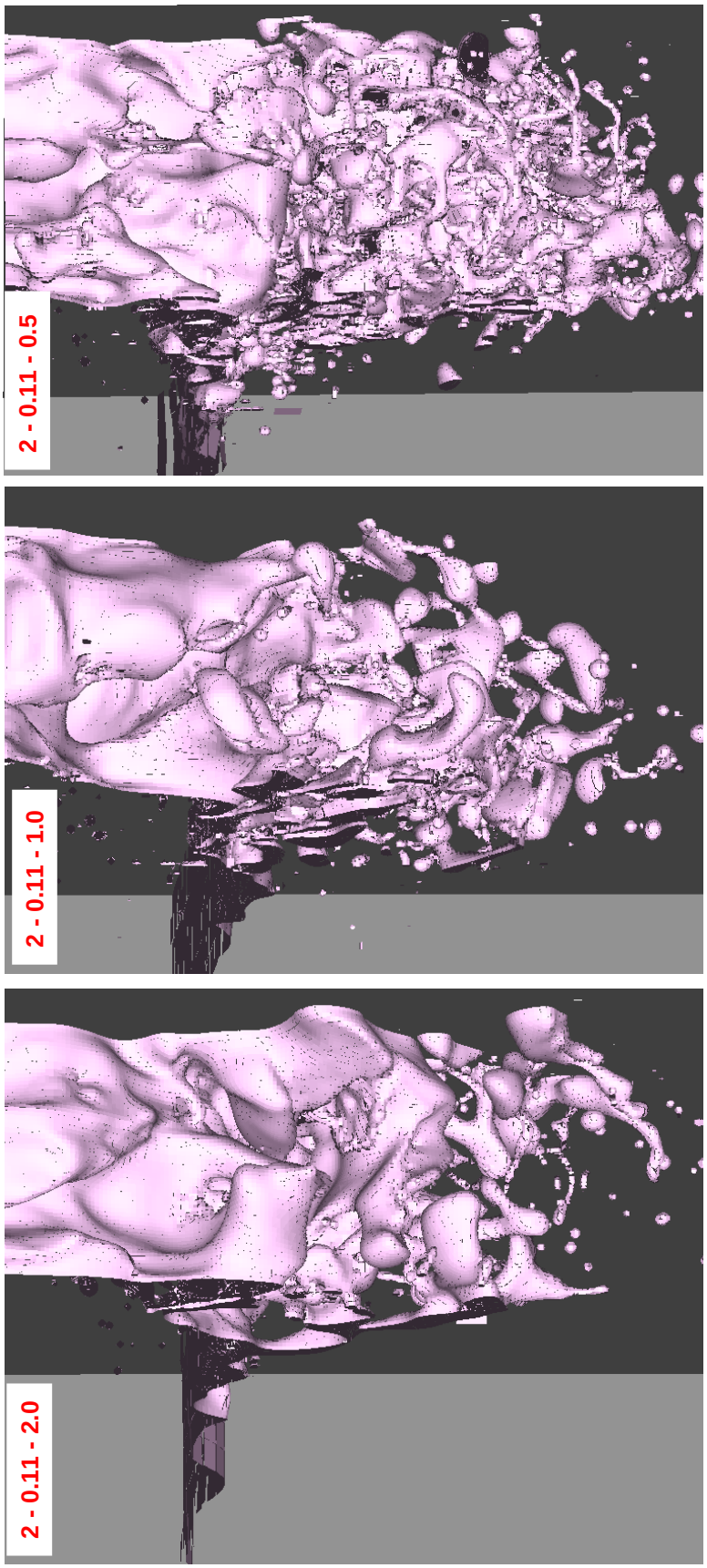

Figure 6.10. Snapshots of VOF surfaces at *ULeye* viewed at an angle from the inlet, for three values of σ at same Q_{sp} and μU. The numbers in the labels at the top left of each figure stand for Q_{sp} lpm/ton, μU, Pa.s and σ, N/m, respectively.

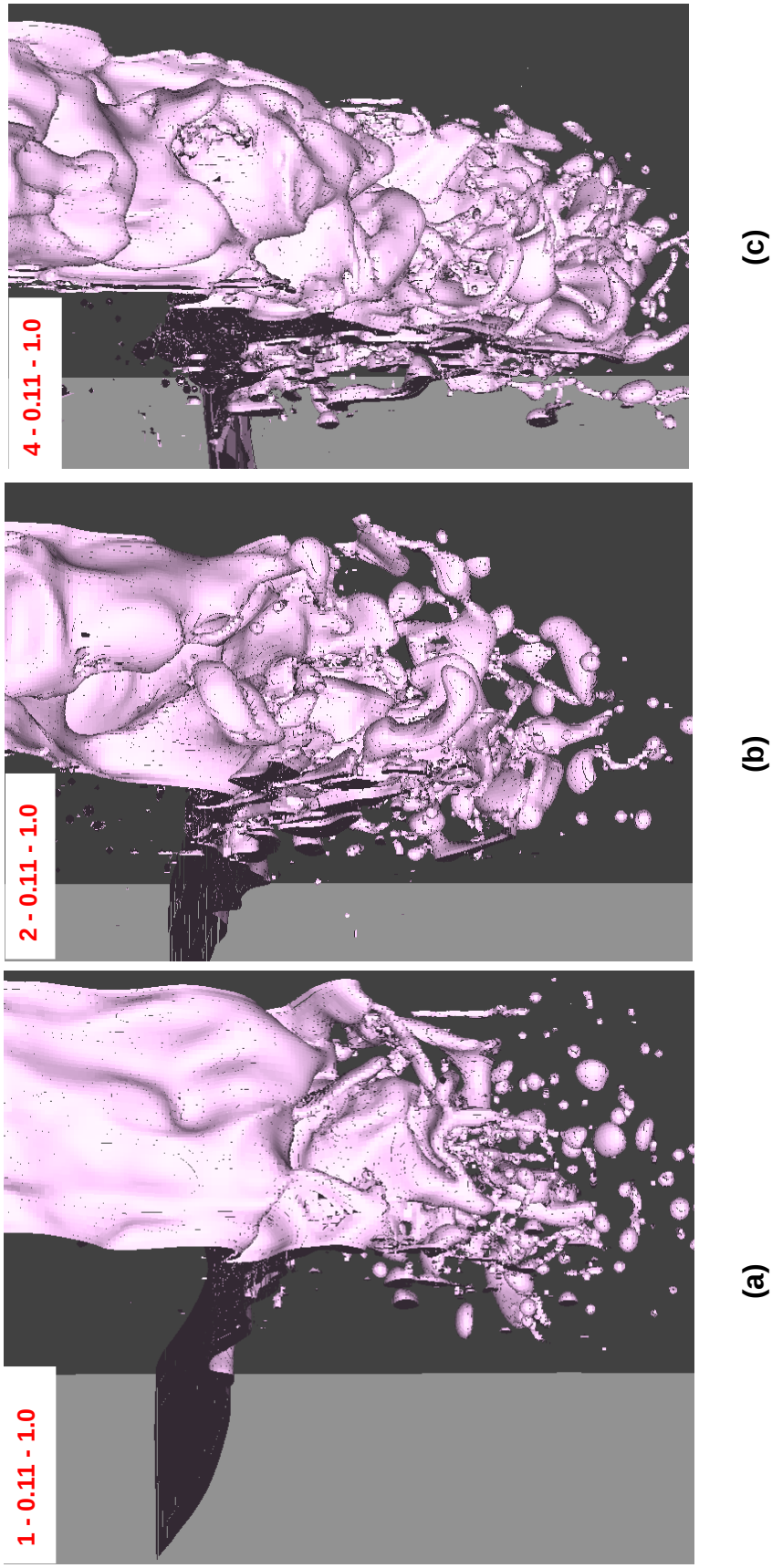

Figure 6.11 Snapshots of VOF surfaces at *ULeye* viewed at an angle from the inlet for three values of Q_{sp}. The numbers in the labels at the top left of each figure stand for Q_{sp} lpm/ton, μU, Pa.s and σ, N/m, respectively.

6.2.3 Effect of Length Scale Factor

In the LES of the aqueous model in Ch. 5 the length scale factor, *LSfac*, had a large effect on the entrainment characteristics. To see its effect in this steel slag scenario, two more length scale factors, half and double the base value of 1/10 were considered. Six simulations were performed, namely Cases 16 to 21 in Table 6.2, for three values of Q_{sp} while fixing μ_U and σ at 0.11 Pa.s and 1.0 N/m, respectively. With the addition of cases 5, 11 and 14 performed already, we now have a 3×3 matrix to see the effect of *LSfac* completely.

For each of the cases, the ratio of their entrainment rates with that of their respective base cases are compared in Fig. 6.12. With decreasing Q_{sp} the deviation from unity increases, although not significantly. The droplet size distributions shown in Fig. 6.13 shows almost no effect of *LSfac*. If we are to extrapolate the deviation from unity *vs* Q_{sp} to smaller values of Q_{sp}, we can say that the pronounced effect of *LSfac* in the cases of aqueous model may have been due to very small flow rates used in those experiments. It can be thus surmised that while turbulence fluctuations are essential to disturb the interface, the mean flow is the major driving source for entrainment.

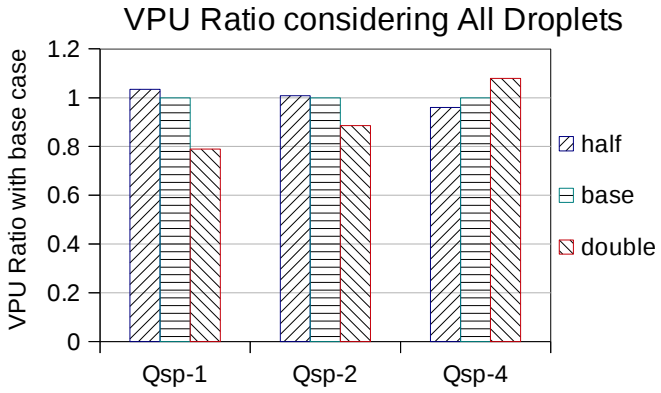

Figure 6.12. Effect of length scale factors, 1/20 (half) 1/10 (base) and 1/5 (double) on droplet size distribution for various gas injection rates (Qsp, lpm/ton) on entrainment rate

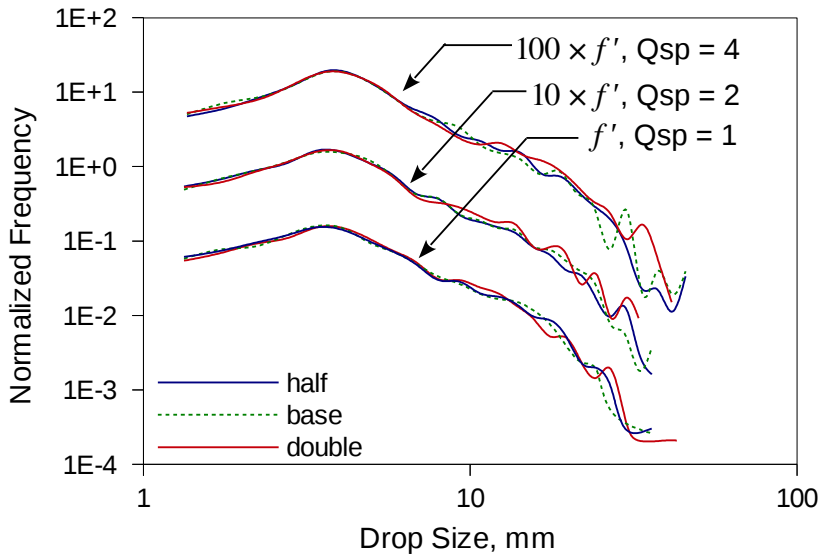

Figure 6.13. Effect of length scale factors, 1/20 (half) 1/10 (base) and 1/5 (double) on droplet size distribution for various gas injection rates (Qsp, lpm/ton) on droplet size distribution. f' is normalized frequency.

6.2.4 Effect of VOF Mesh Refinement

All simulations until now have used a constant refinement level along the VOF surface. To see the effect of increased mesh refinement along the VOF surface, the refinement level was increased by unity (to Level 7) that would decrease the smallest cell size to 0.8 mm (without changing the refinement schemes elsewhere). Interface curvature, that affects the shapes of fluid particles, increases with interfacial tension and sufficient mesh resolution is required for its precise estimation. Therefore we expect that the effect of mesh refinement will be a function of interfacial tension. Three simulation cases, namely 22, 23 and 24 in Table 6.2 were considered such that role of interfacial tension and gas injection rate on mesh refinement can be studied simultaneously by comparing with their allied cases, 4, 6 and 15 at Level 6, respectively.

Plots of *VPU* and d_{32} of cases at two VOF refinement levels (7 and 6) are shown in Figs. 6.14 (a) & (b). The entrainment rate is not significantly affected on the whole while the Sauter mean diameter shows some significant changes at σ = 2.0. However, the droplet size distributions plotted in Fig. 6.15 show marked differences between the two refinement levels,

wherein more finer droplets are produced with increased VOF mesh refinement. This is to say that while the overall statistics are somewhat grid independent, the finer statistics are not quite resolved.

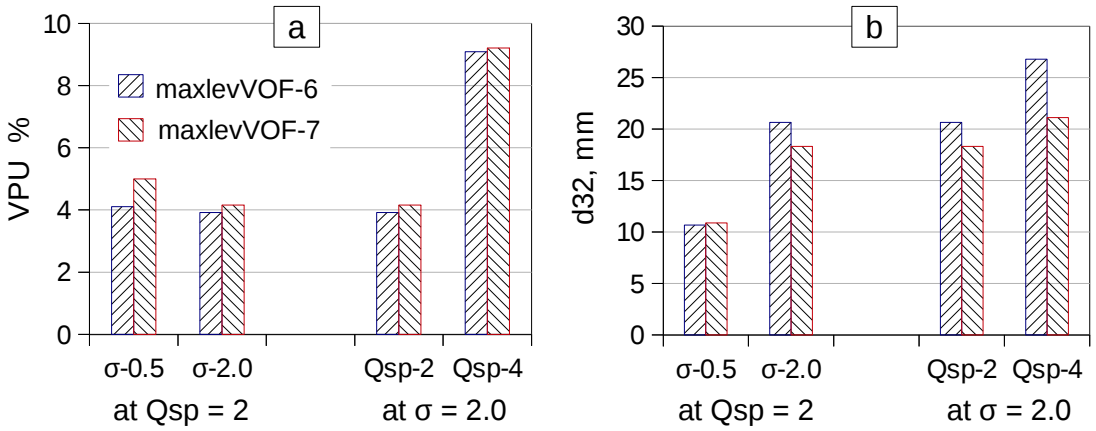

Figure 6.14. Comparison of (a) Entrainment rate (VPU) and (b) Sauter mean diameter (d32) of cases at VOF refinement level of 6 and 7, including all droplets.

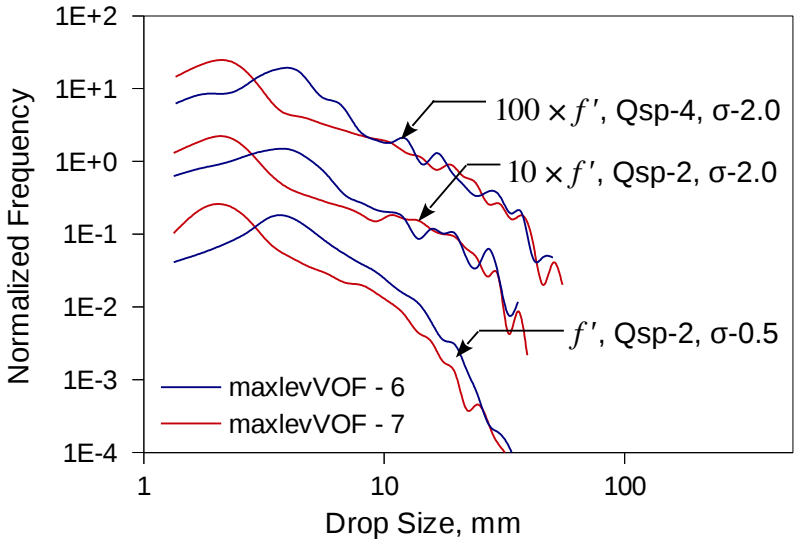

Figure 6.15. Effect of mesh refinement along the VOF surfaces on droplet size distribution. 'maxlevVOF' is the mesh refinement level along the VOF specified in Gerris simulations

6.2.5 Effect of Slag Thickness

Two more LESs were performed, namely Cases 25 and 26 in Table 6.2, with half and 1.2 times the base slag thickness, h_U, while fixing $Q_{sp} = 2$, $\mu_U = 0.11$ and $\sigma = 1.0$. Actually, separate QSP-RANS should be performed with modified slag thicknesses to generate the input to the LES inlet, because the eye radius varies with slag thickness [from Eq. (4.36)] which also changes the velocity profile for the LES inlet. But, presently, only the velocity profile corresponding to the base slag thickness has been used for all cases. Therefore the R_{eye} values for Cases 25 and 26 cannot be found using the relations given by Eqs. (4.36) and (4.38) to scale the entrainment rate in Eq. (6.6); instead, they were obtained by ensemble averaging interface locations from several snapshots of corresponding LESs (values given later in Table 6.3). The VPU thus computed is plotted against h_U in Fig 6.16, along with the plot of 'un-scaled' and 'un-normalized' entrainment rate $(\dot{V})$; a strong linear trend in $\dot{V}$ and the lack of such in VPU is seen. Interestingly when VPU is plotted against A^{nom}_{ULeye} [defined by Eq. (6.4)] a linear trend is displayed. This shows that entrainment rate in the cylindrical vessel (VPU) varies with A^{nom}_{ULeye} whereas entrainment rate in the thinslice $(\dot{V})$ varies with h_U.

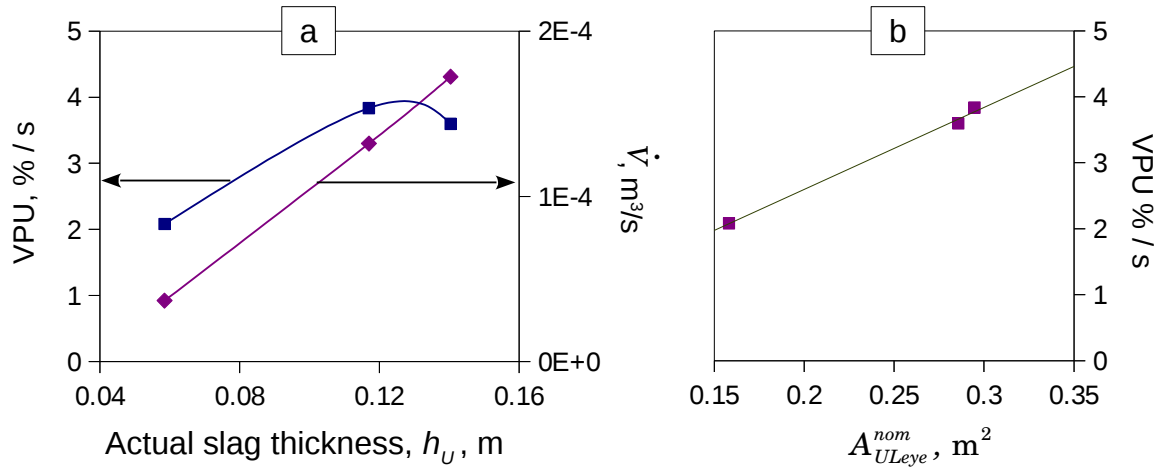

Figure 6.16. Effect of slag thickness on entrainment rate for Q_{sp} = 2, μ_U = 0.11, σ = 1.0. See text for details.

Figure 6.17 shows snapshots of VOF surfaces in the LES; the degree of entrainment is seen to increase with h_U. The increased contact length between two phases at *ULeye* has enabled increased momentum transfer between the phases and hence the increased entrainment rate. Despite the variation in entrainment rate, the droplet size distribution has not changed significantly, as seen in Fig. 6.18.

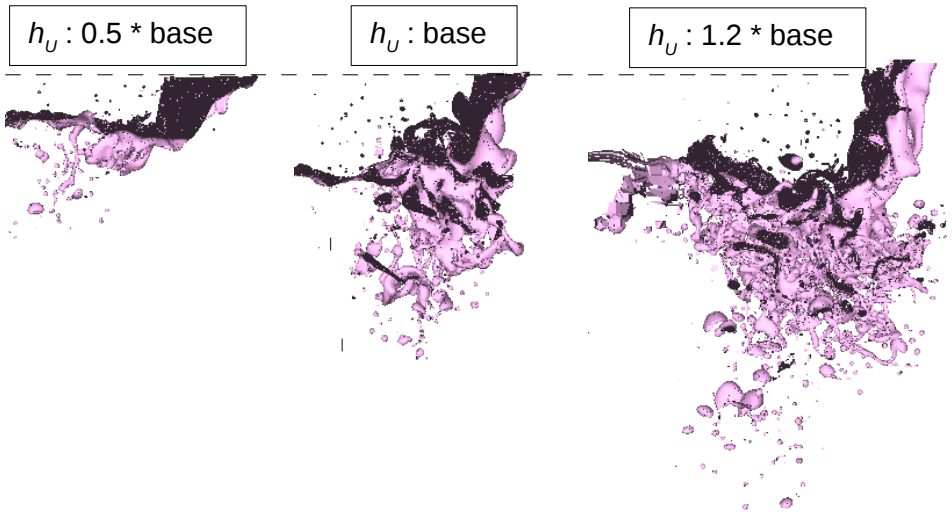

Figure 6.17. Side view of VOF surface around *ULeye*, similar to Fig. 6.9, for three slag thicknesses

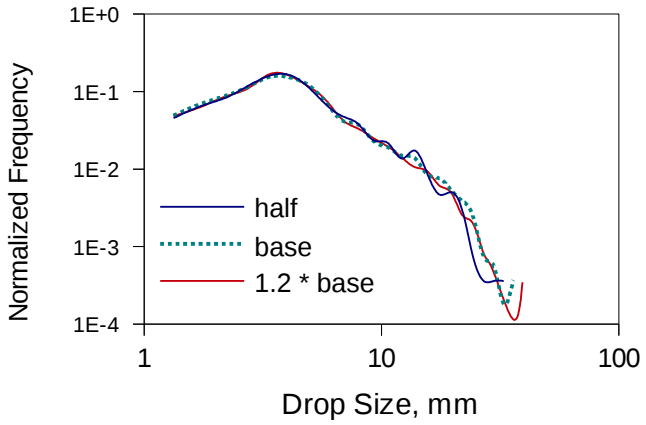

Figure 6.18. Droplet Size distribution for varying slag thickness

6.2.6 Assessment of SEM Performance

From various LES cases for a given Q_{sp}, mean velocities, $\langle u \rangle$ and $\langle v \rangle$ and Reynolds stresses, $\langle u'u' \rangle, \langle v'v' \rangle, \langle w'w' \rangle, \langle u'v' \rangle$ were ensemble averaged at the inlet plane using,

$$\langle \phi \rangle = \frac{1}{N_t N_z} \sum_{i=1}^{N_t} \sum_{j=1}^{N_y} \phi_{ij}, \tag{6.7}$$

where N_z is the number of nodes in the z direction in the inlet plane and N_t is the number of time instances. The LES output of mean velocities compared with that of the QSP-RANS input in Fig. 6.19 show that Gerris has modified the mean velocities to satisfy the continuity, more at the lowest Q_{sp}. However the relative difference in the overall mean of norm of mean velocity $\left(\sqrt{\langle u \rangle^2 + \langle v \rangle^2}\right)$ between QSP-RANS and LES is less than 5% for all Q_{sp}, which is to say that although the mean velocity profile is altered somewhat, the net momentum input is not altered significantly.

Similar comparison of Reynolds stresses in Fig. 6.19 show that the discrepancies between the LES output and QSP-RANS input are significant at the lowest Q_{sp} and that decreases with increasing Q_{sp} except for $\langle u'u' \rangle$. These discrepancies are due to the modification of instantaneous velocities to satisfy the continuity, as mentioned above. However since the entrainment characteristics are not strong functions of turbulence characteristics, as demonstrated in Sec. 6.2.3 and that the mean velocities are reproduced fairly well, the SEM based inflow generation can be remarked as satisfactory.

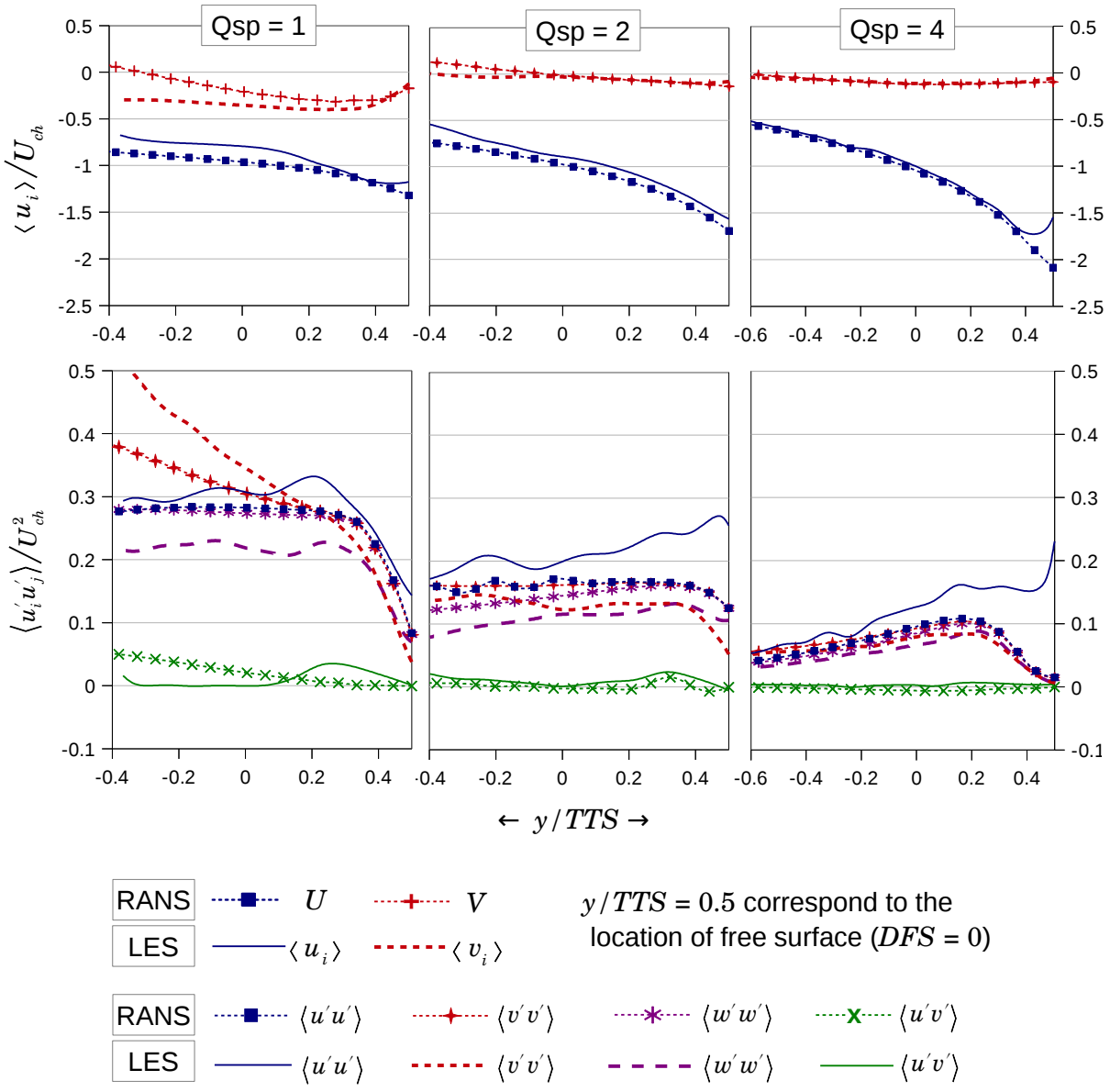

Figure 6.19. Mean velocities, $\langle u_i \rangle$ and Reynolds stresses, $\langle u_i' u_j' \rangle$, ensemble averaged at LES inlet compared against those extracted from QSP-RANS to supply inlet conditions to the LES domain. $U_{ch} = \overline{v}_{RANS}$, defined by Eq. (6.3). The relative difference in the line average of velocity norm between LES and QSP-RANS is less than 5% for all Qsp. Common y-axis and y-axis labels.

6.3 Average Velocity Profiles Across *ULeye*

Instantaneous velocities, u, v, w were extracted from Gerris simulation outputs (post-processing), for 10 to 20 time instances, in a small rectangular box surrounding *ULeye*. This box is marked (schematic) in Fig. 6.20 and it extends the whole thickness of the thin slice. Based on the nearest distance to VOF cells (of *ULeye*) for each node in that box, all collected velocities were sorted and mean and standard deviation statistics were computed. The details and the necessary codes to process the Gerris simulation outputs are attached in Appendix D.4. Profiles of ensemble average velocities, $\langle u \rangle$ and $\langle v \rangle$ †, thus obtained are plotted against η, the normal distance to *ULeye* such that $\eta < 0$ is *UP*, $\eta > 0$ is LP and $\eta = 0$ is at *ULeye*.

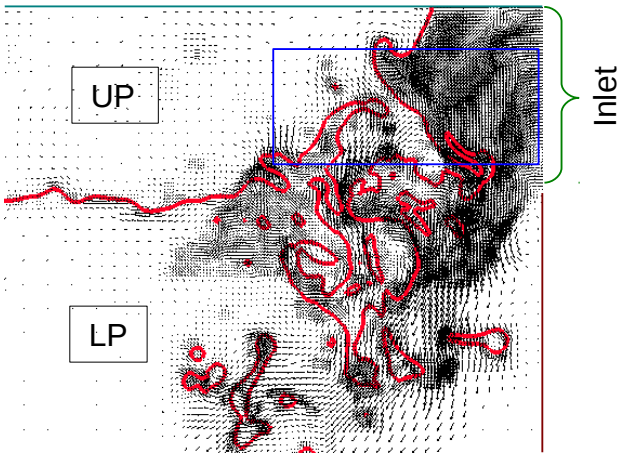

Figure 6.20. Snapshot of LES at certain *z*-plane showing a rectangle surrounding the VOF surface (red lines), represents the domain volume where the velocities were extracted for finding the average velocity profile across *ULeye*

Figure 6.21 has such profiles for various Q_{sp} at $\mu_U = 0.11$ and $\sigma = 1.0$. The horizontal flow entering the LES inlet must be impeded by and directed downward at *ULeye*. This feature is seen in the plots in Fig. 6.21 that shows vanishing horizontal velocities near *ULeye* and increasing vertical velocities in LP as *ULeye* is approached. However in profiles of all cases there is a kink in velocity immediately next to the interface in the *UP*, the reason for which is not clear.

† As expected, $\langle w \rangle$ for all cases was negligible and hence excluded from further analyses.

The standard deviation at each location is also shown for each point in those charts (the length of error bar-like is twice the standard deviation). Close to the interface the standard deviation values are as large as their corresponding mean velocities which is not surprising given the large fluctuations in the two phase interface shown in snapshots of VOF surfaces in the preceding sections. Despite the fluctuations and the gross averaging procedure, the velocity profiles being continuous and physically meaningful is remarkable.

For the same velocities in Fig. 6.21, velocity norm, $v = \sqrt{\langle u \rangle^2 + \langle v \rangle^2}$, was computed and plotted in Fig. 6.22 which also has plot of the velocity vectors for various Q_{sp}. For each $v(\eta)$ profile, the mean of v in LP side was obtained from†,

$$\bar{v}_L = \frac{1}{\eta_{max}} \int_0^{\eta_{max}} v \, d\eta \tag{6.8}$$

where $\eta_{max} \approx 0.05$ m in all the profiles. The $\bar{v}_L$ values are shown in the respective labels in Fig. 6.22 and are seen to increase linearly with Q_{sp}.

Similarly, $v(\eta)$ profiles were obtained for varying interfacial tension and slag viscosity for $Q_{sp} = 2$ and are plotted in Figs. 6.23 (a) and (b), respectively and the $\bar{v}_L$ values are shown in their respective labels. Despite having the same input momentum (at the LES inlet) $\bar{v}_L$ has decreased with increase in σ. Since $VPU \propto 1/\sigma$ (Sec. 6.2.1), we infer that entrainment occurs at the expense of LP momentum. On the same lines, the weaker influence of slag viscosity on VPU (Sec. 6.2.1) is manifested as smaller differences in $\bar{v}_L$ in Fig. 6.23b.

† integrals evaluated using trapezoidal rule

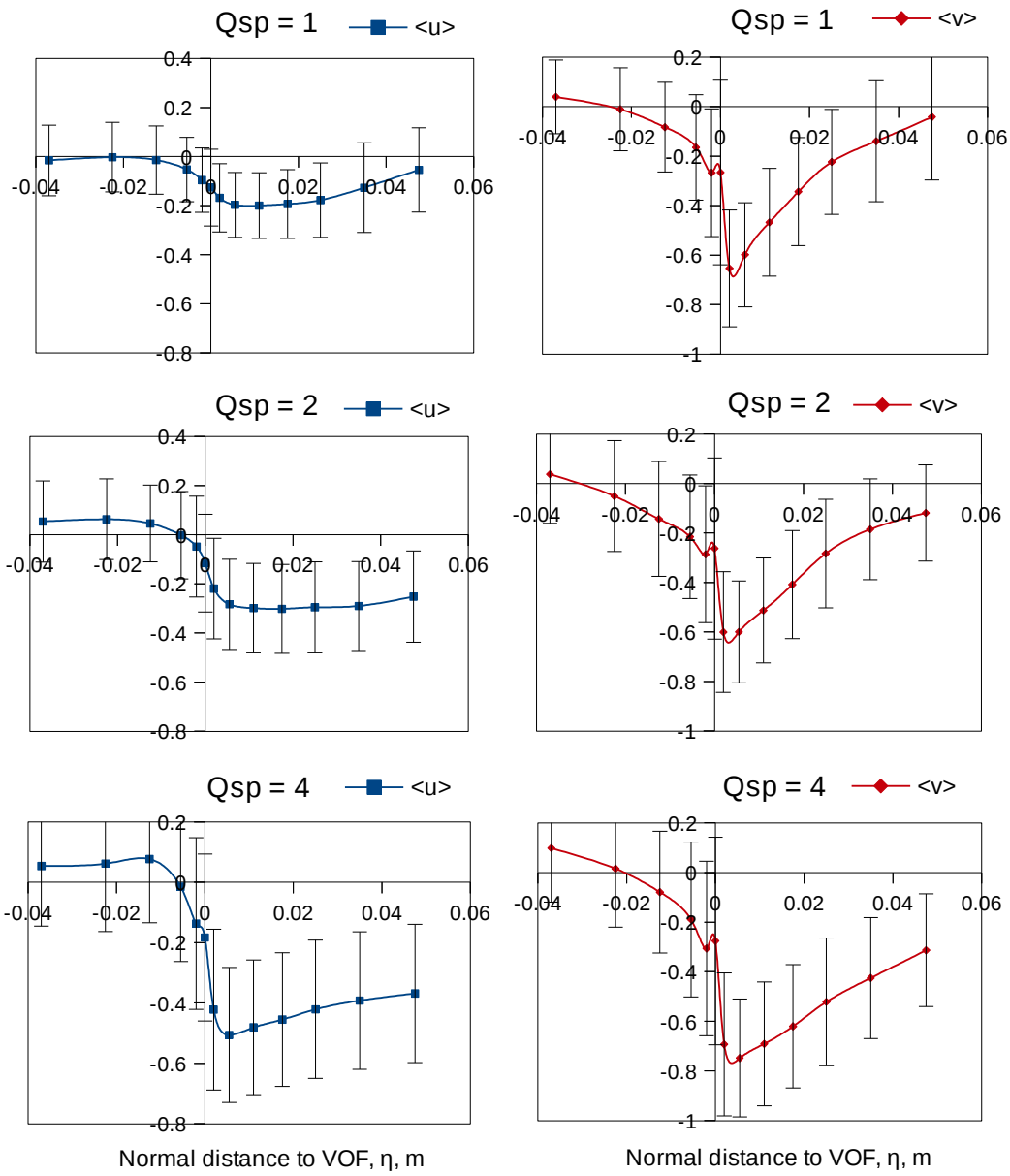

Figure 6.21. Profiles of ensemble averaged velocities, $\langle u \rangle$ and $\langle v \rangle$ across η for μ_U = 0.11 and σ = 1.0. $\eta < 0$ is slag phase and $\eta > 0$ is metal phase. Note that the error bar-like lines are not standard error, but standard deviation, to show the variability of the values sampled. The full length of these lines equal to twice the standard deviation of values at their respective η .

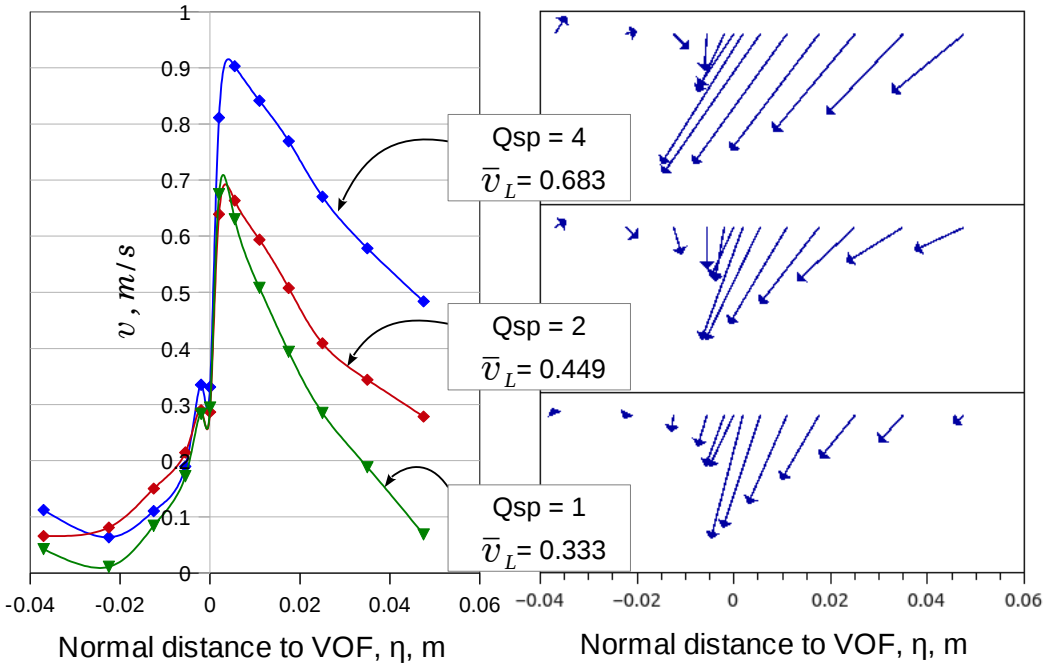

Figure 6.22. Left: Profiles of norm of ensemble averaged velocities, $v = \sqrt{\langle u \rangle^2 + \langle v \rangle^2}$, across η, for various gas injection rates (Qsp, lpm/ton) at μ_U = 0.11 and σ = 1.0.
Right: Plot of $\langle u \rangle$ and $\langle v \rangle$ vectors across η. $\eta < 0$ is UP and $\eta > 0$ is LP.

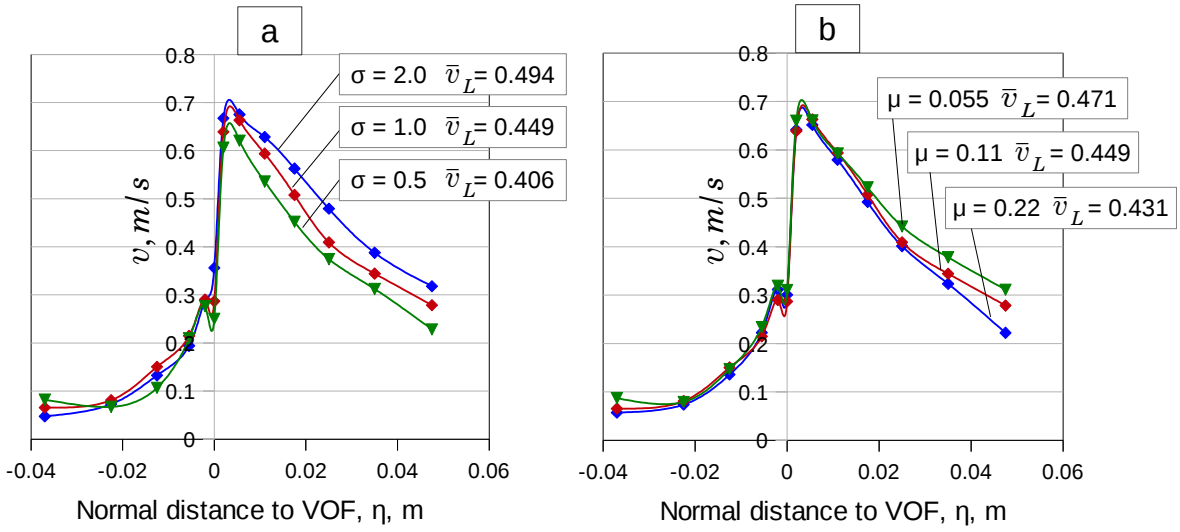

Figure 6.23. Profiles similar to Fig. 6.22 but for (a) varying interfacial tension (σ, N/m) at μ_U = 0.11 and (b) varying slag viscosity (μ, Pa.s) at σ = 1.0, all at Q_{sp} = 2 lpm/ton.

6.4 Entrainment Rate Correlations

The $v(\eta)$ profiles were obtained for further more cases in Table 6.2 and were averaged according to Eq. (6.8) and are tabulated in Table 6.3. From these values, for 9 cases of varying Q_{sp} and σ at μ_U = 0.11, the following correlation for VPU was deduced by linear regression,

$$VPU = 100.18\left(\frac{\bar{v}_L A_{ULeye}^{nom}}{\sigma^{0.25}}\right) - 0.062\,;\ R^2 = 0.995 \tag{6.9}$$

and is plotted in Fig. 6.24a, where, A_{ULeye}^{nom} is defined by Eq. (6.4).

Four more LES cases were performed, namely Cases 27 to 30 in Table 6.2, with half and twice the base value of slag density and gravity, at Q_{sp} = 2, σ = 1.0 and μ_U = 0.11, to see the effect of these parameters on entrainment rate. Again, as discussed in Sec. 6.2.5, the RANS velocity profile corresponding to the base case has been used for the LES inlet of all cases, although separate RANS simulations are required, since the variations in slag density and gravity affects the steady state slag eye radius and thickness. So to scale VPU, R_{eye} values were obtained from LES, same as discussed in Sec. 6.2.5 and for h_U, the base value was taken†. The results tabulated in Table 6.3 show that for varying density, despite significant variations in the resulting $\bar{v}_L$, R_{eye} and θ_{ULeye}, VPU has only changed mildly; whereas, the gravity variations have significantly affected VPU and that $VPU \propto 1/g$. Now, from all the cases in Table 6.3, a new correlation for VPU was deduced as,

$$VPU = 81.16\left[\frac{\bar{v}_L\sqrt{A_{ULeye}^{nom}}}{\left(g\,\Delta\rho\,\sigma\right)^{0.25}}\right] - 0.460;\ R^2 = 0.985 \tag{6.10}$$

The correlation plotted in Fig. 6.24b well represents a wide variety of conditions.

† this approximation is due to the inability to estimate actual h_U for the cylindrical ladle, based on the changes in the thinslice–LES domain. Such an approximation is less serious for h_U than R_{eye} because h_U changes slower than R_{eye} and also that from Eq. (6.6), increase in VPU is slower with h_U than with R_{eye}.

Table 6.3. Values for selected cases with case numbers corresponding to Table 6.2

Case No.	VPU % / s	$\overline{v}_L$ m/s	σ N/m	Q_{sp} lpm/ton	h_U m	R_{eye} m	θ_{ULeye} degree	ρ_U kg/m^3	g m/s^2
4	0.986	0.406	0.5	2.0	0.117	0.336	25	2800	9.81
5	0.960	0.449	1.0						
6	0.840	0.494	2.0						
10	0.300	0.270	0.5	1.0	0.110	0.249	15		
11	0.374	0.333	1.0						
12	0.311	0.375	2.0						
13	2.272	0.596	0.5	4.0	0.134	0.448	30		
14	2.239	0.683	1.0						
15	1.833	0.698	2.0						
25	0.520	0.474	1.0	2.0	0.058	0.332	35		
26	0.899	0.445			0.140	0.294	15		
27	0.996	0.486			0.117	0.285	15	1400	
28	1.085	0.368				0.331	30	5600	
29	0.967	0.396				0.325	20	2800	4.9
30	0.565	0.511				0.278	15		19.6

* R_{eye} for cases 25 to 30 were obtained based on the location of *ULeye* at free surface in the LESs, ensemble averaged from more than 10 snapshots; whereas for the rest of the cases, it was obtained from Eq. (4.36), which was used in the RANS simulations.
* For all the cases, θ_{ULeye} was obtained from LES's by ensemble averaging various snapshots of approximate inclination of *ULeye*.
* The values of h_U were initially calculated using θ_{ULeye} = 40° for the RANS simulations and that was used for the LESs.

From the LES results it was well established that $VPU \propto 1/\sigma$. However the particular form of the group, $\left(g\Delta\rho\,\sigma\right)^{0.25}$, in Eq. (6.10) was inspired from its recurrence in various correlations in the literature, relating it to various forms of critical velocity for onset of entrainment, discussed in Sec. 2.1.1; similar to that in the literature, the velocity scale in Eq. (6.10) is directly proportional to $\left(g\Delta\rho\,\sigma\right)^{0.25}$. The differences between Eq. (6.10) and the literature correlations are that the former, is at its best without a $1/\rho^2$ factor to $\left(g\Delta\rho\,\sigma\right)^{0.25}$, has an interfacial area term, A_{ULeye}^{nom}, and an intercept; it is these differences that describe the

entrainment process beyond the critical conditions. Although obtained only at μ_U = 0.11 and with several other limitations and approximations, both in the LESs and the procedure to obtain $\bar{v}_L$, Eq. (6.10), still able to represent a wide variety of conditions shows that the physics of the entrainment process is well captured by the LESs, while also revealing the functional form of relationship between scaled entrainment rate and various physical properties.

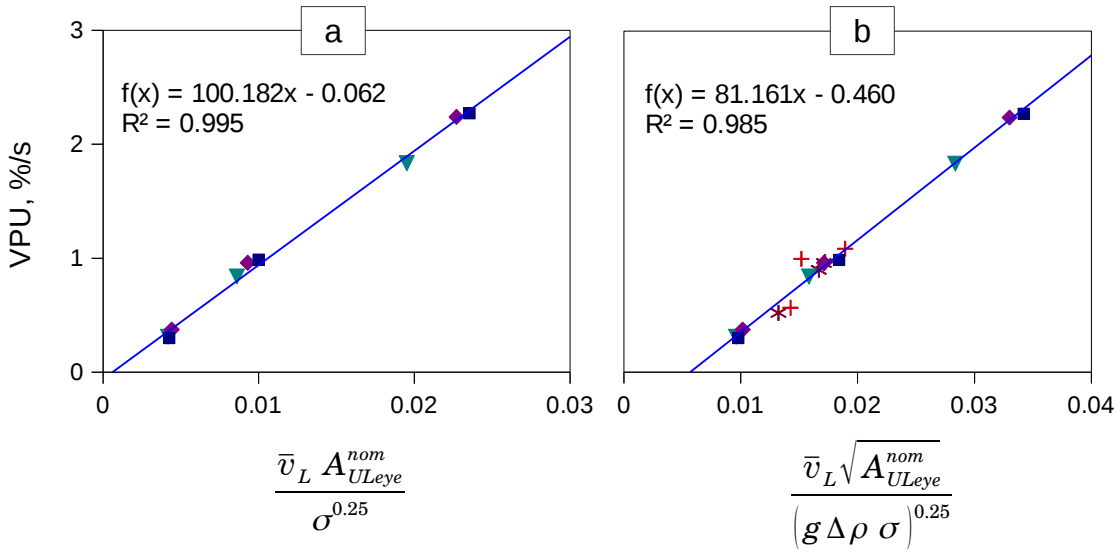

Figure 6.24. Plot of entrainment rate (VPU, %/s) correlations for μ_U = 0.11 Pa.s. Table 6.3 has values for each point in those charts. Common y-axis.

Critical Gas Flow Rate: The intercept in Eq. (6.10) shows the existence of a critical velocity, through $\bar{v}_L$, when *VPU* is zero. It is motivating to correlate Q_{sp} with $\bar{v}_L$ (say, using the values in Table 6.3) and extrapolate to find the critical gas injection rate at critical $\bar{v}_L$. However such attempts gave larger values of critical Q_{sp} for smaller σ while only the converse is true, probably because such $Q_{sp} - \bar{v}_L$ correlations are not valid close to critical conditions. However such calculations showed that the critical gas injection rate should be around 0.5 lpm(STP)/ton or that $Q \approx$ 90 lpm.

6.5 Summary

Multiphase LESs for various parametric combinations were performed to study slag entrainment relevant to steelmaking ladles. The role of some parameters can be ascertained as

- Entrainment rate is predominantly affected by the gas injection rate with smaller role of interfacial tension.
- The droplet size statistics are mainly affected by interfacial tension alone.
- Slag viscosity has only minor effect on entrainment characteristics.
- The effect of *LSfac* that was significant in aqueous model simulations (Ch. 5) was found to be very limited here. This suggests that the role of turbulence is limited to disturbing the interface while the mean flow properties play the dominant role in causing entrainment. This investigation also clarifies that the strong role of *LSfac* on entrainment rate in aqueous model simulations (Ch. 5) was due to the small flow rates in the corresponding experiments.
- Scaled entrainment rate (*VPU*) is found to linearly vary with nominal area at *ULeye*, for a cylindrical ladle (3D), which also means that thicker slag has higher entrainment rate.
- The increased mesh refinement along the VOF surface greatly affected the droplet size distribution although only to lesser extent on *VPU* and Sauter mean diameter.
- Ensemble averaged velocity profiles were extracted by post-processing the LESs and average LP velocity near *ULeye* ($\overline{v}_L$) were estimated from these profiles. These velocities showed a stronger role of LP momentum on entrainment.
- Upon relating *VPU* with $\overline{v}_L$ and physical properties, a strong correlation resulted, with a form similar to that in the literature describing critical conditions for onset of entrainment, which shows that the physics of the entrainment process is well captured by the LESs. It also shows the functional form of various parameters affecting the entrainment rate.

7. Lagrangian Particle Tracking

The next step in the entrainment simulations is to estimate the residence time of slag droplets entrained in the metal phase. This requires tracking of individual droplets from a likely point of their origin in the flow field that they are entrained. The flow field is the 2D QSP-RANS solution in the ladle domain that was used to generate inlet conditions for the multiphase LES. From the forces acting on a particle/droplet and by the nature of its interaction with the flow field, its motion is computed as it travels and hence this method is called 'Lagrangian Particle Tracking'. By tracking a statistically large number of droplets for every droplet size, a distribution of residence times is obtained, whose average for various droplet sizes gives the mean of residence times. The Lagrangian particle tracking (LPT) module of this thesis is two dimensional (spatially) and is constructed using *C* programming language.

Some important assumptions in the model are as follows.

- The particle motion is axisymmetric as was the QSP-RANS flow field
- From LES simulations it was observed that near the eye region, where the droplets concentration was the highest, the droplet-droplet interaction was practically non-existent. The lack of interaction was assumed to prevail in the rest of the ladle.
- No droplet breakup.
- All droplets are spherical.
- Droplets are absorbed as soon as they reach the slag metal interface, *ULflat*.

Throughout the Chapter, 'fluid' refers to the continuous phase (liquid metal) and 'particle' refers to the fluid particle (slag droplet) unless stated otherwise.

7.1 Particle Tracking Equations

Some of the common variables in the following discussion are ρ_F and ρ_P, the fluid and particle densities, respectively, $\boldsymbol{U}$, the RANS mean velocity, $\boldsymbol{U}_F$ and $\boldsymbol{U}_P$, the instantaneous fluid and particle velocities, respectively and $d_P = (6V_P/\pi)^{1/3}$ is the equivalent particle diameter defined based on the particle volume V_P.

The basis of LPT is the Newton's second law, that the particle acceleration is due to sum of forces acting on it,

$$m_P \boldsymbol{a}_P = \sum \boldsymbol{F}_P \tag{7.1}$$

where m_P and $\boldsymbol{a}_P$ are the mass and acceleration of the particle respectively and $\boldsymbol{F}_P$ are the forces acting on the particle consisting of buoyancy, drag, force due to pressure gradient of fluid, added mass and other forces such as the lift forces, Basset history forces; the 'other forces' are *not* considered in the present work. The buoyancy force has a simple expression,

$$\boldsymbol{F}_G = (\rho_F - \rho_P) V_P \boldsymbol{g} \tag{7.2}$$

Another simple force is that due to pressure gradient in the fluid on the particle, expressed as,

$$\boldsymbol{F}_{PG} = \rho_F V_P \frac{D\boldsymbol{U}}{Dt} \tag{7.3}$$

where $D\boldsymbol{U}/Dt$ is the acceleration of the fluid in Eulerian frame of reference (See Appendix E.3.2 for definition and discretization).

7.1.1 Drag Force

The drag force is expressed as,

$$\boldsymbol{F}_D = C_D \rho_F \frac{\pi d_P^2}{8} (\boldsymbol{U}_F - \boldsymbol{U}_P) |\boldsymbol{U}_F - \boldsymbol{U}_P| \tag{7.4}$$

where C_D is the drag coefficient. The drag coefficient has been found to depend on particle size, relative velocity ($|\boldsymbol{U}_F - \boldsymbol{U}_P|$), the nature of particle, solid or fluid and presence of impurities in the fluid particle interface.

Numerous studies have been conducted to find the terminal velocity of *fluid* particles

rising (or falling) in stagnant fluid media, for various combination of two fluid properties. These have been summarized succinctly by three dimensionless numbers namely particle Reynolds number (Re_P), Eotvos number (Eo) and Morton number (Mo) (Clift *et al*, 1978) defined as,

$$Re_P = \frac{\rho_F U_{term} d_P}{\mu_F}, Eo = \frac{g \Delta\rho d_P^2}{\sigma}, Mo = \frac{g \mu_F^4 \Delta\rho}{\rho_F^2 \sigma^3} \tag{7.5}$$

where, U_{term} is the particle terminal velocity and $\Delta\rho = |\rho_F - \rho_P|$. In the present context, the ranges of values for the dimensionless groups are summarized in Table 7.1.

Table 7.1. Ranges of dimensionless numbers for various ranges of properties considered in the present work; the limits are highlighted in bold

σ, N/m	0.5		1.0		2.0	
d_P, mm	0.8	40	0.8	40	0.8	40
Eotvos (Eo)	0.013	**132**	0.007	66	**0.003**	33
Morton (Mo)	**4×10^{-12}**		5×10^{-13}		**6×10^{-14}**	

Since in all those studies, the drag force was balanced by the buoyancy force, the drag coefficient can be found from,

$$C_D = \frac{4}{3} \frac{g d_P}{U_{term}^2} \frac{\Delta\rho}{\rho_F} \tag{7.6}$$

This drag coefficient has been found to be affected by particle shape and presence of internal circulation in the particle. The particle shape is dictated by the combination of Eo and Mo. The internal circulation, which is caused by the momentum transfer from fluid to particle, is impeded by higher density ratio (ρ_P/ρ_F) and viscosity ratio (μ_P/μ_F) and increased interfacial tension due to interface contamination, thereby increasing the drag coefficient (Clift *et al*, 1978).

The correlations for C_D have been refined over years and more recent of them are

summarized in the reviews of Loth (2000), Sokolichin *et al* (2004) and Kolev (2012). Of them, the correlation of Tomiyama (1998) is found to apply for wide range of conditions and despite being simple. The correlation given by,

$$C_D = \mathrm{MAX}\left[\frac{24}{Re_P}\left(1+0.15\,Re_P^{0.687}\right),\ \frac{8}{3}\frac{Eo}{Eo+4}\right], \qquad (7.7)$$

$$10^{-2} < Eo < 10^{3},\ 10^{-3} < Re_P < 10^{6} \text{ and } 10^{-14} < Mo < 10^{7}$$

is plotted in Fig 7.1 and compared against experimental data for air bubbles in water. There are three drag curves in the chart: for solid sphere, for bubbles in contaminated water and for bubbles in pure water. While most of the well known drag correlations, fit any one of those curves and/or only for limited range (not discussed here, Grace *et al*, 1976, Ishii & Zuber, 1979, Johansen & Boysan, 1988, Bozzano & Dente, 2009), Tomiyama's correlation, devised as combination of independent regimes, is much better for contaminated systems.

The drag correlations discussed until now are only for particle rising (or falling) in stagnant medium. Ford & Loth (1998) studied the bubble rising in mixing layer flow for various bubble relative velocities while fixing their sizes. For each size, the bubble Reynolds number (Re_P) variation was solely due to varying relative velocity, unlike the rest of the studies in literature, where Re_P was varied due to varying sizes and their corresponding terminal velocities. The drag coefficients evaluated from their experiments are plotted as four curves in Fig. 7.2 (for each bubble diameter, 1.5 to 4.5 mm from left to right) against drag curves for particle rising in stagnant water. It is seen that C_D decreases rapidly with an increase in relative velocity and C_D decreases slowly with the increasing bubble size. It can be seen that these drag coefficients are much lower than that of the particle rising in stagnant water and use of the latter is therefore questionable. However, follow up studies (to Ford & Loth) are not seen in the literature and much of the multiphase simulation studies have used drag coefficients of particle rising in stagnant medium only!

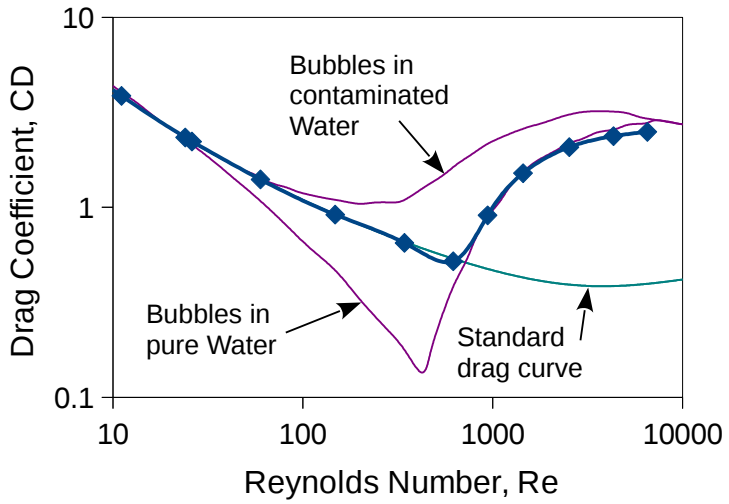

Figure 7.1. Drag correlation of Tomiyama (lines with symbols) plotted against single air-bubble rising in quiescent water and standard drag curve

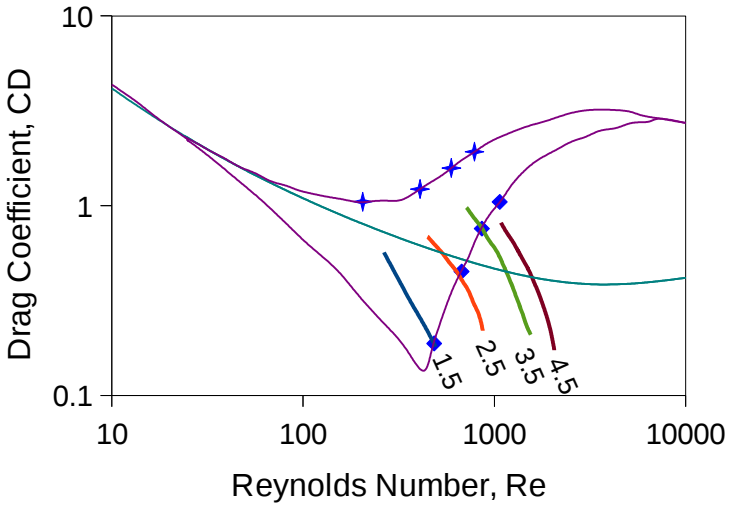

Figure 7.2. Drag coefficients of air-bubble rising in free shear layer water flow of diameters, 1.5, 2.5, 3.5 and 4.5 mm (four curves left to right) plotted against single air-bubble rising in quiescent water (Ford and Loth, 1998) and standard drag curve. Also plotted are the drag coefficients of bubbles of the same size rising in stagnant, pure water (rhombi) and contaminated water (stars) at their respective terminal velocities

7.1.2 Added Mass Force

Some portion of the force on a particle is spent on accelerating its surrounding fluid as if some extra mass is attached to the particle. This extra mass is called the added or virtual mass (Simcik *et al*, 2008) and the force to accelerate is given by,

$$\boldsymbol{F}_{AM} = C_{AM}\,\rho_F V_P \left(\frac{d\boldsymbol{U}_F}{dt} - \frac{d\boldsymbol{U}_P}{dt} \right) \tag{7.8}$$

This force becomes important whenever the particle is accelerating and acts to impede the particle motion. In Eq. (7.8) $d\boldsymbol{U}_F/dt$ is the acceleration of fluid in Lagrangian frame of reference, *i.e.*, moving with the particle (Appendix E.3.2 has the definition and discretization) and C_{AM} is the added mass coefficient. For spherical particle, C_{AM} is equal to 0.5; for ellipsoidal particle with aspect ratio (ratio of minor to major axes lengths) ranging between 1.0 and 0.25, C_{AM} varies between 0.5 and 2.4 correspondingly, as shown in Fig. 7.3. In the LESs in Ch. 6 it was observed that slag droplets are mostly ellipsoidal with less than unity-aspect ratio. However to simplify, C_{AM} was taken to be 0.5 in all the cases run in the sections ahead, although the sensitivity of results to C_{AM} will be assessed in Sec. 7.7.3.

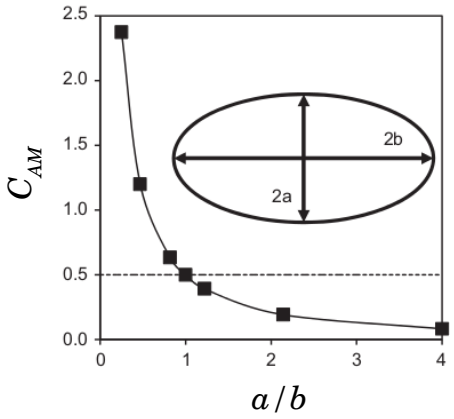

Figure 7.3. Added mass coefficient (C_{AM}) versus aspect ratio (a/b) of ellipsoidal particle whose dimensions are shown in the inset; the length of third axis (normal to paper) of the ellipsoid is equal to the major axis length (*2b*). The curve is the theoretical solution of Lamb (1932) and the points are CFD simulations of Simcik *et al* (2008) from where this figure was taken.

7.2 Time Integration of Trajectory Equations

The velocity of the particle is calculated by integrating the equation,

$$\frac{d\boldsymbol{U}_P}{dt} = \boldsymbol{a}_P = \frac{1}{m_P}\sum \boldsymbol{F}_P \tag{7.9}$$

from which the particle trajectory can be integrated from the equation,

$$\frac{d\boldsymbol{x}_P}{dt} = \boldsymbol{U}_P \tag{7.10}$$

where $\boldsymbol{x_P} = (r_P,\ z_P)$ and $\boldsymbol{U_P} = (U_{P,r},\ U_{P,z})$. Equation (7.9) can be cast as (Fluent Manual, 2009),

$$\frac{d\boldsymbol{U}_P}{dt} = \frac{1}{\tau_R}(\boldsymbol{U}_F - \boldsymbol{U}_P) + \boldsymbol{A} \tag{7.11}$$

where the first term in the RHS is due to drag force and $\boldsymbol{A}$ is the acceleration due to sum of all the other forces, *i.e.*,

$$\boldsymbol{A} = \frac{1}{m_P}\left(\boldsymbol{F}_{AM} + \boldsymbol{F}_{PG} + \boldsymbol{F}_G\right) \tag{7.12}$$

and τ_R is the particle relaxation time defined as,

$$\tau_{R,i} = \frac{2m_P}{A_P \rho_F C_D}\frac{1}{|U_{F,i} - U_{P,i}|},\quad i = r, z. \tag{7.13}$$

Equation (7.11) can be numerically solved in several ways. For the present work, three numerical integration schemes have been considered, namely (i) analytical integration (ii) implicit discretization and (iii) trapezoidal discretization (Fluent Manual, 2009) whose details are provided in Appendix E.3.1.

7.3 Verification of Trajectory Calculations in LPT code

7.3.1 Benchmark Case Description

The LPT code was verified for trajectory calculations against a few of the cases of classic numerical experiments of Maxey (1987) that investigated the settling behavior of particles in a cellular flow field. This is a convenient test case because the particle trajectory equations are exactly the same as described in Sec. 7.2 and also the flow field and the boundary conditions are simple to setup. To run the cases in LPT code, see Appendix E.4.

The domain is two dimensional (x, y), periodic in both the directions and has numerous vortex cells. Within each cell, the flow field given by (known as Taylor-Green Vortices),

$$\begin{aligned} U_x &= U_0 \sin(\pi x/L)\cos(\pi y/L) \\ U_y &= -U_0 \cos(\pi x/L)\sin(\pi y/L) \end{aligned} \tag{7.14}$$

where L is the length of a cell and U_0 is the maximum velocity. The plot of velocity vectors in a four cell domain is shown in Fig. 7.4 wherein the largest velocities occur along the cell boundaries and 'stagnant points' occur at the center and at the corners of each cell.

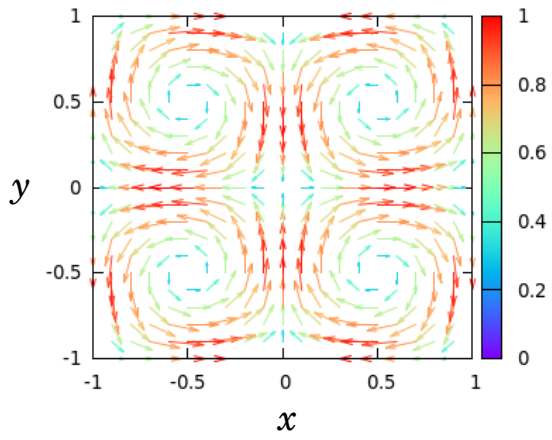

Figure 7.4. Velocity vectors of cellular flow field in the domain of four cells; vector coloured according to their magnitude

All the cases computed by Maxey used the Stokes drag law, the appropriateness of which is not important in this verification exercise. The dimensionless groups used as parameters for the numerical experiments are,

$$R = \frac{1}{\gamma + 0.5}, A = \frac{6\pi\mu\, r L}{(m_P + 0.5\, m_F)\, U_0}, W = \frac{(m_P - m_F) g}{6\pi\nu\, r\, U_0},$$
$$Q = \frac{W}{(1/R - 1.5)}, B = \frac{2A}{R} \text{ where, } \gamma = \frac{\rho_P}{\rho_F} \tag{7.15}$$

of which R, related to the density ratio γ, has been extensively varied.

7.3.2 Present Work

The computations of the present work has the domain with dimensions $[-L, L] \times [-L, L]$ as against Maxey's that has L replaced by L/π †. Due to the simplicity of the domain, periodic BCs were implemented separately bypassing the '`verify boundary condition`' function call of the LPT code. Drag coefficient was taken to be $24/Re_P$ to obtain Stokes drag law, where $Re_P = |U_i - U_{P,i}| d_P / \nu_F$ and $i = x,\ y$.

Three numerical integrations schemes were tested. All computations were run for a dimensionless total time of 200‡, sufficiently long to approach steady state. The following sub-sections presents two groups of verification cases divided based on the particle-fluid density ratio that plays major role on the effect of fluid inertia on the particle. Note that for $R < 2/3$, $\gamma > 1$ and for $R \geq 2/3$, $\gamma \leq 1$.

7.3.2.1 Fluid Inertia Affected

Two cases of Maxey were computed that has $Q = 1.25$ and $B = 10\pi$ as constants and for $R = 0.64$ $(\gamma = 1.06)$ and $R = 1.0$ $(\gamma = 0.5)$. The particle distributions of Maxey for some finite time are shown in Fig. 7.5 and steady state distributions of present work are shown in Fig. 7.6. As noted by Maxey, the particles have tendency to either follow some isolated path through the cells or collect at equilibrium points which need not be necessarily the 'stagnation points' (centre and corners of a cell).

† This must be considered when comparing the dimensionless numbers in Eq. (7.15) between the present and Maxey's works.

‡ Dimensionless time is time scaled by (L/U_0).

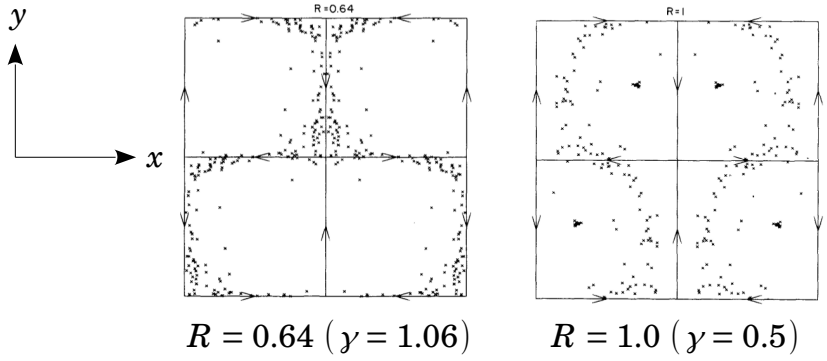

Figure 7.5. Particle positions at dimensionless time, $\tilde{t} = 100$ from computations of Maxey (1987). Gravity is along -y.

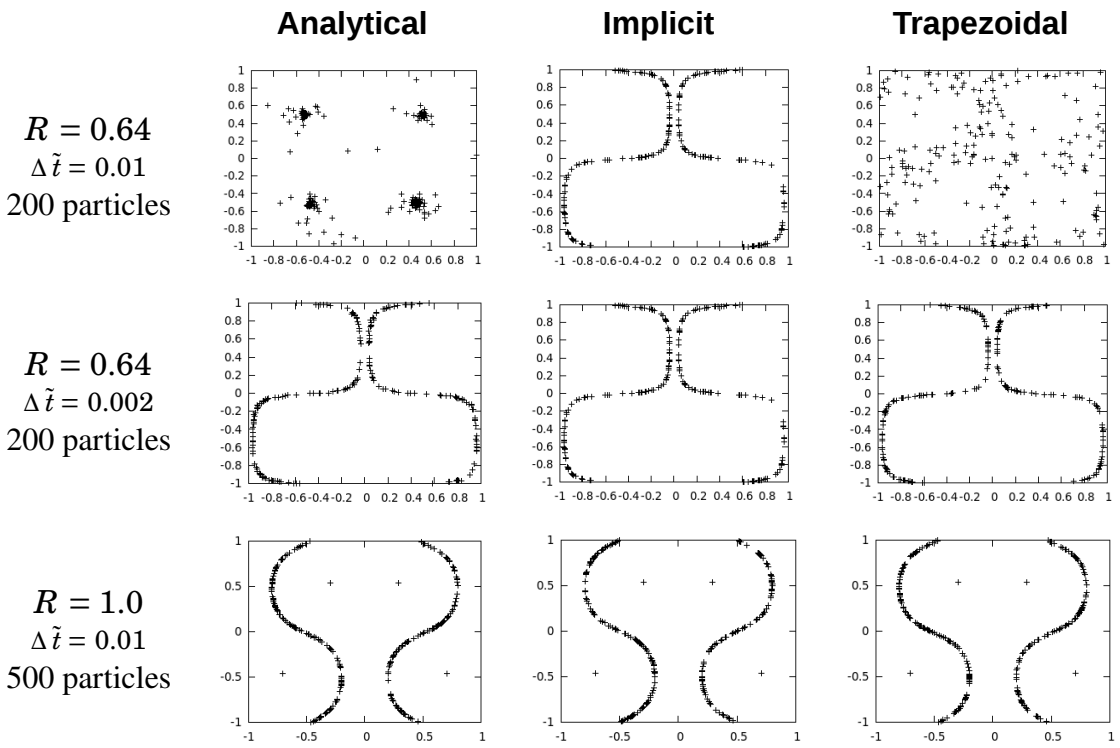

Figure 7.6. Steady state particle positions for various density ratios, integration schemes and dimensionless time step sizes ($\Delta\tilde{t}$). $(\text{abscissa}, \text{orindate}) = (x, y)$. Gravity is along -y.

The cases of $R = 0.64$ with finer time step size and the cases of $R = 1.0$ agree well with the distributions of Maxey's cases. (Note that the computations of Maxey are yet to reach steady state). The implicit integration scheme appears to give time step size independent result as compared to the other two schemes.

7.3.2.2 Fluid Inertia Independent

Under this range, the results presented in Maxey (1987) enable a quantitative comparison between Maxey's computation and the present work. Several cases were run to compute the average settling velocity for varying values of W [Eq. (7.15)], for $R = 10^{-10}\ (\gamma \to \infty)$ and $R = 0.4\ (\gamma = 2)$ while setting $A = 2\,\pi$ as constant. Results of various cases consisting of the three integration schemes and two time steps are shown in Fig. 7.7. The agreement with Maxey's results is generally good and the overlap of various curves of present work prove that there is no appreciable difference in the integration schemes and time step sizes; this may not be applicable for slag-metal system, however, it verifies the trajectory calculations (including the interpolation scheme) implemented in the LPT code.

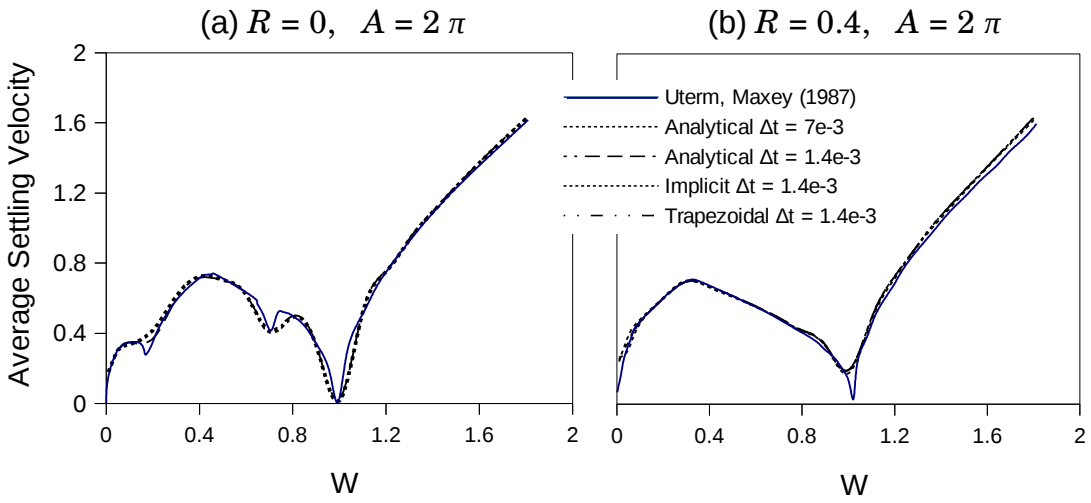

Figure 7.7. Comparison of plots of average settling velocity against dimensionless stokes velocity (W) of Maxey's computations (continuous line) with various integration schemes and time step sizes. Common y-axis and legend

7.4 Turbulence Modeling: The Eddy Interaction Model

The influence of stochastic nature of fluid turbulence on particle motion is accounted by implementing the *Eddy Interaction Model*, originally proposed by Hutchinson *et al* (1971). The present work basically uses the model further developed by Graham & James (1996). In this model there are three parameters that define the interaction of particle with eddies, namely eddy velocity, eddy time scale and eddy length scale and in the most general case, all are random variables with some probability distribution. The eddy velocity adds fluctuating component to the mean component of instantaneous velocity of the particle and the eddy length and time scales determine the duration of this effect on the particle. This information can be derived from the mean flow and turbulence fields of, say, a RANS simulation.

The fluid velocity that a particles sees within an eddy is given by the sum of mean and fluctuating velocities as,

$$\boldsymbol{U}_F = \boldsymbol{U} + \boldsymbol{u}' \tag{7.16}$$

where the mean velocity $\boldsymbol{U}$ is that of the local fluid and the fluctuating velocity $\boldsymbol{u}'$, is taken based on the isotropic turbulence assumption as,

$$u_i' = \psi_i \sqrt{\frac{2k}{3}}, i = r, z \tag{7.17}$$

in which, k is the turbulence kinetic energy, ψ_i are the random variables taken from Gaussian distribution with the following properties:

$$\begin{aligned} \langle \psi_i \rangle &= 0 \\ \langle \psi_i^2 \rangle &= 1 \end{aligned} \tag{7.18}$$

This random variable can be sufficiently approximated by simply adding three independent random variables, ψ_{ind}, with the property, $-1 < \psi_{ind} < 1$.

The characteristic turbulence scales for homogeneous isotropic stationary turbulence are the integral scales; however for non-homogenous turbulence, the dissipation scales of Graham & James are widely used namely,

$$t_{turb} = \sqrt{\frac{3}{2}} C_{\mu}^{3/4} \frac{k}{\varepsilon} \tag{7.19}$$

for time and

$$l_{turb} = C_{\mu}^{3/4} \frac{k^{3/2}}{\varepsilon} \tag{7.20}$$

for length. The eddy life time (t_E) and length scale (l_E) are twice that of the eddy time and length scales, respectively, *i.e.*,

$$\begin{aligned} t_E &= 2\, t_{turb}, \\ l_E &= 2\, l_{turb}. \end{aligned} \tag{7.21}$$

At the heart of the eddy interaction model is the manner in which the length and time scales of the eddy determine the duration of particle-eddy interaction. This is explained as follows, with reference to Fig. 7.8. Let us consider a particle initially located at $\boldsymbol{x}_{P0}$, coincident with the centre of an eddy, $\boldsymbol{x}_{E0}$ of radius l_E assuming that the eddy is circular (in 2D). After some time t (usually small), the particle governed by Newtonian equations of motion moves to $\boldsymbol{x}_P$ while the eddy moves to a location,

$$\boldsymbol{x}_E = \boldsymbol{x}_{P0} + \boldsymbol{U}_E\, t, \tag{7.22}$$

where $\boldsymbol{U}_E$ is the velocity of eddy motion equal to the local fluid velocity at $\boldsymbol{x}_{E0}$. The particle is said to be under the influence of the eddy until either (i) the particle has crossed the eddy or (ii) the life time of eddy is expired. This means the particle-eddy interaction time is the lowest of particle crossing time, t_C and eddy life time t_E:

$$t_i = \mathrm{MIN}(t_C,\ t_E) \tag{7.23}$$

The particle is said to have not traversed the eddy if eddy-particle distance is smaller than the eddy length,

$$|\boldsymbol{x}_P - \boldsymbol{x}_E| < l_E \tag{7.24}$$

or,

$$|\boldsymbol{x}_P - \boldsymbol{x}_{P0} - \boldsymbol{U}_E t| < l_E \tag{7.25}$$

Now the task is to find the time for the particle to cross the eddy, $t = t_C$, from Eq. (7.25). Usually the LHS of Eq. (7.25) has been deduced from the analytical solution of the particle equation of motion in the absence of all forces except drag, on the particle (Graham & James, 1996, Fluent 2009). However Barton (1999) notes that numerical techniques are required to obtain t_C when $\boldsymbol{A} \neq 0$ in Eq. (7.11), as in our present case.

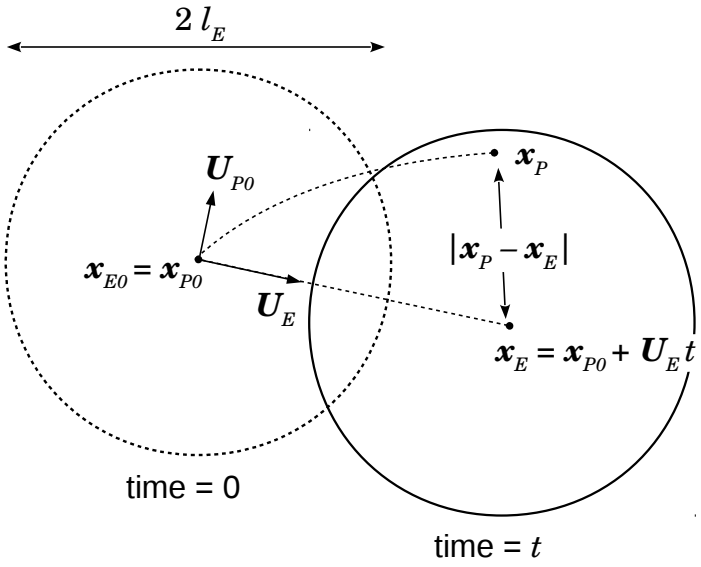

Figure 7.8. Illustration of eddy interaction model showing an eddy and a particle at two instants of time. The eddy is advected by the local mean velocity whereas the particle motion is governed by Newtonian equations of motion and eddy interaction

Once the interaction time is exceeded a new eddy is assigned to the particle. For every new eddy, the mean velocity $(\boldsymbol{U}_E)$ and turbulence parameters $(t_E,\ l_E)$ are taken from the fluid flow field at the particle location at that time instant and new random numbers (ψ_i) are sampled from a Gaussian distribution. In the original eddy interaction model, all these parameters are kept constant throughout the duration of particle-eddy interaction. However in order to avoid the 'spurious drifts' of particle moving from one eddy to another, Wang &

James (1999) proposed a method called 'varied eddy interaction model' and demonstrated that the prediction of particle deposition in boundary layer significantly improves than without it. In this method, except for the random numbers that are sampled only once an eddy interaction time, all the variables namely the mean velocity, fluctuating velocity, eddy time and length scales are varied according to the instantaneous location of particle in motion.

Under such conditions, the spatially varying eddy velocity, $\boldsymbol{U}_E$ becomes temporally varying and therefore, Eq. (7.11) can neither be numerically integrated to estimate t_C beforehand. To circumvent, the following approach is taken:

1. the mean velocity of the eddy is set equal to the local mean velocity (RANS field), *i.e.*,

$$\boldsymbol{U}_E = \boldsymbol{U} \tag{7.26}$$

   and is tracked like an inert particle for every time step;
2. the distance between the eddy location and particle location is calculated and the condition $|\boldsymbol{x}_P - \boldsymbol{x}_E| < l_E$ is verified for every time step

Therefore and the particle - eddy interaction lasts as long as,

1. the eddy life time is less than t_E and
2. $|\boldsymbol{x}_P - \boldsymbol{x}_E| < l_E$.

The flowchart in Fig. 7.9 outlines the steps involved in this model.

Whenever a new eddy is assigned to a particle there is a jump in the fluid velocity and hence the particle velocity and acceleration. A smooth transition from the old to new velocity values was applied to avoid spikes in particle acceleration and the resulting numerical instabilities, whose details are given in the Appendix E.3.3.

The summary of steps involved in the LPT code is given in Fig. 7.10. The details of certain Functions of code highlighted by dashed colored boxes are given in the Appendix E. Of all the steps, verifying boundary conditions is the most time consuming step, followed by interpolation of scalars to particle and eddy location, each consuming more than 75% and around 15% of the total computational time, respectively.

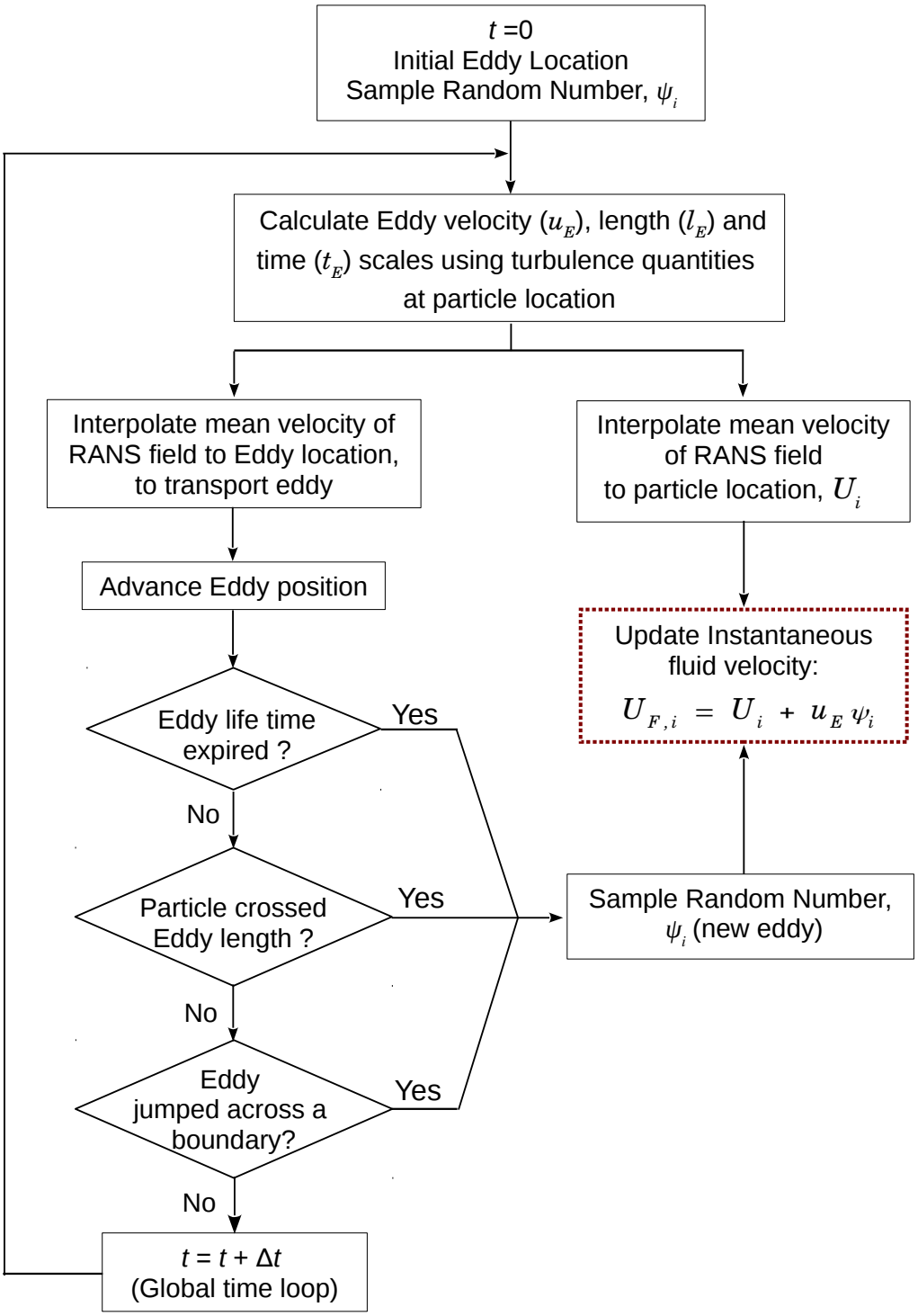

Figure 7.9. Flowchart outlining steps in Eddy Interaction Model

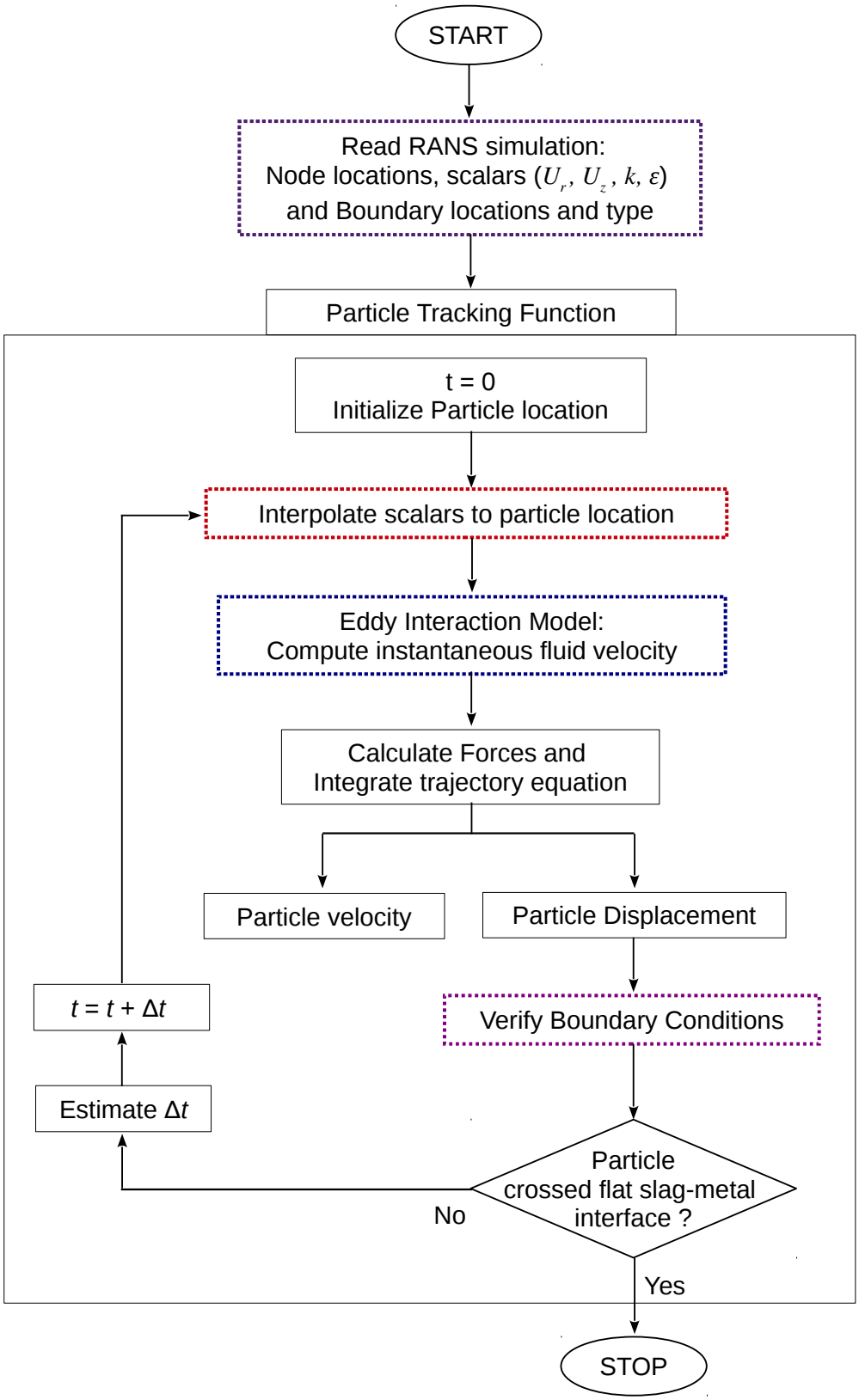

Figure 7.10 Flowchart outlining summary of steps in the LPT code. Separate flowcharts for steps in colored-dashed box are provided elsewhere.

7.5 Modifications to the Geometry of QSP-RANS Domain

It was learnt from the multiphase LESs (Ch. 6) that the velocity field downstream, past the region of entrainment, is quite different from the QSP-RANS simulations that were used to supply inlet conditions for those LESs. The two velocity fields compared in Figs. 7.11 (a) and (b) for $Q_{sp} = 2$ show that in the RANS simulation the flow downstream, past *ULeye*, almost sharply turns in the radial direction and closely follows the solid boundary for *ULflat*; in other words, there is no flow separation at the tip of *ULeye* in RANS simulation. In contrast, the turbulent wavy VOF surface in the LES caused flow separation leading to stronger downward flow.

Moreover, preliminary LPT simulations using the RANS flow field as in Fig. 7.11a, showed that the droplets had very little residence time, since they quickly rejoined the upper phase by the horizontal flow. To enable flow separation, the solid of *ULeye* was projected downwards like a finger to represent the 'lip' of the two phase interface as shown in Fig. 7.12; the vertical height of this lip is equal to half the actual-slag height. Apart from this two more minor modifications were introduced. The angle of inclination of *ULeye* was corrected to that of VOF interface in their respective LES (obtained from ensemble averaging of 15 snapshots of interface: 15, 25 and 30 degrees with vertical axis, for $Q_{sp} = 1$, 2 and 4 lpm/ton, respectively). Secondly, the sharp corner of slag-metal-air three phase point was sliced off, as also seen in Fig. 7.12. This otherwise caused problems due to particles getting trapped in the corner, necessitating sophisticated boundary treatment. With these modifications new QSP-RANS were performed for the three flow rate cases and the velocity fields are shown in Fig. 7.13a, where the flow separates in all three cases, as in the multiphase LES.

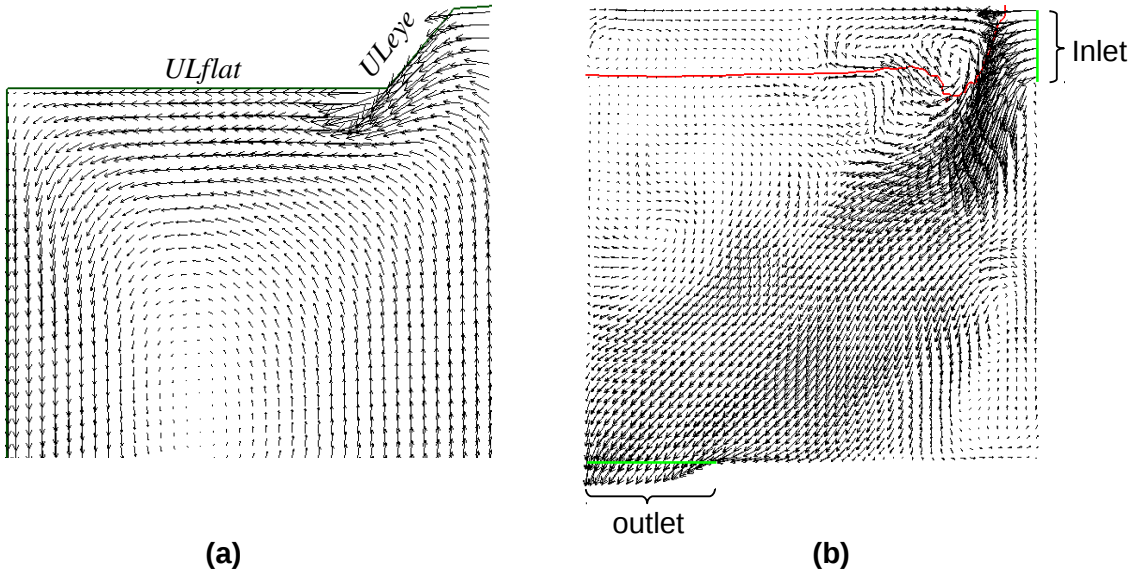

Figure 7.11. Mean velocity fields from (a) 2D QSP-RANS simulation and (b) time averaged 3D LES for $Q_{sp} = 2$. In (b) the red line is the time averaged locations of the VOF surface

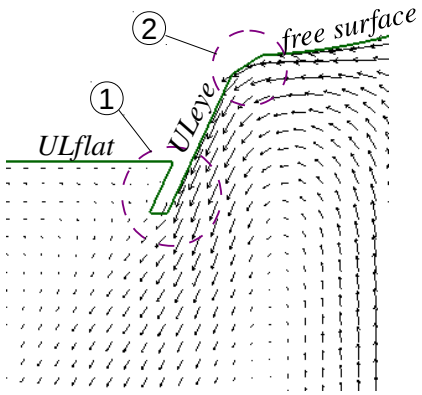

Figure 7.12. Close up of a portion of RANS domain of Q_{sp} = 2 showing the 'lip' along *ULeye* (1), the sliced off 3 phase corner in the top middle (2) and the velocity vectors

In the RANS simulations the turbulence intensity, defined by,

$$TI = \frac{u'}{|\boldsymbol{U}|} \times 100, \qquad u' = \sqrt{2/3\,k},\ |\boldsymbol{U}| = \sqrt{U_r^2 + U_z^2} \tag{7.27}$$

was around 20% near *ULeye*. The actual definition of u' in Eq. (7.27) is,

$$u' = \sqrt{\frac{1}{3}\sum \langle u_i'^{\,2} \rangle} \tag{7.28}$$

where $\langle u_i'^{\,2} \rangle$ are also the square of standard deviation (STDEV) of velocities.

The velocity profiles extracted surrounding *ULeye* from LES in Sec. 6.3 showed that the STDEV of velocities at *ULeye* were as large as their mean. Applying Eq. (7.28) to the STDEV values (to find u') and using the mean of LES velocity profiles ($|\boldsymbol{U}|$), an apparent turbulence intensity can be defined similar to Eq. (7.27) and its value at *ULeye* is approximately 100% (since, STDEV ≈ mean) †.

The true and apparent turbulence intensities are defined based on u' and $|\boldsymbol{U}|$ that are obtained from different averaging procedures, namely Reynolds averaging (Sec. 2.6.1) and the procedure in Sec. 6.3, respectively. Despite this, taking the apparent value for the true turbulence intensity (*i.e.*, 20% replaced by 100%), and by setting the values of k according to Eq. (7.27), for two cell thickness adjoining *ULeye*, another set of QSP-RANS were performed for the three flow rates. This set of simulations is called *RANS*-2 whereas those discussed earlier in this Section is called *RANS*-1. The purpose of *RANS*-2 is to investigate the influence of turbulence due to interface fluctuations at *ULeye* on the nearby flow of LP, which is absent in *RANS*-1.

The computed velocity fields for *RANS*-2 are shown in Fig. 7.13b. Comparison of cases between Fig. 7.13 (a) & (b) shows significant change in velocity field, but only at the highest Q_{sp} case.

† For each *i*, if $\sqrt{\langle u_i'^{\,2} \rangle} \approx U_i$ (STDEV ≈ mean) then $\sqrt{\frac{1}{3}\sum \langle u_i'^{\,2} \rangle} \approx \sqrt{\frac{1}{3}\sum U_i^2} = |\boldsymbol{U}|$, *i.e.*, $u' \approx |\boldsymbol{U}|$

Similar to that in Sec. 6.1.6 the axial distributions of plume velocity between simulation [using Eq. (4.47)] and literature correlation [Eq. (6.2)] are compared in Fig. 7.14 for three Q_{sp} and for *RANS*–1 and 2. In all the cases the agreement is apparently better.

The flow separation phenomenon was not anticipated before doing the LES. Now having introduced this modification how does it affect the RANS flow field around the slag eye, from where the mean velocities and Reynolds stresses were extracted to supply input for SEM in the multiphase LES? This is inferred from charts in Figs. 7.15 and 7.16 comparing those values before and after the new QSP-RANS modifications. The Reynolds stresses are significantly different in almost all cases. However for the mean velocities, significant change is seen only at the lowest flow rate cases: the relative differences in the line-average of norm of mean velocities [$\overline{v}_{RANS}$, defined by Eq. (6.3)] between cases before and after new modifications are approximately -7, 5 and 6 % for *RANS*-1 and -18, 4 and 13 % for *RANS*-2, for Q_{sp} = 1, 2 and 4, respectively.

If the LESs are to be repeated with inlet profiles from these modified QSP-RANS, the entrainment rate should be reduced marginally only for the smallest flow rate due to decrease in velocity and that Reynolds stresses may not have significant effect as demonstrated by the role of turbulence length scales in Sec. 6.2.3. However the changes, if any, do not affect the results of LPT as it now uses the more appropriate flow fields.

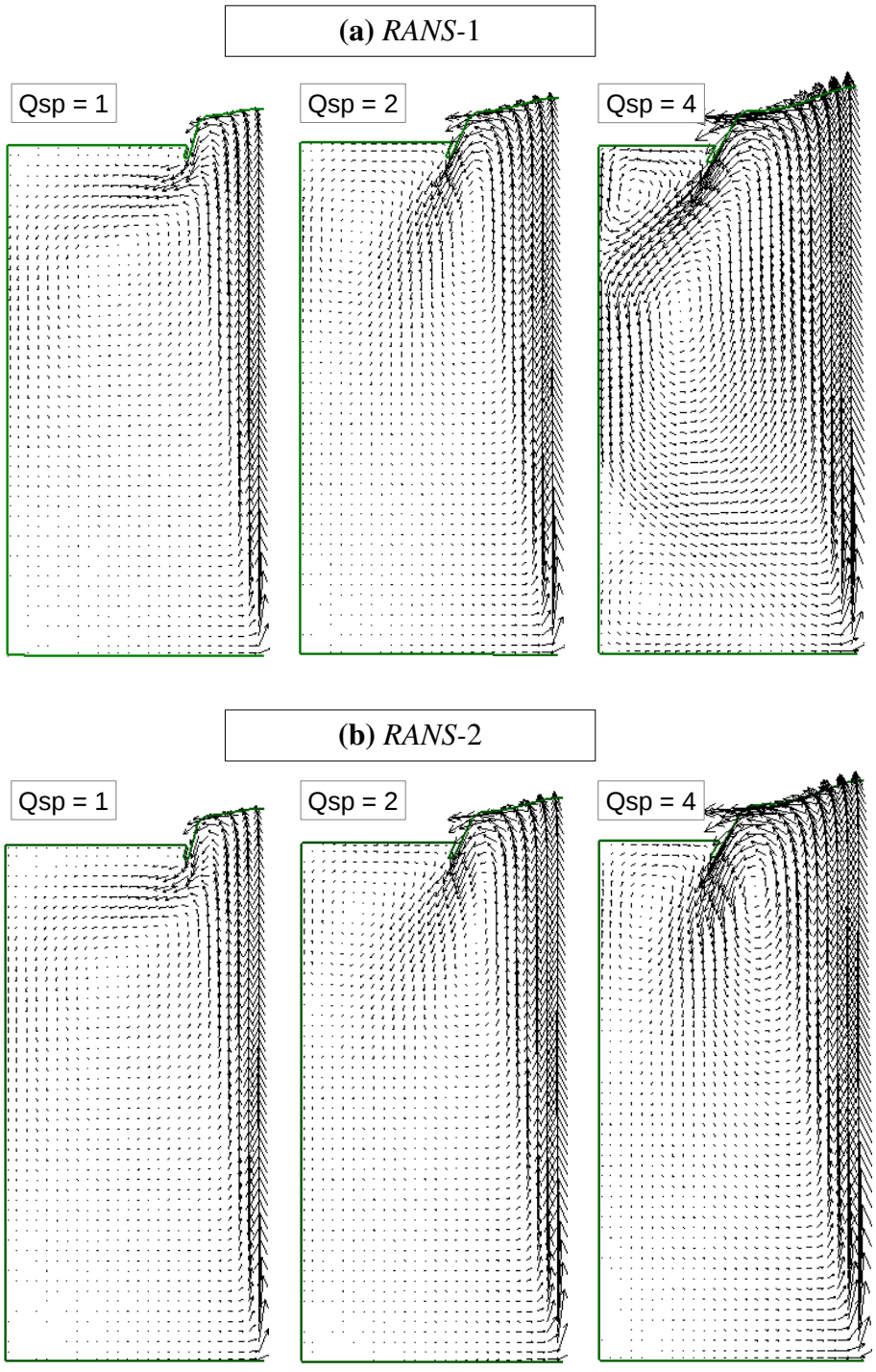

Figure 7.13. QSP-RANS velocity vector fields with modified solid boundary for the three gas injection rates (Qsp)

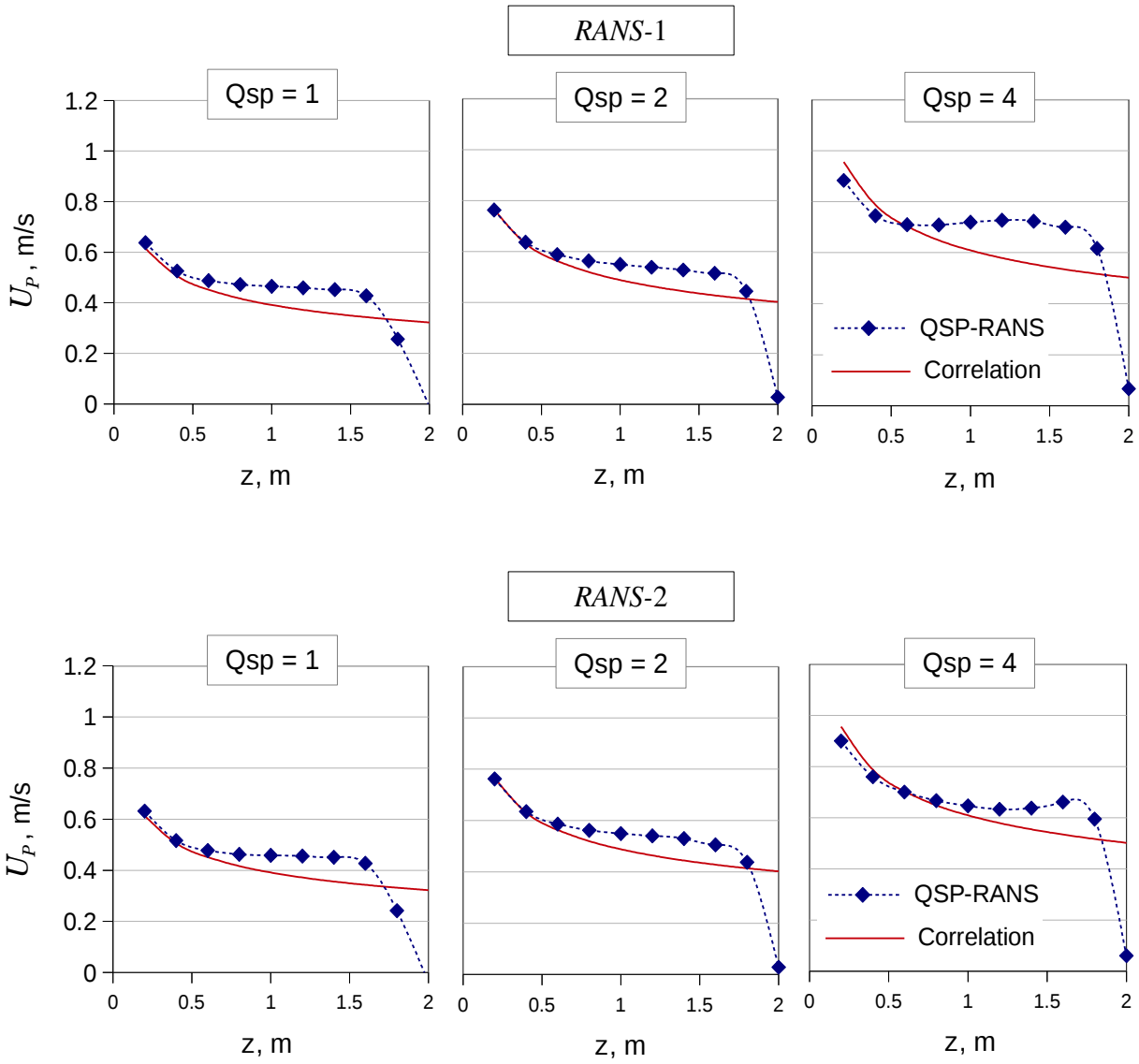

Figure 7.14. Comparisons same as in Fig. 6.1 but with for results due to modified solid boundaries. Common legends and y-axes

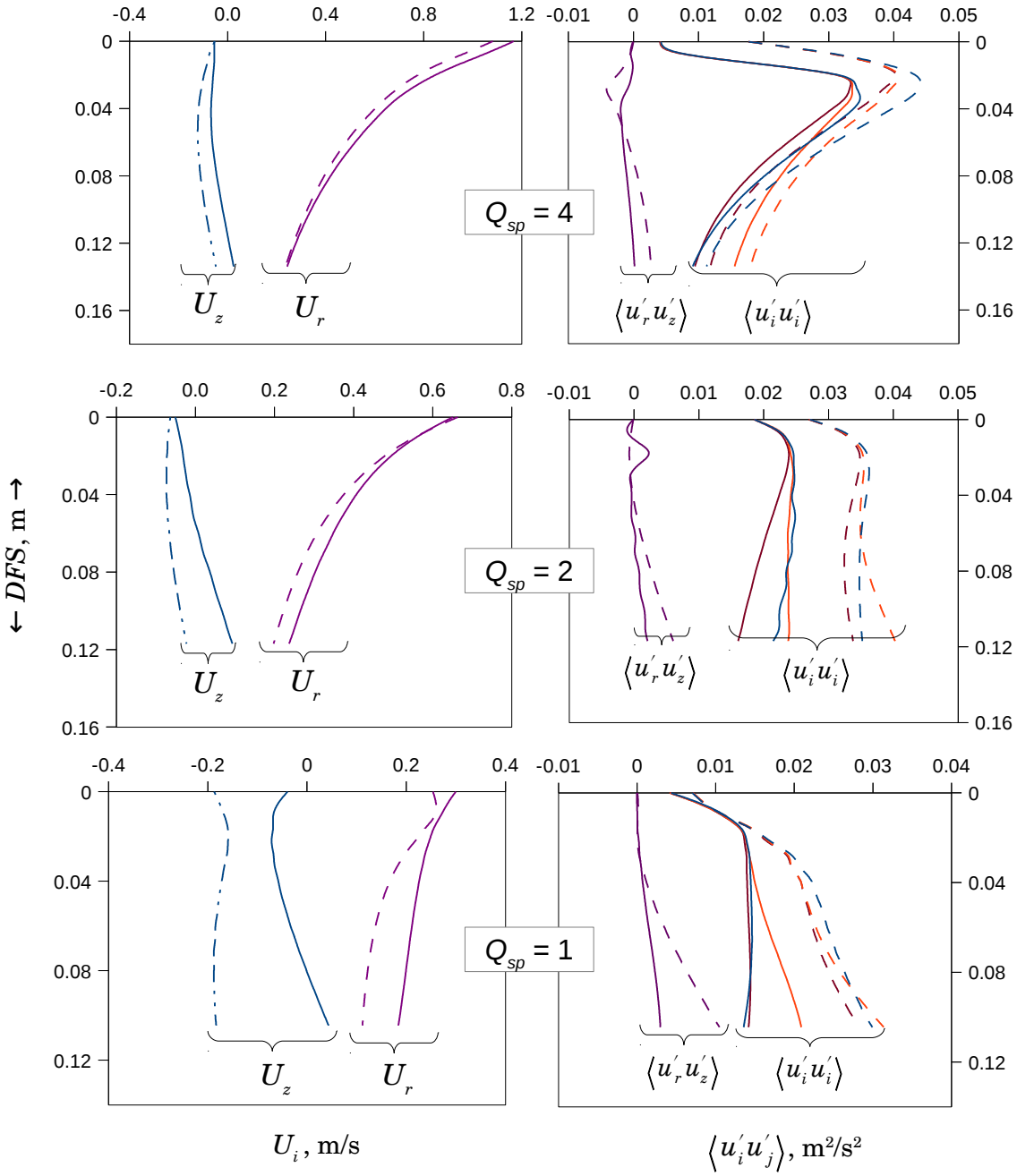

Figure 7.15. QSP-RANS profiles of mean velocities, U_i and Reynolds stresses, $\langle u_i' u_j' \rangle$ *versus* distance to free surface (DFS) before and after the new modifications (*RANS*-1) denoted by continuous and dashed lines, respectively. Common x and y axes labels.

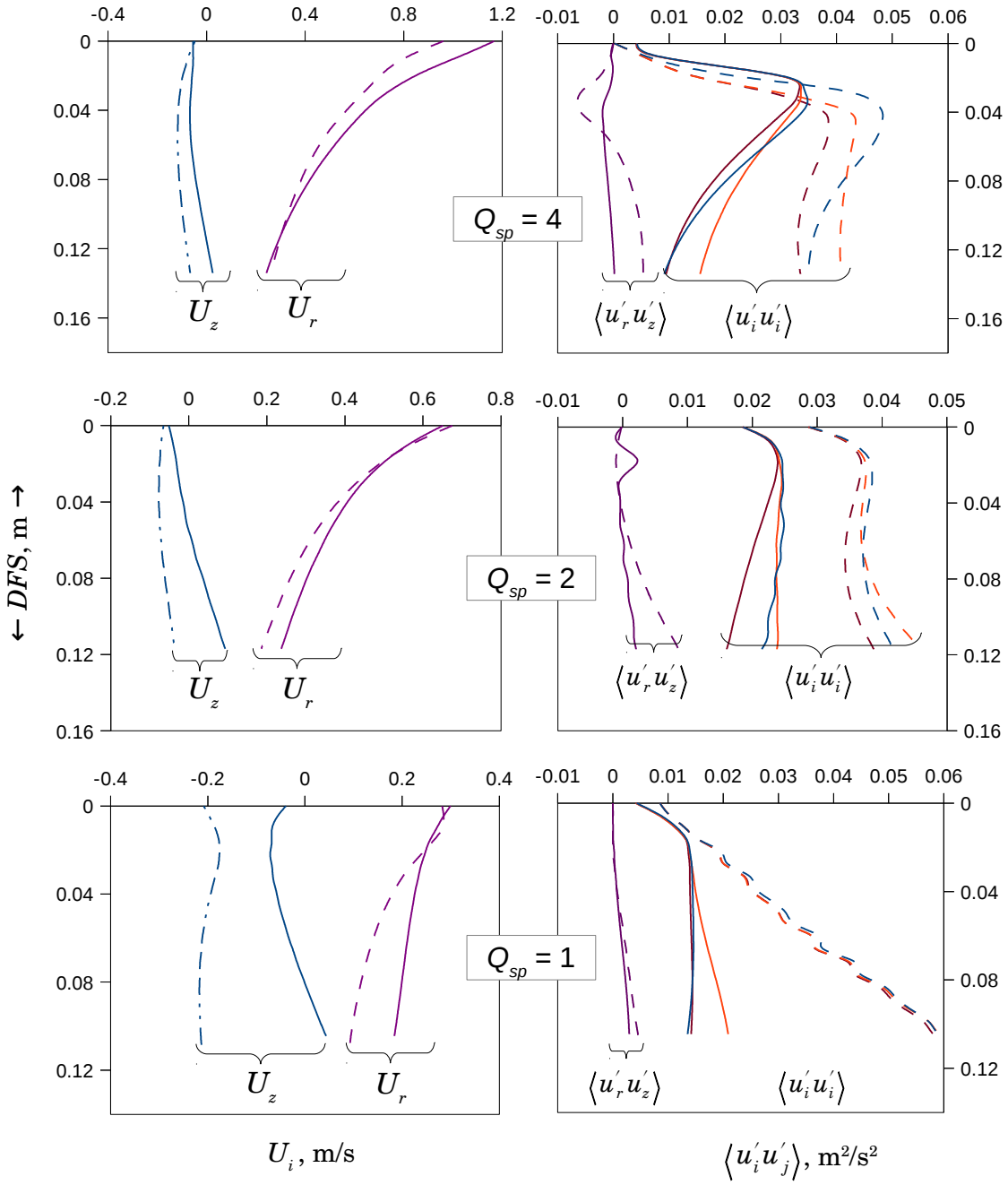

Figure 7.16. Same as Fig. 7.15 but for *RANS*-2

7.6 Residence Time Distribution from Multiphase LES

Multiphase LES discussed in Ch. 6, was again performed for $Q_{sp} = 2$ with $\mu_U = 0.11$ and $\sigma = 1.0$, but for a longer time and *without droplet removal* (*WODR*). The grid refinement scheme remains the same as in Ch. 6. No removal of droplets allowed the droplets to travel further down in the lower phase and eventually float up to the upper phase. Since the LES domain is short and the large eddies are not resolved past the region of onset of entrainment, the aim of this LES is to provide an order of magnitude comparison for mean residence time with that of a corresponding LPT. The extremes, $Q_{sp} = 1$ and 4 were not simulated since entrainment is already little in the former and in the latter, significant amount of droplets were lost through the outlet.

The size distribution from this simulation, compared against the multiphase LES 'with droplet removal' (*WDR*, from Ch. 6), is shown in Fig. 7.17. The little differences in the two size distributions indicate that the droplets in *WODR* did not significantly break up in their life span.

Transitional volume for various droplet size ranges were estimated as the total droplet volume for each size range, in the domain, at a given time instant and is plotted in Figs. 7.18 (a) to (d). The cumulative averages of transitional volume $(V_{tr,\,range})$ shown in these charts are also tabulated in Table 7.2. Since the entrainment rate is the same between *WDR* and *WODR*, the mean entrainment rate for each size range $(\dot{V}_{range})$ was estimated from *WDR* and used to calculate mean residence time for *WODR* using,

$$\bar{t}_{res,\,range} = V_{tr,\,range} / \dot{V}_{range}, \tag{7.29}$$

according to volume continuity (similar to Lin & Guthrie, 1994). These values are plotted in Fig.7.18e and also tabulated in Table 7.2.

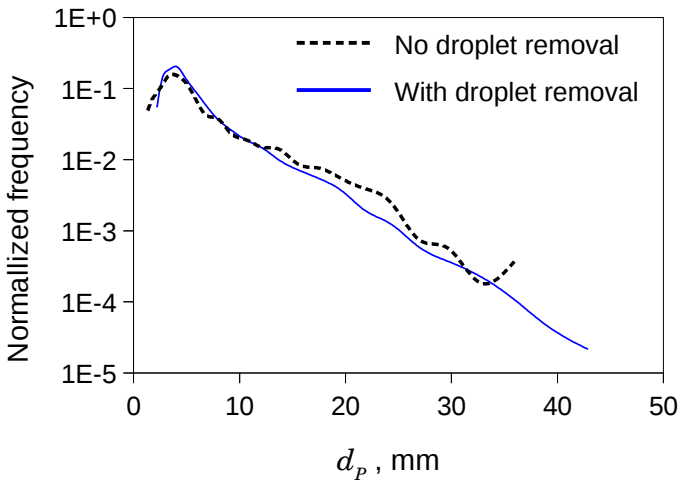

Figure 7.17. Droplet size distribution of multiphase LES 'no droplet removal' (*WODR*) compared against that of 'with droplet removal' (*WDR*, from Ch. 6).

Table 7.2. Transitional volume from *WODR* and Entrainment Rate from *WDR* for $Q_{sp} = 2$, $\mu_U = 0.11$ and $\sigma = 1.0$ and mean residence time for various droplet size ranges.

Droplet Size Range	Mean Transitional Volume, $V_{tr,range}$, m^3 (*WODR*)	Entrainment Rate $\dot{V}_{range}$, m^3/s (*WDR*)	Mean Residence Time, $\bar{t}_{res,range}$, s
4 <= (d_P, mm) < 8	1.753E-5	1.729E-5	1.01
8 <= (d_P, mm) < 16	3.208E-5	4.263E-5	0.75
16 <= (d_P, mm) < 28	2.681E-5	4.930E-5	0.54
28 <= (d_P, mm) < 44	6.081E-6	1.028E-5	0.59
All drops, d_P >= 4 mm	8.250E-5	1.309E-4	0.63

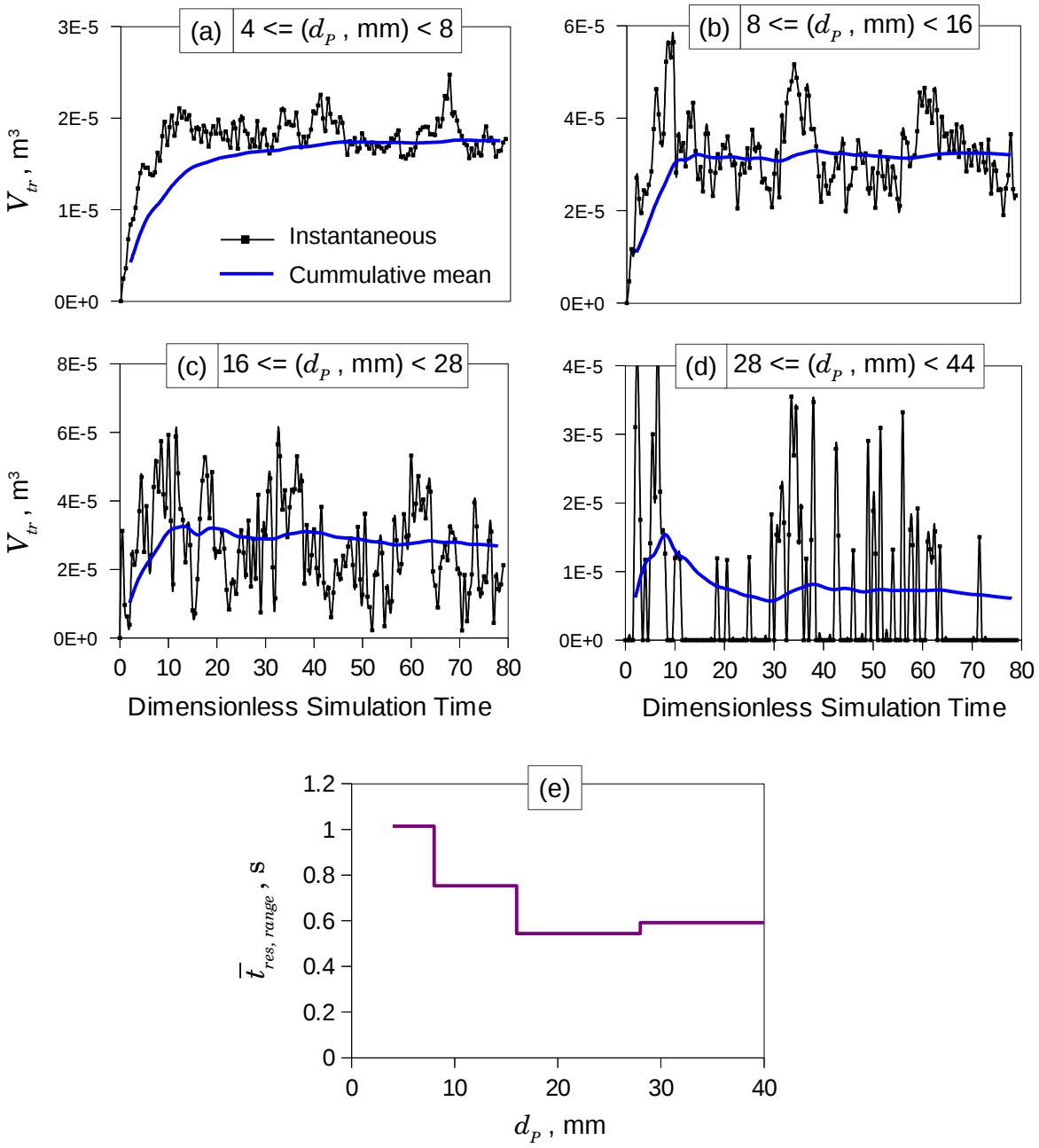

Figure 7.18. Results of multiphase LESs without droplet removal (*WODR*). (a) to (d) Transitional volume of droplets (V_{tr}) of various size ranges. Common legend, x axis and axes labels. (e) Mean residence time ($\bar{t}_{res,\,range}$) for various size ranges, corresponding to charts (a) to (d)

7.7 LPT in the Ladle

With the objective of obtaining mean residence time for various particle sizes for entrainment of slag droplets in ladle, LPT cases were run for various combinations of parameters. This section first discusses the LPT case setup and sensitivity of some parameters, followed by the results. All LPT cases use Tomiyama's drag correlation [Eq. (7.7)] except at the end where few cases use the standard drag curve. As in Tomiyama's drag correlation, interfacial tension is the only variable parameter with regards to fluid properties.

7.7.1 Initial Condition and Sensitivity of Parameters

The choice of initial location of droplets in LPT is crucial as it was found to change the residence time drastically. The detachment of droplets takes place at the tip of ligaments in the LESs; so this could be the initial location of droplets in LPT. However if the Figs. 7.12 and 7.13 are observed, the downward flow is strong not at tip of the lip but only to the right side of it. In the LESs, droplets were seen to be in middle of high velocity streams when they detach. So droplets were radially placed 2 cm off the *ULeye* boundary. Axially, two location were chosen, (1) the base of the lip and (2) axial location of *ULflat*. These locations are shown in Fig. 7.19. Although both the schemes produced similar results, scheme (2) is preferred because, it gives some time for the random velocities to sufficiently disperse the particles before they move past the supposedly-actual location of droplets detachment; this is to accord with the fact that location of droplet detachment itself is fluctuating.

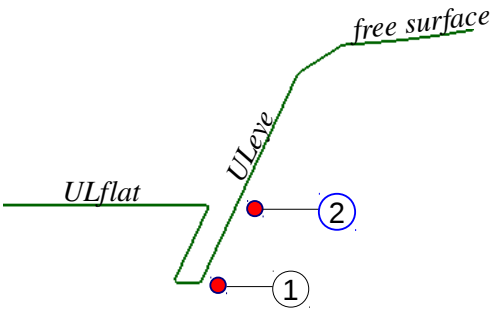

Figure 7.19. Two schemes of initial locations for particle in LPT, of which scheme (2) is preferred

To test the input parameters sensitivity five droplets of diameters, 0.8, 1.6, 4.6, 18 and 44 mm were considered and all test cases correspond to *RANS*-1, $Q_{sp} = 4$ and $\sigma = 1.0$. In this context simulation result means, the average residence time of particles in lower phase, $\bar{t}_{res}$.

Time Step Size, Δt and Integration Scheme: LPTs were performed at four time steps sizes, $\Delta t, s =$ 0.001, 0.002, 0.004 and 0.01 and also for three numerical integration schemes (outlined in Sec. 7.2) and with 500 particles. For various cases tested anything above 500 particles did not produce significant change in the results. The results compared in Fig. 7.20 show that at and above 0.002 s, time step size independence is almost achieved for all integration schemes. Moreover Fig. 7.21a shows that the three integration schemes yield very similar values at $\Delta t = 0.002\,s$. So, for future simulations, $\Delta t = 0.002\,s$ was chosen and implicit integration scheme was preferred.

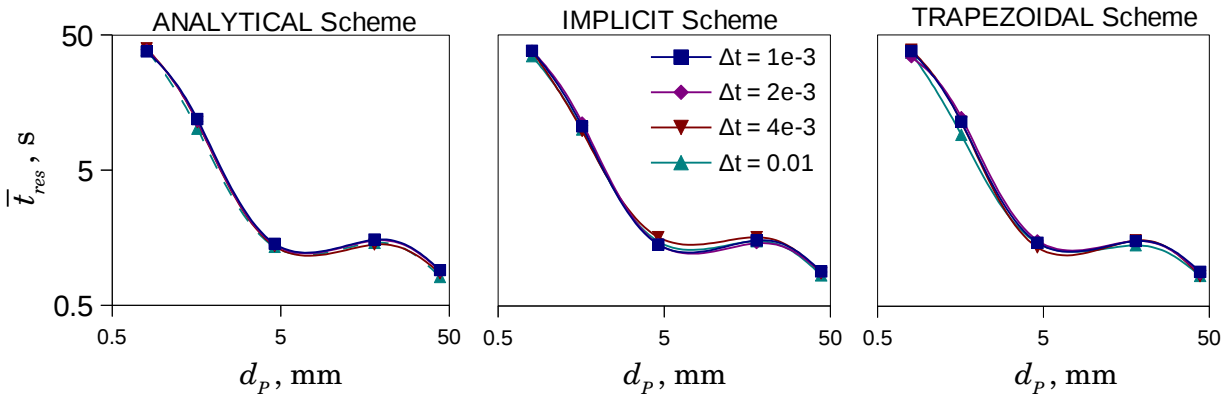

Figure 7.20. Mean residence time $(\bar{t}_{res})$ *vs* particle size (d_P) compared for various time step sizes (Δ*t,* s) and numerical integration schemes, for Q_{sp} = 4, 500 particles and *RANS*-1. Common y-axis and legend.

Input Grid Resolution: The scalar field of a given RANS simulations in Gerris can be outputted at different grid resolutions (`Level`). In the present work, the maximum affordable `Level` is 8. So three input grid resolutions namely `Level` = 6, 7 and 8 were tested and plotted in Fig. 7.21b. The graph shows that probably there would be no significant effect of input grid resolution above 8 and therefore that was used for all simulations.

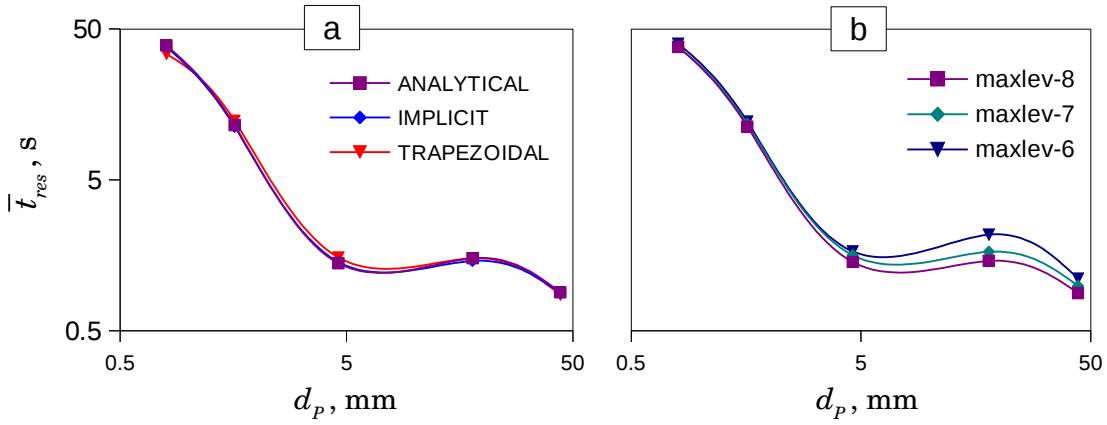

Figure 7.21. Mean residence time $(\bar{t}_{res})$ *vs* particle size (d_P) for (a) comparing three integration schemes and (b) comparing different resolutions of input RANS grid (maxlev), all at Q_{sp} = 4 and $\Delta t = 0.002\,s$, using 500 particles and *RANS*-1. Common y-axis

Total time: Some particles do not leave the lower phase within a given total time of particle tracking. So the total time was varied between cases, until 99% of particles have escaped and 400 s was typical.

7.7.2 Results

7.7.2.1 Mean and Distribution of Residence Times

Fourteen particle sizes, from 0.8 to 44 mm, were chosen and LPTs were performed for three flow rates, three slag metal interfacial tension values, with 500 particles for each size. The mean residence time *versus* particle size for all cases is plotted in Fig. 7.22 (a) and (b). In all curves there is a hump, although more pronounced at higher $\bar{t}_{res}$ cases; this characteristic is inherited from the Tomiyama's drag correlation. In Fig. 7.1 we see that C_D exhibits a minimum at certain Re and since Re is proportional to droplet size and that residence time increases with fluid drag, $\bar{t}_{res}$ also exhibit a minimum at some moderate droplet size. After the minimum, C_D increases with Re and eventually remains constant. Similarly $\bar{t}_{res}$ also increases with droplet size, but only moderately and eventually declines, because the increasing buoyancy floats out the particles more rapidly, altogether giving the characteristic hump.

Except for the $\bar{t}_{res}$ curves for $Q_{sp} = 4$, *RANS*-1, the common trend is the increasing $\bar{t}_{res}$ with increasing flow rate and decreasing interfacial tension. With the increase in flow rate, the downward flow at the point of onset of entrainment is stronger to drag the droplets deeper into the ladle. With decreasing interfacial tension, C_D increases in Tomiyama's correlation as plotted in Fig. 7.23 for the upper limit of C_D for larger particles, namely, $8/3\,Eo/(Eo + 4)$; the increase in drag increases $\bar{t}_{res}$. Figure 7.23 also shows convergence of C_D with particle size for various σ, which is reflected in the convergence of $\bar{t}_{res}$ of various σ, seen in the right end of Figs. 7.22 (a) and (b) at all flow rates.

The residence time distributions (RTD) for each particle size were very similar among three σ within each Q_{sp}; so RTDs only at $\sigma = 1.0$ for various Q_{sp} and *RANS*–1 and 2 are shown in Fig. 7.24 (a) and (b). The RTDs of small particles having large residence times stand out from the rest, in the right side of these charts. The width of RTDs are seen to increase with Q_{sp}, more so in the short RTDs of *RANS*–2 as against that of *RANS*–1, indicating more particle dispersion in the former than the latter.

From the mean velocity vectors in Fig. 7.13, we see that the difference between the two RANS configurations is significant at Q_{sp}=4. Trajectories of 100 particles at this flow rate are shown in Fig. 7.25 for three particle sizes namely, $d_P =$ 0.8, 8.0 and 40 mm. Other than at $d_P = 0.8$, particle dispersion is smaller for *RANS*-1 than *RANS*-2. This is because, the velocity field of *RANS*-1 (Fig. 7.13) has stronger radial component past the 'lip' thereby providing a quick access to *ULflat*, whereby larger droplets rejoin earlier, reducing their dispersion and hence their residence time. This is the reason why in Fig. 7.22, for *RANS*-1, the $\bar{t}_{res}$ curves of Q_{sp}=4 are 'overlapping with' or even lower than that of Q_{sp}=2.

The better of the two RANS configurations will be assessed in Ch. 8.

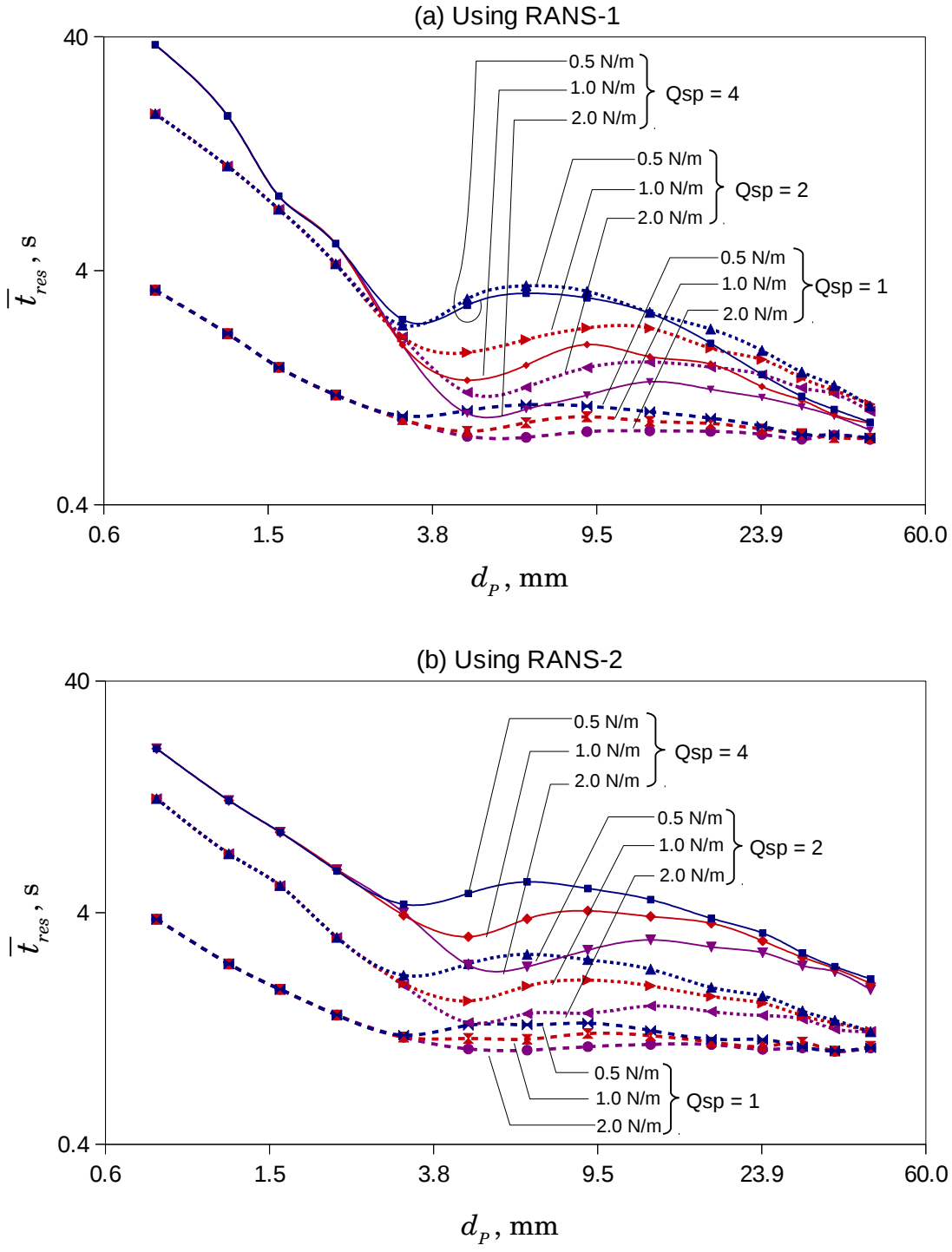

Figure 7.22. Mean residence time $(\bar{t}_{res})$ *vs* particle size (d_P) for three flow rates (Qsp), slag-metal interfacial tension (N/m) and two RANS configurations of input flow fields, (a) and (b).

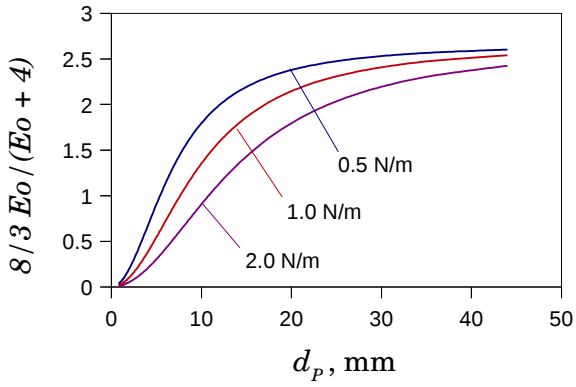

Figure 7.23. Upper limit of drag coefficient for larger particles in Tomiyama's correlation $(8/3\,Eo/(Eo+4))$ *versus* droplet size (d_P).

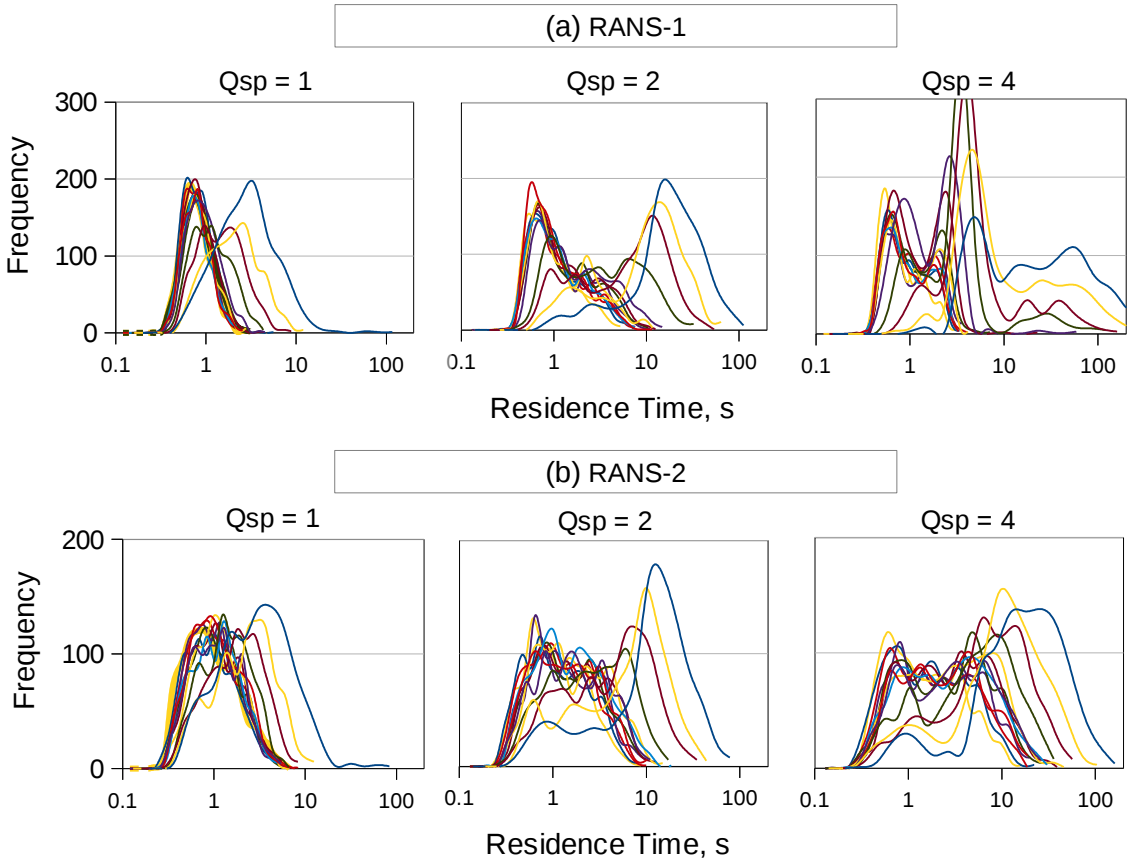

Figure 7.24. Residence time distribution for various droplet sizes and flow rates for $\sigma = 1.0$. The right most curves are for smaller droplets having larger residence times. Common y-axes

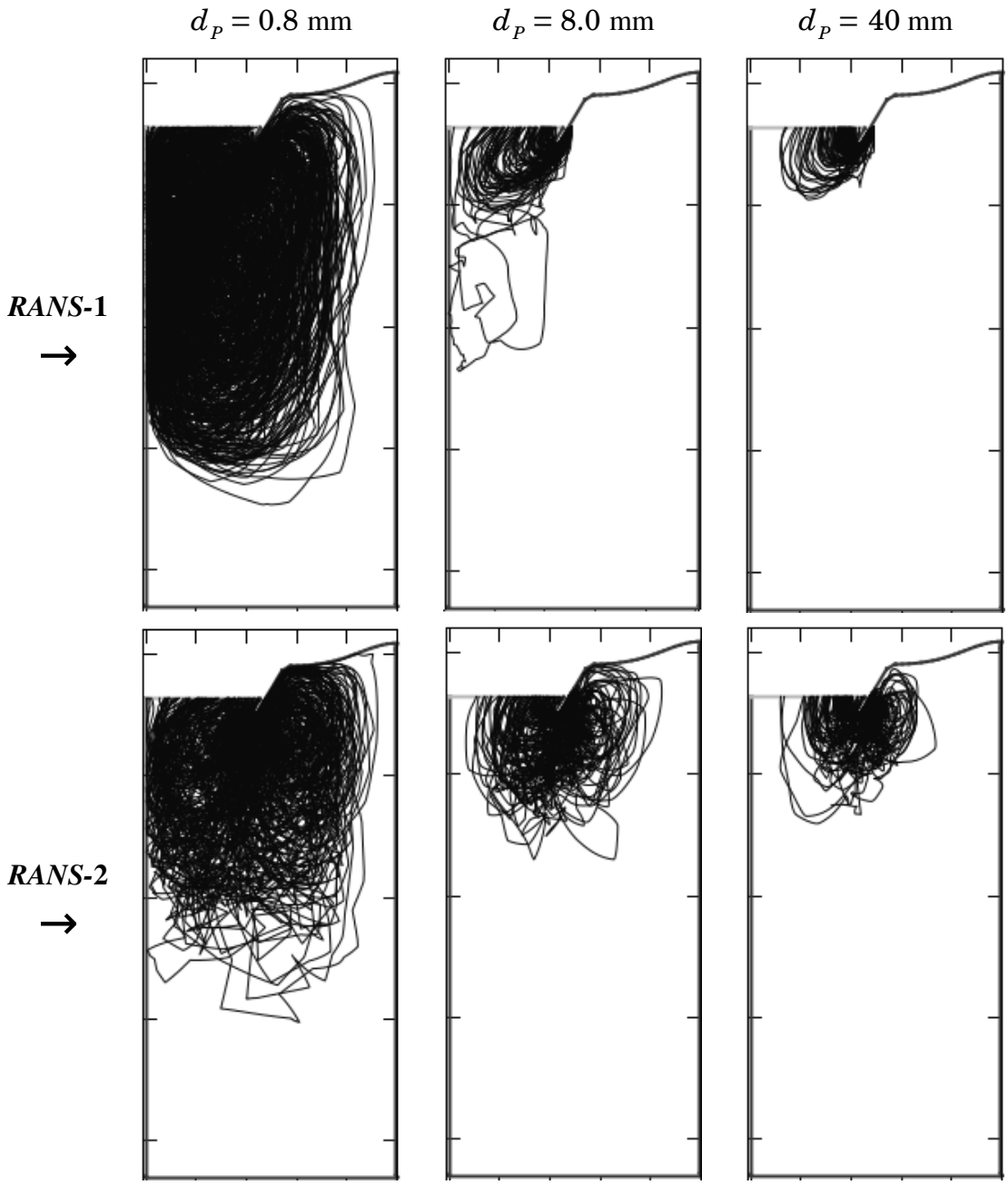

Figure 7.25. Trajectories of 100 particles in the velocity field of $Q_{sp} = 4$ for three particle sizes for two RANS configurations.

7.7.2.2 Statistics of Forces on Particles

In the following, the relative importance of various forces affecting the particle motion are assessed from various overall averages of these forces. First the mean of forces acting on particles of given size were computed in the LPT code for each size group from,

$$\overline{F}_{ij} = \frac{1}{N_{time} N_{part}} \sum_{n=1}^{N_{part}} \sum_{m=1}^{N_{time}} F_{ijmn}, \text{ N} \tag{7.30}$$

where, i correspond to the forces, namely drag (F_D), buoyancy (F_G)†, added mass (F_{AM}) and pressure gradient (F_{PG}), j correspond to particle size group, N_{time} and N_{part} are the total number of time steps a particle is alive and total number of particles in each size group, respectively and $F = \sqrt{F_r^2 + F_z^2}$ is the norm of force vector. These were then normalized as,

$$\overline{F}'_{ij} = \frac{\overline{F}_{ij}}{(\rho_F - \rho_P) V_P}, \text{ N/kg} \tag{7.31}$$

Plots of these normalized forces typical of all cases within each RANS configuration are shown in Fig. 7.26. The mean of the flatter portion of these curves ($d_P > 3$ mm) was calculated from,

$$\overline{\overline{F}}'_{ij} = \frac{1}{N_{size}} \sum_{n=1}^{N_{size}} \overline{F}'_{ij}, \text{ N/kg} \tag{7.32}$$

with N_{size} being the number of size groups, and are plotted for all three Q_{sp} and σ values in Fig. 7.27. Except for some of the small Q_{sp} cases, drag ($\overline{\overline{F}}'_D$) is the largest force followed by buoyancy (F'_G); for all cases, pressure force ($\overline{\overline{F}}'_P$) is small whereas the added mass force ($\overline{\overline{F}}'_{AM}$) is non-negligible, varying between 20 and 25 % of $\overline{\overline{F}}'_D$.

† buoyancy is constant, Eq. (7.2).

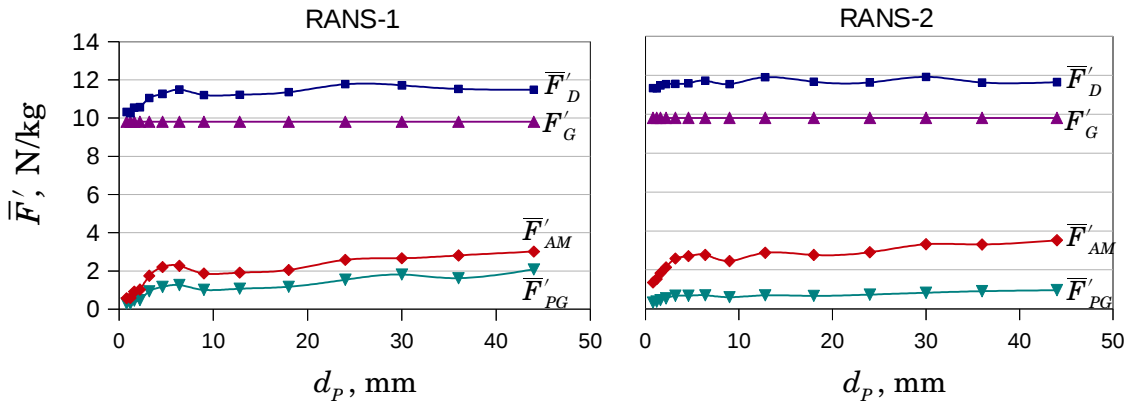

Figure 7.26. Mean of normalized forces that acted on particles of various sizes for $Q_{sp} = 4$ and $\sigma = 1.0$. Common y-axis.

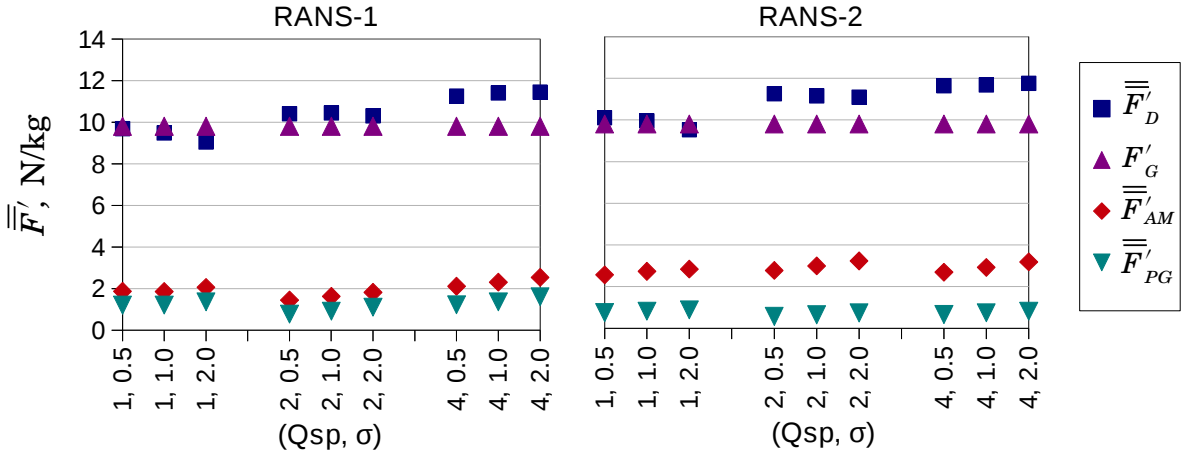

Figure 7.27. Mean of mean forces (normalized) in the more or less flatter portion of curves like in Fig. 7.26 ($d_P > 3$ mm) for various Q_{sp} and σ values. Common y-axis.

7.7.3 Role of Added Mass Coefficient

In Sec. 7.1.2 the range of added mass coefficient, C_{AM}, was discussed in the context of slag droplet entrainment. To study its role, four values namely $C_{AM} =$ 0, 0.5, 1 and 2 were considered and LPTs for $Q_{sp} = 4$ and $\sigma = 1.0$ were performed using those values. The results summarized in Fig. 7.28 show that $\bar{t}_{res}$ only marginally increases with C_{AM}. In fact the maximum and average relative difference with respect to base value, $C_{AM} = 0.5$, of all the

cases were <25% and <20% respectively. The mean of mean forces ($\overline{\overline{F}}'_{ij}$) for drag and added mass, compared in Fig. 7.29 show that despite large variations in $\overline{\overline{F}}'_{AM}$, $\overline{\overline{F}}'_{D}$ has varied only slightly. These results show that of the forces considered, buoyancy and drag are the important forces and pressure and added mass forces have only secondary role on particle trajectories and therefore the choice of C_{AM} is not critical.

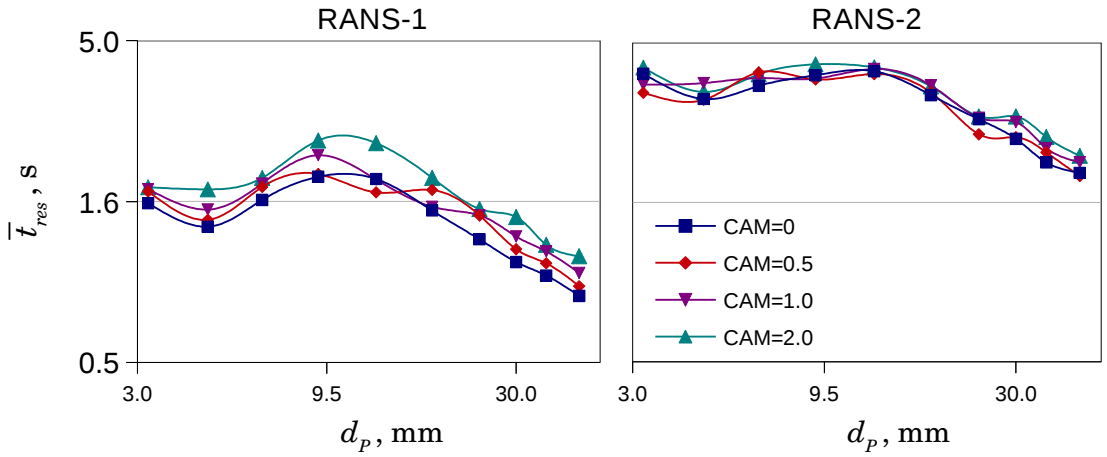

Figure 7.28. Mean residence time ($\bar{t}_{res}$) for various added mass coefficients (CAM) at $Q_{sp} = 4$ and $\sigma = 1.0$. Common y-axis and legend

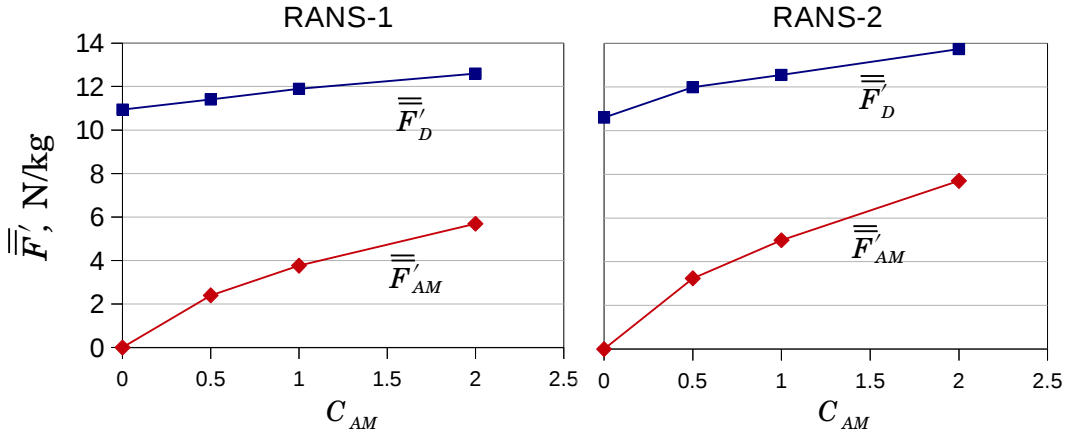

Figure 7.29. Mean of mean forces (normalized) for various added mass coefficients (C_{AM}) values for two RANS configurations. Common y-axis.

7.7.4 Choice of Correlation for Drag Coefficient

It was discussed in Sec. 7.1.1 and Fig. 7.2 about the findings of Ford and Loth that the drag coefficient decreases with increase in particle Reynolds number. To test the effect of lowered drag coefficient, using the standard drag curve (in Fig. 7.1) as an approximation, LPTs were performed for $Q_{sp} = 2$ and *RANS*–1 and 2. Note that this correlation is independent of interfacial tension. The results are presented in Fig. 7.30 along with results obtained using Tomiyama's correlation for $\sigma = 1.0$. Here also the $\bar{t}_{res}$ curves tend to inherit the shape of its drag correlation, the standard drag curve, *i.e.*, the lowered C_D has lowered $\bar{t}_{res}$ in the intermediate size ranges. At higher droplet sizes, due to smaller C_D as compared to Tomiyama's correlation, the droplets take a quite different trajectory at the very beginning, resulting in rise of $\bar{t}_{res}$ curve unlike the fall obtained using Tomiyama's correlation.

In Fig. 7.30 the estimates from *WODR* LES (Sec. 7.6) are also plotted. It is apparent that $\bar{t}_{res}$ of standard drag curve is very close to that of *WODR*, than $\bar{t}_{res}$ of Tomiyama's correlation, although not much at high droplet sizes. However it should be recalled that the LES does not resolve eddies past the region of the onset of entrainment so that the flow downstream is not as intense as an otherwise resolved flow, to drag the droplets deeper downstream. So, as noted in Sec. 7.6, $\bar{t}_{res}$ from *WODR* should be used only for comparing order of magnitudes in which case, results from both the Standard drag curve and Tomiyama's correlation are equally good.

This exercise shows that drag correlation has strong influence on particle residence times, until buoyancy takes over in the larger particle range. In Fig. 7.2 we see that the C_D of Ford and Loth rapidly decreases with Re. When two low values of C_D namely 0.1 and 0.01 were chosen constant for all particle sizes and LPTs were performed, it was found that $\bar{t}_{res}$ was almost invariant with C_D. This is because, when fluid drag is weak, particle buoyancy alone determines the residence time. In the light of these results it can be concluded that Tomiyama's correlation can give reliable estimates for C_D.

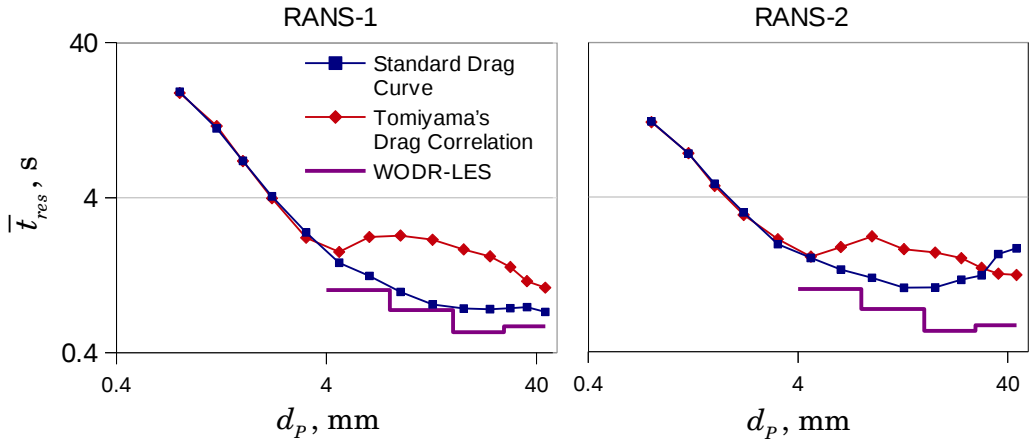

Figure 7.30. Mean residence time $(\bar{t}_{res})$ for $Q_{sp} = 2$ and $\sigma = 1.0$, compared for two drag formulations. Common y-axis and legend.

7.8 Summary

A computer code for Lagrangian particle tracking model was developed specific to the mesh output of Gerris. Four forces namely buoyancy, drag, pressure gradient and added mass were included in the LPT code and the code was verified against literature benchmark cases. An Eddy Interaction Model was implemented to add turbulence effects on particle trajectory. The domain geometry of QSP-RANS was modified to capture the flow separation around the base of *ULeye* that is actually present in the LESs, but missing in the prior QSP-RANS (from Ch. 6). Sensitivity of various parameters were analyzed through various simulation test cases and the optimal parameters were chosen.

Following this LPT cases were run for various combinations of flow rate and slag metal interfacial tension and the mean residence time for various particle sizes were obtained. Another set of LPT cases were performed, based on another set of QSP-RANS performed with 100% turbulence intensity imposed near *ULeye*. The results from two RANS configurations indicate that the particle trajectories/dispersion and hence their residence times are sensitive to the RANS flow field. The better of the two RANS configurations will be assessed in Ch. 8.

The comparison of overall mean of forces acting on particles showed that drag and

buoyancy are the dominant forces with added mass and pressure forces having secondary effects. Consequently, varying the added mass coefficients over a large range showed only a marginal change in computed mean residence times. This also makes the choice of added mass coefficient non-critical and thereby reducing the modeling effort.

From two different drag correlations studied, namely Tomiyama's and Standard drag curve, it was found that the type of drag correlation used has significant influence on the mean residence time. This was well manifested in the shape of mean residence time versus particle size curves. However this becomes ineffective at smaller values of C_D (smaller drag force) since particle buoyancy mostly determines the residence time.

A comparison of mean residence time estimates obtained from an LES performed without droplet removal with that of the corresponding LPTs using the two drag correlations showed all were of similar order of magnitude. This shows that the LPT model predictions are satisfactory. Although it was not further investigated as which of the two drag correlations is more precise, Tomiyama's drag correlation is preferred and hence the mean residence times obtained using the same were used for models in Ch. 8.

Thus reliable formulation for droplet mean residence times has been developed that will be used by various models in Ch. 8.

8. Integration of Models

In this final stage of modeling the entrainment phenomena, various results from QSP-RANS (Ch. 4), LES (Ch. 6) and LPT (Ch. 7) were integrated to estimate mass transfer rate, using the DBD model (Ch. 3*)* and also to assess steel cleanliness, as outlined in Fig. 1.4. The mass transfer rate assessments are based on the kinetics of ladle desulphurization with the assumption of metal side mass transfer control, as implemented in the DBD model. Although the kinetics of ladle desulphurization has been shown to be accompanied by transfer of various elements from metal to slag (Graham, 2008) transfer of only one species (sulphur) is considered because that suffices to assess the role of slag entrainment in mass transfer.

The results of various models hitherto are for the 44 ton ladle (mentioned in Sec. 6.1). Based on correlations developed earlier in this work and scaling relations, mass transfer estimates were also made for a 150 ton ladle, geometrically similar to the 44 ton ladle. Following this an approximate method for estimation of mass transfer rates is explored.

The results hitherto are for gas flow rates well above onset of entrainment, also called as Regime II mass transfer (Sec. 2.4). Estimations for Regime I are also made later under which the differences in literature relations of mass transfer rate are rationalized based on the model results. Other aspects, namely the effect of slag basicity and possibility for scaling are analyzed briefly.

Towards the end, an assessment of steel cleanliness for the 150 ton ladle is presented. Finally the challenges in modeling the entrainment phenomena faced at various stages are summarized.

8.1 Input Parameters for Mass Transfer

LES results for entrainment rate and droplet size distribution were considered for a total of 9 cases, as a combination of three gas injection rate (Q_{sp}) and three interfacial tension values at constant slag viscosity of 0.11 Pa.s. Disregarding the QSP-RANS fields used for LES inlet conditions, for each Q_{sp}, there are two modified QSP-RANS configurations that were used for LPT: without (*RANS*-1) and with (*RANS*-2) imposed turbulence correction near *ULeye*. So there are 6 RANS fields and with three values of interfacial tension there are 18 distributions of mean residence times *vs* particle size. Various other parameters, namely the mass transfer coefficients, fitted droplet size distributions and interfacial areas, extracted from QSP-RANS and multiphase LES, are discussed in this section.

8.1.1 Mass Transfer Coefficients

As in Sec. 3.2.2, separate mass transfer coefficients are considered for the three zones of slag metal interface, namely at the droplet (*ULdrop*), the interface at the eye in contact with high velocity flow of lower phase (*ULeye*) and the more or less flat horizontal interface in contact with weaker flow (*ULflat*); all are metal-side coefficients. In the absence of data these coefficients were estimated using Higbie's Penetration theory.

The penetration theory is briefly reviewed as follows. The schematic in Fig. 8.1 shows a film of certain thickness with uniform velocity (U) flowing past a zone of constant mass transfer flux. Due to laminar flow the mass transfer is solely due to diffusion and the continuous absorption of species across the traversing length (L) enables application of Fick's II law to evaluate the transient concentration profile. Using that concentration profile and Fick's I law, the flux of species is obtained as (Mohanty, 2000),

$$J_{interface} = k\,(C_{interface} - C_{bulk}), \tag{8.1}$$

where, k is average mass transfer coefficient defined as,

$$k = 2\sqrt{\frac{D}{\pi t_c}} \tag{8.2}$$

C is species concentration, D is diffusion coefficient and t_c is the time for which a fluid element is in contact with the interface (contact time). In case of the illustration in Fig. 8.1, where there is constant accumulation over L, the contact time is defined straightforwardly as,

$$t_c = L/U. \tag{8.3}$$

In the case of turbulent flow, where the eddies periodically renew the surface, using the physical length of the transfer zone estimates larger contact time and hence smaller mass transfer coefficient as compared to that obtained using the local eddy length. To see the effect of these length scales, mass transfer coefficients were obtained using both the physical and eddy lengths.

The local eddy length and mean velocities were extracted from QSP-RANS fields (Appendix F.1 has the code snippet for Gerris) and averaged. Along *ULflat*, the averaging was according to

$$\bar{\phi} = \frac{1}{(r_2^2 - r_1^2)} \int_{r_1}^{r_2} \phi \, r \, dr, \tag{8.4}$$

where ϕ is the quantity averaged; along *ULeye* it was arithmetic averaging. Equation (8.3) was applied to these averages to find t_c. In case of physical length, the same mean velocities were used to find t_c.

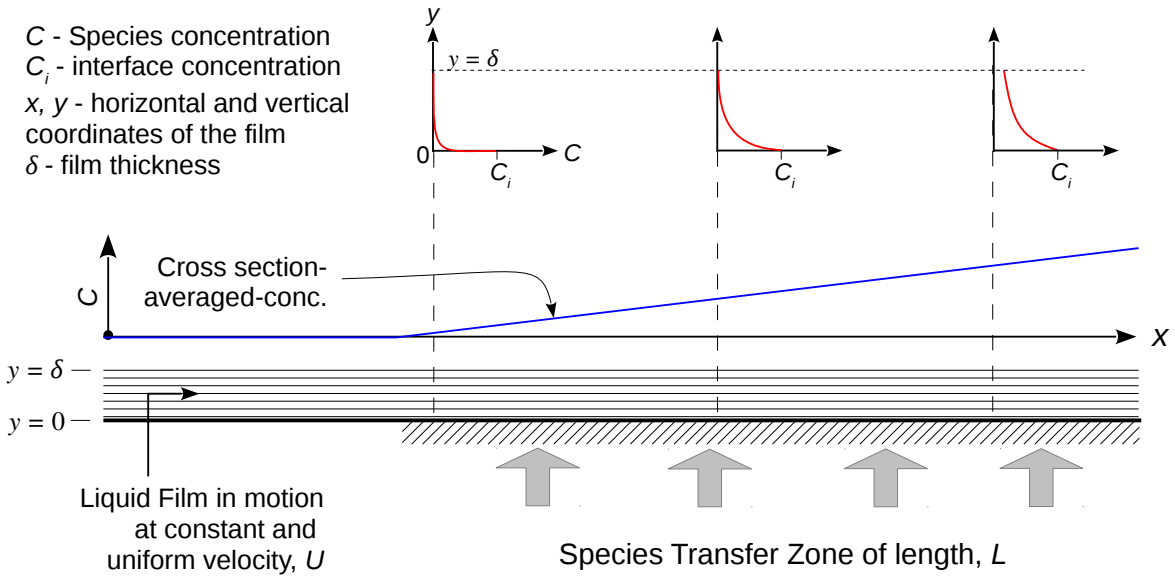

Figure 8.1. Illustration of Penetration theory. Diffusion of species takes place through the film across the hatched zone - depicted by concentration profiles at three locations - resulting in constant accumulation of species - depicted by the 'cross section averaged concentration' profile.

The **diffusion coefficient** was taken from the correlation for diffusion of sulphur in liquid iron (Kawai, 1956),

$$D\left(m^2/s\right) = 4.9\times10^{-8}\exp\left(-4350/T\right),$$
$$\Rightarrow D = 4.8\times10^{-9}\ m^2/s \text{ at } 1873 \text{ K}. \tag{8.5}$$

The average mass transfer coefficients $\left(\overline{k}_L\right)$ thus obtained are plotted in Fig. 8.2. Using the physical length of interface markedly decreases $\overline{k}_L$ in the case of *ULflat*, as noted above, whereas at *ULeye* there are not much differences, primarily due to their large and small physical lengths, respectively.

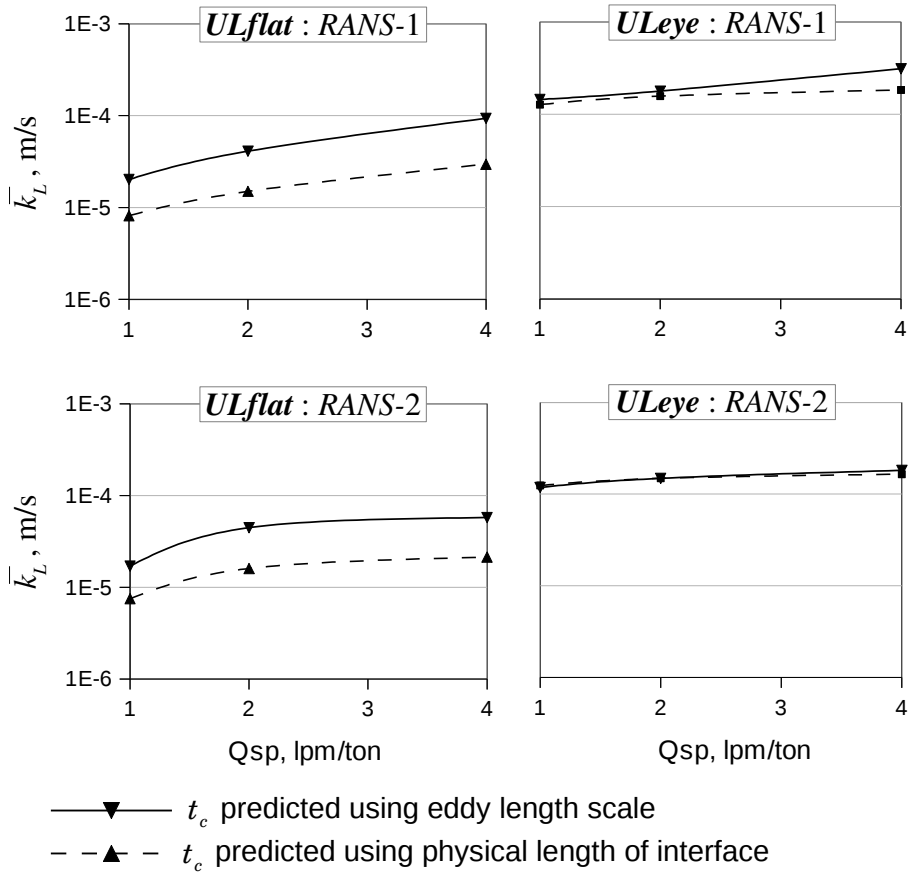

Figure 8.2. Average mass transfer coefficients $(\bar{k}_L)$ *versus* specific gas injection rates (Qsp, lpm/ton) for two QSP-RANS Configurations at two interface zones, *ULflat* and *ULeye*. Common y-axis and legend

In case of drops, Eq. (8.2) is cast as,

$$\frac{k_L d_P}{D} = \frac{2}{\sqrt{\pi}} Re^{1/2} Sc^{1/2}, \tag{8.6}$$

where $Re = U d_P/\nu$ and $Sc = \nu/D$ are the Reynolds number and Schmidt number respectively, $d_P = (6V_P/\pi)^{1/3}$ is the equivalent particle (drop) diameter and ν is the kinematic viscosity of the continuous phase. This form was convenient because, one of the outputs of LPT (Ch. 7) was the average Reynolds number (ensemble averaged) for various particle size classes and therefore can be directly used. The $\bar{k}_L$ values thus obtained are plotted in Fig. 8.3 for the 9 cases corresponding to *RANS*-1, which are also very similar to that of *RANS*-2 (not shown

here) and the differences among various cases are not significant. It is noteworthy that $\bar{k}_L$ values at *ULdrop* are significantly larger than at *ULflat* and *ULeye*.

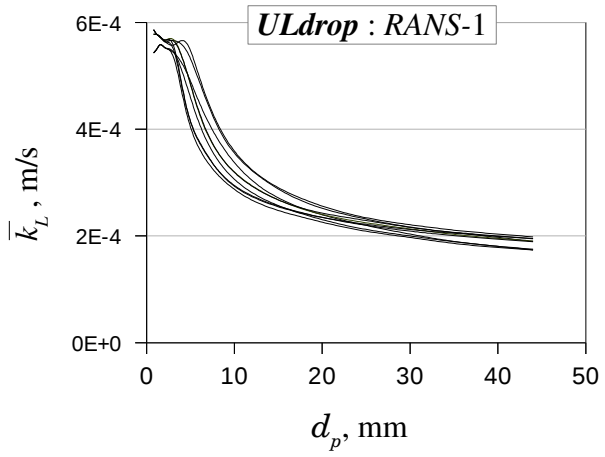

Figure 8.3. Average mass transfer coefficients $(\bar{k}_L)$ versus droplet sizes (d_P) for the 9 cases obtained from Reynolds numbers estimated in LPT using *RANS*-1. Legend is not provided due to the small difference between various cases.

8.1.2 Other Parameters

8.1.2.1 Size Distribution Parameters

Lognormal distributions given by Eq. (3.20) were fitted to the droplet size distributions, obtained from the multiphase LES (Ch. 6). The distribution parameters were derived from the mean and variance of the LES results†. Comparison of two cases of size distributions of LES results against lognormal distributions with their corresponding mean and variances in Figure 8.4 shows that lognormal distribution satisfactorily fits the LES results. The values of these parameters are tabulated in Appendix F.2.

† the footnote in Pg. 42 has the relation between parameters of distribution and its mean and variance.

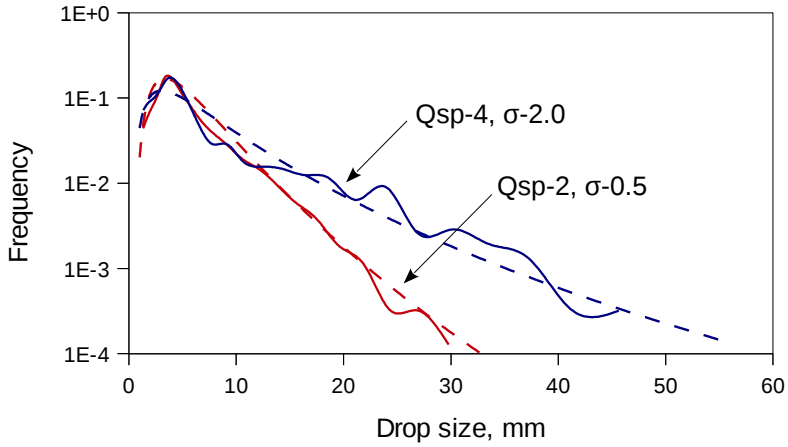

Figure 8.4. Comparison of size distributions of LES results (continuous line) and lognormal fit (dashed lines) for two extremes of the 9 cases

8.1.2.2 Interfacial Areas

The area of *ULflat* was obtained simply from,

$$A_{ULflat} = \pi(R_{ves}^2 - R_{eye}^2), \tag{8.7}$$

where R_{ves} and R_{eye} are the radii of vessel (ladle) and slag eye, respectively.

However, the area at *ULeye*, A_{ULeye}, having large convolutions as seen in Figs. 6.10 and 6.11, must be obtained from the respective multiphase LES cases. Within each case, approximately 15 time instances of Gerris simulation outputs were post processed to extract the areas. Appendix F.3 has the required Shell code to automatically process the Gerris output files. The idea is to first choose the domain where the interface at the eye is supposed to be, as shown in two examples in Fig. 8.5; the extent of this domain varies with each flow rate. At any instant, after all the droplets have been removed, the remaining VOF area in the chosen domain is outputted by running the Gerris simulation for one time step. The area values thus obtained are averaged and are scaled up for the cylindrical vessel using the same factor to scale up *VPU* in Eq. (6.6). These values are plotted in Fig. 8.6a along with A_{ULflat} calculated using Eq. (8.7). It shows that the A_{ULeye} is significantly larger than A_{ULflat} at higher flow rates. The plot of normalized area in Fig. 8.6b shows that A_{ULeye} is several times larger than A_{ULeye}^{nom}.

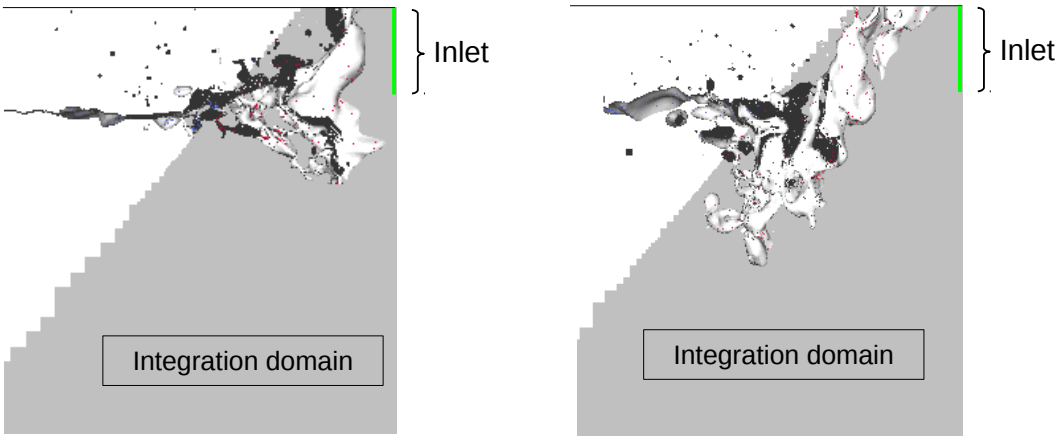

Figure 8.5. Two instances of LES simulations showing the gray area (labeled) to integrate the area of two phase interface at *ULeye*.

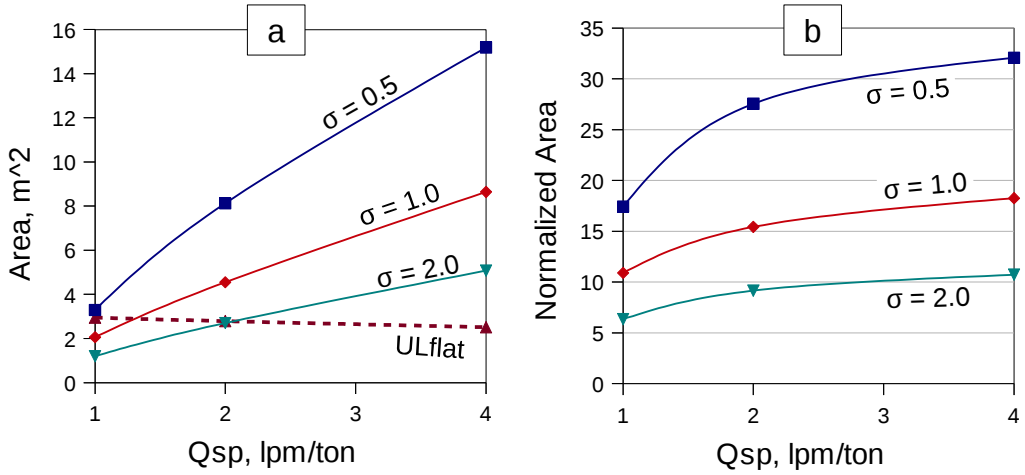

Figure 8.6. Interfacial areas of the bulk phases (ULeye and ULflat) for the 9 LES cases as combinations of three Qsp and σ values (a) dimensional and (b) same as (a) but normalized by A_{ULeye}^{nom} [Eq. (6.4)].

8.1.2.3 Partition Coefficient

As noted Sec. 6.1.3, the slag viscosity of 0.11 Pa.s correspond to a slag of composition, 35–50–7–8 mass% of Al_2O_3–CaO–SiO_2–MgO. The partition coefficient for this composition was found using the data of Bannenberg *et al* (1994) summarized in charts in Fig. 8.7. From Fig. 8.7a, the so called 'lime saturation index' for the present slag (marked at 38–54–8 mass % of Al_2O_3–CaO–SiO_2) is found to be approximately 0.8. For this value, using the chart in Fig 8.7b, the sulphur distribution ratio in mass%, $(\%S)/[\%S]$, is approximately taken as 500 at 0.03 mass% Al dissolved in liquid steel ([%Al]). Using this, the partition coefficient defined in molar ratio as,

$$L_S = \frac{(S)}{[S]} = \frac{\rho_U (\%S)}{\rho_L [\%S]}, \tag{8.8}$$

is therefore **200** for this slag composition. The effect of partition coefficient is discussed later in Sec. 8.2.9.

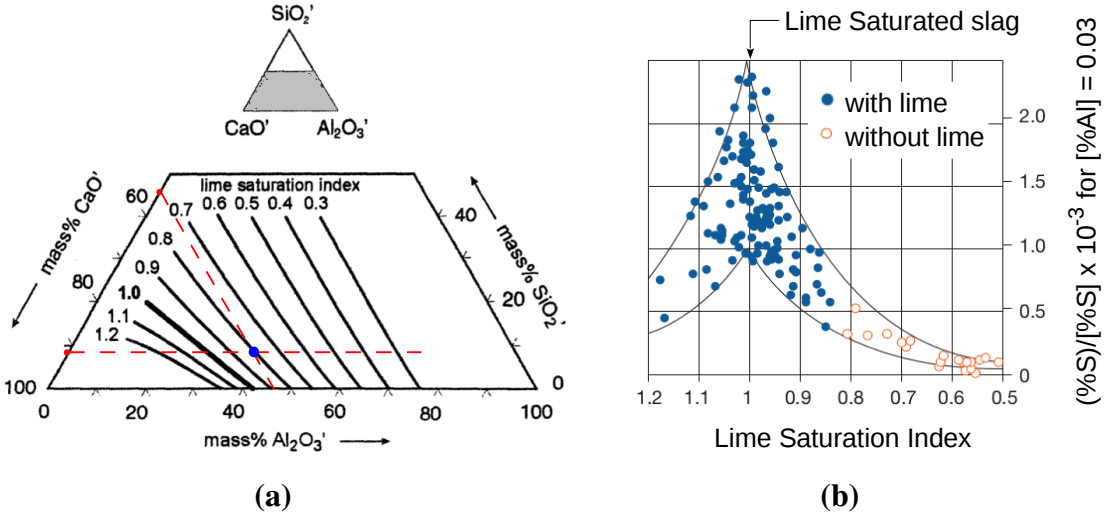

(a) **(b)**

Figure 8.7. Data from Bannenberg *et al* (1994) – (a) Lime saturation indices for the Al_2O_3-CaO-SiO_2 system; the composition marked in the figure (38–54–8 mass%) corresponds to slag composition in the present work (b) Sulphur distribution ratio, (%S)/[%S], versus lime saturation index; in case of 'without lime' MgO content contributes for (%S)/[%S].

8.2 Mass Transfer Rate Computations

Various parameters discussed until now are fed into the DBD model to compute the rate for each case. As discussed in Ch. 3, the principal output of the DBD model, namely the time varying species concentration profile, is fitted with first order exponential decay; the resulting decay constant (λ) is converted to the overall rate constant $(\beta = k_L A/V_L)$. Generally in the literature, for high temperature systems, the rate constant has been plotted against specific stirring power, ε (W/ton) and hence the same is followed in the present work. Despite variations in definitions for ε, the following is used (based on Berg *et al*, 1985, Lachmund *et al*, 2003, Graham, 2008):

$$\varepsilon\,(W/ton) \;=\; \frac{RTQ(STP\,m^3/s)}{m_L(ton)V_N}\ln\left(1+\frac{\rho_L g\,h_L}{101325}\right). \tag{8.9}$$

where m_L is mass of lower phase, $V_N = 22.4$ liter per mole of gas, $R = 8.314$ J/mol/K, $T = 1873$ K and $g = 9.81\,m\,s^{-2}$.

A time step size of 0.1 s was used for all computations. The case with highest *VPU* was run with time step sizes of 0.05 and 0.02 s and various outputs of the DBD model including the rate constant showed no more than a 1% relative difference with respect to the results obtained using the time step size of 0.1 s.

8.2.1 Role of QSP-RANS Field and Choice of Length Scale for Mass Transfer Coefficient

Combination of two QSP-RANS configurations and two schemes of mass transfer coefficients discussed in Sec. 8.1.1 yields four configurations for mass transfer computations, as listed in Table. 8.1. The results of DBD model runs are plotted in Fig. 8.8. Excluding the curves corresponding to σ = 0.5 for a while (discussed later in Sec. 8.2.2), the classic linear relationship between logarithms of stirring rate (ε) and rate constant (β) is more or less well predicted in *MT*-3 and *MT*-4 than the others and hence *RANS*-2 is regarded as better than *RANS*-1. Under *RANS*-2, there is almost no influence of choice of length scale on the overall

rate. This is because,

- the differences in k_L is significant only for *ULflat* (Fig. 8.2)
- *ULflat* has smaller k_L and area fraction compared to *ULeye* and *ULdrop* (Figs. 8.2 and 8.6, respectively) that the mass transfer at *ULflat* is secondary and so the differences in k_L go unmanifested.

Given the simplicity of estimating k_L based on physical length of interface, the configuration, *MT*-3 is preferred and used in all the computations ahead. However it will be shown later in Sec. 8.2.7 that the choice of length scale do affect the estimation of β in the range of ε below the onset of entrainment (Regime I), with the physical length based estimates giving better trends.

Table 8.1. Four configurations of mass transfer rate computations

		Length scale for contact time	
		Physical	Eddy
RANS Configuration used to obtain $\bar{t}_{res}$	*RANS*-1	***MT*-1**	***MT*-2**
	RANS-2	***MT*-3**	***MT*-4**

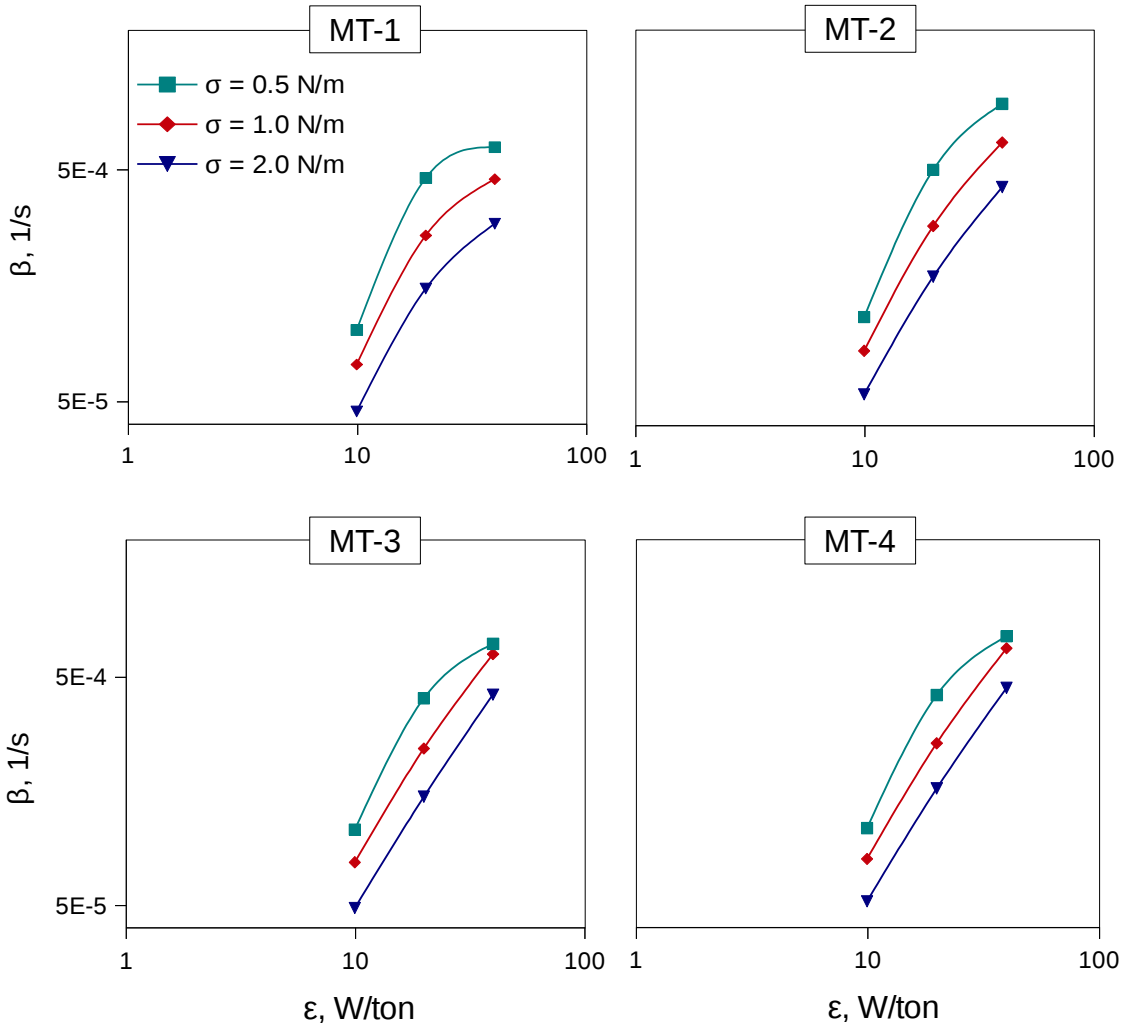

Figure 8.8. Mass transfer rate constant (β) versus specific stirring rate (ε) of cases listed in Table 8.1. Common y-axis and legend

8.2.2 Role of Interfacial Tension and Contribution of Droplets

The cause and effect diagram in Fig. 8.9 depicts the role interfacial tension as follows: the lowering of σ, apart from causing a small increase in *VPU* ($VPU \propto 1/\sigma^{0.25}$, from Sec. 6.4), increases $\bar{t}_{res}$ (in Fig. 7.22) which in turn increases the net transitional volume and interfacial area of droplets; besides, it also increases the interfacial area at *ULeye* (LES results in Fig. 8.6), altogether having pronounced effect on the net interfacial area. While the interfacial area factor acts as doorway for species transfer, the volume factor acts as a reservoir and hence together affect the overall mass transfer. Therefore lowering of σ increases mass transfer rate in three primary ways.

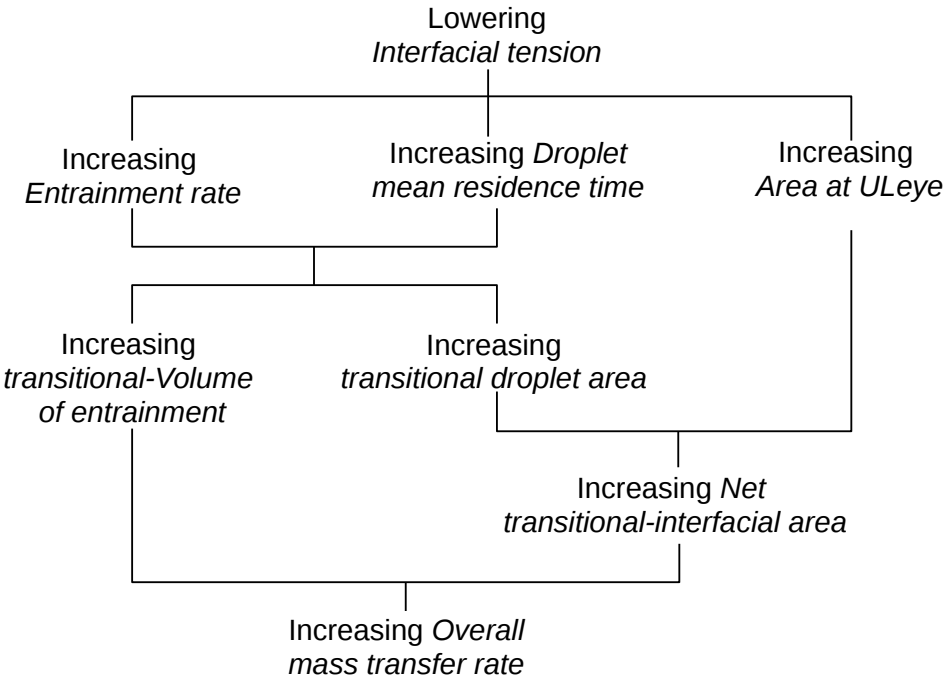

Figure 8.9. Role of interfacial tension on various parameters eventually affecting the overall mass transfer rate

While for other values of σ the $\beta - \varepsilon$ curve is linear (in log-log scale) in Fig. 8.8, *MT*-3 in particular for the present discussion, for $\sigma = 0.5$ at $Q_{sp} = 4$, the rate of increase of β with ε (or Q_{sp}) slows down. To explain this, we look into the contribution of droplets to mass transfer

plotted in Fig. 8.10, defined in the DBD model as,

$$\%\,\text{Droplet contribution} = \frac{\text{Number of moles transferred at droplets}}{\text{Total number of moles transferred}} \times 100. \qquad (8.10)$$

At Q_{sp} = 4 and σ = 0.5, the droplet contribution has decreased drastically. This means the predominance of mass transfer shifts from drops to other interfaces, namely *ULflat* and *ULeye* and particularly to *ULeye* due to its larger area fraction and mass transfer coefficient of the two. The shift occurs because of weaker dependence of *VPU* on σ and ever increasing area at *ULeye* with lowering σ (Fig. 8.6). But the mass transfer coefficient at *ULeye* is significantly smaller than at drops (Sec. 8.1.1); so, the shift has slowed down the rate of increase of β with Q_{sp} (or ε) resulting in the non-linear $\beta - \varepsilon$ curve (in log-log scale).

In most practical applications σ is above 1.0 N/m and may briefly drop to values around 0.5 N/m (Sec. 6.1.4) and therefore the cases of σ = 0.5 are not very representative.

Besides, it is important to note from Fig. 8.10 that while the contribution due to *ULeye* is major only below moderate flow rates, it is still significant at higher flow rates and hence cannot be disregarded.

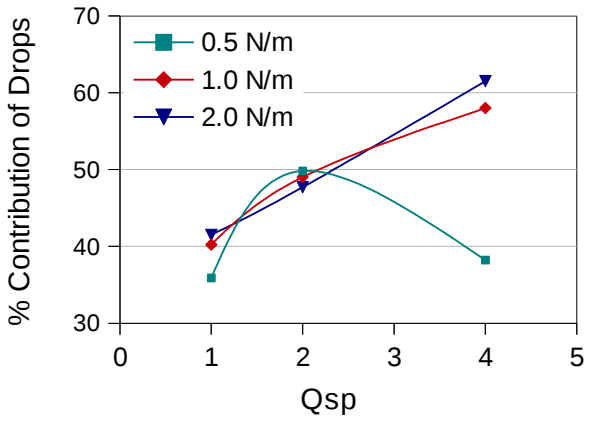

Figure 8.10. Percentage contribution of droplets to mass transfer computed by the DBD model

8.2.3 Comparison with Literature Cases

From four literature sources, Ishida *et al* (1981), Berg *et al* (1985), Lachmund *et al* (2003) and Graham (2008) we have information regarding the $\beta-\varepsilon$ relationship for desulphurization in high temperature steel slag systems, as tabulated in Table 8.2 and plotted in Figure 8.11; in the same order, their metal capacities are 2.5, 4 to 6, 185 and 165 ton. For Berg *et al* (1985), neither the data nor correlations are available in direct form and had to be derived (see Appendix F.4). The correlation for Lachmund *et al* was derived from the $\beta-\varepsilon$ chart in that reference. The correlation of Graham found in the author's thesis is larger by a factor of 1000 and was clarified through a private communication.

In general large variations are seen both in β and ε among the three sources, particularly the break-point indicative of onset of entrainment. Primarily, this is likely because neither of β nor ε are appropriately scaled to accommodate the large variations in metal capacities. The scaling aspects discussed later in Sec. 8.2.8. However, the $\beta-\varepsilon$ curves of Berg *et al* are quite apart despite having a similar metal capacity as Ishida *et al,* probably due to some error in their calculation of proportionality constants.

There is also a significant spread in exponent to ε ranging from 1.0 to 2.1 considering only those above critical gas injection rate (Regime-II), wherein the exponent of Berg *et al* is within the said range. But then, the curves of Graham and Lachmund *et al* do not show the break-point phenomenon even below ε = 10 W/ton; this has been noted in those references as well, but without a definite explanation. In the water modeling studies of Kim & Freuhan (1987) it was shown that the exponent to ε decreased from 2.5 to 2.1 for multiple gas injection tuyeres (see Table 2.1 and Fig. 2.9). This is the reason for smaller exponents in the case of Graham and Lachmund *et al* as compared to Ishida *et al*. A further explanation based on the models of present work is provided in Sec. 8.2.7. Since Graham's case is the nearest available configuration (165 ton, double plug), it is used for various model comparisons ahead.

Table 8.2. Mass transfer rate correlations from literature. See text for conditions

Sources	Capacity	Number of plugs	$\beta-\varepsilon$ Regimes		$\beta-\varepsilon$ Correlation
Ishida *et al* (1981)	2.5 ton	1	I	$\varepsilon < 60$	$\beta = 1.9\times10^{-4}\,\varepsilon^{0.25}$
			II	$\varepsilon \geq 60$	$\beta = 1.2\times10^{-7}\,\varepsilon^{2.1}$
Berg *et al* (1985)	4 to 6 ton	1	I	$\varepsilon < 600$	$\beta = 4.3\times10^{-4}\,\varepsilon^{0.3}$
			II	$\varepsilon \geq 600$	$\beta = 7.2\times10^{-7}\,\varepsilon^{1.3}$
Graham (2008)	165 ton	2	II	$8 < \varepsilon < 60$	$\beta = 6\times10^{-6}\,\varepsilon^{1.4}$
Lachmund *et al* (2003)	185 ton	3	II	$6 < \varepsilon < 300$	$\beta = 1\times10^{-5}\,\varepsilon^{1.0}$

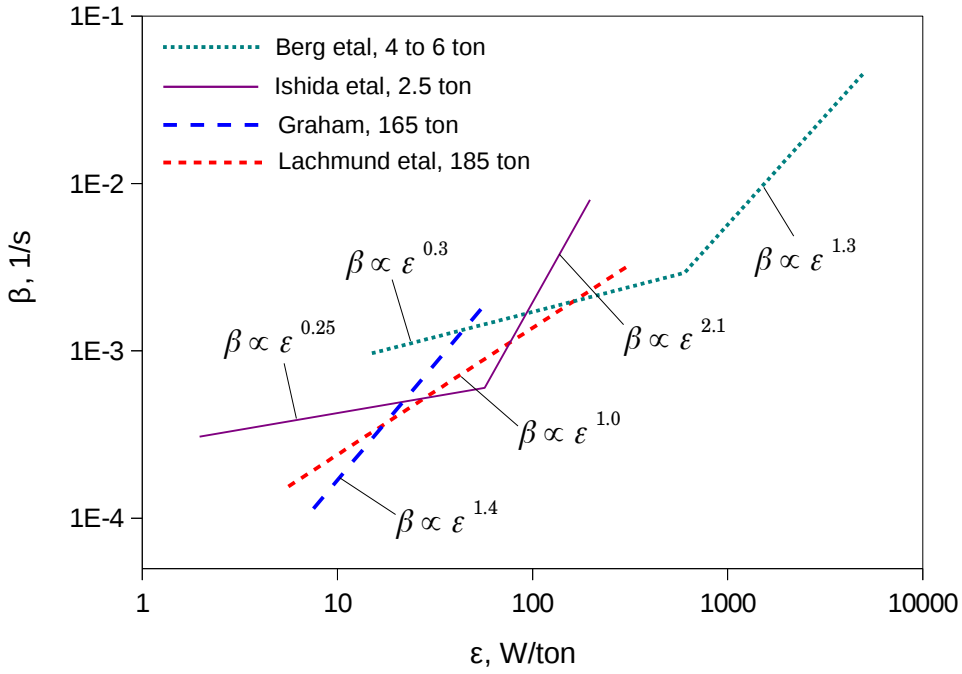

Figure 8.11. Rate constant (β) versus specific stirring rate (ε) plots based on data for desulphurization kinetics in high temperature steel-slag systems found in the literature. The actual data points are omitted for clarity.

Comparison between the results from the present work (*MT*-3) with Graham's correlation is presented in Fig. 8.12; a remarkable similarity is apparent. Power law type of curves fitted to $\beta - \varepsilon$ plots yield exponents to ε of 1.35, 1.51 and 1.55 for each curve, in the increasing order of interfacial tension; these are close to and slightly higher than in Graham's correlation, in accordance with the idea of single plug–centric gas injection in the present work, as against the double plug of Graham's case. The smaller magnitude of β of the present model with that of Graham's correlation is explained later in Sec. 8.2.4.

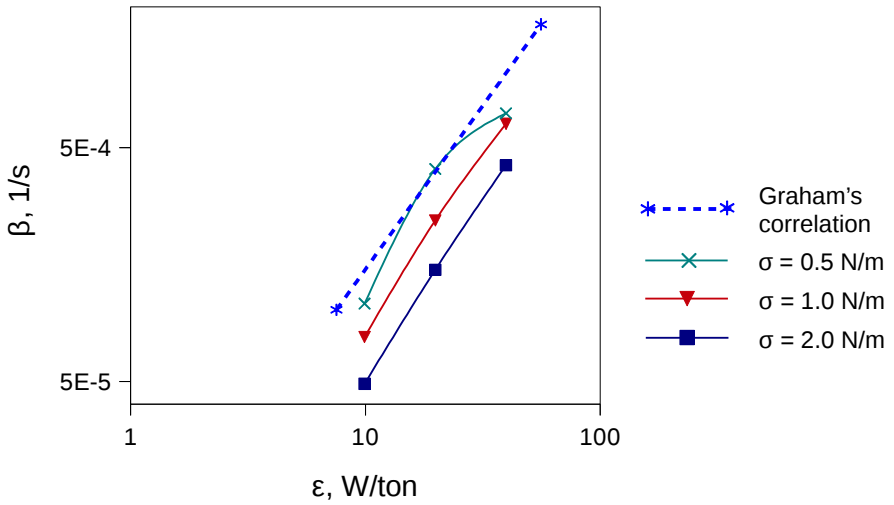

Figure 8.12. Comparison of β–ε plots of model results of configuration *MT*-3 with Graham's correlation that is based on trials in 165 ton industrial ladle

8.2.4 *150* Ton Ladle

It was attempted to estimate mass transfer rates for a larger ladle without performing the expensive LESs but using correlations of the 44 ton ladle and scaling relations, although performing separate QSP-RANS and LPT for $\bar{t}_{res}$. The ladle is of 150 ton capacity, geometrically similar to the 44 ton ladle with bath height (h_L) and vessel diameter of 3.0 m each, *i.e.*, the linear scaling factor,

$$\lambda = \frac{l_{150}}{l_{44}} = 1.5. \tag{8.11}$$

It has been established by Krishnapisharody & Irons (2013) that the dynamic similarity for plume and melt flow in the ladle is ensured through the dimensionless gas flow rate,

$$Q^* = \frac{Q}{g^{0.5} h_L^{2.5}}. \tag{8.12}$$

The resulting similarity is characteristic of Froude similarity criterion, for which the velocity (U) and time (t) in two geometrically similar systems, as in our case the 44 and 150 ton ladles, at corresponding locations follow the ratios,

$$\frac{U_{150}}{U_{44}} = \frac{t_{150}}{t_{44}} = \lambda^{0.5} \tag{8.13}$$

In addition it naturally ensures the geometric similarity of slag eye radius, slag thickness and spout dimensions given by models listed in Sec. 4.4.1.2. Based on these the input parameters for this ladle required by the DBD model were derived as follows.

1. Three gas flow rates at half bath height were chosen *corresponding* to the 44 ton ladle, namely 500, 1000 and 2000 lpm and incidentally the specific gas injection rates for these cases are also, 1, 2 and 4 lpm/ton, respectively. Since interfacial tension mostly varies within 1.0 to 2.0 N/m the 0.5 N/m cases are neglected in this exercise.
2. The entrainment rates were scaled up from 44 ton according to,

$$VPU_{150} = \lambda^{3/2} \left(VPU_{44} + 0.46 \right) - 0.46 \tag{8.14}$$

using Eq. (6.10) and Eqs. (8.11) and (8.13).

3. The same droplet size distribution parameters of the 44 ton cases were used. In Sec. 6.2.2 it was shown that gas flow rate has little influence on mean droplet sizes unlike the interfacial tension. So with respect to gas flow rate, the size distributions can be considered universal and applied to any flow rates, although for corresponding interfacial tension values.
4. The interfacial areas were simply scaled up as,

$$A_{ULeye,150} = \lambda^2 A_{ULeye,44}, \tag{8.15}$$

although strictly it may not be true.

5. For $\bar{t}_{res}$, QSP-RANS with *RANS*-2 configuration and subsequent LPTs were performed for the three flow rates. Expectedly, the flow fields were *similar* to corresponding 44 ton cases (Fig. 7.13) and hence not presented here. The values of $\bar{t}_{res}$ computed from LPT for $\sigma = 1.0$ and 2.0 are plotted in Fig. 8.13. Although somewhat similar to plots corresponding to 44 ton (see Fig. 7.22), the ratios, $\bar{t}_{150} / \bar{t}_{44}$ plotted in Fig. 8.14 show that the Froude similarity criterion for time scaling,

$$\bar{t}_{150} / \bar{t}_{44} = \lambda^{0.5} \approx 1.225 \tag{8.16}$$

is **not valid**. Also, the spread in the ratio questions the existence of any similarity criterion for $\bar{t}_{res}$.

6. The mass transfer coefficients were obtained from QSP-RANS using the same procedure described for 44 ton cases.

The mass transfer rates computed from the DBD model and plotted in Fig. 8.15 show that model results are remarkably similar to the Graham's correlation, appropriately, better than those corresponding to the 44 ton cases. In the 150 ton ladle, the exponents to ε are 1.67 and 1.56 for $\sigma = 1.0$ and 2.0, respectively, slightly higher than that of Graham, again in accordance with the differences in bottom plug configuration (single–centric *vs* double–eccentric plugs).

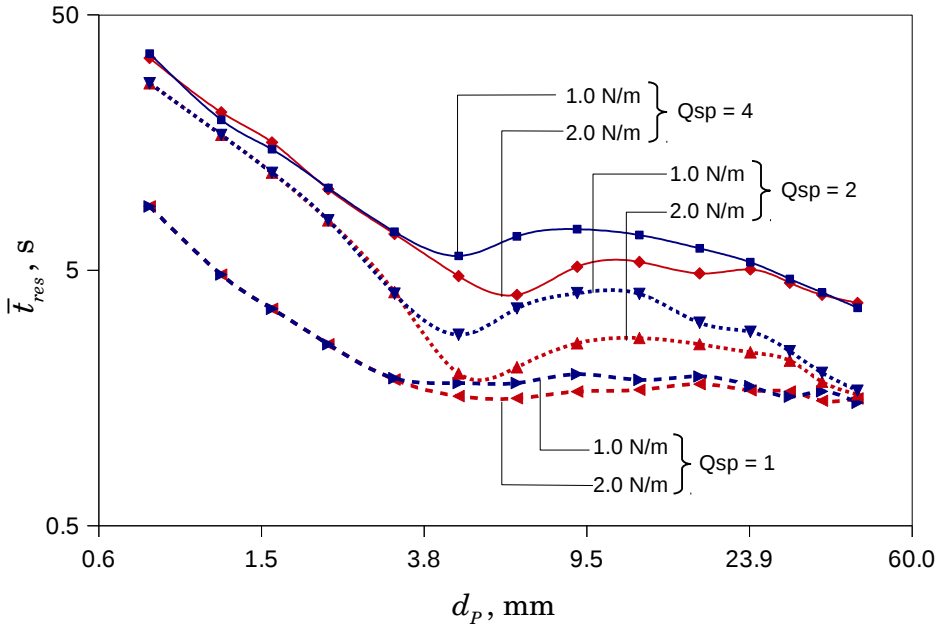

Figure 8.13. Mean residence times vs droplet size for three specific gas injection rates (Qsp) of 150 ton ladle at σ =1.0 and 2.0 N/m.

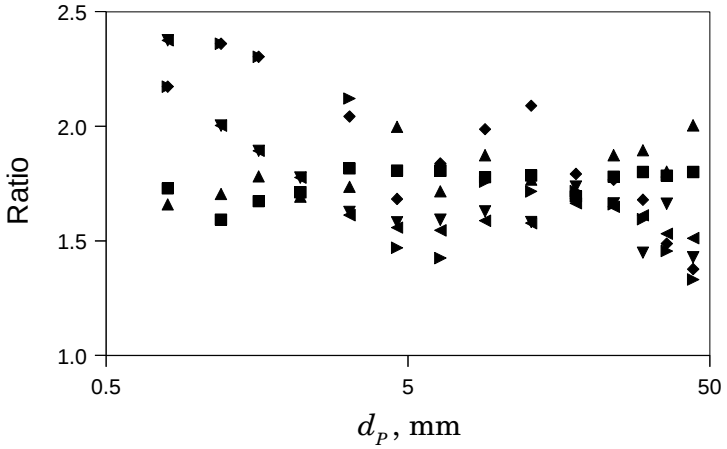

Figure 8.14. Ratio of mean residence times between 150 ton and 44 ton ladles ($\bar{t}_{150}$ / $\bar{t}_{44}$) of all cases in Fig. 8.13

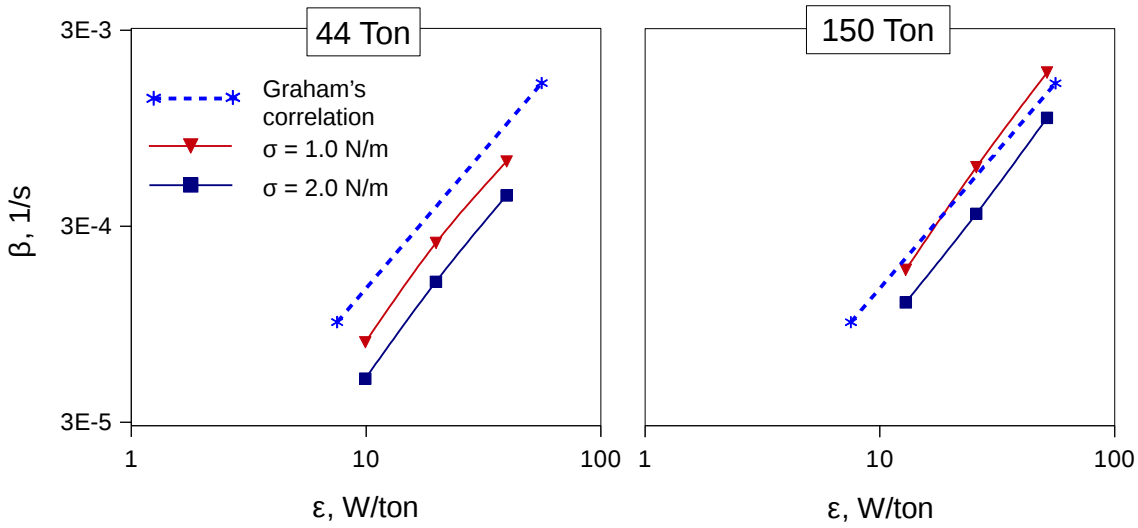

Figure 8.15. Comparison of *β*–*ε* plots of model results of configuration *MT*-3 for 44 ton (shown again for reference) and 150 ton ladles against Graham's correlation for 165 ton ladle. Common y-axis and legend.

In Fig. 8.15, keeping Graham's correlation as reference, we see that the corresponding $\beta - \varepsilon$ curves of 44 ton is below that of 150 ton, despite being *similar* ladles (including flow rate). In other words, for a given ε, the larger vessel has higher mass transfer rate. This is because, for a given ε, the gas flow rate is higher in the larger vessel leading to higher plume velocity and velocity near *ULeye* that results in higher entrainment rate and droplet residence time and also with higher area at *ULeye* due to higher A_{ULeye}^{nom}, mass transfer rate is eventually higher.

The consistent results obtained hitherto support various sub-models of this overall entrainment model on a global level.

8.2.5 Approximate Estimation of Mass Transfer Rates

In Sec. 8.2.4 the need for LES was bypassed by using correlations and scaling laws to scale up the input parameters from a *similar* ladle. Without the requirement of results from a *similar* ladle, a further attempt to derive input parameters solely based on correlations, QSP-RANS and LPT is presented here. The acquisition of input parameters are outlined as follows

1. To find the entrainment rate from Eq. (6.10), A_{ULeye}^{nom} can readily obtained using Eq. (6.4) and the models in Sec. 4.4.1.2, whereas $\bar{v}_L$ requires an LES. To avoid the LES step it was attempted to correlate $\bar{v}_L$ with the line-average of velocity profile extracted from the QSP-RANS ($\bar{v}_{RANS}$, defined by Eq. (6.3)] of the 44 ton ladle cases. The resulting correlation,

$$\bar{v}_L = \bar{v}_{RANS} + \sigma/15; \quad R^2 = 0.978 \tag{8.17}$$

   is a reasonable approximation as shown in Fig. 8.16a.

2. Same droplet size distribution parameters of the 44 ton cases were used (justified in Sec. 8.2.4)
3. To account for the actual area at *ULeye*, which has significant contribution to mass transfer (Sec. 8.2.2), another simple correlation was devised as follows:

$$A_{ULeye} = 27\frac{A_{ULeye}^{nom}\bar{v}_L}{\sigma}; \quad R^2 = 0.975 \tag{8.18}$$

   which uses Eq. (8.17) for $\bar{v}_L$. Figure 8.16b shows that Eq. (8.18) is a reasonable approximation.
4. The mass transfer coefficients were obtained based on the configuration *MT*-3, described in previous sections.
5. For $\bar{t}_{res}$, the required QSP-RANS and LPT are already computed for cases in Sec. 8.2.4.

The input parameters for both 44 ton and 150 ton ladle thus obtained were fed into the DBD model and resulting mass transfer rates are plotted in Fig. 8.17. In comparison with their respective plots in Fig. 8.15, except at the smallest ε, the β values are well reproduced. This

shows that the simple models given by Eqs. (8.17) and (8.18) and the correlation for *VPU* combined with QSP-RANS, LPT and DBD model (*i.e.*, all, excepting the LES step) may be used for faster estimation of mass transfer rates.

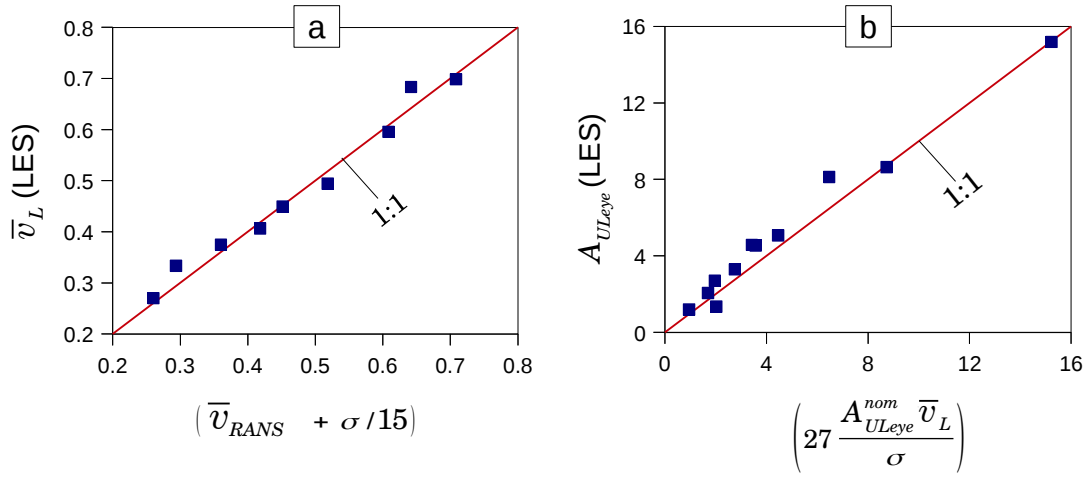

Figure 8.16. Approximate correlations (x-axis) developed from LES results for predicting (a) average velocity near *ULeye* and (b) interfacial area at *ULeye*, compared against their respective LES results (y-axes) using 1:1 lines

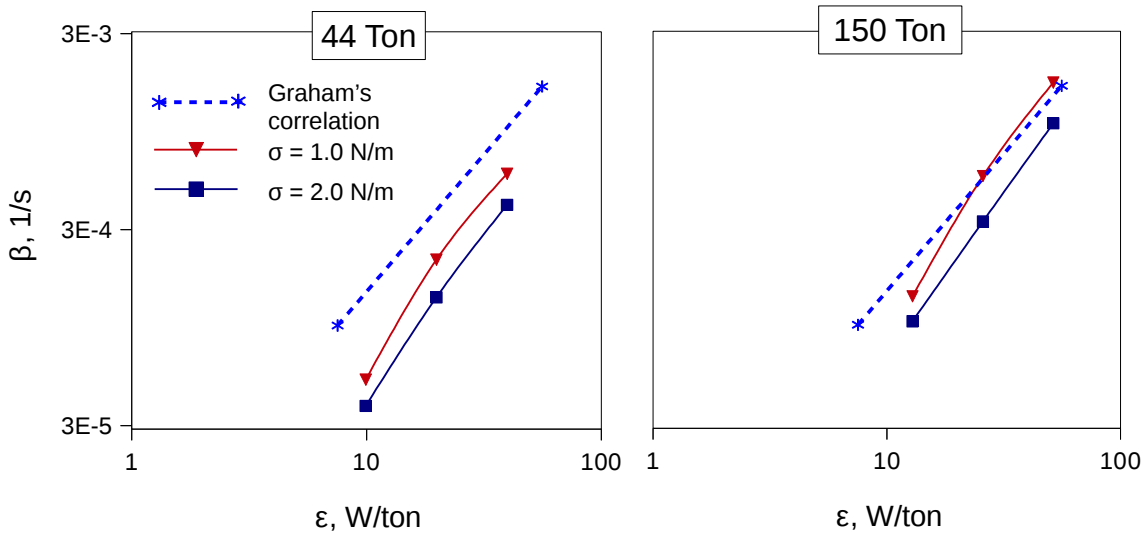

Figure 8.17. Comparison of *β*–*ε* plots of model results of 44 ton and 150 ton ladles against Graham's correlation for 165 ton ladle. The models are based on *MT*-3 and LES correlations. Common y-axis and legend.

Estimation for Multiple Bottom Plugs: For a double plug, β at a given ε cannot be obtained simply by doubling the value of β of centric-single plug at $\varepsilon/2$, because the exponent to ε will still be the same as that of the centric-single plug while it should have decreased for multiple plugs (noted in Sec. 8.2.3, also explained later in Sec. 8.2.6). More generally for multiple plugs,

$$\beta(\varepsilon) \neq N \times \beta(\varepsilon / N) \tag{8.19}$$

where N is the number of plugs. However, it might be possible by following the steps in Sec. 8.2.5 except for following changes:

1. Estimate R_{eye} and h_U for multiple plug (see Appendix F.5 for procedure).
2. Perform QSP-RANS and LPT in three dimensional coordinates due to loss of axisymmetry.
3. From QSP-RANS extract velocity profile on the cylindrical surface near *ULeye* (as against a line in 2D) on each slag eye since axisymmetry within each eye may also have lost; use this to estimate integrated $\overline{v}_L$ and *VPU*.

8.2.6 Why do Multiple Plugs Decrease Exponent to ε?

For illustration a double plug case was derived based on the values of single plug, 44 ton ladle cases and then compared with values of a corresponding single plug case. The double plug case was derived as follows:

1. In case of multiple plugs gas flow rate is distributed among multiple plumes. So, if we take the $Q_{sp} = 4$ case, for single and dual plugs, Q = 710 and 355 lpm/plug, respectively.
2. Since the plume characteristics are governed only by flow rate and bath depth (K&I, 2013) the velocity near *ULeye* ($\overline{v}_L$) and θ_{ULeye} were simply taken from Table 6.3, which correspond to the single plug configuration.
3. R_{eye} and h_U were computed for the above flow rates; for double plug, procedure for multiple plug (Appendix F.5) was applied.
4. A_{ULeye}^{nom} and *VPU* were first estimated for single plug using appropriate relations and

then doubled.

5. Using the relations given by Eqs. (8.2), (8.3) and (8.18) it can be shown that at *ULeye*,

$$k\,A\big|_{ULeye} \;\propto\; A_{ULeye}^{nom}\,\overline{v}_L\sqrt{\overline{v}_L} \tag{8.20}$$

The estimates from above steps are tabulated in Table 8.3.

Table 8.3. Basic and derived parameters of single *vs* double bottom plugs based on 44 ton ladle model

	Single Plug	**Dual Plug**	
Q, lpm/plug	710	355	Table 6.3
$\overline{v}_L$, m/s	0.683	0.449	
θ_{ULeye}, degree	30	25	
R_{eye}, m	0.448	0.319	UP dimensions for multiple plug
h_U, m	0.131	0.133	
A_{ULeye}^{nom}, m^2/plug	0.468	0.330	Eq. (6.4)
A_{ULeye}^{nom}, m^2	0.468	0.660	
VPU , % /s /plug	2.20	1.01	Eq. (6.10)
VPU , % /s	2.20	2.02	
$A_{ULeye}^{nom}\,\overline{v}_L\sqrt{\overline{v}_L}$, S.I.	0.264	0.199	Eq. (8.20)

As compared to single plug, following are the consequences for the dual plug:

1. Due to the division of total flow rate, $\overline{v}_L$ has decreased.
2. Consequently total *VPU* has decreased marginally while $k\,A\big|_{ULeye}$ has decreased significantly.
3. Decrease in $\overline{v}_L$ also decreases the mean droplet residence time (from Fig. 7.22).

Altogether, these factors decrease the overall mass transfer rate for the dual plug and multiple plug ladles in general, thereby giving smaller exponent to ε in the $\beta-\varepsilon$ relation, as compared to a single plug ladle. However the advantage of multiple bottom plugs is that they allow larger gas flow rate without much splashing.

8.2.7 Regime-I Mass Transfer

Towards the end of Sec. 6.4 it was discussed that for the 44 ton ladle, the critical gas flow rate for onset of entrainment is around 90 lpm†. So, three more QSP-RANS were performed for flow rates 90, 60 and 30 lpm† with *RANS*-2 configuration, without the protruding 'lip' structure at *ULeye* and setting $\theta_{ULeye} = 15°$ for all cases. For the same configuration QSP-RANS were performed for flow rates 200, 100 and 50 lpm for the 150 ton ladle. For each case the velocities and eddy length scales near *ULflat* and *ULeye* were extracted, mass transfer coefficients were calculated using both the physical length of interface and eddy length (*i.e.*, *MT*-3 and *MT*-4, respectively), interfacial areas were estimated (simply the nominal areas, due to small flow rates) and finally the overall rate constant was directly estimated from,

$$\beta = \frac{\sum(k_L A)_i}{V_L}, \; i = ULflat, ULeye \tag{8.21}$$

without the need for DBD model, since droplets are absent.

Charts in Fig 8.15 are replotted in Fig. 8.18 with the estimated Regime-I values of β. The differences in the values of k_L between *MT*-3 and *MT*-4 have manifested as clear separation in the $\beta - \varepsilon$ plots in Regime-I that were practically absent in Regime-II (Sec. 8.2.1). Power law type of curves fitted to these Regime-I plots yield exponents to ε between 0.18 and 0.32. Except for the exponent of 0.18, all values are within the range of 0.25 to 0.4 for Regime I as summarized by Asai *et al* (1988, also in Deo & Boom, 1993) for various two phase systems and close to that of Ishida *et al* and Berg *et al* (Table 8.2).

***MT*-3 *versus MT*-4**: For the 44 ton ladle the critical gas flow rate of 90 lpm corresponds to ε = 5.0 W/ton. From Fig. 8.18 for 44 ton we see that only for *MT*-3 the points of intersection of Regimes I & II - $\beta - \varepsilon$ plots are close to 5.0 W/ton. So the relation, $\beta \propto \varepsilon^{0.18}$ is not precise and so the eddy length scale based estimation of k_L. However such differences are secondary when entrainment rate picks up (Regime II, Sec. 8.2.1).

† for *in-situ* temperature and pressure at half bath height

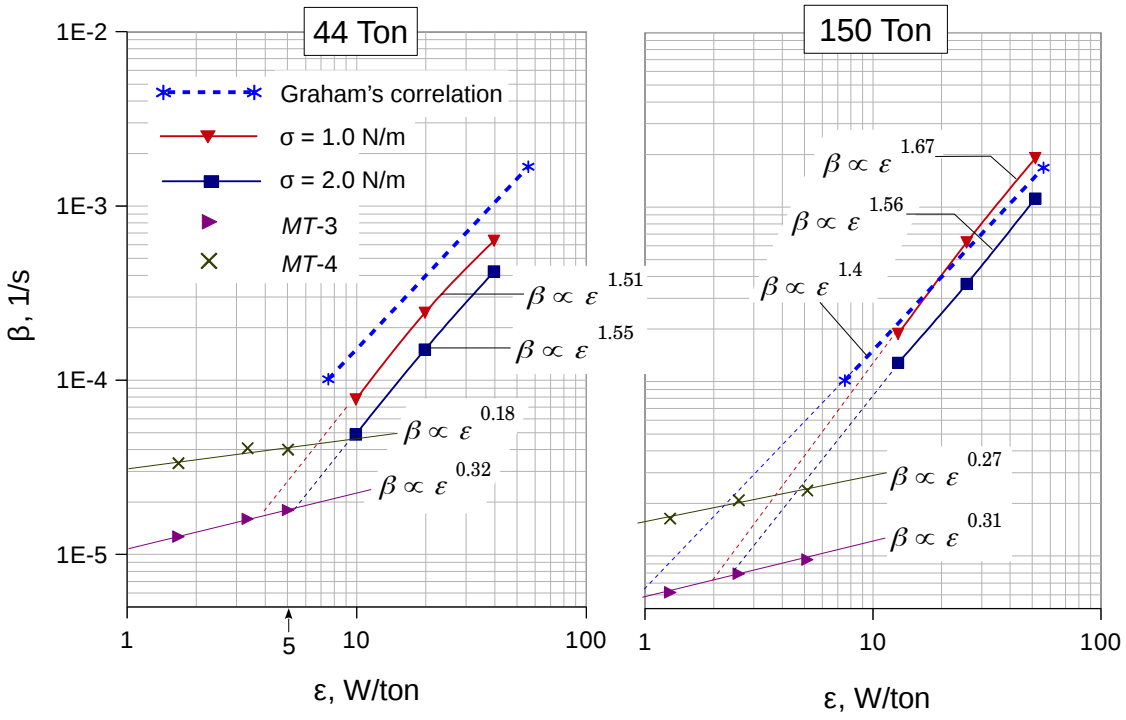

Figure 8.18. Charts in Fig. 8.15 replotted with β values for Regime-I mass transfer obtained for two mass transfer configurations, *MT*-3 and *MT*-4; power-law type trend lines are also shown for these points. Curves of Regime-II mass transfer are extended using dashed lines for illustration. Common legend and y-axis

Transition from Regime I to II: Consider the curves for 44 ton, $\sigma = 2.0$ in Fig. 8.18: At $\varepsilon = 10$ the ratio of β values of Regime II to I, $\beta_{II} / \beta_I \approx 2$, *i.e.*, overall mass transfer is 100% more than that would take place at nominal areas (Regime I, $\beta \propto \varepsilon^{0.32}$). We know from Fig. 8.10, the contribution of droplets to mass transfer for this case at $\varepsilon = 10$ $(Q_{sp} = 1)$ is only 40%. So the remaining contribution has come from the excess area due to A_{ULeye}, *i.e.*, $(A_{ULeye} - A_{ULeye}^{nom})$. If we go further down to $\varepsilon \approx 5$ (critical flow rate), we could appreciate that the 'abrupt increase' in mass transfer rate is primarily due to increase in A_{ULeye} and not due to entrained droplets. In fact, preceding the entrainment is the formation of waves, lip and ligaments at *ULeye* as discussed in Sec. 5.2.2.2, all of which increases A_{ULeye}. Since unlike droplet formation, increase in area is not a critical phenomenon, in reality, transition from Regime I to II will not

be abrupt, but only gradual. This can be clearly observed in the water modeling result of Kim *et al* (1987a) in Fig. 2.7.

In the parametric study in Ch. 3, abrupt increase in β was attributed solely due to onset of entrainment, but that was purely due to choice of parameters, in that the VPU factor dominated over the A_{ULeye} factor.

Location of Point of Transition: Selected $\beta - \varepsilon$ curves of 44 ton and 150 ton from Fig. 8.18 and that of Ishida *et al* from Fig. 8.11 are replotted in Fig. 8.19a. It is vivid that as the ladle size increases, the break-point between Regimes I and II lowers both in β and ε. Excluding Ishida *et al*'s plots and including that of Graham and Lachmund *et al* (from Fig. 8.11), Fig. 8.19a is replotted in Fig. 8.19b. Here we see that the increased number of bottom plugs has resulted in smaller slope of $\ln(\beta) - \ln(\varepsilon)$ lines (smaller exponents to ε) and along with the increased ladle capacity, the break-point has been pushed to very small values of β and ε that it is virtually absent (inferred from the illustrative extension lines). The break-point may appear at some value of ε so small that there would be no entrainment, in which case, increase in A_{ULeye} alone should be the reason for higher exponent to ε than what should be in that range (≈ 0.3). This analysis clarifies that as both the ladle capacity and the number of bottom plugs increase, the transition from Regime I to II becomes more gradual, hiding the break point for onset of entrainment.

8.2.8 Scaling Aspects

Scaling the mass transfer rates and operational variables would be useful to predict mass transfer rate for an unknown system dimensions. However, the existence of simple scaling criteria is questionable, given the elaborate steps that were required to estimate transfer rate for the 150 ton ladle based on values of 44 ton ladle, despite being *similar*. Yet the possibility for scaling is explored in the following.

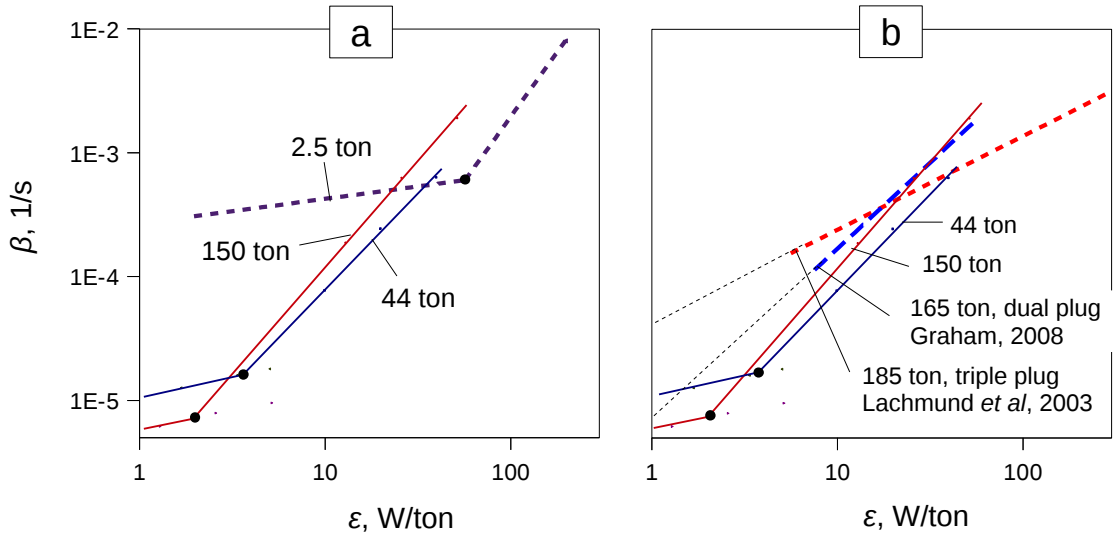

Figure 8.19. Comparison of β–ε plots of (a) Ishida *et al* (2.5 ton) (b) Graham and Lachmund *et al*, with that of 44 ton and 150 ton of present work corresponding to σ = 1.0 for Regime-II and *MT*-3 for Regime-I.

Towards the end of Sec. 8.2.4 it was noted that the $\beta - \varepsilon$ curves for 44 ton and 150 ton are apart, despite being similar ladle, which calls for proper scaling of β and ε.

In Sec. 8.2.4, it was noted that the dimensionless gas flow rate, Q^* [Eq. (8.12)] ensures various similarities related to melt flow in a ladle. So β (1/s) scaled by two possible time scales, namely (i) H/U and (ii) V_L/Q are plotted against Q^* in Fig. 8.20 (a) and (c), respectively. In (i) H is obtained from the ratio of slag-metal interfacial area before gas injection to the metal volume V_L, which gives, $H = h_L$ and U is taken as the plume velocity, U_P at half bath height. The curves do not collapse into one, neither did the plot of β *versus* Q^* (not shown here). The same is the case with plots–with Q^* replaced by ε–in Figs. 8.20 (b) and (d).

These attempts show that as of now we do not have appropriate scales or a similarity criterion to scale the mass transfer rates. The complex weaving of the constituent factors affecting the mass transfer rate, namely $\bar{v}_L$, A_{ULeye}, VPU and $\bar{t}_{res}$ will challenge such approaches to scaling.

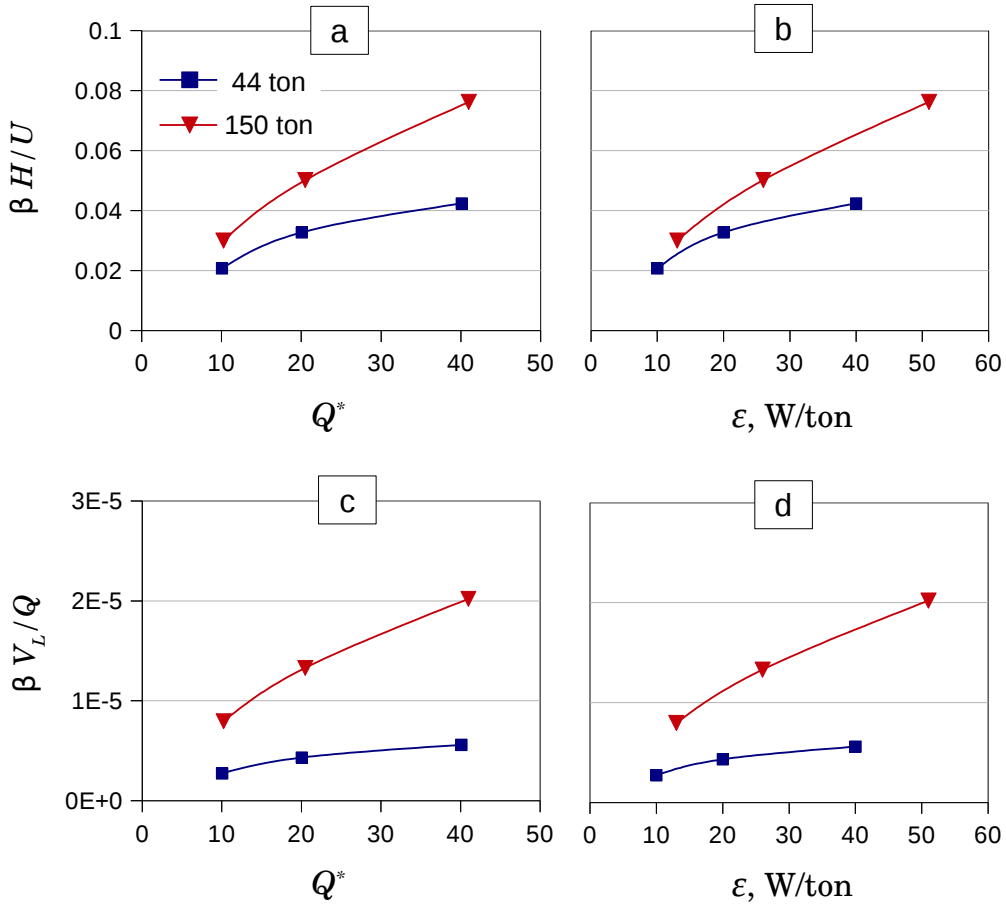

Figure 8.20. Plots of mass transfer rate constants for $\sigma = 1.0$ scaled by H/U and V_L/Q *versus* dimensionless flow rate Q^* and specific stirring rate, ε. Here, $H = h_L$ and U is plume velocity, U_P at $z = h_L/2$. Common legend and y-axes row-wise.

8.2.9 Effect of Slag Basicity

Slag basicity is mostly affected by lime content [(%CaO)] of slag. In Fig. 8.7b, we see that the sulphur partition ratio, $(\%S)/[\%S]$ (indicative of desulphurization capacity) increases rapidly as lime saturation index of unity is approached. Let us assume a hypothetical increase in lime content from the base composition (Sec. 8.1.2.3) such that $(\%S)/[\%S]$ can be quadrupled to 2000 (from the base value of 500) and hence the partition coefficient raised to 800. Now with $L_S = 800$, the DBD model was run for both 44 ton and 150 ton ladles using parameters of *MT*-3 at $Q_{sp} = 4$ and $\sigma = 1.0$. The resulting transient concentration profiles are compared against

that of same configuration but with $L_S = 200$, in Fig. 8.21. The times for reduction of initial concentration by 90% labeled in those plots indicate that (1) the larger ladle has higher mass transfer rate for a given Q_{sp}, for the reasons discussed already (Sec. 8.2.4) (2) higher L_S has higher mass transfer rate. An increase in L_S increases the driving force due to concentration difference and hence the mass transfer rate. However this analysis has not included the role of increased slag viscosity due to more lime addition.

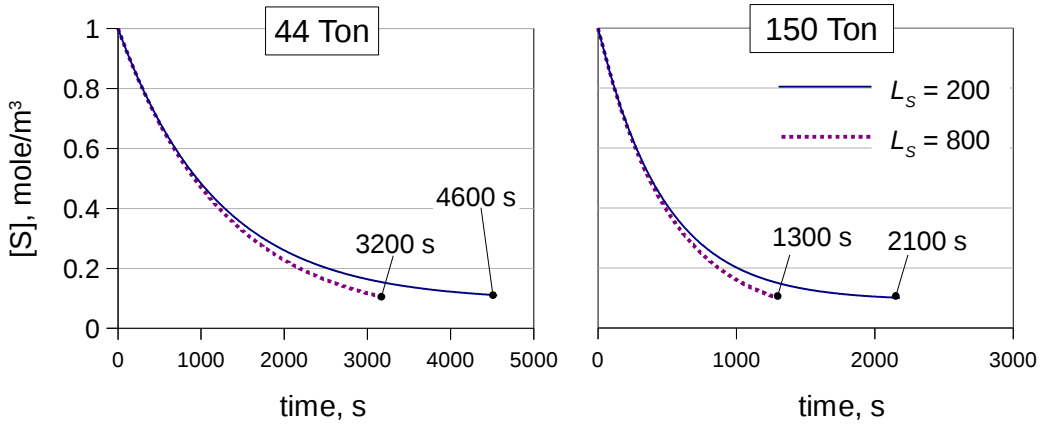

Figure 8.21. Effect of partition coefficient (LS) on mass transfer rate demonstrated by comparing concentration profiles of two cases whose parameters correspond to Qsp = 4 and σ =1.0. The time to reach 0.1 mole/m^3 is also labeled for each case. Common y-axis and legend.

In Fig. 8.7b, for lime saturation index, $LSI > 1$, $(\%S)/[\%S]$ decreases rapidly because the undissolved lime decreases the relative amount of liquid slag and also increases the effective viscosity of slag that lowers the kinetics (Bannenberg *et al*, 1994, see Appendix F.6 for more discussion). If in the vicinity of $(\%S)/[\%S] = 2000$ and $LSI < 1$, the slag viscosity has doubled, *i.e.*, from base value of 0.11 to 0.22 Pa.s, then from LES results we know that the entrainment characteristics are more or less unaffected and therefore the results in Fig. 8.21 are still valid. This weaker role of slag viscosity should be the reason, in Fig. 8.7b, for the unhindered increase in the desulphurization capacity ($(\%S)/[\%S]$) with lime addition until $LSI = 1$.

These results show that as long as the slag is fluid, higher basicity yields higher mass transfer rate, which is in accordance with the industrial observations (Fig. 8.7b).

8.3 Slag Entrainment and Steel Cleanliness

With confidence in models, namely *RANS*-2 and LPT, we are now in a position to assess the role of slag entrainment on steel cleanliness. Since the assessment for 44 ton was found to be more or less identical with the 150 ton cases, discussion of the former is omitted.

Particles (slag droplets) of various sizes smaller than the smallest size tracked in Ch. 7, were tracked for three Q_{sp} cases; the interfacial tension has no role in these size ranges. The results plotted in Fig. 8.22 show that for all Q_{sp}, $\bar{t}_{res}$ increases with lowering droplet size and eventually levels out to become independent of droplet size.

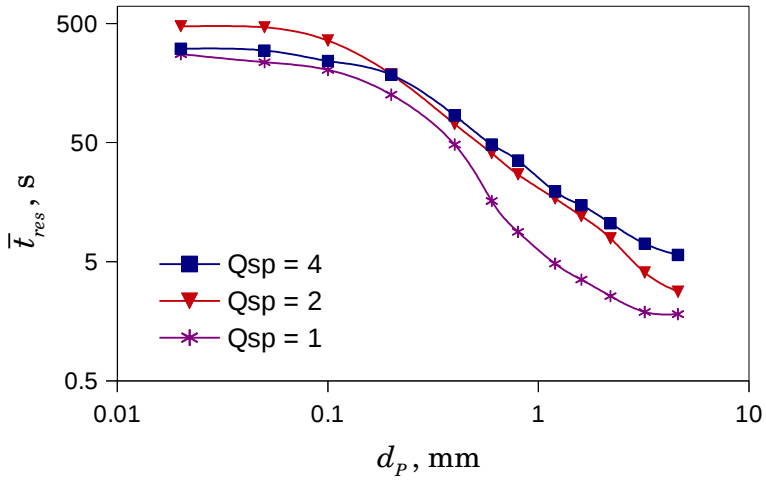

Figure 8.22. Mean residence time vs droplet size in the finer size range for 150 ton ladle at three gas injection rates (Qsp)

The cumulative distributions of residence time for various droplet sizes are plotted in Fig. 8.23 for the three Q_{sp} cases. Strangely, for Q_{sp} = 2, the residence times are larger than at Q_{sp} = 4 (although in accordance with its own $\bar{t}_{res}$ plot in Fig. 8.22). The predictions are that, generally 95 % of droplets ($d_P \geq 0.1$ mm) rejoin with the upper phase within 10 minutes (600 s), excepting the finest droplets in case of Q_{sp} = 2. Gas stirring is rather vigorous during a

refining process which culminates by gentle stirring for around 10 minutes to allow inclusion floatation. Since gentle stirring would equal the case of $Q_{sp} = 1$, it can be said that by the end of gentle stirring more than 95% of the entrained slag droplets ($d_P \geq 0.1\,\text{mm}$) would rejoin the bulk slag.

The assessment hitherto show that slag droplets with $d_P \geq 0.1\,\text{mm}$ are not mostly entrapped in steel. Much finer droplets may be produced due to transitory lowering of interfacial tension (Sec. 6.1.4); otherwise it is difficult for these to be produced by the entrainment process. Moreover it was noted in Sec. 7.6 that droplet breakup is negligible. So all these results indicate that steel cleanliness is not mainly related to slag entrainment.

It was discussed in Sec. 2.3 regarding the work of Valentin *et al* (2009b) that inclusion composition was largely influenced by the slag entrainment whose mechanism is unclear. However in the classic review of inclusions in secondary steelmaking by Zhang & Thomas (2003) slag entrainment during gas stirring was not mentioned as a source of inclusions. Also Dr. S. S. Sun (Private communication, March, 2016) remarked that neither any change in inclusion composition towards slag composition nor observation of entrapped slag was found in their numerous plant trials at Dofasco, ON, Canada.

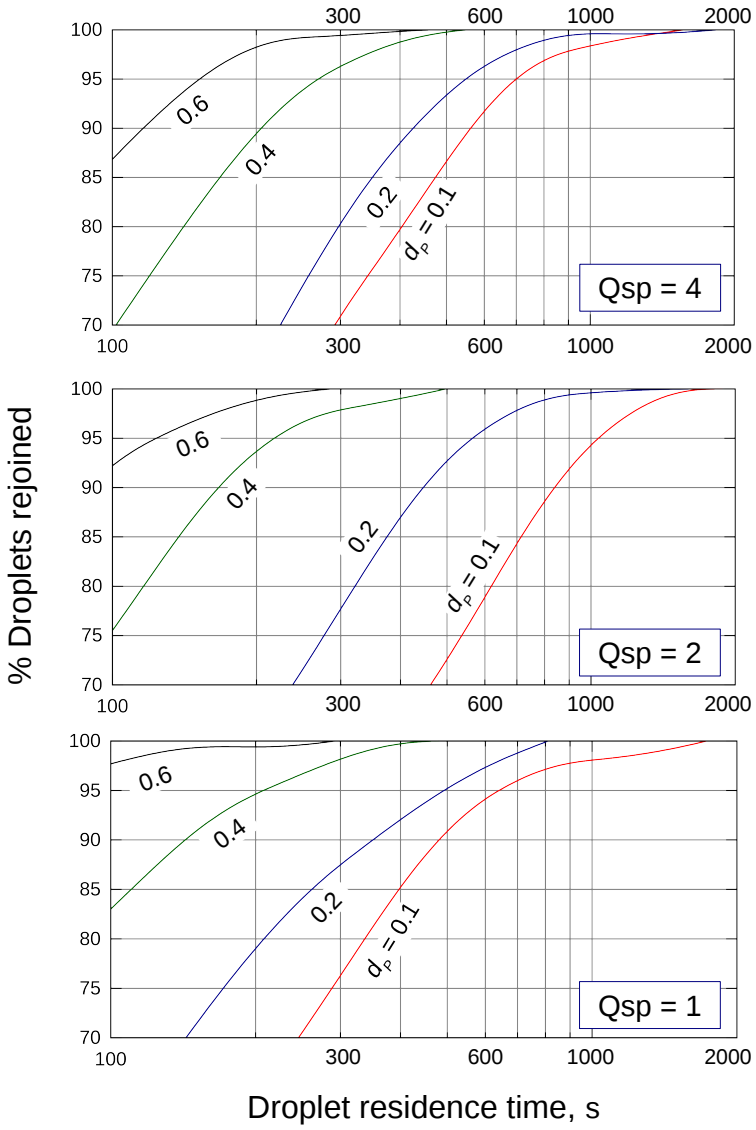

Figure 8.23. Cumulative distribution of residence times for four droplet sizes (d_P, mm) and three gas injection rates (Qsp) estimated for the 150 ton ladle. Common x and y axes labels.

8.4 Modeling Challenges

The aim of the present modeling work was to present a systematic approach to study the entrainment phenomena in a tractable manner than to address a specific industrial problem. Four major models, namely QSP-RANS, LES, LPT and DBD were brought together to study the role of entrainment on mass transfer rate and steel cleanliness. Each of the individual models were shown to produce physically meaningful results in their respective Chapters. The integrated model for mass transfer estimation yielded results close to a literature correlation. Moreover the correlations developed were able to explain the discrepancies in literature correlations. These aspects support the individual as well as the integrated models.

However, in the process, many approximations have been used within each models as well as the integrated models. The significant approximations are listed in Table 8.4 under 'Drawback' and wherever possible, justifications are provided. The approximations have arisen out of two main reasons: 1) inability to model precisely a phenomenon 2) lack of prior knowledge about a phenomenon, such as the LES models using the QSP-RANS fields without the 'lip' structure at *ULeye*. The latter of these can be avoided hereafter. However, precise modeling (1) requires more fundamental models as in case of those listed under Ch. 4 or more computing resources for those under Ch. 6, in Table 8.4. If the approximations can be regarded acceptable then the present modeling approach will suffice to gain insights into the process pertaining to slag entrainment in metal.

Table 8.4. Drawbacks in the present modeling work and possible justifications

Drawback	Justification
QSP-RANS in Chapter 4	
- Lack of precise model for free surface turbulence correction; water model based empirical model was used - Wall function implementation was unsuccessful in the axisymmetric version of Gerris.	Comparison against plume velocity correlation of K&I (2010) for large ladle was satisfactory (Sec. 6.1.6, Fig. 6.1 and Sec. 7.5, Fig. 7.14)
- Bubble induced turbulence not accounted and hence TKE boundary condition for LES inlet is uncertain	The influence of turbulence is not major on entrainment characteristics (Sec. 6.2.3)
-The approach for QSP-RANS is satisfactory under the present implementation in Gerris; but may require modifications for other solvers.	
Multiphase LES in Chapter 6	
- LES input was derived from QSP-RANS fields that did not have appropriate flow separation past *ULeye* - Only a reduced domain (thin slice) was considered - The slag-metal-air-three phase contact was not modeled resulting in issues mentioned at the end of Sec. 5.2.2.2 - Affordable grid resolution permits only droplets greater than 4 mm	Although these assumptions tend to decouple the role gas injection rate on final mass transfer rates, the results of entrainment characteristics are still physically valid for the given LES setup and the strong correlation resulted for VPU from a wide range of conditions supports that.
-Grid independency was not strictly achieved	Not serious in case of VPU and mean droplet size (Sec. 6.2.4)

Mass Transfer Rates in Chapter 8	
-Entrainment rate and interfacial area from 'old' QSP-RANS (Ch. 6) were combined with $\bar{t}_{res}$ obtained from modified QSP-RANS (Ch. 7) to calculate mass transfer rate	The mean momentum being the major driving source for the multiphase phenomena is not very different between the 'old' and 'modified' QSP-RANS (at the end of Sec. 7.5)

8.5 Summary

Values of various parameters namely, entrainment rate, droplet size distribution, mean residence time, interfacial areas of bulk phases, mass transfer coefficients were gathered from Chapters 6 and 7 as well as derived in the present Chapter. Mass transfer rate and steel cleanliness assessments were made based on separate computations. The estimations were performed for two ladle models, namely 44 ton and 150 ton. Various results obtained can be summarized as follows, of which the first few are exclusive to the 44 ton ladle.

- QSP-RANS field obtained by imposing 100% turbulence intensity along *ULeye* (*RANS*-2) yielded more physically meaningful results than without (*RANS*-1).
- The choice of length scale to obtain mass transfer coefficient was found not to be critical for Regime II mass transfer.
- Decreasing interfacial tension increases mass transfer rate through increasing 1) entrainment rate, 2) droplet residence time and 3) two phase area at *ULeye*.
- Mass transfer actively takes place both at droplets and *ULeye* with the latter contribution being major at small flow rates, yielding to droplets at larger flow rates, while still being significant.
- Comparison of mass transfer rates for the 44 ton ladle with literature correlation for 165 ton ladle yielded close similarity.
- Based on entrainment rate correlations and scaling relations, estimates similar to the 44 ton ladle were made for the 150 ton ladle. Remarkable similarity of results were apparent in comparison with the literature correlation for 165 ton. This supports the

overall and numerous sub models for entrainment developed hitherto, on a global level.

- Exploratory computations performed show that mass transfer rates may be estimated purely based on correlations developed in this work without the need to perform the expensive LESs. Besides, extension of such an approach to ladles with multiple plug was also proposed.
- The role of multiple plugs in decreasing the mass transfer rate for a given flow rate was systematically analysed based on correlations developed in the present work. This explained the decreasing exponent to ε with increasing bottom plugs.
- Relations for Regime I mass transfer rate were investigated based on parameter values derived from QSP-RANS. Estimates for mass transfer coefficient based on physical length of interfaces yielded exponents to specific stirring rate (ε) of about 0.3, typical of those found in the literature. It was shown that transition from Regime I to II will not be abrupt and becomes more gradual or even vanishing with increase in ladle capacity; this explains the missing Regime I in two of the literature correlations for large capacity ladles. Moreover, the intersection of Regimes I and II for 44 ton case occurred well around the critical gas injection rate predicted using the entrainment rate correlation.
- It was rationalized that the discrepancies in literature correlations are primarily due to differences in ladle capacity and number of bottom plugs.
- Based on the attempts to scale the mass transfer rates, it was shown that simple scaling arguments are not sufficient.
- Model results showed that as long as the slag is fluid, higher slag basicity yields higher mass transfer rate, in accordance with industrial data.
- Assessment of steel cleanliness based on the droplet residence times in the 150 ladle showed that steel cleanliness is not primarily due to slag entrainment, in accordance with industrial observations.
- Various challenges in modeling the entrainment phenomena were summarized.

9. Summary and Conclusions

9.1 Summary

This thesis presents a numerical modeling approach to characterize the degree of entrainment of slag into metal and its effects in a gas stirred ladle. It consists of four major sub models namely the drop by drop kinetic model (DBD, Ch. 3), quasi single phase RANS simulations of flow in an axisymmetric ladle (QSP-RANS, Ch. 4), large eddy simulations of slag entrainment (LES, Ch. 6) and Lagrangian particle tracking of entrained slag droplets (LPT, Ch. 7). Various models were integrated in Ch. 8 to assess the role of slag entrainment in slag metal interfacial mass transfer and in affecting the steel cleanliness. All CFD simulations were carried out using Gerris flow solver that was primarily chosen for its 'accurate surface tension model' for precise interface tracking capabilities. Following is the summary of each chapters:

- **Chapter 3**: The DBD model was developed to calculate mass transfer rate incorporating the entrainment parameters, namely entrainment rate, droplet size and residence time distributions. In the parametric studies conducted using the model, three flow rate–regimes of mass transfer were simulated similar to that in literature, which demonstrates the model capability. Attempts to develop analytical models of the DBD model showed that they are primitive; yet, they served to verify the implementation of the population balance and mass transfer calculations in the DBD model. The parametric studies also prove that the DBD model is a potential tool analyze influence of various other parameters than that are derived in this thesis.
- **Chapter 4**: The methodology to perform multiphase LES of slag entrainment in steel ladle was presented in this Chapter, which can be summarized as performing QSP-RANS simulations in the ladle to supply mean velocities and Reynolds stresses to the Synthetic Eddy Method (SEM) which generates turbulent inflow at the inlet of multiphase LES domain where Navier-Stokes equations with an LES model are solved along with VOF method to track the two phase interfaces. Development of the QSP-

RANS model for the ladle, its implementation in Gerris and verification against data were presented. Implementation of SEM in Gerris and its verification against a benchmark case were also discussed.

- **Chapter 5**: Experiments were performed in an aqueous-thin slice model to measure entrainment rate and droplet size distribution for entrainment of oil into water for three flow rates. Multiphase LESs were performed for these three flow rate cases based on methodology presented in Ch. 4. Although the simulated droplet formation was qualitatively similar to experiments, the agreement of simulation with data for entrainment rate and droplet size distribution showed large dependence on the choice of turbulence length scale, which is determined by the length scale factor, $LSfac$. Upon manipulating $LSfac$, better agreement between the data and the LES results for entrainment rate and mean droplet size were obtained, although not for the droplet size distribution and also that the optimal value of $LSfac$ was different for each flow rate case.
- **Chapter 6**: Multiphase LESs were performed for steel slag system corresponding to a 44 ton ladle, based on the methodology detailed in Ch. 4 and applied to aqueous model in Ch. 5. The effect of various parameters on entrainment rate and droplet size distribution namely, slag viscosity, slag metal interfacial tension, slag thickness, turbulence length scale and VOF mesh refinement were studied. Ensemble averaged velocity profiles were extracted by post-processing the LESs and average LP velocity near *ULeye* were estimated from these profiles. Relating the average LP velocity and various physical properties to entrainment rate a correlation was developed.
- **Chapter 7**: A computer code for LPT model was developed specific to the 2D mesh output of a QSP-RANS performed using Gerris. Four forces on the droplets, namely buoyancy, drag, pressure gradient and added mass were included in the LPT code and the code was verified against literature benchmark cases. An Eddy Interaction Model was implemented to add turbulence effects on particle trajectory. The domain geometry of QSP-RANS was modified to capture the flow separation around the base of *ULeye* that is actually present in LES simulations, but missing in the prior simulations (from

Ch. 6).

LPT cases were run for various combinations of gas injection rate and slag metal interfacial tension and the mean residence time for various particle sizes were obtained. Another set of LPT cases were performed with input flow field obtained from QSP-RANS with 100% turbulence intensity imposed near *ULeye* to investigate the influence of turbulence due to interface fluctuations on RANS field, which is otherwise absent. The results from two RANS configurations (without and with imposed turbulence intensity) indicate that the particle trajectories/dispersion and hence their residence times are sensitive to the RANS flow field.

Comparison of mean of forces acting on particles showed that drag and buoyancy are the dominant forces with added mass and pressure forces having secondary effects.

A comparison of mean residence time estimated from LES performed without droplet removal with that of the corresponding LPT simulations using the two drag correlations, namely Tomiyama's and Standard drag curve showed all were of similar order of magnitude. This shows that the LPT model predictions are satisfactory. Although it was not further investigated as which of the two drag correlations is more precise, Tomiyama's drag correlation is preferred and hence the mean residence times obtained using the same were used for models in Ch. 8.

- **Chapter 8**: Using the values of various parameters gathered from Chapters 6 and 7 as well as derived in this Chapter, mass transfer rate for the 44 ton ladle was computed. Using the correlations developed for the 44 ton ladle and scaling relations, parameters for a 150 ton ladle were derived along with dedicated QSP-RANS and LPT to estimate mass transfer rates for this ladle. An approach to approximate estimation of mass transfer rate bypassing the expensive LES step was proposed and demonstrated to provide reasonable estimates. The decreasing exponent to stirring rate (ε) in the $\beta-\varepsilon$ relation with increasing number of bottom plugs, found in the literature, was systematically analyzed and explained based on correlations developed in the present work. Based on separate QSP-RANS simulations for Regime I of mass transfer rate for

both 44 and 150 ton cases, the exponents to ε were estimated to be about 0.3, typical of those found in the literature. Following this the transition from Regime I to II was critically analysed. The possibility for scaling the mass transfer rate with possible length and time scales was explored. The effect of slag basicity on mass transfer rate was analysed. Based on separate LPT calculations for much finer droplets steel cleanliness assessments were made for the 150 ton ladle.

9.2 Conclusions

This is the first time a rigorous modeling approach has been taken to characterize slag metal entrainment. While the past works have focused on limited aspects of entrainment, the present work investigates a wider range. This was achieved by breaking down the complex problem into tractably smaller modules, developing a model for each of them and finally integrating them. While the DBD model is completely novel, the present formulation of multiphase LES and LPT models are the first of their kind to be applied to study slag entrainment in metal. Wherever possible these models were tested against literature data, correlations, benchmark cases or results of other models developed in this work. The following conclusions are drawn for this work:

- The DBD model is a reliable tool to estimate mass transfer rate incorporating the entrainment parameters and mass transfer coefficients.
- Multiphase LES of slag metal system:
  - Entrainment rate is predominantly affected by the gas injection rate with smaller role of interfacial tension.
  - The droplet size statistics are mainly affected by interfacial tension alone.
  - Slag viscosity has only minor effect on entrainment characteristics.
  - The effect of *LSfac* that was significant in aqueous model simulations (Ch. 5) was found to be very limited here. This suggest that the role of turbulence is limited to triggering the disturbance of interface while the mean flow properties play the dominant role in causing entrainment. This investigation also clarifies that the

strong role of *LSfac* on entrainment rate in aqueous model simulations (Ch. 5) was due to the small flow rates in the corresponding experiments.

- The scaled entrainment rate was found to linearly vary with nominal two phase contact area at the eye (*ULeye*) for a cylindrical ladle (3D), which also means that a thicker slag has higher entrainment rate.
- The increased mesh refinement along the VOF surface greatly affected the droplet size distribution although only to lesser extent on the entrainment rate and Sauter mean diameter.
- Upon relating the entrainment rate with the average LP velocity near *ULeye* and physical properties, a strong correlation resulted, with a form similar to that encountered in the literature describing critical conditions for onset of entrainment. This shows that the physics of the entrainment process is well captured by the LESs despite performed only for a thin slice of a ladle domain.

- LPT for mean residence times:
  - Simulation of flow separation near *ULeye* is important to obtain realistic droplet residence times.
  - Particle trajectories/dispersion and hence their residence times are sensitive to the RANS flow field.
  - Drag and buoyancy are two major forces to influence the droplet trajectories and hence the mean residence times.
  - Comparison of mean residence times estimated from an LES performed without droplet removal with that of the corresponding LPT showed that the LPT model predictions are satisfactory.
- Integrated Models:
  - Decreasing interfacial tension increases the mass transfer rate in three primary ways: through increasing 1) entrainment rate, 2) droplet residence time and 3) two phase area at *ULeye*.
  - Mass transfer actively takes place both at droplets and *ULeye* with the latter

contribution being major at small flow rates, yielding to droplets at larger flow rates, while still being significant.

- In comparison with literature correlation for mass transfer rate constants (β) of a dual plug 165 ton ladle, the single plug cases of the present models, namely the 44 ton and 150 ton ladles yielded close similarity, of which the 150 ton showed remarkable similarity with the literature correlation. The difference in the number of bottom plugs correctly manifested in the model results of 150 ton case as higher exponent to stirring rate (ε) compared to that of the 165 ton ladle.
- Exploratory computations performed show that mass transfer rates may be estimated with the correlations developed in this work replacing the expensive LESs. Furthermore, the extension of such an approach to ladles with multiple plug was also proposed.
- The decreasing exponent to ε in the $\beta-\varepsilon$ relation with increasing number of bottom plugs was shown to be due to the division of gas flow rate between the plumes and slag eyes formed for each bottom plug.
- Investigation of Regime I mass transfer showed that the transition from Regime I to II will not be abrupt and becomes more gradual or even vanishing with increase in ladle capacity; this explained the missing Regime I in two of the literature correlations for large capacity ladles. Moreover, the intersection of Regimes I and II for 44 ton case occurred well around the critical gas injection rate predicted using the entrainment rate correlation.
- It was rationalized that the discrepancies among literature correlations are primarily due to differences in ladle capacity and number of bottom plugs.
- Based on the attempts to scale the mass transfer rates, it was shown that simple scaling arguments, for *eg*., based on ladle Froude number, are not sufficient.
- Model results showed that as long as the slag is fluid, higher basicity yields increasing mass transfer rate, in accordance with industrial data.
- Assessment of steel cleanliness based on the droplet residence times in the 150 ladle showed that steel cleanliness is not primarily due to slag entrainment, in

accordance with industrial observations.

A strong correlation for entrainment rate in Ch. 6 and the various results presented in Ch. 8 being in agreement with industrial data or observation demonstrate the internal consistency of the numerous sub models and the overall modeling approach presented in this Thesis.

9.3 Future Work

There is enormous scope for future work along the lines of the present modeling approach both for overcoming the 'drawbacks' listed in Sec. 8.4. and for developing new models. The latter of these are listed as follows:

- The approach for approximate estimation of mass transfer rates can be applied to ladles of multiple bottom plugs, say Graham (2008) and Lachmund *et al* (2003) (see Table 8.2), based on the steps outlined in Sec. 8.2.5, to verify it against the available mass transfer rate correlations.
- All models in this Thesis are based on a centric gas injection, the same as the numerous modeling studies in the literature concerning ladle metallurgy. However in real systems the gas injection is at an eccentric location. A dedicated model can be developed for a known system that has sufficient data to validate the model.

The entrainment of metal in slag is not modeled in this thesis. It has been well observed in the plant trials and its basic mechanism described (discussed in Sec. 2.2) as due to the rejoining droplets of UP carrying with them a film of LP. However the degree of such entrainment has not been quantified, other than the limited estimates provided by Ekengard *et al* (Sec. 2.3) based on their sampling trials in industrial ladle. A method to model this phenomenon is proposed as follows: Since the estimates for entrainment rate and size distribution of slag droplets in metal can be obtained using the approach presented in this Thesis, the unknown is the metal film thickness surrounding the slag droplets.

Entrainment of metal into slag was observed at many instances in the LESs of the present work, although to a smaller extent due to the low mesh resolution in regions where slag

droplets rejoin the bulk slag phase. So this type of entrainment can be studied by high resolution simulation of droplets rejoining in a confined domain, accompanied by experiments in aqueous systems. The experiments can be performed by injecting series of droplets of known size from the bottom of a small vessel containing both the bulk lower and upper phases. The mass of LP entrained per droplet in UP should be measured by sampling the UP, for various droplet sizes and two fluid properties. Following this high resolution simulations should be performed in a confined domain to measure the amount of LP entrained in UP per droplet and that should be compared against the corresponding data. Once the approach is validated, simulations should be performed for steel-slag properties. From the amount of metal entrained per slag droplet, the film thickness can be estimated.

Bibliography

ANSYS CFX-Solver Modeling Guide , April 2009.

ANSYS FLUENT 12.0, Theory Guide, 2009

Asai, S., Muchi, I. and Kawachi, M., 1988, "Fluid Flow and Mass Transfer in Gas Stirred Ladles", Foundary Processes, Their Chemistry and Physics, pp. 261-289

Balaji, D. and Mazumdar, D., 1991, "Numerical Compuation of Flow Phenomena in Gas Stirred Ladle Systems", Steel Research, Vol 62, pp. 16-23

Bannenberg, N, Lachmund, H. and Prothmann, B., 1994, "Secondary Metallurgy for Clean Steel Production by Tank Degassing," Steelmaking Conference Proceedings, pp. 135–143.

Barton, I., 1999, "Simulation of particle trajectories in turbulent flow over a backwards facing step", R & D Journal, Vol 15(3), pp. 65-78.

Berg, B., Carlsson, G. and Bramming, M., 1985, "Ladle Metallurgy-Influence of Different Stirring Methods", Scandinavian J. of Met., Vol 14, pp. 299-305.

Beskow, K, Dayal, P., Bjorkvall, J., Nzotta, M. and Du Sichen , 2006, "A New Approach for the Study Of Slag–metal Interface in Steelmaking ", Ironmaking and Steelmaking, Vol 33, pp. 74-80.

Bozzano, G., Dente, M., 2009, "Single Bubble and Drop Motion Modeling", AIDIC Conference Series, 09, pp. 53-60.

Brackbill, J. U., Kothe, D. B. and Zemach, C., 1992, "A Continuum Method for Modeling Surface Tension", J. of Computational Physics, Vol 100, pp. 335-354.

Castillejos, A. H., Salcudean, M. E. and Brimacombe, J. K., 1989, "Fluid Flow and Bath Temperature Destratification in Gas Stirred Ladles", Met. Trans. B, Vol 20B, pp. 603-611.

Clift, R., Grace, J. R., Weber, M.E., 1978, "Bubbles Drops and Particles", published in 2005 by Dover Publications. p27.

Dayal, K., Beskow, P., Bjorkvall, J., Nzotta, M. and Du Sichen , 2006, "Study of Slag/Metal Interface in Ladle Treatment", Ironmaking and Steelmaking, Vol 33, pp. 454-464

Dean, R. D., 1978 "Reynolds Number Dependence of Skin Friction and Other Bulk Flow Variables in Two-Dimensional Rectangular Duct Flow". J. Fluids Eng. Vol 100, pp. 215–222.

Deo, B. and Boom, R., 1993, "Fundamentals of Steelmaking Metallurgy", Prentice Hall Intl.

Ekengard, J., Andersson, A. M. T. and Jonsson, P. G., 2008, "Distribution of Metal Droplets in Top Slags During Ladle Treatment," Ironmaking and Steelmaking, Vol 35, pp. 575–588.

Ferry, J., Balachandar, S., 2001, "A Fast Eulerian Method for Disperse Two-phase Flow ", Intl. J. of Multiphase Flow, Vol 21, pp. 1199-1226.

Ford B. and Loth, E., 1998, "Forces on ellipsoidal bubbles in a turbulent shear layer", Physics of Fluids, Vol 10(1), pp. 178-188

Fuster D.,Bagué, A., Boeck, T., Moyne, L. L., Leboissetier, A., Popinet, S., Ray P., Scardovelli, R. and Zaleski , S., 2009, "Simulation of Primary Atomization with an Octree Adaptive Mesh Refinement and VOF method ", Intl. J. of Multiphase Flow, Vol 35, pp. 550–565 .

Gaye, H., Lucas, L. D., Olette, M. and Riboud, 1984, "Metal-Slag Interfacial Properties: Equilibrium Values and "Dynamic" Phenomena", Canadian Met. Qart., Vol 23, pp. 179-191.

Gosh, A., Chatterjee, A., 2008, "Ironmaking and Steelmaking", Prentice Hall India Pvt. Ltd.

Grace *et al*, 1976: Cited in Clift *et al*, 1978, p176—Grace, J. R., Wairegi, T. and Nguyen, T. H., Trans. Inst. Chem. Eng., Vol 54, pp. 167-173.

Graham, D. I. and James, P.W., 1996, "Turbulence dispersion of particles using eddy interaction models", Int. J. Multiphase flow, Vol 22 (1), pp. 175-178.

Graham, K., 2008, "Integrated Ladle Metallurgy Control", PhD Thesis, McMaster Univ., Canada.

Grevet, J. H., Szekely, J. and El-Kaddah, N., 1982, "An Experimental and Theoretical Study of Gas Bubble Driven Circulation Systems", Int. J. Heat and Mass Transfer, Vol 25, pp. 487-497.

Guo, D. and Irons, G. A., 2000, "Modeling of Gas-Liquid Reactions in Ladle Metallurgy: Part II. Numerical Simulation", Met. Trans B, Vol 31B, pp. 1457-1464.

Handler , R. A., Swean, T.F Jr., Leighton, R.I., And Swearingen, J.D., 1993, "Length scales and the energy balance for turbulence near a free surface", AIAA Journal, Vol 31, pp. 1998-2007.

Han, H. W., Heo, S. H., Kam, D. H., You, B. D., Pak, J. J. and Song, H. S., 2001, "Transient Fluid Flow Phenomena in a Gas Stirred Liquid Bath with Top Oil Layer–Approach by Numerical Simulation and Water Model Experiments ", ISIJ, Vol 41, pp. 1165-1173

Hirt, C. W. and Nichols, B. W., 1981, "Volume of Fluid Method for the Dynamics of Free Boundaries", J. pf. Comp. Phy., Vol 39, pp. 201-225.

Hutchinson, P., Hewitt, G. F. and Dukler, A. E., 1971, "Deposition of liquid or solid dispersions from tuburlent gas streams: A stochastic model", Chem Eng Sci, Vol 26, pp. 419 –439.

Ilegbusi, O. J. and Szekely, J., 1990, "The Modeling of Gas-Bubble Driven Circulation Sytems" ISIJ Intl., Vol 30, pp. 731-739

Ishida, J., Yamaguchi, K., Sugiura, S., Yamano, K., Hayakawa , S.and Demukai, N., Denki-Seiko (Electric Furnace Steel), 1981, p2 (cited in Asai *et al* 1988).

Ishii, M., Zuber, N., 1979, "Drag Coefficient and Relative Velocity in Bubbly, Droplet or Particulate Flows," AIChE J., Vol 25, p843.

Jakobsen, H., Sannaes, H. B., Grevskott, S. and Svendsen, F. H., 1997, "Modeling of Vertical

Bubble-Driven Flows", Ind. Eng. Chem. Res., Vol 36, pp. 4052-4074.

Jarrin, N., 2008, "Synthetic Inflow Boundary Conditions for the Numerical Simulation of Turbulence" PhD Thesis, University of Manchester, UK.

Jarrin, N., Prosser, R., Uribe J.-C., Benhamadouche, S., Laurence, D, 2009, "Reconstruction of turbulent fluctuations for hybrid RANS/LES simulations using a Synthetic-Eddy Method", Intl. J. Heat and Fluid Flow, Vol 30, pp. 435–442 .

Jimbo, I., Chung, Y. and Cramb, A. W., 1996, "Interfacial Tensions of Liquid Iron-alloys and Commerical Steels in Contact with Liquid Slags", ISIJ Intl., Vol 36, pp. S42-S45.

Johansen, S. T., and Boysan, F., 1988, "Fluid Dynamics in Bubble Stirred Ladles: II. Mathematical Modeling," Metallurgical Trans. B., Vol 19B, pp. 755-764.

Johansen, S. T., Robertson, D. G. C., Woje, K. and Engh, T. A., 1988, "Fluid Dynamics in Bubble Stirred Ladles: I. Experiments," Metallurgical Trans. B., Vol 19B, pp. 745-754.

Jonsson, L., and Jonsson, P., 1996, "Modeling of Fluid Flow Conditions around the Slag/Metal Internface in Gas-stirred Ladle", ISIJ Intl, Vol 36, pp. 1127-1134.

Kawai, 1956, "Diffusion of Sulfur in Liquid Iron. I, Diffusion in Pure Iron", The Research Institute of Mineral Dressing and Metallurgy, pp. 78-83.

Krishnapisharody, K., 2006, "Model Studies of Fluid Mechanic Interaction Between Steel and Slag in Gas Stirred Ladles", PhD Thesis, McMaster Univ., Canada.

(K&I) Krishnapisharody, K. and Irons, G.A., 2007a, "A Study of Spouts on Bath Surfaces from Gas Bubbling: Part II. Elucidation of Plume Dynamics", Met. Trans B., 38B, pp. 377-388.

(K&I) Krishnapisharody, K. and Irons, G.A., 2007b, "A Study of Spouts on Bath Surfaces from Gas Bubbling: Part I. Experimental Investigation", Met. Trans B., 38B, pp. 367-375.

(K&I) Krishnapisharody, K. and Irons, G.A., 2008, "An Extended Model for Slag Eye Size in Ladle Metallurgy " ISIJ (Note), Vol 48, pp. 1807-1809.

(K&I) Krishnapisharody, K. and Irons, G.A., 2010, "An Analysis of Recirculatory Flow in Gas-Stirred Ladles", Steel Research, Vol 81, pp. 880–885.

(K&I) Krishnapisharody, K. and Irons, G.A., 2013, "A Critical Review of the Modified Froude Number in Ladle Metallurgy", Met Trans B, Vol 44, Issue 6, pp. 1486-1498.

Kim, S-H. and Freuhan, R. J., 1987, "Physical Modeling of Liquid/Liquid Mass Transfer in Gas Stirred Ladles", Met. Trans. B, Vol 18B, pp. 381-390.

Kim, S-H., Freuhan, R. J. and Guthrie, R. I. L., 1987, "Physical Model Studies of Two Phase Mass Transfer in Gas Stirred Ladles", Steelmaking Conf. Proc., Vol 70, pp. 107-118.

Kim, J., Moin, P. and Moser, R., 1987b, "Turbulence Statistics in Fully Developed Channel Flow at Low Reynolds Number", J. Fluid Mech., Vol 177, pp. 133-166.

Kolev, N. I., 2012, "Multiphase Flow Dynamics 2: Thermal and Mechanical Interactions", Springer-Verlag Berlin Heidelberg, Chap. 2.

Kuzmin, D., Turek, S. and Haario, H., 2005, "Finite element simulation of turbulent bubbly flows in gas-liquid reactors." *Ergebnisberichte Angew. Math.* 298, University of Dortmund.

Lachmund, H., Xie, Y., Buhles, T. and Pluschkell, W., 2003, "Slag Emulsification during Liquid Steel Desulphurization by Gas Injection into the Ladle", Steel Research, Vol 74, pp. 77-85.

Li, B., Yin, H., Balajee, S. R., Chaubal, P. and Zhou, C. Q., 2007, "CFD Analysis on Behavior of Slag-Steel Interface in an Argon Gas Stirred Ladle", AISTech Proceedings, pp. 1355-1368.

Lin, Z. and Guthrie, R. I. L., 1994, "Modeling of Metallurgical Emulsions", Met. Trans. B, Vol 25B, pp. 855-864.

Loth, E., 2000, "Numerical Approaches for Motion of Dispersed Particles, Droplets and Bubbles ", Progress in Energy and Combustion Science Vol 26, pp. 161–223 .

Maxey, R, 1987, "The motion of small spherical particles in a cellular flow field ", Physics of Fluids Vol 30, pp. 1916-1928.

Mazumdar, D. and Guthrie, R. I. L., 1994, "An Assessment of a Two Phase Calculation Procedure for Hydrodynamic Modelling of Submerged Gas Injection in Ladles ", ISIJ, Vol. 34, pp. 384-392.

Mazumdar, D. and Guthrie, R. I. L., 1985, "Hydrodynamic Modeling of Some Gas Injection Procedures in Ladle Metallurgy Operations", Met. Trans. B, Vol 16B, pp. 83-90.

Mazumdar, D. and Guthrie, R. I. L., 1995, "The Physical and Mathematical Modelling of Gas Stirred Ladle Systems", ISIJ, Vol 35, pp. 1-20.

Menter, F. R., Kuntz, M. and Langtry, R., 2003, "Ten Years of Industrial Experience with the SST Turbulence Model " Turbulence, Heat and Mass Transfer 4

Mietz, J., Schneider, S. and Oeters, F., 1991a, "Model Experiments on Mass Transfer in Ladle Metallurgy", Steel Research, Vol 62, pp. 1-9.

Mietz, J., Schneider, S. and Oeters, F., 1991b, "Emulsification and Mass Transfer in Ladle Metallurgy", Steel Research, Vol 62, pp. 10-15.

Mills, K. and Keene, B., 1987, "Physical Properties of BOS Slags," International Materials Reviews, Vol. 21, No. 1–2, pp. 1–120.

Mohanty, A. K., 2000, "Rate Processes in Metallurgy", Prentice-Hall of India Pvt. Ltd., p303.

MSTS, 1998, "Secondary Steelmaking or Ladle Metallurgy", The Making Shaping and Treating of Steel, The AISE Steel Foundation, 11th edition, Chap. 19.

Nakayama, A. and Yokojima, S., 2003, "Modeling Free-Surface Fluctuation Effects for Calculation of Turbulent Open-Channel Flows", Environmental Fluid Mechanics, Vol 3, pp. 1–21.

Naot, D., Rodi, W., 1981, "Interactions of Turbulent Eddies with a Free Surface ", Third Beer-Sheva International Seminar on Magneto-hydrodynamic Flows and Turbulence, Ben-Gurion University of the Negev, Beer-Sheva, Israel, March 23-27, 1981, pp. 98-112

Popinet, S., 2009, “An Accurate Adaptive Solver for Surface-Tension-Driven Interfacial Flows”, J. of Comp. Phy., Vol 228, pp. 5838–5866 .

Popinet, S., 2003, “Gerris: A Tree-Based Adaptive Solver for the Incompressible Euler Equations in Complex Geometries ”, J. of Comp. Phy., Vol 190, pp. 572-600.

Qtiplot: http://www.qtiplot.com/

Rajaratnam, N., 1976, “Turbulent Jets”, Elsevier Scientific, New York, p304

Reiter, G. and Schwerdtfeger, K., 1992, “Observations of Physical Phenomena occurring during Passage of Bubbles through Liquid/Liquid Interfaces ”, ISIJ, Vol 32, pp. 50-56

Riboud, P. V. and Lucas, L. D., 1981, “Influence of Mass Transfer upon Surface Phenomena in Iron and Steelmaking”, Canadian, Met. Quat., Vol 20, pp. 199-208.

Ridenour, P., Yin, H., Tetrault, C., Balajee, S R., Chaubal, P. and Zhou, C. Q., 2006, “CFD Study on Slag-Steel Interaction in an Argon Bottom-Stirred Ladle ”, AISTech Proceedings, Vol 1, pp. 721-729.

Rzehak, R. and Krepper, E., 2013, “Bubble-induced Turbulence: Comparison of CFD Models”, Nuclear Eng. and Design, Vol 258, pp. 57-65.

Sahai, Y. and Guthrie, R. I. L., 1982, “Hydrodynamics of gas stirred melts: Part II. Axisymmetric flows”, Met. Trans. B, Vol 13B, pp. 203-211.

Sampaio , P.T., Braga, A. P. and Fujii, T., “Neural Network Thermal Model of a Ladle Furnace ”, Part of the Proceedings of the 10th International Conference on Engineering Applications of Neural Networks (EANN-2007), pp. 80 to 86

Savolainen, J., Fabritius, T. and Mattila, O., (2009), “Effect of Fluid Physical Properties on the Emulsification”, ISIJ Intl, Vol 49, pp. 29-36.

Shen, L., Triantafyllou, G. S. and Yue, D. K. P. , (2000), “Turbulent Diffusion Near a Free Surface ”, J. Fluid Mech. , Vol 407, pp. 145–166 .

Sheng, Y., 1992, “Modeling and Measurement of Unconfined Bubbly Two-phase Plume Flow”, PhD Thesis, McMaster Univ., Canada.

Sheng Y. Y. and Irons G. A., 1995, “The impact of Bubble Dynamics on the Flow in Plumes of Ladle Water Model” Metallurgical Trans. B., Vol 26B, pp. 625-635.

Sheng Y. Y. and Irons G. A., 1993, “Measurement and Modeling of Turbulence in the Gas/Liquid Two Phase Zone during Gas Injection” Metallurgical Trans. B., Vol 24B, pp. 695-705.

Simcik, M., Ruzicka, M. C., Drahoš, J., 2008, “Computing the added mass of dispersed particles”, Chem Eng Sci, Vol 63, pp. 4580-4595

Smagorinsky, J., 1963, “General Circulation Experiments with the Primitive Equations. I. The Basic Experiment”. *Month. Wea. Rev.*, Vol 91, pp. 99-164.

Sokolichin, A., Eigenberger , G. and Lapin , A., 2004, “Simulation of Buoyancy Driven

Bubbly Flow: Established Simplifications and Open Questions ", Fluid Mechanics and Transport Phenomena , Vol 50, pp. 24-45.

Sulasalmi, P., Karna, A., Fabritius, T. and Savolainen, J., 2009, "CFD Model for Emulsification of Slag into the Steel", ISIJ Intl, Vol 49, pp. 1661-1667.

Tanaka, S., 1986, "Modeling Inclusion Behavior And Slag Entrainment In Liquid Steel Processing Vessels", PhD Thesis, McGill University Canada (Cited in Verhelst, 1991).

Theissen, W., 2004, "The Ultra Slag Droplet Detector ", Millenium Steel.

Thunman, M., Eckert, Hennig, S., Bjorkvall J. and Du Sichen, 2007, "Study on the Formation of Open-Eye and Slag Entrainment in Gas Stirred Ladle", Steel Research Intl, Vol 78, pp. 849-856.

Tomiyama, A., 1998, "Struggle with computational bubble dynamics. In", Third International Conference on Multiphase Flow, ICMF, Lyon, France, June 8-12.

Turkoglu, H. and Farouk B., 1990, "Numerical Compuations of Fluid Flow and Heat Transfer in Gas-Stirred Liquid Bath", Met. Trans. B, vol 21B, pp. 771-781.

Valentin, P., Bruch, C., Kyrylenko, Y., Köchner, H. and Dannert, C., 2009a, "Influence of the Stirring Gas in a 170-t Ladle on Mixing Phenomena – Formation and On-line Control of Open-Eye at an Industrial LD Steel Plant", Steel Res. Int, Vol 80, pp. 552-558.

Valentin, P., Bruch, C. and Gaule, J., 2009b, "Emulsification of Top Slags during Argon Stirring through a Porous Plug in the Ladle of Si Deoxidised Carbon Steels", Steel Res. Int, Vol 80, pp. 746-752.

Verhelst, D., 1991, "Physical Modeling of Gas Stirred Metallurgical Reactors Containing Two Liquids", Master Thesis, McGill University, Canada.

Villiers, E., 2006, "The Potential of Large Eddy Simulation for the Modeling of Wall Bounded Flows ", PhD Thesis, Imperial College of Science, Technology and Medicine.

Wang, YI, and James, P.W., 1999, "Assessment of an eddy-interaction model and its refinements using predictions of droplet deposition in a wave-plate demister", Trans IChemE, Vol 77A, pp. 692-698.

Wei, T. and Oeters, F., 1992, "A Model Test for Emulsion in Gas-stirred Ladle", Steel Research, Vol 63, pp. 60-68.

Wilcox, D. C., 1994, "Turbulence Modeling for CFD", DCW Industries Inc.

Youngs, D. L., 1982, "Time-Dependent Multi-Material Flow with Large Fluid Distortion" in K. W. Morton and M. J. Baines (eds), "Numerical Methods for Fluid Dynamics", Academic Press, New York.

Zhang, L. and Thomas, B., 2003, "State of the Art in Evaluation and Control of Steel Cleanliness ", ISIJ, Vol 43, pp. 271-291.

A. Appendix for Chapter 3

A.1 *C* Code for the Drop by Drop Model

See attached file `drop-by-drop.c`

A.2 Random Sampling of Droplet Size

A technique known as *Inverse Transform Sampling* is used to generate random numbers according to a given distribution and can be described as follows (Wolfram, 2014). Let X be the random variable of the given distribution and F_X be its cumulative distribution function (CDF). By passing random values sampled from a uniform random variable, U_{RN} in the range of [0, 1], to the inverse CDF of X, as $F_X^{-1}(U_{RN})$, random values of X can be sampled. Inversion of CDF may result is an analytical expression for simple distributions while for others a root finding iterative method is required.

Following are the steps to randomly sample from the lognormal distribution considered for droplet size distribution. The probability density function is

$$f(x) = \frac{C}{x}\exp\left[-\left(\frac{\ln x - A}{B}\right)^2\right],\ x > 0. \tag{A.1}$$

Step 1. Find CDF:

The definition of CDF,

$$F(x) = \int_{-\infty}^{x} f(x)dx. \tag{A.2}$$

applied to Eq. (A.1) gives,

$$F(x) = \int_0^x f(x)dx = \sqrt{\frac{\pi}{4}} BC\left[1 + \text{erf}\left(\frac{\ln(x)-A}{B}\right)\right]. \quad \text{(A.3)}$$

Step 2. Normalize CDF:

For a finite upper limit on the droplet size, say x_∞, CDF has to be normalized as $F(x)/F_\infty$ where, F_∞ is obtained by setting $x = x_\infty$ in Eq. (A.3).

Step 3. Invert x from CDF, setting $F(x) = U_{RN}$:

From Eq. (A.3) we get,

$$x = \exp\left[A + B\,\text{erf}^{-1}\left(\frac{F_\infty U_{RN}}{\sqrt{\pi/4}\,BC} - 1\right)\right] \quad \text{(A.4)}$$

where x is now the randomly sampled droplet size.

To evaluate the inverse error function in Eq. (A.4) the following approximation of Winitzki (2008) is used:

$$\text{erf}^{-1}(z) \approx \text{sign}(z)\sqrt{\sqrt{\left(\frac{2}{\pi a} + \frac{\ln(1-z^2)}{2}\right)^2 - \frac{\ln(1-z^2)}{a}} - \left(\frac{2}{\pi a} + \frac{\ln(1-z^2)}{2}\right)}, \quad \text{(A.5)}$$

where $a \approx 0.147$ yields a maximum error of 1.2×10^{-4}.

A.3 Physical Dimensions of Upper Phase for Parametric Studies

The eye radius, UP thickness and UL areas for the parametric studies are presented in this section with reference to Fig. A.1.

In reality, the increasing gas injection rate

1. pushes *ULeye* to sides by the radial flow and increases R_{eye} in turn increasing h_U due to volume continuity
2. causes entrainment of UP that increases R_{eye} and may decrease h_U.

So the dimensions of R_{eye} and h_U are affected both before and after entrainment.

In the parametric studies it was formulated that

1. before entrainment ($t=0$ or $VPU=0$), there is fixed value for R_{eye}, ($R_{eye,0}$ in Fig. A.1) for a given *Trail Number*, and a corresponding h_U (from volume continuity).
2. once entrainment starts ($t>0$ and $VPU>0$), the loss of UP volume increases R_{eye} alone and h_U is set constant.

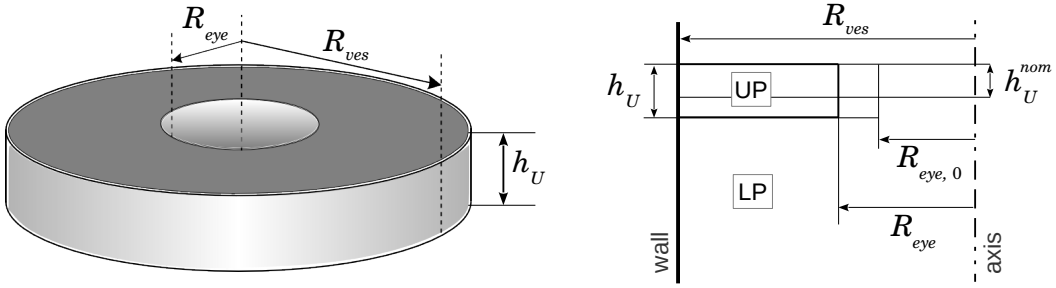

Figure A.1. Defining sketches concerning the dimensions of upper phase (UP) considered in the parametric studies of the DBD model. The circular slab in the left is the shape of UP contained in a cylindrical vessel with the hole in the centre representing the slag eye. Refer 'List of Symbols' for symbol definitions.

Before Entrainment: The increase in R_{eye} with *Trial number* is achieved through a parameter called, X_{EV}, defined as,

$$X_{EV} = R_{eye} / R_{ves}. \tag{A.6}$$

For a given *Trial*, R_{eye} is calculated from Eq. (A.6) and the corresponding h_U is calculated from the volume continuity,

$$\pi R_{ves}^2 h_U^{nom} = \pi h_U \left(R_{ves}^2 - R_{eye}^2 \right) \tag{A.7}$$

and using Eq. (A.6),

$$h_U = h_U^{nom} \Big/ \left(1 - X_{EV}^2 \right). \tag{A.8}$$

The **areas** at *ULeye and ULflat* are calculated from

$$A_{ULeye} = 2\pi R_{eye} h_U \tag{A.9}$$

and

$$A_{ULflat} = \pi\left(R_{ves}^2 - R_{eye}^2\right) \tag{A.10}$$

After onset of entrainment: Since the volume of UP (V_U) is dynamic, R_{eye} is updated from

$$R_{eye} = \sqrt{R_{ves}^2 - \frac{V_U}{\pi h_U}} \tag{A.11}$$

for every time step and so are the areas at *ULeye* and *ULflat* updated from Eqs. (A.9) and (A.10), respectively, using Eq. (A.11).

References:

"The Method of Inverse Transforms" from the Wolfram Demonstrations Project
http://demonstrations.wolfram.com/TheMethodOfInverseTransforms/
(accessed August 2014)
Winitzki, S., 2008, "A handy approximation for the error function and its inverse ",
https://scholar.google.com/citations?user=Q9U40gUAAAAJ (accessed, August 2014).

B. Appendix For Chapter 4

This Appendix consists of SST $k-\omega$ model equations, its implementation in Gerris and verification against benchmark cases.

B.1 Standard SST $k-\omega$ model

The model equations were taken from NASA-1 which has the correct version of the model. The model solves separate transport equations for k and ω given by,

$$\frac{\partial k}{\partial t} + \boldsymbol{U}\cdot\nabla k = \nabla\cdot\left(\nu + \sigma_k \nu_T \nabla k\right) + P_k - \beta^* \omega k \tag{B.1}$$

$$\frac{\partial \omega}{\partial t} + \boldsymbol{U}\cdot\nabla \omega = \nabla\cdot\left(\nu + \sigma_\omega \nu_T \nabla \omega\right) + \frac{\gamma}{\nu_T} P_k - \beta\omega^2 + 2(1-F_1)\frac{\sigma_{\omega_2}}{\omega}\nabla k \cdot \nabla \omega \tag{B.2}$$

and calculates the eddy viscosity as,

$$\nu_T = \frac{a_1 k}{\mathrm{MAX}[a_1\omega,\ F_2\sqrt{2S_{ij}S_{ij}}]}. \tag{B.3}$$

In Eqs. (B.1) and (B.2), P_k represents the generation of turbulence kinetic energy, k expressed for incompressible flows as,

$$P_k = \mathrm{MIN}[2\nu_T S_{ij} S_{ij},\ 10\beta^* \omega k] \tag{B.4}$$

where,

$$S_{ij}S_{ij} = \left[\left(\frac{\partial U}{\partial x}\right)^2 + \left(\frac{\partial V}{\partial y}\right)^2 + \left(\frac{\partial W}{\partial z}\right)^2\right] + \frac{1}{2}\left[\left(\frac{\partial U}{\partial y} + \frac{\partial V}{\partial x}\right)^2 + \left(\frac{\partial U}{\partial z} + \frac{\partial W}{\partial x}\right)^2 + \left(\frac{\partial W}{\partial y} + \frac{\partial V}{\partial z}\right)^2\right], \tag{B.5}$$

in Cartesian coordinate systems (`GfsSimulation`) and

$$S_{ij}S_{ij} = \left[\left(\frac{\partial U}{\partial x}\right)^2 + \left(\frac{\partial V}{\partial y}\right)^2 + \left(\frac{V}{y}\right)^2\right] + \frac{1}{2}\left(\frac{\partial V}{\partial x} + \frac{\partial U}{\partial y}\right)^2 \tag{B.6}$$

in Axisymmetric coordinate system (`GfsAxi`),

$$\nabla k \cdot \nabla \omega = \frac{\partial k}{\partial x}\frac{\partial \omega}{\partial x} + \frac{\partial k}{\partial y}\frac{\partial \omega}{\partial y} + \frac{\partial k}{\partial z}\frac{\partial \omega}{\partial z} \tag{B.7}$$

in Cartesian coordinate systems (`GfsSimulation`) and

$$\nabla k \cdot \nabla \omega = \frac{\partial k}{\partial y}\frac{\partial \omega}{\partial y} + \frac{\partial k}{\partial x}\frac{\partial \omega}{\partial x} \tag{B.8}$$

in Axisymmetric coordinate system. The blending Function for model constants is given by,

$$\phi = F_1\phi_1 + (1-F_1)\phi_2 \tag{B.9}$$

where,

$$F_i = \tanh(arg_i^4),\ i = 1, 2 \tag{B.10}$$

$$arg_1 = \text{MIN}\left[\text{MAX}\left(\frac{\sqrt{k}}{\beta^* \omega d},\ \frac{500\nu}{d^2\omega}\right),\ \frac{4\sigma_{\omega_2} k}{CD_{k\omega} d^2}\right] \tag{B.11}$$

$$CD_{k\omega} = \text{MAX}\left[\frac{2\sigma_{\omega_2}}{\omega}\nabla k \cdot \nabla \omega,\ 10^{-20}\right]$$

$$arg_2 = \text{MAX}\left[\frac{2\sqrt{k}}{\beta^* \omega d},\ \frac{500\nu}{d^2\omega}\right] \tag{B.12}$$

in which d is the nearest distance to wall from a node. The list of model constants is,

Constants	ϕ_1	ϕ_2
γ	5/9	0.44
β	0.075	0.0828
σ_k	0.85	1.0
σ_ω	0.5	0.856
β^*	0.09	
κ	0.41	
a_1	0.31	

B.1.1 Near Wall Treatment

The SST $k-\omega$ model can be integrated up to the wall; however, this requires the grid size near the wall to be of the order of 1.0 for the dimensionless wall distance y^+ which makes it is expensive. To allow coarser mesh, a wall treatment was suggested by Menter (2003). It consists of calculating wall friction velocity, u_τ that gives the correct wall shear stress, specifying wall ω and applying a zero flux boundary condition for k. The friction velocity and wall ω are blend of two expressions, one of the viscous sublayer $y^+ < 5$ and the other of the log-law region $y^+ > 11$.

However, the near wall treatment considered for this work is based on the wall treatment implemented in ANSYS-CFX, known as "Automatic Wall Treatment for Omega based Models". This is a modified version of Menter (2003) in that it partly replaces the friction velocity, u_τ by an alternative velocity scale, u_*. The model is described as follows:

The eddy viscosity can be defined as (this definition does not appear in the ANSYS-CFX reference, but from their definition of, u_τ^2 as $u_\tau u_*$, the definition is adapted),

$$\nu_T = \frac{u_\tau \, u_*}{U_P / y_P} \tag{B.13}$$

in which,

$$u_\tau = \left[u_{\tau,\, vis}^4 + u_{\tau,\, \log}^4 \right]^{1/4} \tag{B.14}$$

$$u_* = \left[u_{\tau,\, vis}^4 + \left(\sqrt{a_1 k} \right)^4 \right]^{1/4} \tag{B.15}$$

$$u_{\tau,\, vis} = \sqrt{\nu \, U_P / y_P} \tag{B.16}$$

$$u_{\tau,\, \log} = \frac{U_P}{\frac{1}{\kappa} \ln(y^+) + 5.25} \tag{B.17}$$

In Equations (B.13) to (B.17), U_P is the tangential velocity at the near wall cell, and y_P is

distance of the centre of near wall cell to wall, $y^+ = y_P u_\tau / \nu$ and $\kappa = 0.41$ is the Von Kármán constant.

For ω the following value is set:

$$\omega = \sqrt{\omega_{vis}^2 + \omega_{\log}^2}$$
$$\omega_{vis} = \frac{6\nu}{\beta y_P^2};\ \omega_{\log} = \frac{u^*}{a_1 \kappa y_P} \tag{B.18}$$

A further modification was required to the near wall treatment, based on various benchmark cases tested. In the region of transition from linear to log law regions occurring in $5 < y^+ < 11$, Eq. (B.17) did not give a better estimate for friction velocity; probably the implementation in Gerris is not compatible with the type of blending used. To allow smooth transition without the requirement of any blending approaches a universal velocity profile of Spalding (1961) was used. The velocity profile, scaled in wall units ($y^+$and u_τ) is,

$$y^+ = u^+ + \frac{1}{E}\left[\exp(\kappa u^+) - 1 - \kappa u^+ - \frac{1}{2}(\kappa u^+)^2 - \frac{1}{6}(\kappa u^+)^3\right], \tag{B.19}$$
$$\text{where, } y^+ = y_P u_\tau / \nu,\ u^+ = U_P / u_\tau \text{ and } E = 9.1$$

The friction velocity is found as the root of Eq. (B.19) using the Newton-Raphson method.

Equation (B.19) also enables us to find the eddy viscosity, ν_T as noted by Kalitzin *et al*, (2004). Considering a flat plate and zero pressure gradient, for which case wall functions were derived, the momentum equation simplifies to

$$\frac{d}{dy}\left((\nu + \nu_T)\frac{dU}{dy}\right) = 0 \tag{B.20}$$

Integrating over the wall normal coordinate, *y*,

$$(\nu + \nu_T)\frac{dU}{dy} = \nu \left.\frac{dU}{dy}\right|_{wall} = u_\tau^2 \tag{B.21}$$

which can be non-dimensionalized using the wall units,

$$(1+\nu_T^+)\frac{du^+}{dy^+}=1 \tag{B.22}$$

from which eddy viscosity can be calculated as,

$$\nu_T = \nu\nu_T^+ = \nu\left(\frac{dy^+}{du^+} - 1\right), \tag{B.23}$$

using the profile, Eq. (B.19). In summary, the wall treatment involves the same equations as that of ANSYS CFX, except for deducing u_τ and ν_T.

The turbulence model implementation and verification using benchmark cases namely turbulent plane channel flow, backward facing step, free jet, wall jet, pipe flow and round jet are discussed in the Appendix.

B.2 Implementation of the SST $k-\omega$ model in Gerris

B.2.1 Transport Equations

The transport equations for k and ω are typical advection–diffusion equations with source terms, of the form,

$$\underbrace{\frac{\partial\phi}{\partial t} + \nabla\cdot(\boldsymbol{u}\phi)}_{\text{advection}} = \underbrace{\nabla\cdot(D_\phi\nabla\phi)}_{\text{diffusion}} + \underbrace{S_\phi}_{\text{source}} \tag{B.24}$$

where ϕ is the generic scalar transported, D_ϕ and S_ϕ are the diffusion coefficient and source terms. Equation (B.24) can be implemented within Gerris parameter file through addition various Gerris objects as follows:

- `GfsVariableTracer phi`

  is to solve the advection of variable ϕ (`phi` = `TKE`, `omg` for k and ω, respectively).

- `GfsSourceDiffusion phi D_phi`

adds the diffusion term through the `GfsFunction`, `D_phi`

- ```
  GfsSource phi S_phi
  ```

  adds various source terms through the `GfsFunction`, `S_phi`.

For the control of parameters for the advection and diffusion terms refer the Gerris manual (Gerris syntax reference).

B.2.2 Near Wall Cell

The location of the near wall cells are required for various functions described ahead. The identification of these cells is made simpler if the wall boundaries of the domain are represented by solid surface defined using `GfsSolid`. As a first step, a `GfsFunction` of various boolean operations and that returns a `GfsSurface` is declared in `GfsGlobal` under the name, `DistSolidFn`. This function can be used to define `GfsSolid` and also to return the approximate distance to nearest solid surface.

B.2.2.1 Find Distance to Nearest Solid Boundary

```
GfsVariable DistSolid
```

Distance to nearest solid boundary is required by the SST $k-\omega$ and the following description is with reference to the file, `nearest-distance-turb-model.gfs`. This is achieved using Gerris objects in the parameter file in two simulation-time steps as follows:

1. In the initialization step:
   1. Initialize `DistSolid` with an approximate value returned by `DistSolidFn`.
   2. Collect the coordinates of solid cells namely, `ax,ay,az` and
   3. Under `GfsInit` define the solid boundary using `GfsFunction` as,

      ```
      wall = GfsFunction
      ```

   4. Output the `GfsVariables` containing the variables in steps 1 and 2 as text
2. In the first simulation-step, within the `GfsFunction` of `DistSolid`:
   1. Read the output file from the above initialization step
      ```

2. For every cell in the domain traversed, find the distance to the nearest 'wall' cell and return the value to `DistSolid` which is accessed by the SST $k-\omega$ model later.

These steps are executed only once in a simulation.

B.2.2.2 Distance to Centre of Near Wall Cell to Wall

```
GfsVariable yP
```

The wall functions require the value of y_P. Although `DistSolid` at the near wall can give y_P, there are situations when the solid surface do not lie exactly on the boundary face of the near wall cell (*eg*., an inclined solid surface), whereby `DistSolid` may tend to zero leading to very large values of ω (see Eq. B.18) and in turn lead to instability. To circumvent, y_P is limited by the cell thickness according to,

```
yP = MAX(DistSolid, dL/2)
```

where `dL` is the length of a cell.

B.2.2.3 Tangential Velocity near the wall cell

```
GfsVariable uP
```

The snippet is in `wall-tangential-velocity.gfs` and has the following steps:

1. Find solid normal (wall cell), $\boldsymbol{n}$.
2. Find the solid tangential vector, $\boldsymbol{t}$:
    1. If 2D, find $\boldsymbol{t}$ from $\boldsymbol{n}\cdot\boldsymbol{t} = 0$
    2. If 3D, find $\boldsymbol{t}$ in the direction of velocity vector, $\boldsymbol{U}$,

$$\boldsymbol{t} = \boldsymbol{U} - (\boldsymbol{U}\cdot\boldsymbol{n})\frac{\boldsymbol{n}}{|\boldsymbol{n}|}, \tag{B.25}$$

    which formula for projection of a vector $(\boldsymbol{U})$ on a plane (whose normal is $\boldsymbol{n}$).
3. Find the component of $\boldsymbol{U}$ in the direction of $\boldsymbol{t}$ from $|\boldsymbol{U}\cdot\boldsymbol{t}|$.

B.2.3 Verification Cases

The implementation of the SST $k-\omega$ turbulence model in the Cartesian version of Gerris (`GfsSimulation`) is verified with 1) plane channel flow 2) backward facing step 3) free jet and 4) wall jet. In the following, the highest and lowest mesh levels (`Level`), are denoted by `maxlev` and `minlev`, respectively. Since ω tends to infinity as a wall boundary is approached (See Eq. B.18), to prevent instabilities due steep gradients in ω, the mesh `Level` at the wall is extended to at least four cells in the domain interior, in all the cases using the SST $k-\omega$ model. All verification cases were run until the largest of differences in a given variable between the current and previous time step falls below a threshold; the variables are usually, U and V and the threshold was set between 10^{-3} and 10^{-4}. This was achieved using `GfsEventStop`.

B.2.3.1 Plane Channel Flow

The simplest of verification cases is the flow between two infinite parallel planes that is essentially 2D. DNS data are available at various Reynolds number (from Kim *et al*, 1987), although here only the case of $Re_\tau = 395$ is simulated. Consider a 2D channel in which fluid flows in the x direction. Under steady state flow, the advection terms in the RANS is zero since,

$$\partial_t \phi = \partial_x \phi = V = 0, \tag{B.26}$$

where ϕ is any scalar transported. So in Gerris parameter file, the advection terms are set to zero for momentum, k and ω. Consequently the entrance length for flow development is short and therefore a short channel is sufficient, whose length is only four times its half width, H.

Inlet Condition: At the inlet, U, k and ω are set to uniform values whereas, $V = 0$. The inlet values of k and ω are set according to (CFD wiki),

$$\begin{aligned} k_{in} &= 3/2\ (U_{in} I_{in})^2, \\ \omega_{in} &= \sqrt{k_{in}}/LS_{in}, \end{aligned} \tag{B.27}$$

where U_{in} is the inlet velocity, I_{in} is the turbulence intensity at inlet, set to 5% and LS_{in} is the

inlet turbulence length scale given by,

$$LS_{in} = 0.038(4H) \tag{B.28}$$

where $(4H)$ is the hydraulic diameter of the plane channel.

Mesh: The mesh consists of separate and uniform grid `Level` along the walls and in the interior. For the size of `GfsBox` set to unity, (`GfsPhysicalParams {L = 1}`) three values of `maxlev`, namely 5, 6 and 7 were chosen at the wall while the interior grid, `Level` is set to 5. The file `plane-channel-SSTko.gfs` has the implementation of this case.

Results: The profiles of normalized U, k and ω across the channel width for three refinement schemes are presented in Fig. B.1. The agreement between the DNS data and results of the SST $k-\omega$ is comparable to that obtained by Uribe (2009).

B.2.4 Backward Facing Step

This is another popular RANS verification case, based on the experiments of Driver and Seegmiller (1985), as if offers significant challenges to a turbulence model to simulate the flow separation past the backward step in a channel. This case is for a Reynolds number of 37500 based on inlet free stream velocity and step height. Much of the details of the case setup is based on AnuPravahaKiit (2010) and hence not repeated here, although the data for comparisons were taken from NASA-2. The inlet condition for k and ω was formulated as follows. In the near wall regions at inlet, the profile of k measured by Driver and Seegmiller was applied:

$$k_{profile} = \begin{cases} U_{in}^2(0.004/0.15\ Y) & Y < 0.15H \\ U_{in}^2(0.004/2.5\ (2.5-Y)) & \text{otherwise} \end{cases}, \tag{B.29}$$

where, U_{in} is the inlet velocity and Y is the distance to wall. The value of k given by Eq. (B.29) was limited by,

$$k_{in} = \text{MAX}(k^*,\ k_{profile}) \tag{B.30}$$

in which,

$$k^* = 3/2\,(U_{in} I_{in})^2, \tag{B.31}$$

The inlet ω was calculated from,

$$\omega_{in} = k_{in}/\mu_{T,fs}. \tag{B.32}$$

For the turbulence intensity, I_{in}, a value of 0.0061 was taken and the value for the free stream turbulence viscosity, $\mu_{T,fs}$, a value of 0.009 was taken, both according to NASA-3.

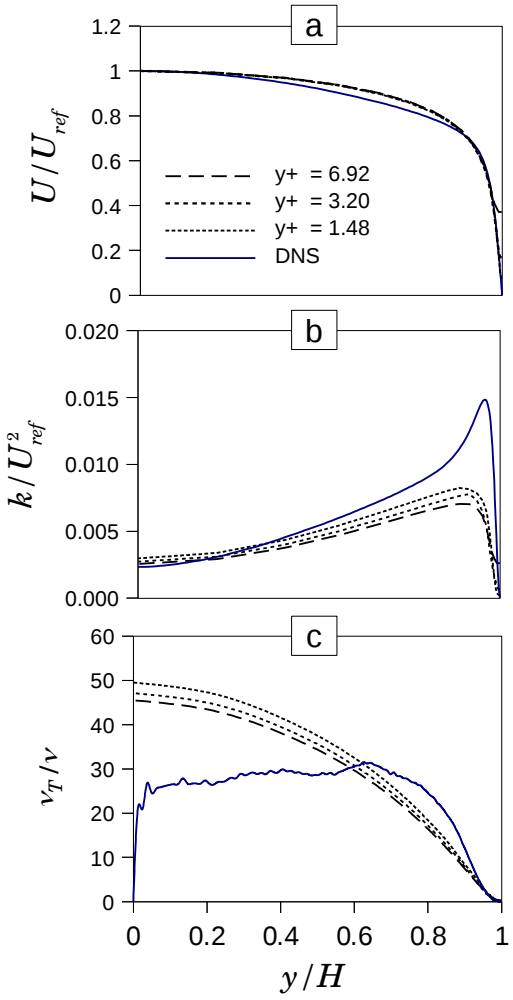

Figure B.1. Comparison of DNS data and RANS simulation profiles across the plane channel width, namely (a) horizontal velocity, (b) turbulence kinetic energy and (c) eddy viscosity. The reference velocity, $U_{ref} = U_{in}$, and H is the half channel width. Common x-axis and legend.

Mesh: The snapshot of meshes corresponding to `maxlev` of 12 and `minlev` of 8 are shown in Fig. B.2. The near wall regions were given the finest mesh. For the regions around the step until the point of flow separation, finer meshes that coarsened with distance to wall were given. While fixing the `minlev` at 8, two other cases of `maxlev` of 10 and 11 were also simulated. The file `BFS-SSTko.gfs` has the implementation of this case.

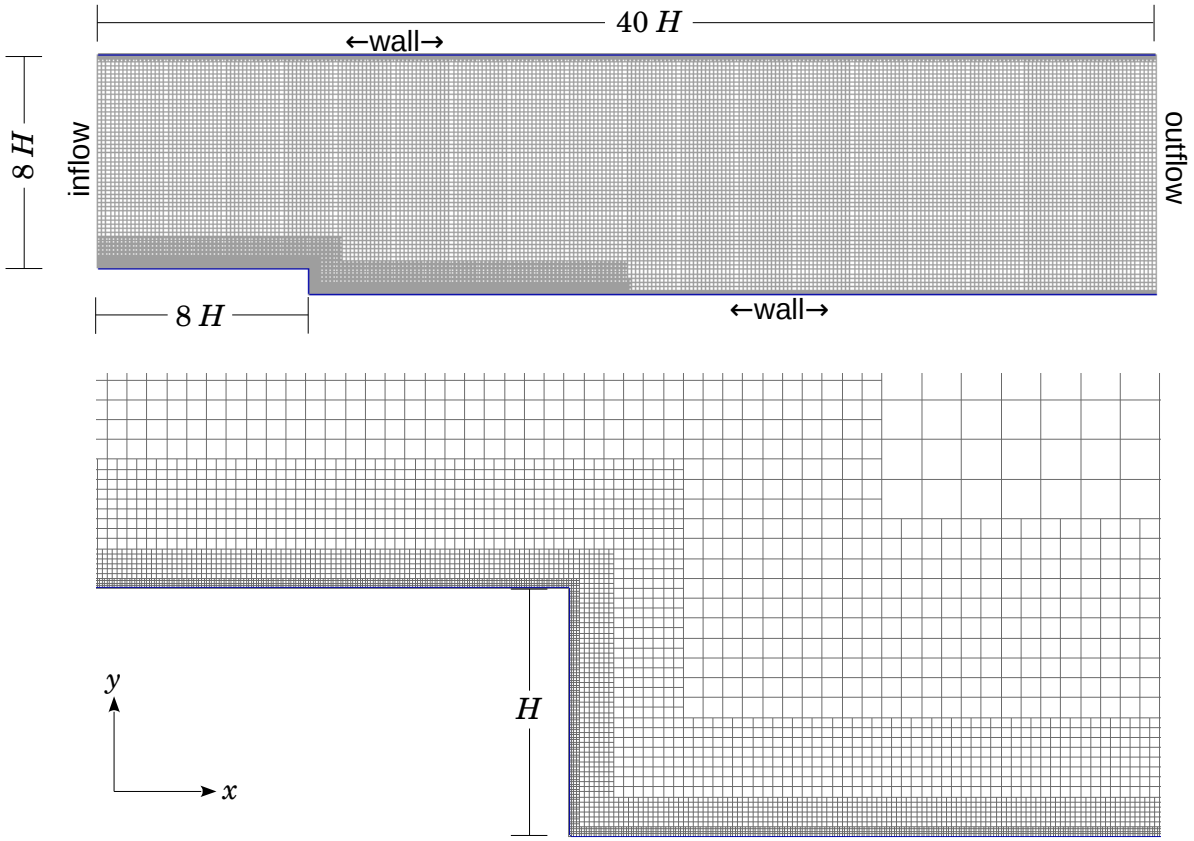

Figure B.2. Domain and mesh details of the backward facing step verification case: (a) overall domain and (b) region around the step. Inflow is at the left of the domain and *H* is the step height. These snapshots correspond to `maxlev` = 12 (at walls) and `minlev` = 8 (at interior).

Results: The profiles of normalized horizontal velocity and Reynold shear stress from Gerris simulation are compared with the data in Fig. B.3. The agreement is comparable to that obtained in NASA-3 for the SST $k-\omega$ model. Figure B.4 compares the skin friction coefficient of Gerris simulation with the data for various `maxlev` values. It is seen that with increased mesh refinement the deviation from the data increases which says that the wall friction velocity, u_τ, predictions are not precise in the present implementation. However this is not critical in the present context because the velocity and Reynolds shear stress profiles are sufficiently well predicted.

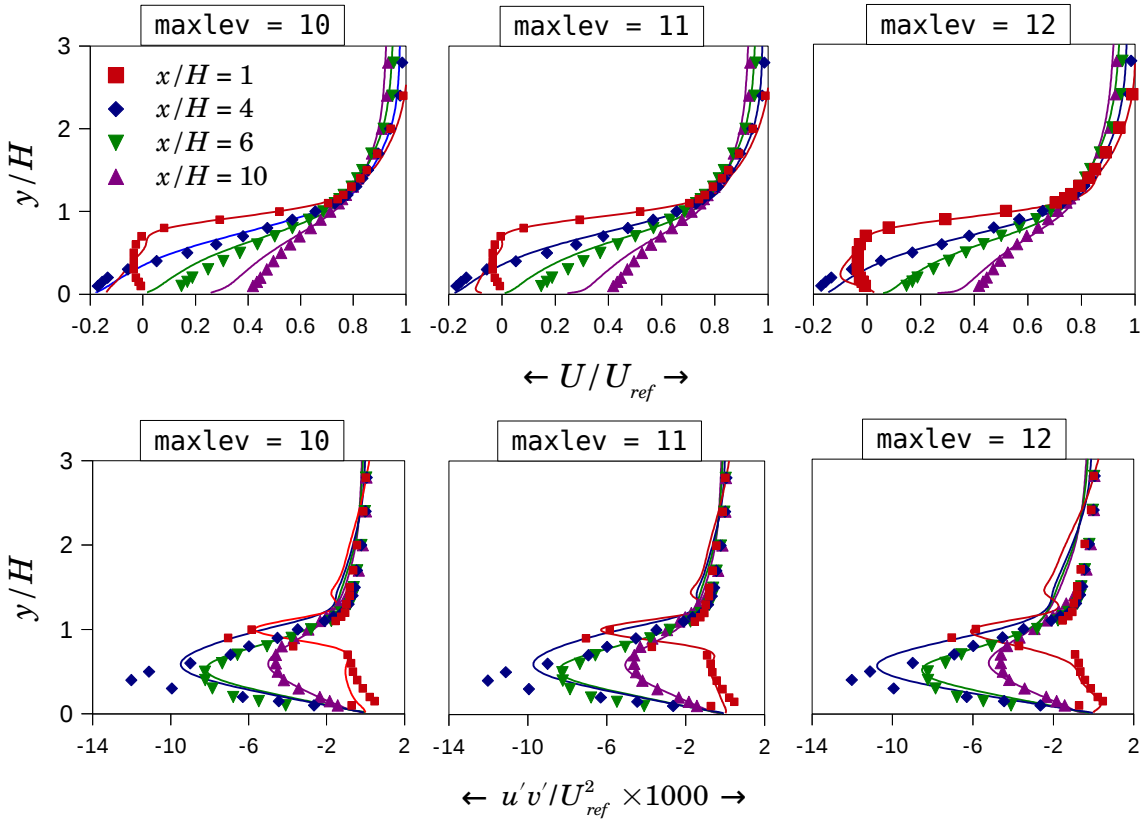

Figure B.3. Comparison of Gerris simulation (lines) with data (points) for normalized profiles of horizontal velocity U/U_{ref} and Reynolds shear stress $u'v'/U_{ref}^2$ across the channel width at various x locations, for three `maxlev` values. The reference velocity U_{ref} is the average inlet velocity. Common legend and y-axis.

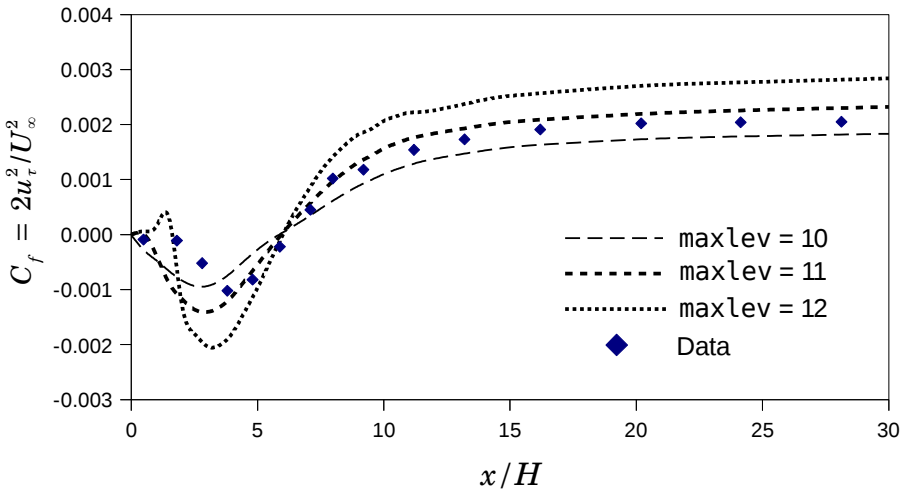

Figure B.4. Comparison of data (Driver and Seegmiller, 1985) and Gerris simulation for skin friction coefficient (C_f) along the channel wall downstream of the step for three `maxlev` values. u_τ is the wall friction velocity and U_∞ is the free stream velocity.

B.2.5 Plane Jets

Two plane jets, namely 2D free jet and wall jet were considered for another set of verification cases, whose schematic are provided in Fig. B.5. Due to their similarity, the two jets are discussed in parallel. Each case consist of 2D RANS simulation of the jet and comparison of jet half width $(x_{1/2})$ and jet velocity $(V(x))$ profiles against empirical correlations of Rajaratnam (1976), tabulated in Table B.1. For simulation of both the plane jets the size of `GfsBox` was 0.5 m and the width of nozzle, R_{in} was 0.0025 m. The jet Reynolds numbers based on uniform inlet velocity and $2R_{in}$ for free jet and R_{in} for wall jet were chosen as 10,000 and 9600. The Reynolds number for wall jet case is based on the experiments of Eriksson *et al* (1998) for which data on Reynolds stress distribution are available.

Mesh: Each simulation domain was divided into four regions, as labeled in Fig. B.6, and each region was given different levels of mesh refinement. Based on this scheme various combinations of mesh refinement were used to test grid indepedency.

Results: The jet spread of the two plane jets obtained from simulations are compared with correlations in Fig. B.7; in both cases closer agreement with respective correlation is obtained for the highest mesh refinement scheme. The normalized velocity profiles plotted in Fig. B.8

for the highest mesh refinement scheme show close agreement with respective correlation. In Fig. B.9b a fair agreement is seen in the comparison of turbulence kinetic energy distribution for the wall jet between data and simulation for the highest refinement scheme.

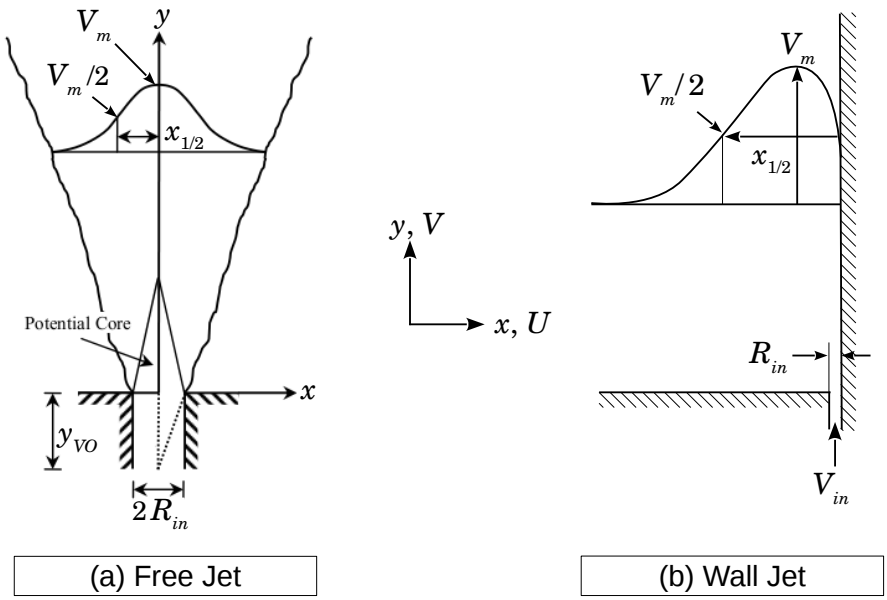

Figure B.5. Defining sketches of plane jets. y_{VO} is the location of virtual origin of jet (in (a)); R_{in} is the half width of inlet; V_{in} is the inlet velocity; V_m is the maximum velocity; $x_{1/2}$ is the jet half width.

Table B.1. Plane jet characteristics, Rajaratnam (1976). See Fig. B.5 for nomenclature.

	Free Jet	**Wall jet**
Jet Spread	$x_{1/2} = 0.097(y+y_{VO})$ $y_{VO} = 5R_{in}$	$x_{1/2} = 0.073(y + y_{VO})$ $y_{VO} = 12R_{in}$
Axial Velocity profile	$\frac{V}{V_m} = \exp\left[-0.693\left(\frac{x}{x_{1/2}}\right)^2\right]$	$\frac{V}{V_m} = 1.48\left(\frac{x}{x_{1/2}}\right)^{1/7} erfc\left(0.68\frac{x}{x_{1/2}}\right)$

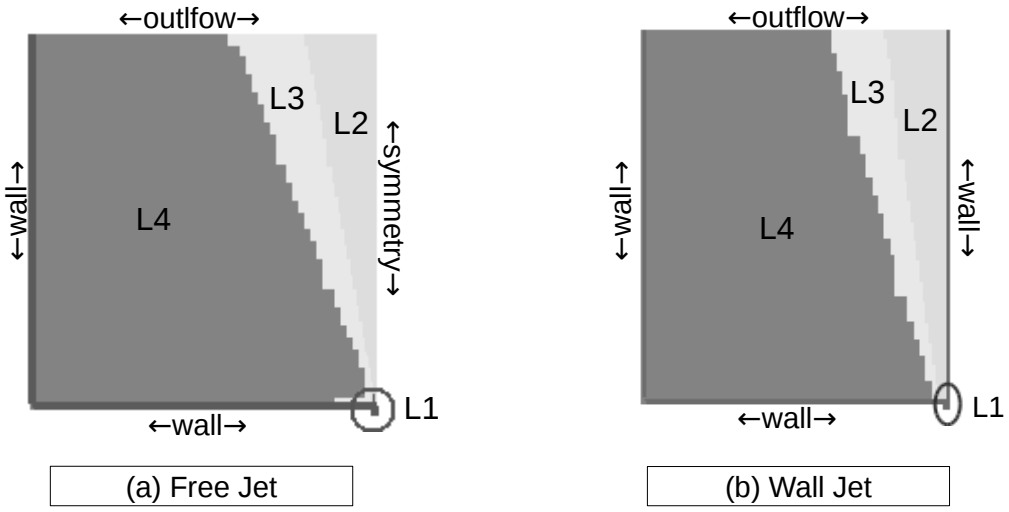

Figure B.6. Meshing schemes and boundary conditions for plane jets. Labels L1 to L4 indicate `maxlev` 9 to 6 for a `GfsBox` length of 0.5 m.

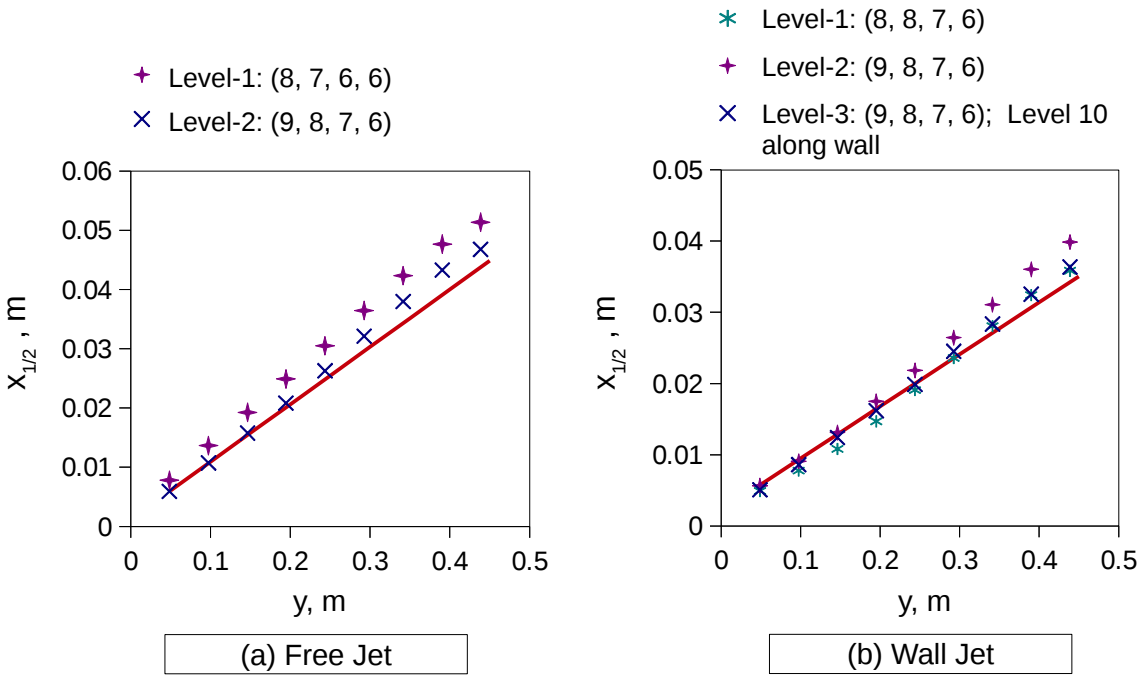

Figure B.7. Comparison of jet half width ($x_{1/2}$) of RANS simulations (points) with empirical correlation (lines).

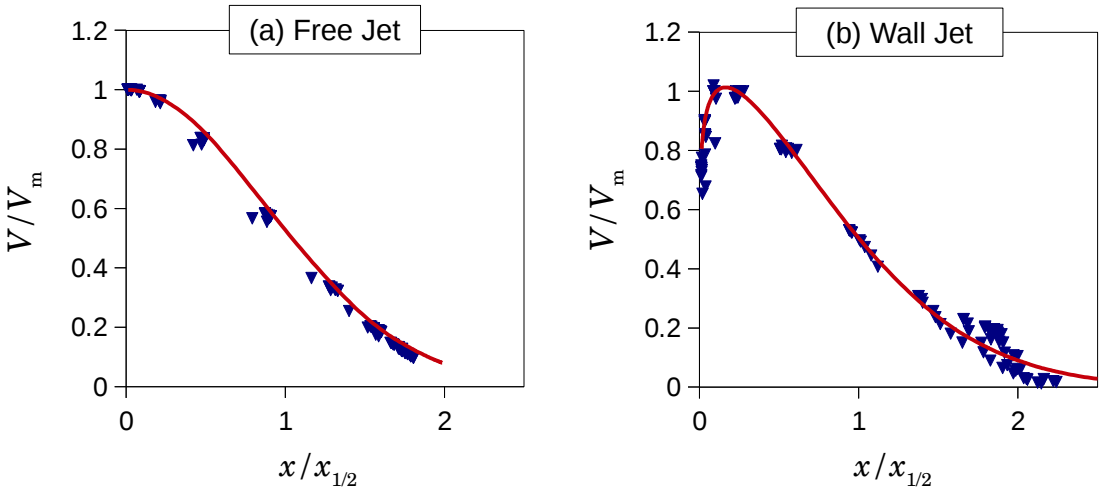

Figure B.8. Comparison of normalized velocity profiles of RANS simulations with empirical correlation (lines) for the cases of highest levels of mesh refinement.

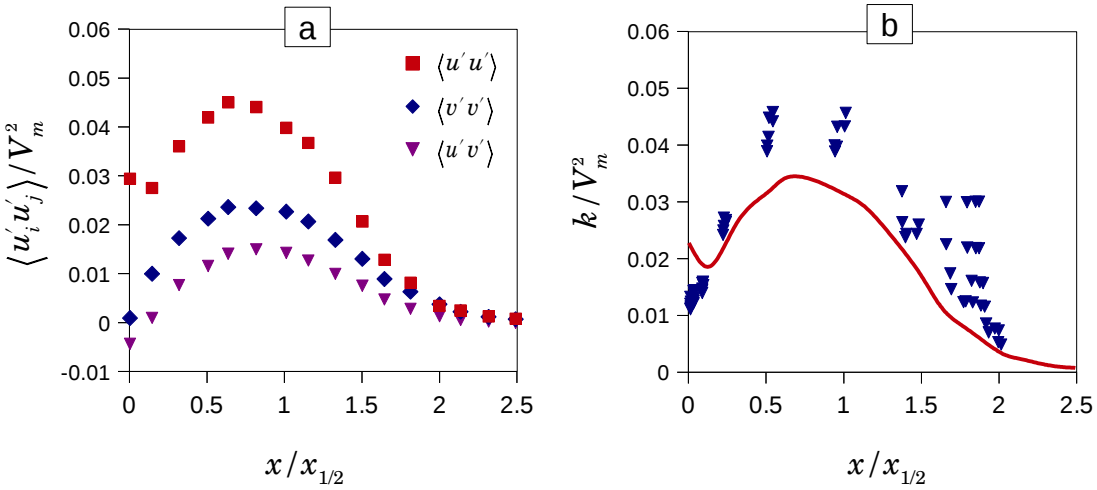

Figure B.9. (a) Data for Reynolds stress distribution in wall jet (Eriksson *et al*, 1998). (b) Comparison of turbulence kinetic energy (k) distribution data (line) extracted from values in Fig. (a) with results of RANS simulation (points). In Fig. (b), k is extracted using $k = 1/2\langle u_i'u_i' \rangle$ and setting $\langle w'w' \rangle = 1/2(\langle u'u' \rangle + \langle v'v' \rangle)$.

B.3 SEM Implementation Within Gerris Parameter File

See attached file, `channel-LES-SEM.gfs`.

B.4 Probable Issue due to Parallelization in SEM Implementation

The apparent obstacle in the implementation of SEM in Gerris is the inability to communicate between various processors (at the user level) during computations. As discussed below, fortunately no such obstacle is encountered in Gerris.

Why to communicate between processors? SEM involves dispersion of N eddies within the eddy box initially and later at the inlet plane for every time step. When the simulation is parallelized, the domain is distributed among various processors, based on the number of cells in each domain. This could result in distribution of cells of the inlet plane among many processors. Due to lack of communication, the eddies generated and convected in one processor is unknown to the rest. However, the eddy generation and convection take place virtually, *i.e.*, the cells in the inlet plane do not see any of these eddies[†], but only their effect is known to them through the addition of fluctuating velocity components generated by SEM[‡]. In conformity the following is ensured:

1. Every processor generates the same number of eddies and disperses in the whole volume of the eddy box (or area of inlet plane of eddy box in later times steps) and not just the volume (or area) limited by the domain covered by the processor.
2. The random numbers that take care of random distribution of eddies and their strength, are generated in the same order for every processor, always, by the inbuilt random number generator provided by the C library that Gerris uses.

Consequently, every processor is dispersing the same number of eddies, at same locations and of same strength throughout the eddy box and therefore any discrepancies resulting otherwise is avoided. It can be seen that the random number generation in the same order is an essential condition to be able to parallelize the inlet domain.

† CFD calculations of Gerris are oblivious
‡ through `GfsFunction`

References:

AnuPravahaKiit, 2010, “Validation Problems for AnuPravahaKiit, the DAE-IITK General Purpose CFD Solver”, prepared under supervision of V. Eswaran.

CFD wiki, http://www.cfd-online.com/Wiki/Turbulence_free-stream_boundary_conditions, accessed on August 2011.

Driver, D. M. and Seegmiller, H. L., 1985 "Features of a Reattaching Turbulent Shear Layer in Divergent Channel Flow," AIAA Journal, Vol. 23, No. 2, p163.

Eriksson, J. G., Karlsson, R. I., Persson , J., 1998 “An experimental study of a two-dimensional plane turbulent wall jet ” Experiments in Fluids, Vol. 25, p50 .

Gerris syntax reference, http://gfs.sourceforge.net/wiki/index.php/Object_hierarchy

Kalitzin, G., Medic, G., Iaccarino, G. and Durbin , P., 2005, “Near-Wall Behavior Of RANS Turbulence Models and Implications For Wall Functions ” J. of Computational Physics 204 p265.

Kim, J., Moin, P. and Moser, R., 1987, “Turbulence Statistics in Fully Developed Channel Flow at Low Reynolds Number”, J. Fluid Mech., vol., 177, p133.

Menter, F., Ferrerirai, J. C., Eschi, T. and Konno, B., 2003, “The SST Turbulence Model with Improved Wall Treatment for Heat Transfer Predictions in Gas Turbines ”, Proceedings of the International Gas Turbine Congress 2003 Tokyo , p1.

NASA-1: http://turbmodels.larc.nasa.gov/sst.html, last accessed on August 2014

NASA-2: http://turbmodels.larc.nasa.gov/backstep_val.html, last accessed on August 2014

NASA-3: http://turbmodels.larc.nasa.gov/backstep_val_sst.html, last accessed on August 2014

Rajaratnam N (1976). Turbulent Jets. Elsevier Scientific, New York, 304

Spalding D.B., 1961, “A single formula for the law of the wall”, Journal of Applied Mechanics, Trans. ASME, Series E, Vol. 28, p455.

Uribe, Juan, http://cfd.mace.manchester.ac.uk/twiki/bin/view/CfdTm/TestCase001Res002, last revision on May 2009.

C. Appendix for Chapter 5

C.1 Eddy Box Dimensions

As depicted in Fig. 4.1b, the LES inlet is in the *x*-direction and the eddy box of SEM encloses this *y*-*z* plane. Now to find the eddy box dimensions according to Eq. (4.10), the extremes of *y* and *z* coordinates within the inlet plane and the maximum turbulence length scales (LS, from Eq. (4.26)] at these extremes have to be identified. The *y* coordinate is bound by the top and bottom edges of the inlet and the *z* coordinate is are bound by the lateral walls of TSM. The largest LS from each of these four edges is the maximum LS in their respective directions, whereas for the *x* direction, the largest LS in the entire inlet plane is the maximum LS. The maximum LS values are tabulated in Table 5.4; due to symmetry in the *z* direction only values at one edge is listed. However since the length scale in the *z* direction is too small it was set to 2.0 mm in all cases.

C.2 Compensation of Lost Volume of UP

The volume of upper phase lost due to removal of entrained droplets is compensated by a constant velocity boundary condition applied at the 'rear' face of the LES domain in the UP region. This results in pumping fluid of UP in the bulk UP. This boundary condition was activated whenever the difference in the initial and current UP volumes was greater than 1.0 % and the time span for which it lasted was calculated from,

$$\Delta t = \frac{\Delta V_{UP}}{U_{comp} A_{in,UP}} \tag{C.1}$$

where, ΔV_{UP} is the difference in initial and current UP volumes, $A_{in,UP}$ is the area of the rear face of the LES domain, U_{comp} is the constant velocity. The pumping has be to slow enough to be least intrusive while making up the lost UP quick enough. So following conditions were set:

$$U_{comp} = 0.3\, U_{ch}$$
$$A_{in,UP} = TTS\, h_U/2 \tag{C.2}$$

where, U_{ch} is the characteristics velocity used to non-dimensionalize the velocities in the simulation, TTS is thickness of thin-slice and h_U is the actual thickness of UP.

D. Appendix for Chapter 6

D.1 Coordinate Transformation from QSP-RANS to LES

The transformation of velocity from cylindrical to Cartesian coordinate systems is given by:

$$\begin{aligned} u &= u_r \cos\theta - u_\theta \sin\theta \\ w &= u_r \sin\theta - u_\theta \cos\theta \\ v &= u_z \end{aligned} \tag{D.1}$$

where (u_r, u_θ, u_z) and (u, v, w) are the velocities in cylindrical and Cartesian coordinate systems, respectively, and their corresponding coordinates are (r, θ, z) and (x, y, z), respectively. Since for an axisymmetric coordinate system, θ and u_θ are zero we have,

$$\begin{gathered} (U, V, W) = (U_r, U_z, 0) \\ (\overline{u'u'},\ \overline{v'v'},\ \overline{w'w'},\ \overline{u'v'},\ \overline{v'w'},\ \overline{w'u'}) = (\overline{u_r'u_r'},\ \overline{u_z'u_z'},\ \overline{u_\theta'u_\theta'},\ \overline{u_r'u_z'},\ \overline{u_z'u_\theta'},\ \overline{u_\theta'u_r'}) \end{gathered} \tag{D.2}$$

where U_i and u_i' are the mean and fluctuating velocities in both Cartesian and cylindrical coordinate systems and $\overline{u_i'u_j'}$ are the Reynolds stresses and in `GfsAxi`, $(r, z) = (y, x)$ and $(U_r, U_z) = (V, U)$.

D.2 Extract Reynolds Stresses from QSP-RANS

For this we consider the Boussineq eddy viscosity approximation in cylindrical coordinates, which, after applying the θ -symmetry conditions yields (in `GfsAxi` coordinate system),

$$\begin{aligned}
\overline{u_r' u_r'} &= -2\,\nu_T \frac{\partial V}{\partial y} + \frac{2}{3}k & \qquad \overline{u_r' u_z'} &= -\nu_T\left(\frac{\partial V}{\partial x} + \frac{\partial U}{\partial y}\right) \\
\overline{u_z' u_z'} &= -2\,\nu_T \frac{\partial U}{\partial x} + \frac{2}{3}k & \qquad \overline{u_z' u_\theta'} &= 0 \\
\overline{u_\theta' u_\theta'} &= -2\,\nu_T \frac{V}{y} + \frac{2}{3}k & \qquad \overline{u_\theta' u_r'} &= 0
\end{aligned} \tag{D.3}$$

where, k is the turbulent kinetic energy, ν_T is the turbulent or eddy viscosity. In `GfsAxi`, $(r, z) = (y, x)$ and $(U_r, U_z) = (V, U)$.

D.3 Gerris Parameter File for QSP-RANS and LES

QSP-RANS: See Appendix. E.1.

LES: See the attached file: `ladle-mutilphase-LES.gfs`

D.4 Extract Velocity Profiles Near *ULeye* from LES

This consists of four program files written in Shell and *C*. Following are the steps:

1. Copy-Paste the Gerris simulation outputs in a folder that contains all the four executables for this module.
2. Extract instantaneous velocities and the VOF variable (u, v, w, F) from Gerris simulation outputs, in a small volume of rectangular box surrounding the VOF surface, marked in Fig. 6.20.
    1. Edit the file `velocity-nomal-to-VOF.sh` for `$volume_condition` and `$VOF_condition` that are essentially `GfsFunctions`, to define the 'rectangular box'
    2. Execute `velocity-nomal-to-VOF.sh`; this edits and executes the Gerris simulation output files and outputs u, v, w, F in the 'rectangular box'.

3. Find nearest distance to VOF cells at *ULeye* from each cell in the 'rectangular box' (Sec. D.4.1).
    1. Edit `process-gerris-output.sh` for `$dL` , `$dist_max` and `$x_Ref`, wherever applicable. Each of the latter variables follow the dimensions used in the Gerris simulations. `$x_Ref` is any reference location in the x direction.
    2. Execute `process-gerris-output.sh`.
4. Calculate the mean and standard deviation (Sec. D.4.2)

Note that the portion of code for finding the area at *ULeye* in this set of codes is not the area mentioned in Appendix F.3, but the area confined to the rectangular box.

D.4.1 Find the Nearest Distance to VOF Nodes at ULeye

This is executed by the *C* program, `dist-to-VOF.c`.

1. Since in reality it is often it is difficult to differentiate between *ULeye* and *ULflat* around the corner, a (x, y) cutoff-location is first estimated (`xCutoff` and `yCutoff`) to narrow down the interface at *ULeye*. Edit criteria for `xCutoff` and `yCutoff`, if necessary.
2. Under 'Collect ids of vectors...' (Step-5 in code) edit the condition for location of *ULeye* with respect to `xCutoff`, if necessary.
3. For a given node in the 'rectangular box', find the nearest VOF node. Since the number of combinations between each node and the group of VOF nodes is very large and hence time consuming, the search for the nearest distance was limited to few z-planes from a certain node. It was found from trials that searching of three planes each in $+z$ and $-z$ directions with respect to the node in question gave very close results with the case where all nodes searched all VOF nodes.
4. Sort all nodes in the 'rectangular box' based on their distance to VOF nodes.

D.4.2 Averaging

This is executed by the *C* program, `stats-near-VOF.c`.

1. Choose coordinates for η.
2. For each η coordinate, find vectors in the range $\eta - \Delta < \eta < \eta + \Delta$, where Δ is slightly

greater than the smallest cell size in the LES and put them in their respective bin for η.

3. Mean and standard deviation of velocities in each η-bin are computed and outputted.

E. Appendix for Chapter 7

This Appendix is divided into two major sections. The first section discusses how information from Gerris simulation is imported into the Lagrangian Particle Tracking (LPT) code. The next section deals with various steps of the LPT code. Clarification of some terminology used in this Appendix:

- *Cell* refers to the unit of discretized volume in Gerris and it is square in 2D with a length of `dL`.
- *Node* refers to the location of a cell in Gerris that is not necessarily the centre of mass when imported to the LPT code. In the LPT code it also refers to the C-structure type and structure variable in which all information pertaining to that location is stored.
- The rectangular array of node locations in LPT code is referred to as *grid*.

E.1 Necessary Codes

The following is the list of attached program files.

- QSP-RANS in Gerris: `qsp-rans-for-lpt.gfs`
- LPT *C* code: `particle-tracking.c`
- Scripts to generate movie of particle trajectories:
  - Edit `gnuplot-script-for-movie.gnu` for necessary field to visualize.
  - Execute `generate-movie.sh`

Code snippets appearing in the rest of the Appendix are already included in the above codes.

E.2 Processing of Domain Variables

The LPT code reads from a Gerris simulation output, the node locations, boundary information and various scalars like velocity components and turbulence components for every node. Since Gerris uses a quadtree (in 2D) data structure importing of values on to a rectangular grid of the LPT code can be achieved with little effort. Rectangular grid is advantageous because every node can be rapidly accessed by their indices. However importing from Gerris simulation needs a tailored procedure. So this section walks through those details. In the code snippets provided in this section, Gerris domain variables have been used without any explanation or declaration. They can be referred from Gerris Manual.

E.2.1 In Gerris Parameter File:

This section discusses two types of outputs extracted from a Gerris simulation (QSP-RANS in Sec. E.1): 1) node locations and various scalars of *fluid domain* and 2) locations and type of *domain boundary*. For fluid domain, all outputs in this section are concerned with obtaining values at the node locations that is the centre of mass of a cell and achieved through the Gerris object, `GfsOutputSimulation` (in contrast with obtaining values at prescribed locations using `GfsOutputLocation`, see Gerris manual). The definition of various `GfsVariable`s used in the Gerris parameter file are also provided in this section.

E.2.1.1 Output of Fluid Domain:

For the rectangular grid of the LPT code, we need spatially uniform cell size in the Gerris simulations. Since grid refinement varies spatially in Gerris simulations, direct output of cell locations and scalars is not possible. So the 'cell level' (`Level`) of the Gerris output (`depth` parameter in `GfsOutputSimulation`) is changed to a level at and below which the cell sizes are uniform. Figure E.1 depicts a refinement scheme where above `Level = 8` the refinement is not uniform, in which case, the `depth` should be less than or equal to 8.

By simply setting, for example,

```
depth = 8
```

in the parameters of `GfsOutputSimulation`, the scalar values of cells (`GfsVariable`) whose `Level` is greater than 8 are averaged to their parent cell at `Level = 8` and is outputted by

`GfsOutputSimulation`. However it is not that simple in case of getting the node locations.

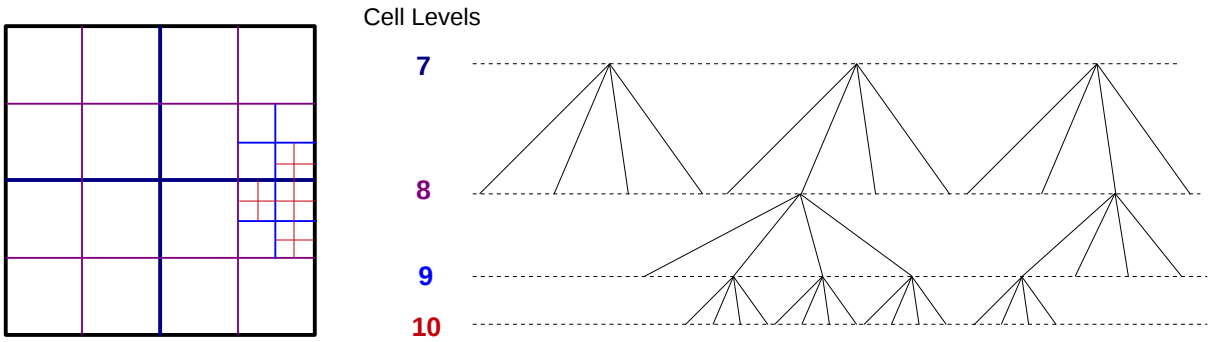

Figure E.1. Schematic of spatial variation of cell refinement. At and above `Level = 8` only some the cells have children.

The cells cut by the solid at the domain boundaries, have their centre of mass (x, y), displaced away from the geometric centre of the cell (cx, cy) (depicted in Fig. E.2a). As a result, the node locations (x, y), outputted by `GfsOutputSimulation` by default, are misaligned at the boundaries, with respect to the domain-interior node locations as shown in Fig. E.2b; this makes it difficult to apply the scalar values to the rectangular grid of the LPT code. To obtain a uniform grid, the *geometric centres* of the cells are outputted instead. To do this, coordinates of geometric centre have to be first declared as `GfsVariables`, say `CX, CY`:

```
1   . Init {} {
2   .   CX = cx
3   .   CY = cy
4   . }
```

and then outputted using `GfsOutputSimulation`. However for cells whose `Level` is greater than `depth`, the averaging of `GfsVariables` will average out `CX, CY` also, thereby resulting in incorrect geometric centres along the boundaries. So the following steps are done to overcome this:

1. Find the cell's parent at `Level = depth`
2. Find geometric centre of that parent
3. Store *that* location as `GfsVariables` in `CX, CY`.

This procedure applies to any other variable whose value has to be precise irrespective of the output `Level`. The snippet added to the Gerris Parameter file can be found in the file, `output-fluid-domain-for-LPT.gfs`

Also note the following in the file: The boundary type for spout region has been flagged so as to remove gravity in those nodes in the LPT code. The order of printing of variables has been reversed as `CY, CX, V, U` so that it is r, z, U_r, U_z when read at the LPT code, respectively.

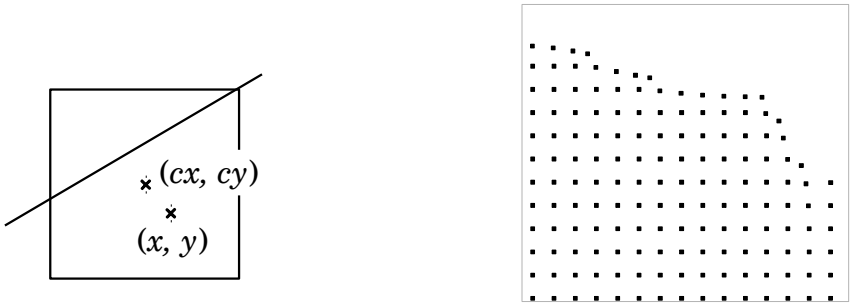

(a) **(b)**

Figure E.2. (a) Schematic of a cell cut by a solid surface has its centre of mass (x, y) displaced from geometric centre (cx, cy). (b) Node Location of cells cut by solid, misaligned with respect to the domain interior node locations

E.2.1.2 Output of Domain Boundary:

The domain boundary consists of a symmetry boundary at the ladle axis and various combinations of solid surfaces used for describing the ladle walls, the slag metal interfaces and the spout. The location of symmetry boundary can be extracted from the condition, `y < dL` while location of the solid surfaces are just the centre area of solid surface, `(ax, ay)`. The snippet to obtain the boundary location is,

```
1   . Init {} {
2   .   BX = (S > 0 ? ax : (y < dL ? x : 0))
3   .   BY = (S > 0 ? ay : (y < dL ? y : 0))
4   . }
```

In LPT code, to verify if a particle has stepped out of domain or not, a direction guide known as 'Point of Inward Vector' (pIV) is devised. A pIV is defined as the *end point* of an

inward pointing vector, originating from centre area of solid surface (`ax , ay`), passing through centre of mass of cell, for a distance of `dL` into the domain. The pIV is obtained as `GfsVariables`, say `xIV , yIV` as follows:

```
1   . Init {} {
2   .   xIV = (S ? x + dL*(sign(x-ax) : (y < dL ? x : 0))
3   .   yIV = (S ? y + dL*(sign(y-ay) : (y < dL ? dL : 0))
4   . }
```

Note that for the symmetry boundary, which does not have solid surface, a specific condition has to be given for pIV as seen in the secondary conditions in the snippet above. The result will be shown in Figs. E.5 (b) and (c)

All the boundary nodes of the domain are flagged according to their boundary type. The are two types of boundaries

1. the slag metal interface where particles are absorbed and
2. the remaining domain boundaries which are impermeable to particles

each flagged by values of two and one respectively and the domain interior gets a value of zero. The snippet added to the Gerris Parameter file can be found in the file, `output-domain-boundary-for-LPT.gfs`

E.2.2 In LPT Code

Flow chart in Fig. E.3 outlines the steps described in this section. In this context, input grid means the node locations and various scalars read from Gerris-RANS simulation output.

Step-1: Gerris output is read at LPT code

Step-2: First the distinct coordinates in the r and z directions are collected in z and `zdist`, respectively. With these coordinates, a grid with NC and NR number of columns are rows, respectively, is formed. Then for matching node locations of the grid with the Gerris output, the scalar values are stored in the nodes of the LPT grid. The locations in the $NR \times NC$ grid that have no corresponding nodes from the Gerris Output are flagged as non-existing. A typical LPT grid is shown in Fig. E.4a.

Wrapper Nodes: Since the fluid domain and boundary information from Gerris are outputted

at different `Levels` the boundaries may lie outside the edges of fluid domain grid as illustrated in Fig. E.4b. Problem occurs when a particle lands exactly in the region in between: since that region is outside the fluid domain grid, the particle has no information regarding any domain variables and crashes the code.

So extra nodes called wrapper nodes (similar to ghost cells) are created,

- for just one cell thickness in the direction normal to edge of the fluid domain so as to wrap around the boundary
- and has all scalar values copied from their 'associated' neighbors (read caption in Fig. E.4b)

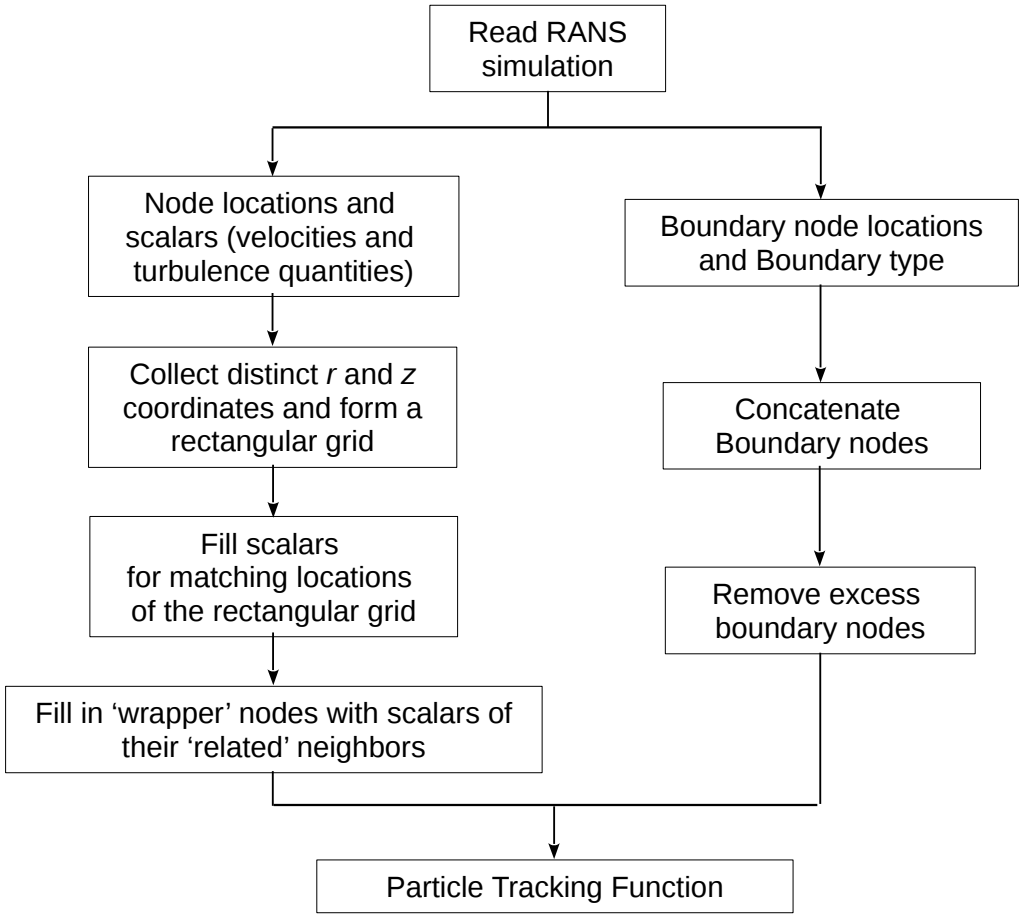

Figure E.3. Flowchart showing various steps done in LPT code to process domain variables

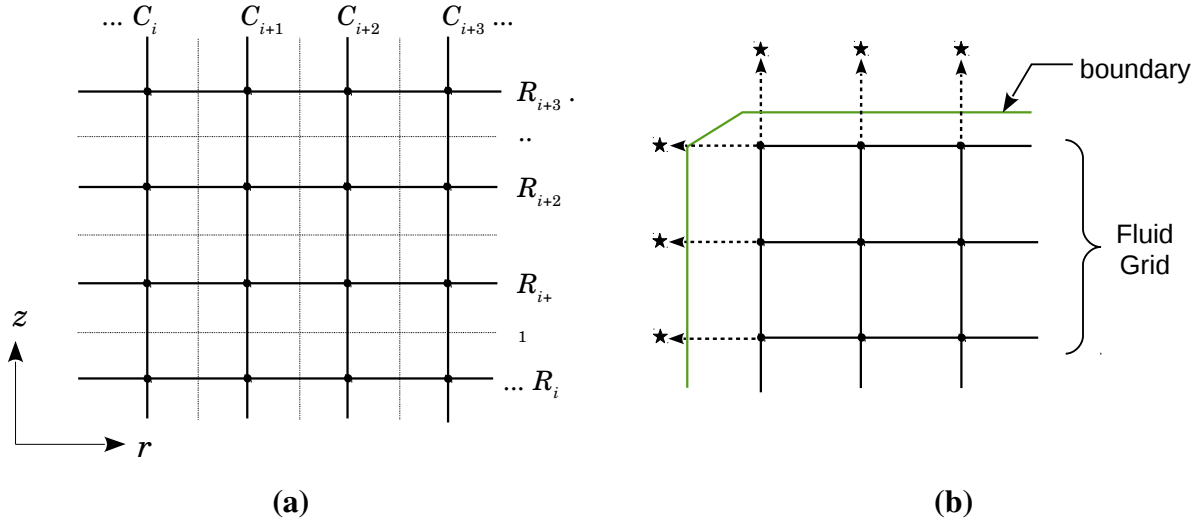

Figure E.4. (a) Various columns (*C*) and rows (*R*) of a rectangular grid and nodes at the intersection of rows and columns, in the LPT code. Each column and row correspond to unique *r* and *z* values respectively. The intersection of faint dotted lines form the cells in Gerris and the nodes in LPT code are at their centres (dark circles).
(b) The case where 'boundary' is outside the edges of fluid domain so that extra nodes called as 'wrapper nodes' (stars) are placed outside the grid of fluid domain, in the direction normal to edge of the fluid domain. The arrows show that these nodes get their scalars from their 'related' neighbors (also see Fig. E.9)

Step-3: Boundary information from Gerris, namely the node locations and the boundary type are read. The boundary nodes are sifted and stored in the array, `bp`.

Concatenate boundary nodes: 1) Node locations are sorted in ascending order with respect to the *r* coordinate. 2) Starting from the first node, its nearest node is found and added to the `bp` array and this way the entire old `bp` array is sorted.

Reduce the number of boundary edges: Detailed in Sec. E.2.3.

The result is shown in Fig. E.5.

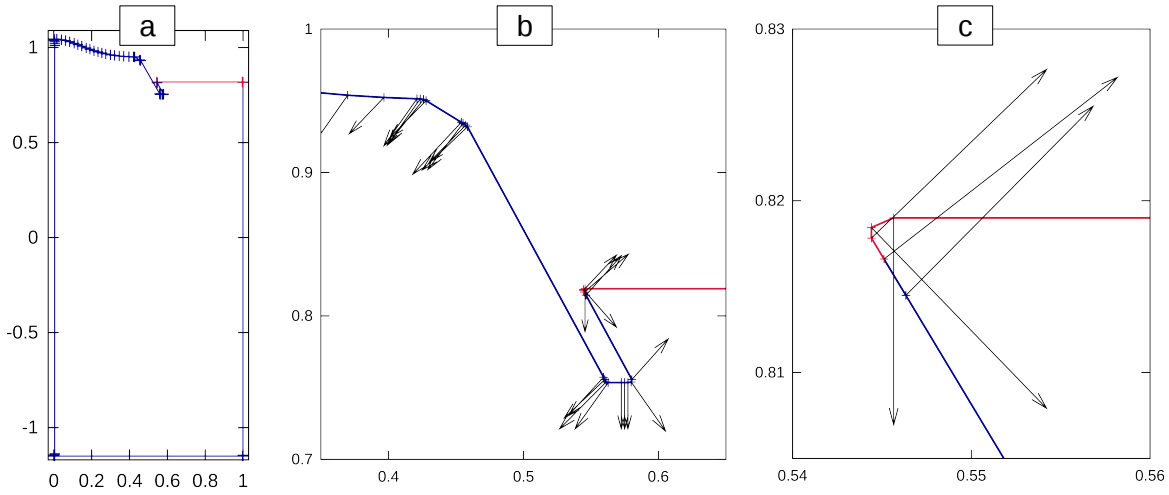

Figure E.5. (a) Rendered boundary in LPT code showing only fewer nodes (plus symbols) and the edges are colored according to `BcType`.
(b) and (c) Close ups of boundaries and inward pointing vectors in the lip and slag-eye regions

E.2.3 Reduce Boundary Nodes

Often, a boundary is just a straight line that only a few nodes at the ends of the line are sufficient to represent the boundary (*i.e.,* to supply the necessary boundary information). So the intermediate nodes can be removed and that saves enormous computational effort, since verifying the boundary conditions takes more than 75% of the total computational time, despite reducing the boundary nodes. This Function [`reduce_boundary_edges ()`] can reduce the number of nodes from around 3000 nodes to around 100 nodes. The idea is to remove all boundary points except when the boundary makes a significant turn and when the boundary type changes. In this context, solid surface means the undiscretized domain boundary in Gerris simulations and points refer to as boundary node, `bp`.

Algorithm - with reference to Fig. E.6:

- Start with i^{th} boundary point.
- Does the boundary type (`BcType`) changes?
  - If yes count i^{th} and $(i+1)^{th}$ points.
- Find the angle between vectors formed by $(i-1)^{th}$–i^{th} and i^{th}–$(i+1)^{th}$ points.

- Is the *angle* greater than 10° ?
  - If yes there is a turn in the boundary; count three consecutive points starting from i, if not counted before.
  - else if *angle* greater than 0.1°, count the i^{th} point, once in every few points, say 10 (specified by *interval* variable in the LPT code). This step will remove most of the points without compromising the shape of the domain boundary.

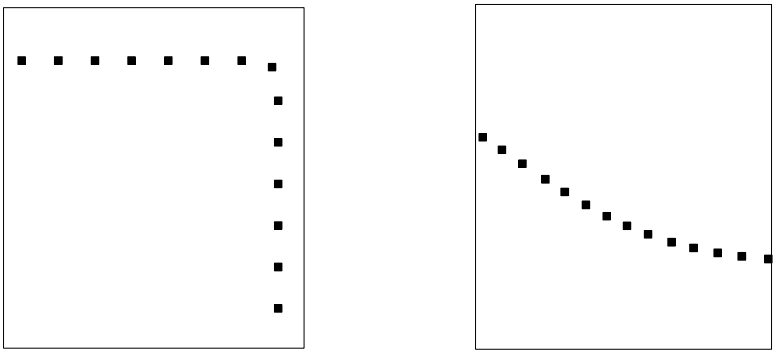

Figure E.6. The two figures show locations of centre of solid surface of a discretized solid surface (not shown in the figure). It is in the left figure, the solid surface is actually making a significant turn, whereas in the right, the local turns are very gradual

E.3 Particle Tracking Function

The various steps involved in this Function [`lagrangian_particle_tracking ()`], outlined in the Flowchart in Fig. 7.10, are detailed here.

E.3.1 Numerical Integration Schemes

Time integration of the particle trajectory equations (already stated in Ch. 7),

$$\frac{d\boldsymbol{U}_P}{dt} = \frac{1}{\boldsymbol{\tau}_R}(\boldsymbol{U}_F - \boldsymbol{U}_P) + \boldsymbol{A} \tag{E.1}$$

and

$$\frac{d\boldsymbol{x}_P}{dt} = \boldsymbol{U}_P \tag{E.2}$$

was performed using three numerical schemes taken from Fluent Manual, (2009).

Analytical Time Integration of Eq. (E.1) over a small time step Δt, within which the scalar components of $\boldsymbol{A}$, $\boldsymbol{U}$ and $\boldsymbol{\tau}_R$ are assumed to be constants, gives,

$$\boldsymbol{U}_P^{n+1} = \boldsymbol{U}_F + \boldsymbol{A}\,\boldsymbol{\tau}_R - \left(\boldsymbol{U}_F + \boldsymbol{A}\,\tau_R - \boldsymbol{U}_P^n\right)\exp\left(-\frac{\Delta t}{\tau_R}\right) \tag{E.3}$$

and that of Eq. (E.2) yields,

$$\boldsymbol{x}_P^{n+1} = \boldsymbol{x}_P^n + \left(\boldsymbol{U}_F + \boldsymbol{A}\,\boldsymbol{\tau}_R\right)\Delta t - \left(\boldsymbol{U}_F + \boldsymbol{A}\,\tau_R - \boldsymbol{U}_P^n\right)\left[1 - \exp\left(-\frac{\Delta t}{\boldsymbol{\tau}_R}\right)\right]\boldsymbol{\tau}_R \tag{E.4}$$

where, the components of $\boldsymbol{A}$, $\boldsymbol{U}$ and $\boldsymbol{\tau}_R$ correspond to the values at previous time step.

Special Case: When $(U_F - U_P) = 0$, $i = r$ or z, $\tau_{R,i} \to \infty$ and causes instability. To avoid this, setting $(\boldsymbol{U}_F - \boldsymbol{U}_P) = 0$ in Eq. (E.1) and integrating we get,

$$\boldsymbol{U}_P^{n+1} = \boldsymbol{U}_P^n + \boldsymbol{A}\Delta t \tag{E.5}$$

and Euler Implicit Discretization of Eq. (E.1) gives,

$$\boldsymbol{U}_P^{n+1} = \frac{\boldsymbol{U}_P^n + \Delta t\left(\boldsymbol{A} + \boldsymbol{U}_F/\boldsymbol{\tau}_R\right)}{1 + \Delta t/\boldsymbol{\tau}_R}, \tag{E.6}$$

whereas **Trapezoidal discretization** of Eq. (E.1) yields,

$$\boldsymbol{U}_P^{n+1} = \frac{\boldsymbol{U}_P^n\left(1 - \frac{1}{2}\frac{\Delta t}{\boldsymbol{\tau}_R}\right) + \frac{\Delta t}{\boldsymbol{\tau}_R}\left(\boldsymbol{U}_F + \frac{1}{2}\Delta t\,\boldsymbol{U}_P^n \cdot \nabla \boldsymbol{U}_F\right) + \Delta t\,\boldsymbol{A}}{\left(1 + \frac{1}{2}\frac{\Delta t}{\boldsymbol{\tau}_R}\right)}. \tag{E.7}$$

For both discretization schemes, the new particle location is computed from,

$$\boldsymbol{x}_P^{n+1} = \boldsymbol{x}_P^n + \frac{1}{2}\Delta t\left(\boldsymbol{U}_P^n + \boldsymbol{U}_P^{n+1}\right) \boldsymbol{x}_P^{n+1} = \boldsymbol{x}_P^n + \frac{1}{2}\Delta t\left(\boldsymbol{U}_P^n + \boldsymbol{U}_P^{n+1}\right). \tag{E.8}$$

In both the schemes when, $(U_F - U_P)_i = 0$, Eq. (E.5) is applied instead of (E.6) and (E.7), correspondingly and no such correction is required for particle displacement equation since it does not contain, $\tau_{R,i}$.

E.3.2 Computation of Acceleration Terms

The **fluid acceleration** in the Eulerian reference frame is defined and discretized as,

$$\begin{aligned}\frac{D\boldsymbol{U}}{Dt} &= \frac{\partial \boldsymbol{U}}{\partial t} + U_r\frac{\partial \boldsymbol{U}}{\partial r} + U_z\frac{\partial \boldsymbol{U}}{\partial z} \\ &= 0 + U_{r,C}\frac{\boldsymbol{U}_R-\boldsymbol{U}_L}{2\Delta} + U_{z,C}\frac{\boldsymbol{U}_T-\boldsymbol{U}_B}{2\Delta}\end{aligned} \tag{E.9}$$

and in the Lagrangian reference frame it is defined and discretized as,

$$\begin{aligned}\frac{d\boldsymbol{U}_F}{dt} &= \frac{\partial \boldsymbol{U}}{\partial t} + U_{P,r}\frac{\partial \boldsymbol{U}}{\partial r} + U_{P,z}\frac{\partial \boldsymbol{U}}{\partial z} \\ &= 0 + U_{P,r}\frac{\boldsymbol{U}_R-\boldsymbol{U}_L}{2\Delta} + U_{P,z}\frac{\boldsymbol{U}_T-\boldsymbol{U}_B}{2\Delta}\end{aligned} \tag{E.10}$$

where, $\boldsymbol{U}$ is the RANS mean velocity, subscripts C, R, L, T and B stand for current, right, left, top and bottom nodes, respectively, Δt and Δ are the time step and cell size, respectively.

The **particle acceleration** in Lagrangian reference frame can be computed directly from Eq. (E.1), however oscillating values leads to numerical instability. To overcome this, the average of acceleration given by Eq. (E.1) and the particle acceleration in the previous time step are used:

$$\boldsymbol{a}_{P,n+1} = \frac{1}{2}\left[\left(\frac{1}{\tau_R}(\boldsymbol{U}_F-\boldsymbol{U}_P) + \boldsymbol{A}\right) + \boldsymbol{a}_P\right]_n \tag{E.11}$$

E.3.3 Tackling Velocity Jumps Due to New Eddy

Whenever a new eddy is assigned to a particle there is a jump in the fluid velocity and hence the particle velocity and acceleration. This jump is due to the fluctuating velocity and more specifically due to the new random number. To enable smooth transition between the old and new values, the following steps are taken:

1. Split Δt as $\Delta t/N_{split}$ and apply for N_{split} steps.
2. For those N_{split} time steps, compute fluid velocity from,

$$\boldsymbol{U}_F = \boldsymbol{U} + u_E\left[BF\,\boldsymbol{\psi} + (1-BF)\,\boldsymbol{\psi_0}\right] \tag{E.12}$$

where the $\boldsymbol{\psi}$ and $\boldsymbol{\psi_0}$ are the random numbers of current and old eddies, respectively, and BF is a blending function calculated using a hyperbolic tangent function,

$$BF = \frac{1}{2} + \frac{1}{2}\tanh\left[\frac{i - N_{split}/2}{2}\right] \tag{E.13}$$

where i is the time step increment.

N_{split} was taken as 10 for all computations performed in this Thesis.

E.3.4 Interpolation of Scalars to Particle and Eddy Locations

Linear interpolation is applied to compute scalars for the particle moving in the rectangular grid, for every time step; since the present work is 2D, it is bilinear interpolation. The same scheme is applied to instantaneous eddy location, only to compute velocities for its motion. Following are the steps involved in this Function [`interpolate_scalars ()`] with reference to Figs. E.7 (a) to (c).

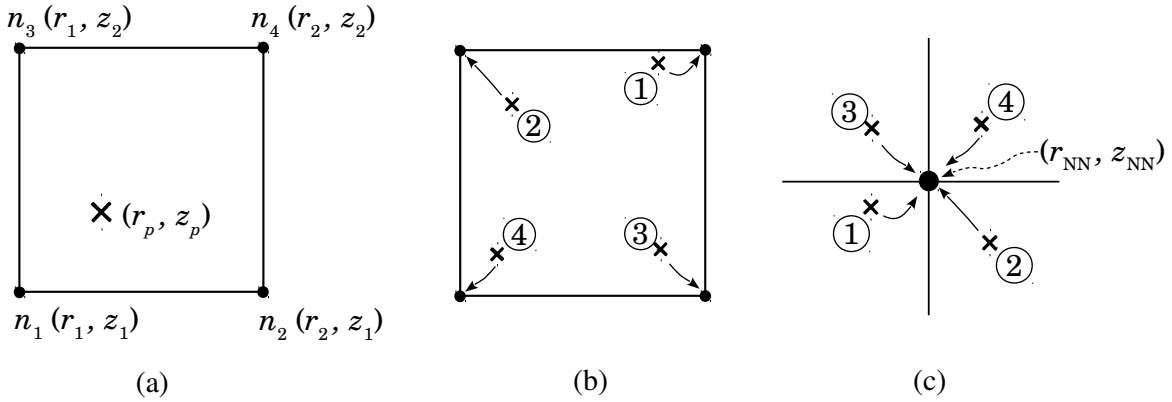

Figure E.7. (a) Coordinates of four nodes surrounding a particle (b) Depiction of four ways in which a particle can be oriented with respect to the nearest node. (c) Concept in Fig. b from a different perspective

Step-1: For a certain particle location, the indices of the row and column (`idrow` & `idcol`) nearest to that location are identified, and the nearest node is `node[idcol][idrow]`.

Step-2: At any instant a particle is surrounded by four nodes (except when being collinear with two nodes or lying on a node). There are four ways in which a particle can be oriented with respect to the nearest node

$$\begin{aligned}
&\texttt{case-1:}\quad r_p < r_{NN};\quad z_p < z_{NN}\\
&\texttt{case-2:}\quad r_p > r_{NN};\quad z_p < z_{NN}\\
&\texttt{case-3:}\quad r_p < r_{NN};\quad z_p > z_{NN}\\
&\texttt{case-4:}\quad r_p > r_{NN};\quad z_p > z_{NN}
\end{aligned}$$

where, (r_P, z_P) is the particle location and (r_{NN}, z_{NN}) is the location of the nearest node. Based on the orientation, the rest of the surrounding nodes are identified. The procedure can be illustrated for Case 1: The nearest node, `node[idcol][idrow]` is at n_4. The rest of the nodes at n_2, n_1 and n_3 are obtained by incrementing or decrementing indices by unity, to the indices of the nearest node; so the surrounding nodes are, `node[idcol][idrow−1]`, `node[idcol−1][idrow−1]` and `node[idcol−1][idrow]`, respectively. Since r and z have originally been filled in ascending order in the `node[][]`, by incrementing or decrementing the array indices the neighboring nodes can be accessed.

Step-3: The scalar values at the surrounding nodes are interpolated to the particle location using bilinear interpolation given by the equation,

$$\phi = \frac{1}{(r_2 - r_1)(z_2 - z_1)}\begin{bmatrix}\phi_{11}(r_2 - r)(z_2 - z) + \phi_{21}(r - r_1)(z_2 - z) + \\ \phi_{12}(r_2 - r)(z - z_1) + \phi_{22}(r - r_1)(z - z_1)\end{bmatrix} \tag{E.14}$$

where, ϕ is the scalar to be interpolated.

E.3.5 Verifying Boundary Conditions

Boundary conditions are verified for both particles and eddies, although for particles, while some boundaries are impermeable, for eddies, they are removed once they have jumped across any boundary. The steps involved in this Function [`verify_boundary_conditions ()`] are outlined in Fig. E.8 and detailed as follows, with reference to Fig. E.9:

1. From the `bp` array (Step 3, Sec. E.2.2) the nearest distance from the point (r_P, z_P) to various edges are found. The nearest distance from (r_P, z_P) to any edge bp_i–$bp_{(i+1)}$, is the distance to either of bp_i and $bp_{(i+1)}$, if the point is outside the edge or the perpendicular distance to the edge. The edge that gives the smallest distance is the *nearest boundary* edge, say bp_1–bp_2. This search for the nearest boundary edge is the most time consuming in the entire LPT code despite greatly reducing the boundary nodes.
2. The signed perpendicular distance between a point (r, z) and an edge $[(r_1, z_1),(r_2, z_2)]$ is given by

$$d = \frac{(r_2 - r_1)(z_2 - z) - (r_2 - r)(z_2 - z_1)}{\sqrt{(r_2 - r_1)^2 + (z_2 - z_1)^2}} \tag{E.15}$$

   Now, using Eq. (E.15) the distances from the nearest edge bp_1–bp_2 to the particle location, (r_P, z_P) and to the point of inward vector (Sec. E.2.1.2), (r_{IV}, z_{IV}) are calculated and their two signs compared; if they are both the same, the particle is within the fluid domain; else the particle is attempting to cross a boundary at that given time step.
3. If a particle is attempting to cross a slag metal interface, the particle is considered to have rejoined into slag phase and removed from further calculations.
4. If a particle is attempting to cross an impermeable boundary it is simply put back into the fluid domain at a distance dL from the nearest boundary edge, in the direction of inward pointing vector pIV, as demostrated in Fig. E.9. Moreover its velocity is set to the local fluid velocity and its acceleration is set to previous value.

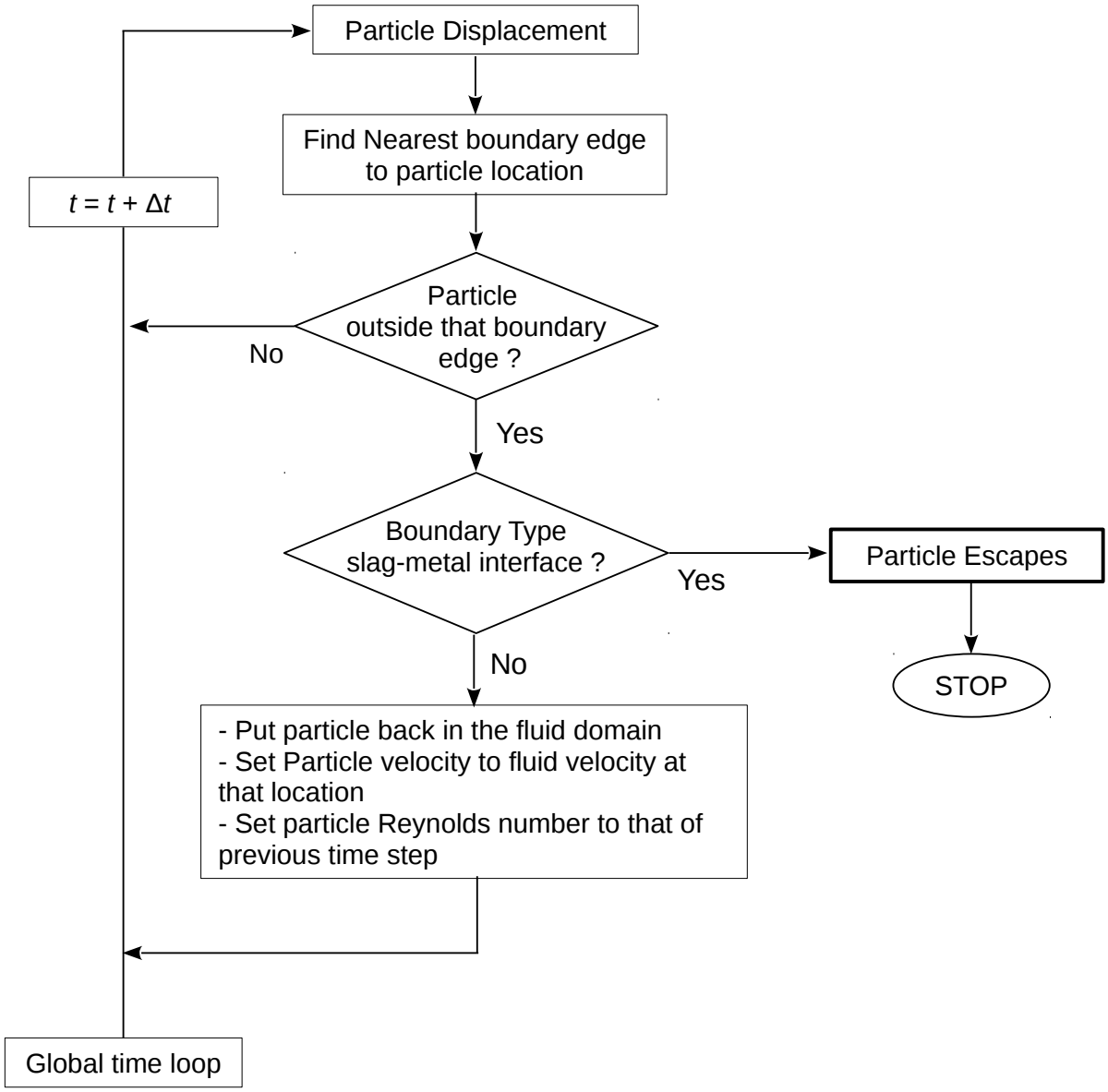

Figure E.8. Flowchart listing the steps involved in verifying boundary conditions

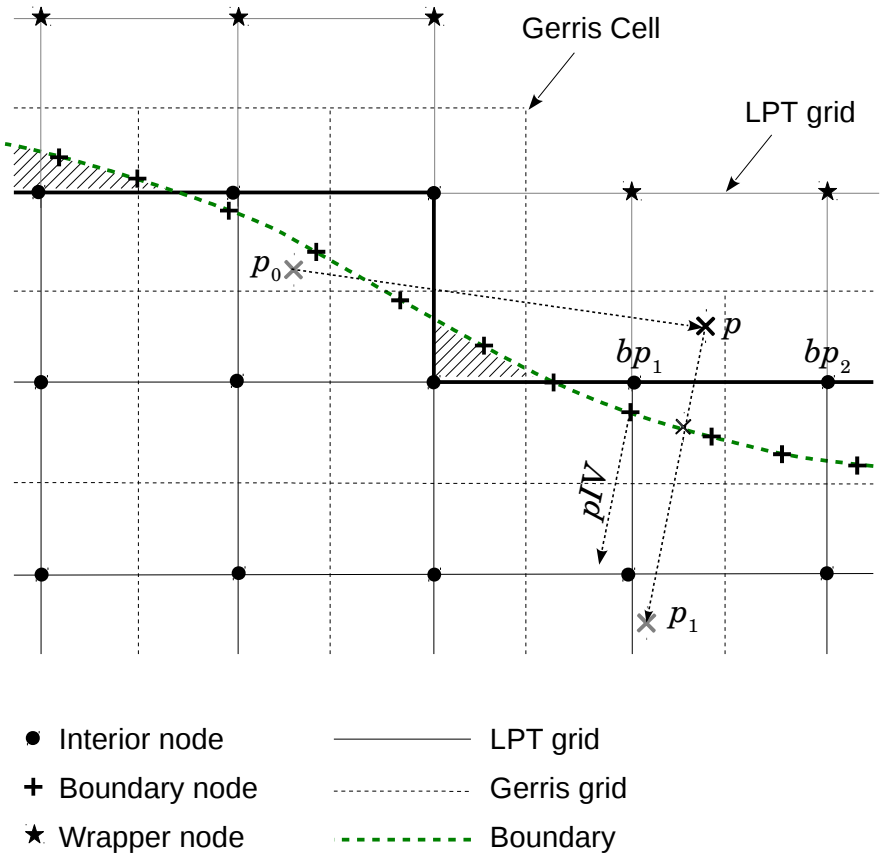

Figure E.9. Illustration of a particle at p having crossed a boundary from initial location p_0, is put back into the fluid domain at a distance of dL, from the nearest boundary edge $bp_1 - bp_2$, in the direction of pIV.

The figure also shows the Gerris cells surrounding the nodes of LPT code and the boundary of the latter and the pIV vector for a certain boundary node.
The hatched regions illustrate the need for wrapper nodes (described in Sec. E.2.2)

E.4 Run Cellular Verification Cases

For instructions, see the header of the code: `particle-tracking.c`. Compile and Execute the code and enter the choice of test cases and value for R when prompted.

F. Appendix for Chapter 8

F.1 Extract Length and Velocity Scales from QSP-RANS

See attached file `length-and-velocity-for-MTC.gfs`.

F.2 Droplet Size Distribution Parameters

Parameters of the lognormal distribution given by Eq. (3.20), fitted to the droplet size distribution obtained in the multiphase LES of 44 ton ladle cases in Ch. 6.

Table F.1. Parameters of droplet size distribution

Q_{sp}, lpm/ton	σ, N/m	A	B	C
4.0	0.5	1.636	0.926	0.609
	1.0	1.642	1.034	0.545
	2.0	1.738	1.114	0.506
2.0	0.5	1.564	0.834	0.676
	1.0	1.623	0.971	0.580
	2.0	1.705	1.064	0.530
1.0	0.5	1.513	0.836	0.674
	1.0	1.623	0.932	0.605
	2.0	1.665	1.039	0.542

F.3 Extract Interfacial Area at *ULeye* from LES

1. Copy-Paste Gerris simulation outputs in the folder that contains executables for this module.
2. Edit `code-for-ULeye-Area.sh` for `$area_condition` which is essentially a `GfsFunction` to mark the domain where area of *ULeye* is to be extracted. Execute `code-for-ULeye-Area.sh` to generate modified Gerris simulation outputs.

3. Run `code-to-run-gerris.sh` that will output the area of *ULeye* for each simulation output.

F.4 Derivation of $\beta - \varepsilon$ Curves of Berg *et al*

The following information appear in Berg *et al* (1985): for $\varepsilon < 600$ W/ton, $\beta \propto \varepsilon^{0.3}$ and $\beta \propto \varepsilon^{1.3}$, otherwise; secondly it is mentioned that for $\varepsilon = 15$ W/ton, $\beta = 0.058$ min^{-1}. From these, the correlations are derived as, $\beta = 4.3\times10^{-4}\varepsilon^{0.3}$ for $\varepsilon < 600$ W/ton, otherwise, $\beta = 7.2\times10^{-7}\varepsilon^{1.3}$.

Verification: There is actually a plot of rate constant versus ε in the paper; however the rate constant has indirect units of $(\Delta S/S_0)/min$ where S_0 and ΔS are the initial and the difference between initial and final sulphur concentrations, respectively. Let us say $\Delta S/S_0 \approx 0.9$. The rate constant at $\varepsilon = 600$ W/ton is read from the plot as $\beta \approx 0.2\ (\Delta S/S_0)/min$ which would mean that $\beta \approx 0.003\, s^{-1}$. From this we obtain the following correlations: $\beta \approx 4.4\times10^{-4}\varepsilon^{0.3}$ and $\beta \approx 7.3\times10^{-7}\varepsilon^{1.3}$ which are very close to the above correlations.

F.5 UP Thickness and Eye Radius for Multiple Bottom Plugs

In case of single bottom plug the following are readily available:

- The correlation for eye area of UP given by equations in Sec. 4.4.1.2.
- The equilibrium UP thickness, h_U be obtained iteratively from,

$$\pi R_{ves}^2 h_U - \frac{\pi}{3}(R_1^2 + R_1 R_2 + R_2^2) h_U = \pi R_{ves}^2 h_U^{nom}$$
$$R_1 = R_{eye},\ R_2 = R_{eye} + h_U \tan\theta_{ULeye} \qquad \text{(F.1)}$$

When multiple eyes appear due to multiple plugs and if single plug relations are applied the following occur:

1. The excess volume of UP removed due to additional eyes has to accommodated elsewhere that manifests as increase in h_U.
2. In the single plug correlations, for a given h_U^{nom}, there is a definite h_U and R_{eye}.

Therefore increase in h_U due to multi-plug would necessitate decrease in R_{eye}.

The increase in h_U due to multi-plug is as if excess UP as been added to a single plug ladle such that

$$h_{U,\,eq}^{nom} > h_U^{nom} \tag{F.2}$$

where $h_{U,\,eq}^{nom}$ is the single plug-equivalent nominal thickness of UP. So the radius of each eye has to be calculated using this $h_{U,\,eq}^{nom}$ in the eye-area correlations. Due to non-linearity, the system of equations are solved iteratively as follows:

For a given initial UP thickness, h_U^{nom}, gas flow rate and other parameters,

1. Estimate R_{eye}
2. Increase in h_U: Estimate h_U for multi-plug iteratively from,

$$R_{ves}^2 h_U \; - \; \frac{N_{plug}}{3}(R_1^2 + R_1 R_2 + R_2^2) h_U \; = \; R_{ves}^2 h_U^{nom} \tag{F.3}$$

   where N_{plug} is the number of bottom plugs and R_1 and R_2 are the same as in Eq. (F.1).

3. Decrease in R_{eye}: Estimate $h_{U,\,eq}^{nom}$ from single eye relation [rearranged Eq. (F.1)],

$$h_{U,eq}^{nom} \; = \; h_U \left[1 \; - \; \frac{1}{3 R_{ves}^2}(R_1^2 + R_1 R_2 + R_2^2) \right] \tag{F.4}$$

   using which estimate R_{eye}.

4. Using h_U^{nom} (not $h_{U,\,eq}^{nom}$) and updated R_{eye} go to step 2. Repeat these steps until convergence.

F.6 Kinetic Role on Desulphurization Potential

In Bannenberg *et al* (1994) the desulphurization potential (DSP) is defined as,

$$\mathrm{DSP} = \frac{(\%S)}{[\%S]}\frac{1}{[\%Al]^{2/3}} = K\frac{a_{CaO}}{a_{Al_2O_3}^{1/3}} \tag{F.5}$$

It was mentioned in the reference that oxide activities in multicomponent slags cannot be measured easily. So it is clear that DSP was calculated from the first ratio in Eq. (F.5) than the second, wherein the quantities were measured from plant trials and the plot against lime content is Fig. 8.7b. Since in actual practice, equilibrium is rarely achieved, the ratio $(\%S)/[\%S]$ has both the thermodynamic and kinetic influence on it. Thermodynamic influence is through the lime activity which is lowered when *LSI* < 1 and also when *LSI* > 1 because of undissolved lime reducing the (%CaO). Kinetic influence is through slag viscosity that increases with *LSI*, leading to lowered DSP, although that happens only above *LSI* > 1 as in Fig. 8.7b.